

Rare and low-frequency variants and predisposition to complex disease



Patrick K. Albers

Wellcome Trust Centre for Human Genetics
Green Templeton College
University of Oxford

Supervised by
Professor Gil McVean
Professor Mark McCarthy

Submitted in Partial Fulfilment of the Requirements for the Degree of
Doctor of Philosophy (DPhil)

Hilary 2017

Acknowledgements

This work would not have been possible without the patience of my supervisors, Gil McVean and Mark McCarthy. If my work will prove to be useful, it is because of their guidance.

I dedicate this thesis to my parents, for their unconditional love and their relentless efforts to support me in my studies. I also want to express my gratitude to my mentors, who have guided me over the years, and those who taught me valuable lessons, during my time as a Bachelor student, during my time as a Master student, and in between; to Nico Michiels (Eberhard Karls Universität Tübingen, Germany) who was the first to spark my interest in statistics, to Christopher Bartlett (James Cook University, Australia) who made my first research project possible, to the people of Vanuatu who will always have a special place in my heart (I was the scientific advisor to a marine protected area), to the people of Laos who taught me to appreciate the small things in life (I was a teacher in a Buddhist temple school), to Mikeal Thollesson (Uppsala Universitet, Sweden) who fostered my enthusiasm for Evolutionary Biology, to Sophie Caillon (Université de Montpellier II, France) who showed me that communication is key, to Scott Edwards (Harvard University, United States) who stopped working on a crucial grant application to write a recommendation letter for my application to the University of Oxford, to Dirk Mentzler (Ludwig-Maximilians Universität Munich, Germany) who taught me to not blindly trust any statistical results. Lastly, I want to thank my friends for their support and their understanding.

Rare and low-frequency variants and predisposition to complex disease

Patrick K. Albers

Wellcome Trust Centre for Human Genetics
Green Templeton College
University of Oxford

Submitted in Partial Fulfilment of the Requirements for the Degree of
Doctor of Philosophy (DPhil)

Hilary 2017

Recent advances in high-throughput genomic technologies have enabled the collection of DNA information for thousands of individuals, providing unprecedented opportunities to learn about the genetic architecture of complex disease. One important finding has been that the majority of variants in the human genome are low in frequency or rare. It has been hypothesised that the recent explosive growth of the human population afforded unexpectedly large amounts of rare variants with small but deleterious effects, suggesting that rare variants may play a significant role in the predisposition to complex disease. Moreover, properties specific to rare variants embody a rich source of information relating to their evolutionary history.

In this thesis, I develop several statistical methods to address problems associated with the analysis of rare variants in the context of large cohorts linked to biomedical phenotype data, and to leverage the information they encode. Firstly, one constraint in genome-wide association studies is that lower-frequency variants are not captured by genotyping methods, but instead must be predicted through imputation from a reference panel. I develop a method to improve imputation accuracy by integrating genotype data from multiple reference datasets, which outperformed imputations from separate references in almost all comparisons (mean correlation with masked genotypes $r^2 > 0.9$). In a series of simulated case-control experiments, I demonstrate that this approach (meta-imputation) increases power to identify low-frequency variants of intermediate or high penetrance, improving power by 2.2–3.6%. Secondly, I utilise rare variants as identifiers for recently co-inherited shared haplotypes, as rare variants are likely to have originated recently through mutation, making them highly population-specific. I develop a non-probabilistic method to detect shared haplotype segments that are identical by descent (IBD) from patterns of allele sharing and the detection of recombination breakpoints. I show that the latter can be inferred with higher accuracy at very low allele frequencies ($\leq 0.05\%$, $r^2 > 0.99$) using either haplotype or genotype data. Thirdly, I show that genotype error poses a major problem in the analysis of empirical data, for example as obtained through whole genome sequencing or SNP genotyping, in particular towards lower allele frequencies (false positive rate, FPR = 0.1, at frequency $\leq 0.05\%$). I therefore subsequently propose a novel approach to infer IBD from genotype data using a Hidden Markov Model (HMM) under an empirical error model, which I construct by identifying misclassified genotypes in existing datasets, showing that the HMM is robust in presence of error ($\leq 0.05\%$, $r^2 > 0.98$) while previous methods fail ($r^2 < 0.02$). Finally, the age of a rare allele (time since its creation through mutation) may provide evidence about the selective forces that resulted in its observed frequency, and its impact on fitness. I further develop a novel method to estimate rare allele age, based on the inferred IBD structure of a sample. I demonstrate that allele age can be estimated with high accuracy using the HMM-based approach for IBD detection, even in presence of genotype error (Spearman correlation coefficient $r_S = 0.74$, compared to $r_S = 0.82$ when true IBD data is available). I apply this method to data from the 1000 Genomes Project, showing that there are notable age differences between rare alleles of varying predicted phenotypic consequences.

Contents

List of Figures	vii
------------------------	-----

List of Tables	x
-----------------------	---

1 Introduction	1
1.1 Aims and structure of this thesis	3
1.2 Basic concepts and terminology	6
1.2.1 Mutation	9
1.2.2 Recombination	10
1.3 Models in population genetics	12
1.3.1 Wright-Fisher model	12
1.3.2 Coalescent theory	16
1.4 Advances in high-throughput genomic technologies	28
1.4.1 Next-generation sequencing	29
1.4.2 Exploration of the human genome	31
1.5 Genome-wide association studies	34
1.6 Identity by descent	36
1.6.1 Single-locus concept	37
1.6.2 Genealogical concept	37
1.7 Allele age estimation	40
1.7.1 Theoretical results	40
1.7.2 Application in human disease research	42
2 Meta-imputation of reference data to increase accuracy and power in association analysis	45
2.1 Introduction	45
2.2 Approach	48
2.2.1 Description of the method	49
2.2.2 Score metrics	51
2.2.3 Merge operations	53
2.3 Generation of reference datasets	54
2.4 Accuracy of estimated genotypes	56
2.4.1 Methods	57
2.4.2 Results	59
2.5 Power to detect significant risk signals	70
2.5.1 Methods	70
2.5.2 Results	74
2.6 Discussion	79

3 Using rare variants to detect haplotype sharing and identity by descent	84
3.1 Introduction	84
3.2 Rare variants as indicators of haplotype sharing by descent	87
3.3 IBD detection around rare variants	89
3.3.1 Inference of historical recombination events	91
3.3.2 Description of the algorithm	93
3.3.3 Anticipated limitations	95
3.4 Genotype phasing by inference of the shared haplotype	98
3.4.1 Genealogical constraints arising from IBD	99
3.5 Evaluation	101
3.5.1 Data generation	101
3.5.2 Accuracy analysis	104
3.6 Results	105
3.7 Discussion	123
4 Consideration of genotype error in the inference of haplotype sharing by descent	125
4.1 Introduction	125
4.1.1 Probability of genotype error	127
4.2 Generation of platform-specific genotype error profiles	129
4.2.1 High-confidence genome data as benchmark for comparisons	130
4.2.2 Selection and preparation of datasets from different platforms	131
4.2.3 Penetrance of genotype error in sequencing and genotyping data	134
4.3 Impact of genotype error on IBD detection	140
4.3.1 Integration of empirical error distributions in simulated data	141
4.3.2 Results	142
4.3.3 Discussion	150
4.4 A Hidden Markov Model for IBD inference	151
4.4.1 The algorithm for probabilistic IBD inference	153
4.4.2 Description of the model	154
4.4.3 Integration of empirically determined genotype error rates	162
4.4.4 Inference of IBD segments	167
4.4.5 Results	170
4.4.6 Discussion	174
5 Estimation of rare allele age	177
5.1 Introduction	177
5.2 Approach	179
5.2.1 Coalescent time estimators	180
5.2.2 Cumulative coalescent function	184
5.2.3 Composite likelihood estimation of mutation time	185

5.2.4	Inference of IBD around shared and unshared alleles	188
5.3	Evaluation	192
5.3.1	Data generation	192
5.3.2	Accuracy analysis	195
5.4	Results	196
5.4.1	Validation of the method under different thresholds	197
5.4.2	Comparison of IBD detection methods	203
5.4.3	Impact of genotype error on allele age estimation	209
5.5	Age of alleles with predicted effects in 1000 Genomes data	221
5.5.1	Quality control	221
5.5.2	Error correction based on allele frequency	222
5.5.3	Results	223
5.6	Discussion	226
6	Discussion	228
6.1	Implications for genome-wide association studies	228
6.2	The importance of haplotype sharing by descent	230
6.3	The potential of estimating the age of alleles	232
Abbreviations		234
Bibliography		236

List of Figures

1.1	The chemical structure of DNA	7
1.2	Alleles, haplotypes, and genotypes	8
1.3	Illustration of recombination during meiosis	11
1.4	Example genealogy in a Wright-Fisher model	13
1.5	Allele frequency changes over time simulated under the Wright-Fisher model	15
1.6	Topology of a genealogical tree in the coalescent	17
1.7	Mutation events on a genealogical tree in the coalescent	23
1.8	Illustration of the ancestral recombination graph	26
1.9	Timeline of sequencing technologies and milestone projects	30
1.10	Timeline of cost reduction in DNA sequencing	31
1.11	Allele frequency spectrum in the 1000 Genomes Project	33
1.12	Significant risk-associated variants listed in the NHGRI-EBI Catalogue	35
1.13	Risk-related variants by allele frequency and effect size	36
1.14	Illustration of haplotype sharing by descent	39
2.1	Illustration of the meta-imputation concept	50
2.2	Generation of reference panels in each scenario	55
2.3	Illustration of the accuracy assessment process	58
2.4	Accuracy comparison of score metrics and merge operations in meta-imputation	61
2.5	Accuracy comparison between meta-imputation and direct imputations	65
2.6	Difference between imputed and masked minor allele frequency	69
2.7	Illustration of the simulation process	73
2.8	Inflation observed in simulated case-control experiments	76
2.9	Power measured under a moving significance threshold	77
3.1	IBD structure and pairwise variant sharing	88
3.2	Rare variant sharing in the 1000 Genomes dataset	90
3.3	Breakpoint detection using the four-gamete test (FGT)	92
3.4	Breakpoint detection using the discordant genotype test (DGT)	93
3.5	Illustration of shared haplotype detection in a pair of diploid individuals .	94
3.6	Examples of the underlying IBD structure in each pair of four chromosomes	97
3.7	Genealogical constraints from haplotype sharing	100
3.8	Demographic model used in simulations	102
3.9	Accuracy of breakpoint detection in simulated data	108
3.10	IBD segment lengths inferred in simulated data	109

3.11 Accuracy of breakpoint detection in simulated data using Refined IBD in Beagle 4.1	112
3.12 IBD segment lengths inferred using <i>Refined IBD</i> in Beagle 4.1	114
3.13 Distribution of inferred IBD lengths in 1000 Genomes data, chromosome 20	20117
3.14 Accuracy of alleles inferred through IBD-based phasing by focal allele frequency	119
3.15 Error distribution of alleles inferred through IBD-based phasing	120
3.16 Cumulative shared haplotype coverage by focal allele count in 1000 Genomes data	122
4.1 CEPH pedigree 1463	130
4.2 Illustration of the matching process in the generation of error profiles	133
4.3 Positional genotype error density in sequencing and genotyping datasets	135
4.4 Frequency-dependent distribution of genotype penetrance in sequencing and genotyping data	139
4.5 Misclassification of target sites in presence of genotype error	143
4.6 Accuracy of IBD detection using <i>tidy</i> after inclusion of genotype error	145
4.7 Length distribution of IBD segments using <i>tidy</i> after includion of genotype error	147
4.8 Example of the effect of genotype error on IBD detection	148
4.9 Accuracy of IBD detection using <i>Refined IBD</i> after inclusion of genotype error	149
4.10 IBD length detected using <i>Refined IBD</i> after inclusion of genotype error	150
4.11 Illustration of the Hidden Markov Model for IBD inference	155
4.12 Probability distribution of transition dependent on IBD	158
4.13 Expected frequency distribution of genotype pairs under non-IBD and IBD	161
4.14 Difference between empirical and expected proportions of genotype pairs	164
4.15 True positive rate of identified genotype pairs at focal sites	167
4.16 Accuracy of IBD breakpoint detection using the Hidden Markov Model on simulated data, before and after error	172
4.17 Length distribution of shared haplotype segments using the Hidden Markov Model on simulated data	173
4.18 IBD inference using the Hidden Markov Model on 1000 Genomes data, chromosome 20	174
4.19 Empirical emission probabilities of genotype pairs dependent on time	175
5.1 Allele age in relation to concordant and discordant pairs	186
5.2 Example of the age estimation result for a focal variant	187
5.3 Breakpoint detection in discordant pairs	189
5.4 Initial state probability of discordant pairs in the Hidden Markov Model (HMM)	191
5.5 Expected estimation bias due to deficient IBD inference	193

5.6	True and inferred age under varying numbers of discordant pairs	198
5.7	Relative age under varying numbers of discordant pairs	201
5.8	Distribution of true and inferred age using different IBD detection methods	205
5.9	Relative age using different IBD detection methods	207
5.10	Length distribution of inferred IBD segments	208
5.11	Density distribution of allele age before and after the inclusion of genotype error in simulated data	211
5.12	Length distribution of inferred IBD segments before and after error	217
5.13	Estimated correction factors before and after error	219
5.14	Allele age estimated on functionally annotated data in 1000 Genomes . . .	224
5.15	Allele age after correction on population-specific frequency in 1000 Genomes	225

List of Tables

2.1	Dimensions of generated reference data used for imputations	56
2.2	Variants retained after quality control per meta-imputation setting	60
2.3	Accuracy measured for each meta-imputation setting	62
2.4	Effect of quality control on imputed genotype data	64
2.5	Accuracy of imputation strategies at rare, low-frequency, and common variants	67
2.6	Estimated power per imputation strategy	80
3.1	Shared haplotype inference from genotype pairs	101
3.2	Accuracy of detected breakpoints per f_k category	106
3.3	Inferred IBD length per chromosome in 1000 Genomes	116
4.1	Penetrance functions in genotype and allele-based error models	129
4.2	Measured genotype penetrance in sequencing and genotyping data	137
4.3	Punnett squares of genotype pair partitions under non-IBD and IBD	160
4.4	Accuracy comparison per f_k category after error	171
5.1	Estimation accuracy under varying numbers of discordant pairs	200
5.2	Estimation accuracy per IBD detection method	206
5.3	Conflicted estimates in analyses before and after error	209
5.4	Effect of genotype error on age estimation accuracy	220
5.5	Allele age per population in the 1000 Genomes sample	226

Two distinct elements are included under the term “inheritance” – the transmission, and the development of characters.

— Charles Darwin, The Descent of Man

1

Introduction

Contents

1.1	Aims and structure of this thesis	3
1.2	Basic concepts and terminology	6
1.2.1	Mutation	9
1.2.2	Recombination	10
1.3	Models in population genetics	12
1.3.1	Wright-Fisher model	12
1.3.2	Coalescent theory	16
1.4	Advances in high-throughput genomic technologies	28
1.4.1	Next-generation sequencing	29
1.4.2	Exploration of the human genome	31
1.5	Genome-wide association studies	34
1.6	Identity by descent	36
1.6.1	Single-locus concept	37
1.6.2	Genealogical concept	37
1.7	Allele age estimation	40
1.7.1	Theoretical results	40
1.7.2	Application in human disease research	42

It is perhaps surprising that the old question of how many angels can dance on the head of a pin has been answered in the following way: the human genome consists of 23 chromosome pairs which harbour more than 20 thousand genes embedded in a filigree molecular filament that encodes a sequence which is more than 3 billion nucleotides long and which itself is the result of an ongoing evolutionary process that began when life emerged on this planet around 3.5 billion years ago; yet all of this information is compacted into the 10 µm wide nucleus of a cell. The genetic material contained within

this microscopic dot determines the development of an organism, its ability to interact with and react to the environment, as well as its predisposition to disease.

One of the main goals of modern genetic research is to learn about the genetic architecture that underpins heritable disease traits. Early efforts in disease research were directed towards the identification of genetic variants with highly penetrant effects on disease traits; *e.g.* mutations that contribute to distinct phenotypes, such as cystic fibrosis or Huntington's disease, which typically segregate within families (*i.e.* *monogenic* or *Mendelian* diseases). The classical approach to locating (or *mapping*) the genetic factors involved in such 'simple' diseases is linkage analysis within affected families (*e.g.*, see Morris and Cardon, 2007). While linkage studies have been successful in the identification of genetic factors underlying Mendelian diseases (Altshuler *et al.*, 2008), they have been less powerful with regard to locating variants that influence complex disease risk, such as type 2 diabetes, because each variant individually may only contribute modestly to disease susceptibility (Risch, 2000; Botstein and Risch, 2003). Genome-wide association (GWA) studies have become the preferred method to interrogate common variants in the context of complex traits; they have uncovered significant associations between thousands of genetic factors and major common diseases, and have been a driving force in the ongoing accumulation of more, larger, and denser genomic datasets.

One major insight gained from the extensive study of the (human) genome is that the genetic variation between individuals is mostly determined by *common* variants (*e.g.* $\geq 5\%$ frequency), but most variant sites in the genome are *rare*; that is, a particular allele is shared by only a few individuals in the population (*e.g.* 1 in 1,000). In general, low-frequency variants tend to be population-specific, but may also be highly differentiated between demographic groups on a finer scale (Henn *et al.*, 2011; Bustamante *et al.*, 2011; Mathieson and McVean, 2014). This is because rare variants are likely to have a relatively recent origin through mutation; *i.e.* they are "young" in age and therefore have less time to spread. In comparison, genetic factors that contribute to substantial disease risk (particularly with early onset) are likely to be under purifying selection, which implies that they should be observed at relatively low frequencies (Kryukov *et al.*, 2007; Marth *et al.*,

2011). Recent research has indicated that the human genome harbours an unexpectedly high number of rare, deleterious variants due to the recent, exponential growth of the human population (Coventry *et al.*, 2010; Keinan and Clark, 2012; Tennessen *et al.*, 2012).

Rare variants are now widely considered to play an important role in the predisposition to complex disease (Bodmer and Bonilla, 2008; Schork *et al.*, 2009; Manolio *et al.*, 2009; McClellan and King, 2010; Cirulli and Goldstein, 2010), though their contribution has been hypothesised for more than a decade (Pritchard, 2001). However, the interrogation of alleles found at lower frequencies is not straightforward. For instance, rare variants may not exert large enough effects to be detected by family-based linkage studies. Conversely, rare alleles are generally too low in frequency to achieve statistical significance in association tests. An additional complication applies, namely that genotyping arrays are typically not designed to capture low-frequency variants and, on the other hand, sequencing coverage may be insufficient to call rare variants with confidence. Hence, there are considerable challenges to be addressed.

1.1 Aims and structure of this thesis

The overall aim of this thesis is to develop novel strategies and computational methods to harness the information represented by rare and low-frequency variants, and to demonstrate that these methods provide workable solutions for application to existing genomic datasets. In particular, I address the problems typically associated with the analysis of rare variants but, primarily, I focus on the opportunity that arises from the genealogical properties of alleles found at lower frequencies. Thus, the aims of this work relate to the “heads and tails” of rare variants and can be summarised as follows.

- To increase the statistical power to detect significant signals in GWA studies by developing a method that integrates information from multiple reference datasets for imputation into a given study sample; thus attempting to optimise the ability to implicate low-frequency and rare variants as contributing factors to disease risk.

- To utilise rare variants as a source of information about relatedness and haplotype sharing by descent, which aligns with two objectives; first, to develop a method for the inference of the underlying identity by descent (IBD) structure in which a given allele of interest is embedded, and second, from this, to develop a method to reconstruct the sequence of coalescent events such that the age of the allele can be estimated.

These two main goals entail distinct analytical paradigms, both being motivated by the overarching purpose to learn more about the genetic architecture that predisposes disease risk. Under the first paradigm, the genetic variation observed in a sample is examined in order to discern variants that associate with a certain phenotypic (disease) trait; this approach can therefore be described as being *phenotype-focused*, which I cover only in the first chapter following this introduction. In the chapters thereafter, I advocate a *variant-centric* approach, which aims to better understand the patterns of descent that led to the emergence of a disease phenotype in a population. In particular, knowledge about allele age is of interest to a wide range of problems studied in both population and medical genetics, as it allows us to observe demographic changes over time and to learn more about past events and evolutionary processes which came into effect somewhere along the branches of a genealogical tree.

In the following, I further describe the structure of this thesis by briefly presenting the objectives as addressed in each chapter. In the remainder of this introduction (**Chapter 1**), I explain the basic terminology and provide further information about the subjects touched upon below.

Chapter 2. I focus on the population or cohort-specific coverage of genetic variation as a limiting factor to the imputation and subsequent interrogation of low-frequency and rare variants in GWA studies. I propose a new method which integrates genotype data after performing separate imputations from multiple reference panels into a given study sample, such that the combined set of variants across references is available for association analysis.

Chapter 3. I propose a non-probabilistic method for the detection of recombination events around target sites in either haplotype or genotype data. The method capitalises on the presumed young age of rare variants to identify (recent) relatedness in samples of reportedly unrelated individuals, thereby facilitating the detection of relatively long stretches of pairwise shared haplotypes that are identical by descent (IBD).

Chapter 4. I characterise the extent of genotype error in data obtained on different genotyping and sequencing platforms, so as to investigate the impact of error on IBD detection. The results of this analysis are incorporated in a probabilistic model that is enabled for the inference of IBD tracts using a Hidden Markov Model (HMM), thereby improving on the method presented in Chapter 3.

Chapter 5. I propose a novel method for the estimation of (rare) allele age, *i.e.* the time since a mutation event gave rise to a particular allele that is observed in sample data. The method is a coalescent-based composite likelihood approach and operates on insights gained from the inferred IBD structure of the sample; thus, prior knowledge of the demographic history of the population or the genealogy of the sample is not required. I apply this method to data from the 1000 Genomes Project (1000G) Phase III on variants with predicted consequences.

Lastly, I conclude this thesis by providing a summary of the relevant results and by highlighting the implications of the presented methodology for future research (**Chapter 6**).

In the following, I outline the biological concepts relevant to define basic terminology (Section 1.2, next page), as well as the principal definitions in population genetics that underpin the methodology developed in this thesis (Section 1.3, page 12). I then provide a summary of available genomic technologies which are the essential tools for the exploration of the human genome (Section 1.4, page 28). I reserve the remaining sections of this chapter to provide an introduction to genome-wide association (Section 1.5, page 34), the definition of identity by descent (Section 1.6, page 36), and the implications of allele age estimation (Section 1.7, page 40).

1.2 Basic concepts and terminology

The term *genome*, which was coined almost a century ago (Winkler, 1920), refers to the totality of the genetic hereditary information and its organisation into *chromosomes*. The number of chromosomes is characteristic for an organism, as is the number of chromosome sets, referred to as *ploidy*. Cells with only one set of chromosomes, are said to be *haploid*. In most animal species, including humans, somatic cells typically carry two sets of chromosomes, where one set is derived from each parent; *i.e.* they are said to be *diploid*. Chromosomes can be further distinguished into *autosomes* and *allosomes* (or “sex chromosomes”) in sexually reproducing organisms. Human cells carry 22 autosome pairs, which are *homologous* in both males and females, and one set of allosomes (X and Y chromosomes), which determine sex and thus differ in males and females.

Deoxyribonucleic acid (DNA) forms the molecular basis of what is commonly referred to as “genetic material”. The molecular structure of DNA was first described by Watson and Crick (1953) on basis of X-ray diffraction data by Rosalind Franklin. A chromosome is a single DNA molecule composed of two strands that form a double helical structure. Each strand is a chain of *nucleotide* subunits containing one of four *nucleobases*; adenine (A), guanine (G), cytosine (C), and thymine (T), which constitute the alphabet of the genetic code. The DNA double helix is held together through hydrogen bonds between complementary nucleobases on opposite strands. The human genome contains more than 3 billion such *basepairs*. The chemical structure of the DNA double helix is illustrated in Figure 1.1 (next page).

It is the sequence of base pairs along a chromosome which stores and thereby constitutes “genetic information”. The expression of information typically occurs at a *gene* coding region of a chromosome. A gene is an organised structure of DNA elements, which can be divided into regulatory sequence regions and protein-coding regions (*exons*) that can be separated by non-coding DNA segments (*introns*). The sequence of basepairs instructs the *transcription* from double-stranded DNA into single-stranded ribonucleic acid (RNA) and the *translation* into proteins. Regulation of gene expression directs cell

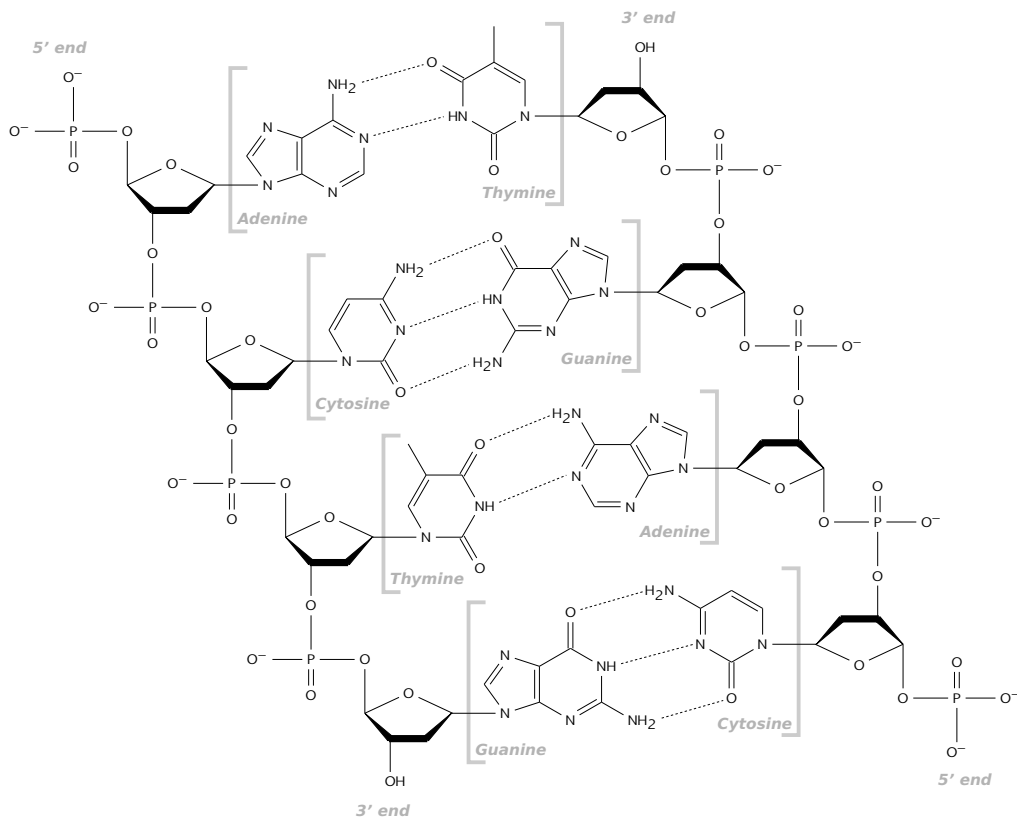


Figure 1.1: The chemical structure of DNA. The DNA molecule is a long chain polymer of individual nucleotide building blocks. Each nucleotide is composed of a phosphate residue, a deoxyribose sugar (pentose), and a nucleobase (adenine, guanine, cytosine, or thymine). The phospho-deoxyribose subunits are identical at each nucleotide and form the backbone of a DNA strand along which the sequence of nucleobases may vary. The DNA in living cells is typically composed of two complementary strands, which are connected through hydrogen bonds between complementary nucleobases. The figure shows a hypothetical sequence of four base pairs, where hydrogen bonds (*dotted lines*) can only be formed between nucleobases as indicated. This figure was generated in L^AT_EX.

growth and maintenance, as well as the development of an organism and its ability to interact with and react to the environment.

The sum of observable characteristics is referred to as the *phenotype* of an individual. The expression of phenotypic traits varies among the members of a population due to genetic variation as well as environmental influences. For example, traits such as blood type or eye colour are determined genetically, whereas most of the phenotypic variability seen in a population arises from interactions between genetic and environmental factors.

Typical examples are the effects of diet or stress on complex traits such as body weight or health.

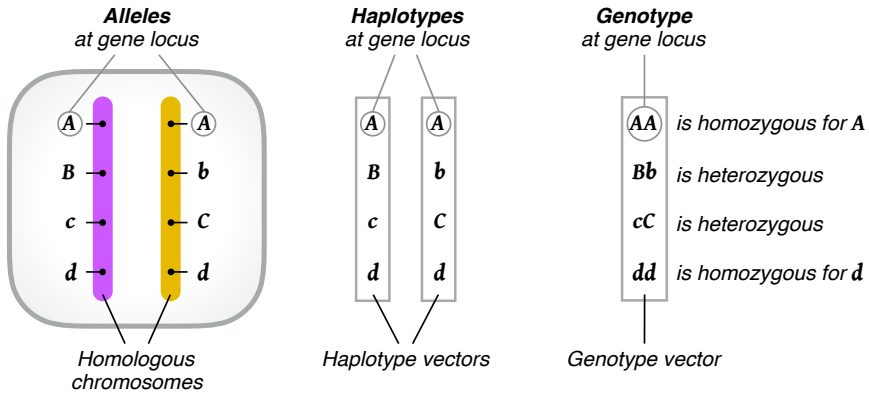


Figure 1.2: Alleles, haplotypes, and genotypes. A pair of homologous chromosomes is shown (left) on which four gene loci are highlighted; labelled as A , B , C , and D . Maternal and paternal chromosomes are shown in *purple* and *yellow* (arbitrarily coloured). Each gene may have two allelic states (in this example), distinguished by capitalisation of the label. Each chromosome has a corresponding haplotype at each locus (middle). Genotypes do not distinguish chromosomes and are represented as the sum of allelic information inherited from both parents (right). Note that the term *haplotype* may refer to the allelic state observed at a single nucleotide or a set of alleles observed along a chromosome. Likewise, the term *genotype* may refer to the allelic dosage at a single site or a vector of observed genotypic information.

Note that the meaning of the word *gene* has changed over time (e.g. see Slack, 2014). Historically, before the molecular basis of DNA was discovered, a gene was informally defined as the smallest unit of heredity, referring to the determinant of a characteristic that is transmitted from parent to offspring. This definition is convenient to mathematically describe the process of genetic inheritance and shall therefore be used in the remainder of this thesis. A gene may be observed in different variant forms in the population, each distinguished as an *allele*. Further, a *locus* (plural *loci*) refers to the physical location of a gene on a chromosome, but may also be used in reference to the position of a single nucleotide (or *site*) in the genome. When a set of sites on a single chromosome is considered, *i.e.* the alleles observed at one or more loci, the term *haplotype* is used. While one *maternal* and one *paternal* haplotype can be distinguished in a diploid individual, its *genotype* refers to the sum of the inherited genetic information at one or more loci in the two chromosomes. An individual can be *homozygous* for a particular allele at a given

site if the allele is identical in both parents, or *heterozygous* if the inherited alleles differ. This terminology is further clarified in Figure 1.2 (page 8).

The following sections describe the main processes which generate genetic variation and, thereby, phenotypic variation in a population; namely mutation (Section 1.2.1, this page) and recombination (Section 1.2.2, next page).

1.2.1 Mutation

A mutation constitutes a lasting change in the genetic sequence, *e.g.* caused by imperfect DNA replication during cell division or due to errors in the DNA repair process. The change may initially be only present in one cell, but it is passed on to daughter cells in the course of successive cell divisions (*mitosis*). If mutations occur in the germline, *i.e.* germ cells which give rise to haploid *gametes* (sperm and egg cells) during *meiosis*, the nucleotide sequence is permanently altered in all cells of the progeny. If a mutation has no effect on the reproductive success of an individual, it is said to be selectively *neutral*; otherwise, a mutation may lead to a selective advantage or disadvantage, *e.g.* due to a *beneficial* or *deleterious* effect on the phenotype, respectively. In humans, the average rate of mutation per site and per generation, denoted by μ , is typically as low as one mutation event every 100 million base pairs. More specifically, recent studies suggest a mutation rate of $\mu \approx 1.1 \times 10^{-8}$ (Roach *et al.*, 2010) or $\mu \approx 1.2 \times 10^{-8}$ (Scally and Durbin, 2012).

Mutations generate the genetic variation that is observable in a population; several classes of genetic *variants* can be distinguished (*e.g.* see Frazer *et al.*, 2009). A change at a single position on the chromosome results from a *substitution* of one base for another, which in sample data is observed as a single-nucleotide polymorphism (SNP). Nucleotides may be added to or removed from the sequence, due to *insertions* or *deletions* respectively, commonly referred to as *indels*. Larger changes to the chromosomal structure may also be distinguished. This thesis is mainly concerned with genetic variation observed at individual positions in the genome. In the following, the term “mutation” is used in reference to substitutions at single loci that result in observable SNPs in sample data. It is further assumed that SNP loci are *biallelic*, *i.e.* there are two alleles that segregate in a population (sample) at a given locus; this is the case for the vast majority of SNPs.

1.2.2 Recombination

Recombination refers to the reorganisation of alleles during meiosis in sexually reproducing organisms, which is facilitated through the physical exchange of genetic material between maternal and paternal chromosomes, such that new combinations of alleles are generated and transmitted to the offspring. Two main mechanisms of recombination can be distinguished.

Chromosomal crossover refers to the overlap of two chromatids (replicated maternal and paternal chromosomes) with subsequent, mutual exchange of homologous DNA segments.

Gene conversion is a non-reciprocal exchange of genetic material. The DNA sequence at a section in one of the chromatids is replaced by a copy of the sequence on the other chromatid, resulting in the loss of its original sequence.

In a general context, chromosomal crossover is implied as the acting mechanism of recombination, whereas gene conversion is asserted specifically.

Consider the haplotypes at two loci in an individual which is heterozygous for both the alleles at these loci. Given gene locus \mathcal{A} with alleles A and a , and locus \mathcal{B} with alleles B and b , the observed allelic configurations are (A, B) on one of the chromosomes and (a, b) on the other. If no recombination occurs between the two loci during meiosis, the resulting gametes retain the configuration as present in the parental chromosomes; *i.e.* the offspring may either receive (A, B) or (a, b) . In presence of recombination, in particular if the number of recombination events between loci is odd, the association between the two loci is broken such that either (A, b) or (a, B) are transmitted to the offspring. An even number of recombination events between the two loci reverts the configuration of alleles. Both cases (odd and even numbers of recombination events) are illustrated in Figure 1.3 (next page).

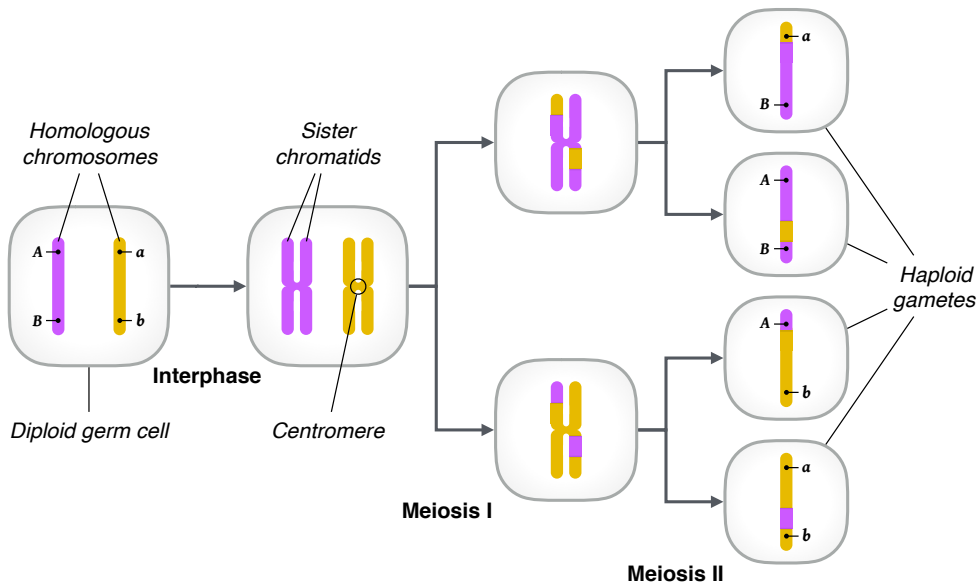


Figure 1.3: Illustration of recombination during meiosis. One pair of homologous chromosomes is shown at the beginning of the meiotic cell cycle (left). Maternal and paternal chromosomes are shown in *purple* and *yellow* (arbitrarily coloured). The allelic configuration at two sites is indicated on both chromosomes; (*A, B*) and (*a, b*). DNA sequences are replicated during the *Interphase* of meiosis, where each chromosome forms two identical *sister chromatids* which are held together at the *centromere*. Homologous chromosomes are paired at the beginning of the first cell division (*Meiosis I*), during which sequence segments are exchanged between chromatids through crossover. In the second cell division (*Meiosis II*), the four chromatids are then separated into haploid gametes (right).

Genetic linkage

A direct consequence of meiotic recombination is the phenomenon of genetic linkage, which was discovered by Morgan (1911) in experiments on *Drosophila*. Linkage describes the concept that genetic markers located in close proximity to each other are less likely to be separated by recombination during meiosis. This concept was further developed by Sturtevant (1913), who proposed that the frequency of recombination between a set of markers can be used to determine the linear order of genes on a chromosome. It was this idea that paved the way for the development of molecular and statistical methods for the purpose of *linkage analysis*, through which it became possible, for example, to detect the chromosomal location of genetic variants implicated in human disease.

The earliest models of recombination go back to Haldane (1919), who defined *genetic distance* as the expected number of recombination events per meiosis between two loci. The

unit of genetic distance is called a *Morgan*. However, it is more common to express genetic distance in units of centiMorgan (cM), where 1 Morgan is equal to 100 cM. For example, if two loci sit 1 cM apart on a chromosome, the expected number of recombination events between them is 0.01 per generation, meaning that the two loci are separated once every 100 meioses on average. In humans, a distance of 1 cM corresponds to about 1 million base pairs; *i.e.* 1 Megabase (Mb). The genetic distance translates into the rate of recombination, here denoted by ρ . The human genome exhibits an average rate of $\rho \approx 1 \times 10^{-8}$ per site per generation. However, the recombination rate varies among chromosomes and more so along the length of each chromosome.

1.3 Models in population genetics

Over the last century, the field of population genetics has evolved from a mainly theoretical area of study into a more applied area of research. More recently, the field has adapted to the exponential growth of available molecular data and continues to fill a niche in the computational sciences so as to be able to analyse the increasing amounts of data and to answer questions of biological as well as medical meaning. This section outlines the statistical concepts on which many of the current analytical approaches are based. Coalescent theory is of particular importance for the understanding of the statistical methods developed in this thesis, for which the Wright-Fisher model may serve as an introduction.

1.3.1 Wright-Fisher model

One of the most influential models in population genetics is the Wright-Fisher model of reproduction (Fisher, 1930; Wright, 1931), which describes how gene frequencies evolve over time in a finite population. Because the Wright-Fisher model is often implied in other statistical applications in population genetics, it is pertinent to explore its properties in greater detail. In particular, the following describes the effects of “random genetic drift” in an idealised population.

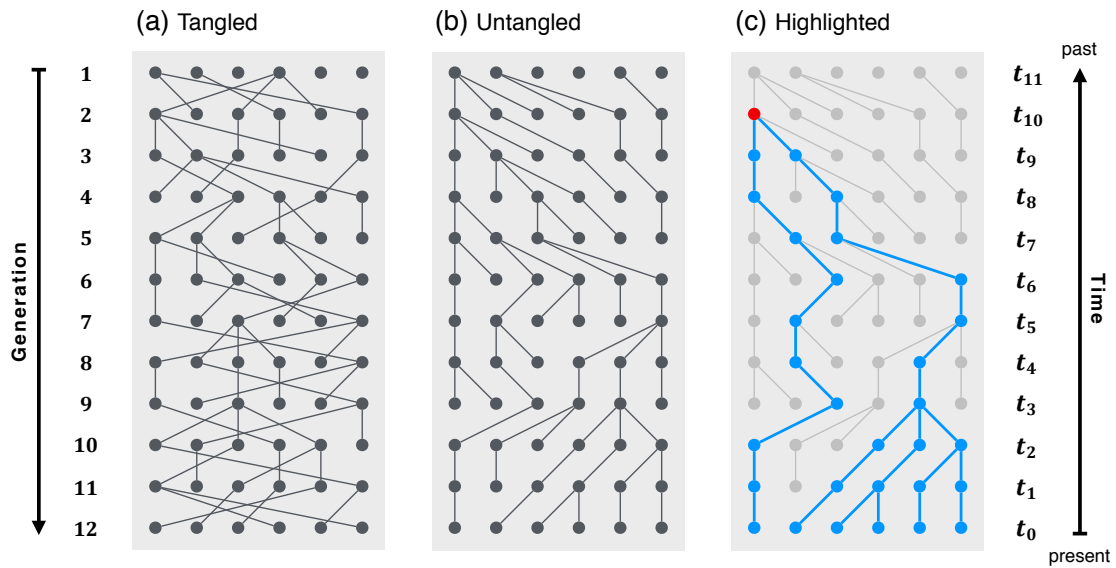


Figure 1.4: Example genealogy in a Wright-Fisher model. A population of size $N = 6$ is shown in Panel (a), which is observed over 12 generations. In the neutral Wright–Fisher model, one individual is chosen at random (with replacement) in each generation to produce offspring for the next generation, repeated N times. The genealogy of the population is more clearly seen after individuals have been sorted such that their lineages do not cross; see Panel (b). Note that not every individual produces offspring, such that some lineages go extinct. If this process is repeated over many generations (forward in time), it can be seen that all individuals in the present generation derive from a single individual in the past, which is indicated in Panel (c). The ancestry of the present population (blue) is traced back to a single ancestor (red) at time $t = 10$ generations ago.

In its simplest form, the Wright-Fisher model considers a gene locus at which two alleles, A and a , are observed; *i.e.* the locus is *biallelic*. A population of N haploid individuals is assumed, where N remains constant in each generation. All individuals die at the same time at which all individuals in the next generation are born; *i.e.* time is measured in discrete, non-overlapping generations. The effects of mutation or selection are ignored, such that alleles are *neutral* and the probability of producing offspring is equal for each individual. It follows that reproduction is considered as a random sampling process, in which the alleles that are transmitted into the next generation are drawn (with replacement) from the gene pool of the current population. An example is illustrated in Figure 1.4 (this page).

Since each draw has only two possible outcomes, A or B , each generation is produced by a series of independent Bernoulli trials such that allele frequencies are binomially

distributed. Let X_t denote the number of A alleles in generation t . Given $X_t = i$ allele copies (or individuals which carry the allele), the probability of drawing the A allele is equal to its frequency in the current generation, denoted by $\pi_i = i/N$. The probability of observing $X_{t+1} = j$ copies in the next generation is

$$P(j | i) = \binom{N}{j} \pi_i^j (1 - \pi_i)^{N-j} \quad (1.1)$$

for $0 \leq i, j \leq N$, and where $\sum_{j=0}^N P(j | i)j = i$. From the binomial distribution follows that the expected number of alleles in the next generation can be expressed as

$$\mathbb{E}[X_{t+1} | X_t] = N\pi_i = N\frac{X_t}{N} = X_t \quad (1.2)$$

and the variance is given by

$$\text{Var}[X_{t+1} | X_t] = N\pi_i(1 - \pi_i) = X_t\left(1 - \frac{X_t}{N}\right). \quad (1.3)$$

Equation (1.2) implies that $\mathbb{E}[X_t] = \mathbb{E}[X_{t-1}]$ and thereby $\mathbb{E}[X_t] = \mathbb{E}[X_0]$; *i.e.* the expected number of alleles in each generation is (on average) equal to the initial allele count. This result is reminiscent of the Hardy-Weinberg principle (Hardy, 1908; Weinberg, 1908), which states that the relative allele frequency remains constant in each generation if mating is random, but in which the population size is assumed to be infinite. However, due to the behaviour of a stochastic process in a finite population, the number of allele copies may eventually *drift* to 0 or N , even in a single generation. Several examples of how the allele frequency may change in populations of different sizes are shown in Figure 1.5 (next page).

Because the frequency of an allele in a particular generation only depends on the frequency distribution in the previous generation, it follows from this property that the reproductive process is itself a Markov chain, with transition probabilities as described by Equation (1.1) and a state space in $\{0, \dots, N\}$. The states 0 and N are absorbing, which means that if the population consists of $X_t = 0$ or $X_t = N$ alleles, it remains so

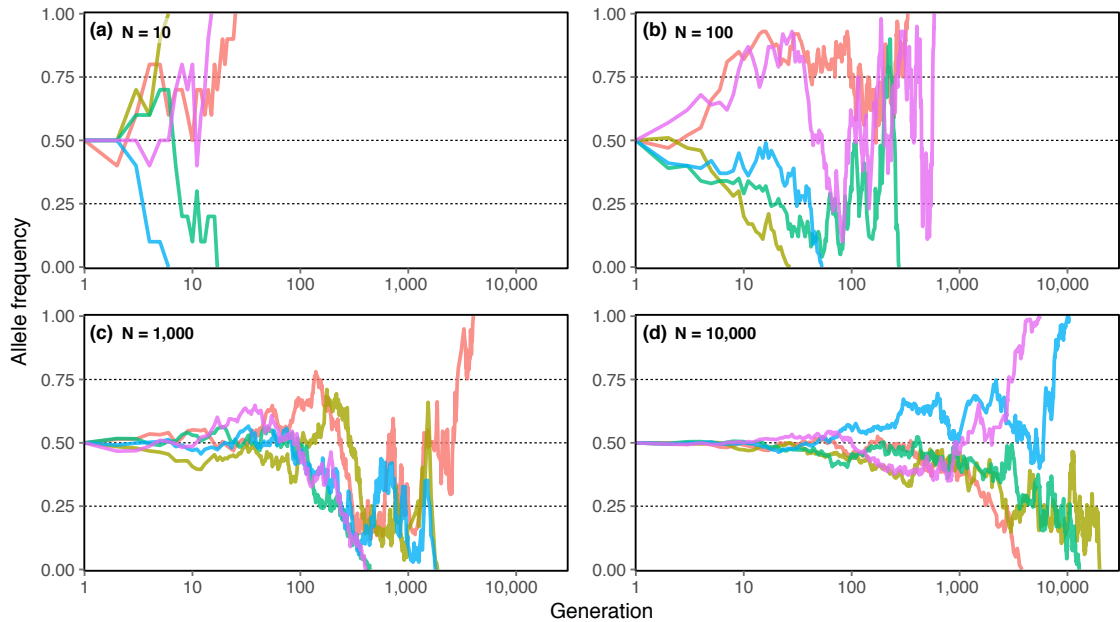


Figure 1.5: Allele frequency changes over time simulated under the Wright-Fisher model. A haploid population was simulated under four different constant values of population size, N , as indicated in each panel. The change in allele frequency is shown by generation. For each value of N , five replicate simulations were conducted (distinguished by colour). Note that the allele frequency does not change after it has reached 0 or 1; *i.e.* the allele is said to have become *fixed* in the population.

in all future generations. A consequence of this Markov process is that an allele will either go extinct or reach *fixation* (*e.g.*, see Ewens, 2012). Let the time until either of the two alleles has reached fixation be denoted by T . From Equation (1.2) follows that the probability that an allele reaches fixation is

$$P(X_T \in \{0, N\}) = \frac{X_0}{N} \quad (1.4)$$

which means that the probability of a given allele reaching fixation is equal to its initial frequency.

Without the introduction of new alleles through mutation, the Wright-Fisher model predicts that genetic variation is inevitably lost over time, due to random drift resulting from sampling error in a finite population. Hence, an important extension of the Wright-Fisher model is the incorporation of mutations. Suppose that allele A mutates into allele a with rate μ_A , and a into A with rate μ_a . The transition probability given in

Equation (1.1) still holds, but allele frequency can be expressed such that π_i is dependent on mutation rate, namely

$$\pi_i = \frac{i}{N} (1 - \mu_A) + \left(1 - \frac{i}{N}\right) \mu_a. \quad (1.5)$$

If $\mu_A, \mu_a > 0$, then transitions from any state into any other state remain possible in each generation and permanent fixation is avoided. Note that in a population in which the effects of mutation and genetic drift are in statistical equilibrium allele frequencies are expected to follow the Hardy-Weinberg principle; *i.e.* the population is in Hardy-Weinberg equilibrium (HWE).

1.3.2 Coalescent theory

The coalescent is arguably the most frequently employed genealogical method in population genetics. The concept and the statistical properties of the coalescent were first described by Kingman (1982a,b,c) and it is therefore often referred to as “Kingman’s coalescent”. The term “ n -coalescent” is also frequently used to emphasise the importance of the sample size, n , in the genealogical process within a much larger population. The coalescent, at its core, is a collection of stochastic models which provide the means to generate predictions about population dynamics under a variety of models of genetic variation and demography (Wakeley, 2008). Note that the term “prediction” may sound odd given that the coalescent looks backward in time to reconstruct a possible genealogy given a set of population parameters. The coalescent is often used to simulate the ancestry of a sample, from which particular model parameters can be inferred, for example, on basis of biological observations. The first computational algorithm for simulations under the coalescent (named “ms”) was devised by Hudson (1990). Over the past decades, coalescent theory has grown extensively. Hence, this section provides only a summary of the basic properties of the coalescent as relevant for this thesis. For a more thorough presentation of the subject see, for example, Fu and Li (1999), Neuhauser (2001), Nordborg (2001), Hein *et al.* (2004), and Wakeley (2008).

In contrast to the Wright-Fisher model, as well as other approaches which model the genealogical history of a population forward in time, the coalescent process reconstructs the genealogy of a sample by tracing the ancestry of individuals (or genes) backward in time. Ancestral relationships between individuals are represented as lineages in a genealogical tree. In each generation, each individual independently chooses one ancestor at random. If two individuals choose the same ancestor by chance, their lineages are joined; *i.e.* they *coalesce*. The time at which two lineages join is referred to as a *coalescent event*. This process is repeated until only one lineage is left, which belongs to the most recent common ancestor (MRCA) of the sample.

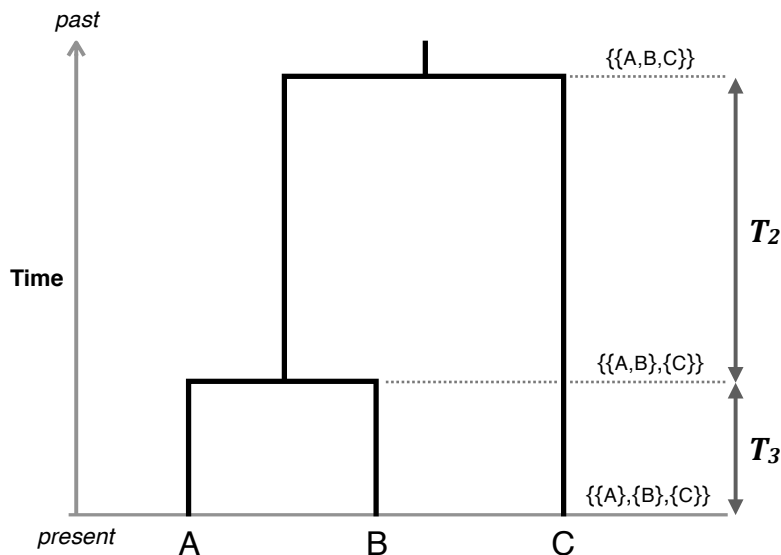


Figure 1.6: Topology of a genealogical tree in the coalescent. The genealogical relationship of three haploid individuals is shown, A , B , and C , which represent separate lineages at present, but where A and B are the first to coalesce (back in time). The waiting time between successive coalescent events is denoted by T_n , where n is the number of ancestral lineages at a given time interval, which changes from n to $n - 1$ at coalescence. Figure modified from Nordborg (2001).

The history of a sample is reflected in its genealogy and can be described in terms of the topology of the tree and the lengths of the connecting branches. The branch length corresponds to the time interval between two successive coalescent events, which is of central interest in describing the coalescent process. Let this waiting time be denoted by T_n , where n corresponds to the number of distinct lineages during the time interval,

which changes from n to $n - 1$ at coalescence. An example of a simple genealogical tree is shown in Figure 1.6 (page 17), in which the waiting times between coalescent events are indicated. In the following, the concept of the standard coalescent is described by assuming a haploid population of constant size, N , in which the effects of mutation, selection, recombination, or other biological processes are not involved.

For now, consider a sample of $n = 2$ individuals taken at the present time, which are followed back in time until the first coalescent event. Since there are N possible ancestors, the probability that a particular ancestor is chosen by one of the individuals is equal to N^{-1} . The probability that two individuals choose the same ancestor independently is N^{-2} . Hence, the probability that any of the possible ancestors is chosen by two individuals is equal to $N \times N^{-2} = N^{-1}$, and the probability that none is chosen is $1 - N^{-1}$. To arrive at the probability that two lineages coalesce $t > 0$ generations back in time, it is implied that they do not choose the same ancestor in previous generations. Because generations are independent, the probability that the two lineages are distinct over $t - 1$ generations is

$$P(T_2 > t | N) = \left(1 - \frac{1}{N}\right)^{t-1}. \quad (1.6)$$

Therefore, the probability that two lineages coalesce t generations back in time is geometrically distributed with rate N^{-1} , such that

$$P(T_2 \geq t | N) = \left(1 - \frac{1}{N}\right)^{t-1} \frac{1}{N} \quad (1.7)$$

which arises from the number of independent Bernoulli trials needed until the same ancestor is chosen by two lineages. It follows from the geometric distribution that the expected number of generations up to and including the coalescent event is

$$\mathbb{E}[T_2 | N] = \frac{1}{N^{-1}} = N \quad (1.8)$$

and the variance is

$$\text{Var}[T_2 | N] = \frac{1 - N^{-1}}{N^{-2}} = N^2 \left(1 - \frac{1}{N}\right). \quad (1.9)$$

A notable result is that the expected time to the first coalescent event is equal to the size of the population; see Equation (1.8). It is therefore convenient to scale time in units of N generations, namely

$$\tau = \frac{t}{N} \quad (1.10)$$

where the time, τ , is continuous (as opposed to time measured in distinct generations) and referred to as the *population-scaled* time. The probability that a pair of lineages remains distinct during a given time interval is given below, and can now be approximated using the exponential distribution if the population size is sufficiently large, *i.e.* as N tends to infinity;

$$P(T_2 > \tau | N) = \left(1 - \frac{1}{N}\right)^{\lfloor N\tau \rfloor} \xrightarrow{N \rightarrow \infty} e^{-\tau} \quad (1.11)$$

where $\lfloor N\tau \rfloor$ is the largest integer that does not exceed $N\tau$ (*e.g.*, see Nordborg, 2001).

The above can now be extended to consider n lineages, which in the previous generation may have n distinct ancestral lineages if no coalescent event has occurred, or $n - 1$ otherwise. The probability of no coalescence at a given time can be derived as follows. Let the first lineage choose among N ancestors with probability $N/N = 1$, the second lineage then chooses among the remaining $N - 1$ ancestors with probability $N - 1/N$, the third chooses among $N - 2$ ancestors with probability $N - 2/N$, and so on; *i.e.*

$$\left(\frac{N}{N}\right)\left(\frac{N-1}{N}\right)\left(\frac{N-2}{N}\right) \cdots \left(\frac{N-(n-1)}{N}\right)$$

which is equal to

$$\prod_{k=0}^{n-1} \frac{N-k}{N} = \prod_{k=1}^{n-1} \left(1 - \frac{k}{N}\right) = 1 - \binom{n}{2} \frac{1}{N} + \mathcal{O}\left(\frac{1}{N^2}\right) \quad (1.12)$$

where the binomial coefficient, $\binom{n}{2} = \sum_{k=1}^{n-1} k$, corresponds to the number of possible pairs. Similarly, the probability that any two of the n lineages coalesce at a given time implies

that the remaining lineages do not coalesce, therefore

$$\begin{aligned} P(T_n = \tau \mid N) &= \binom{n}{2} \frac{1}{N} \times \left(1 - \frac{1}{N}\right) \left(1 - \frac{2}{N}\right) \cdots \left(1 - \frac{n-2}{N}\right) \\ &= \binom{n}{2} \frac{1}{N} \times \prod_{k=1}^{n-2} \left(1 - \frac{k}{N}\right) \\ &= \binom{n}{2} \frac{1}{N} + \mathcal{O}\left(\frac{1}{N^2}\right). \end{aligned} \quad (1.13)$$

Note that the term $\mathcal{O}(N^{-2})$ describes the limiting behaviour of Equations (1.12) and (1.13) and captures all terms that decrease more rapidly than $1/N$ as N tends to infinity. Mathematically, $\mathcal{O}(N^{-2})$ corresponds to the *diffusion* limit of the continuous process, which can be ignored if the population size is sufficiently large (e.g., see Wakeley, 2008). By doing so, it is assumed that not more than two lineages coalesce at a given time, such that the resulting tree has a binary topology. In the limit, and if $n \ll N$, the probability of a coalescent event at a given time is

$$P(T_n = \tau \mid N) \approx \binom{n}{2} \frac{1}{N} \quad (1.14)$$

and, as before, the waiting time can be approximated in terms of the exponential distribution as given below.

$$P(T_n > \tau \mid N) \approx \left(1 - \binom{n}{2} \frac{1}{N}\right)^{\lfloor N\tau \rfloor} \xrightarrow{N \rightarrow \infty} e^{-\binom{n}{2}\tau} \quad (1.15)$$

Thus, in the continuous-time coalescent, the approximate waiting time between successive coalescent events, T_n , is exponentially distributed with rate $\binom{n}{2}$, from which follows that the expected value is

$$\mathbb{E}[T_n] = \frac{1}{\binom{n}{2}} = \frac{2}{n(n-1)} \quad (1.16)$$

and the variance is

$$\text{Var}[T_n] = \frac{1}{\binom{n}{2}^2} = \frac{4}{n^2(n-1)^2}. \quad (1.17)$$

An important result of the coalescent is that an expectation for the time to the most recent common ancestor (T_{MRCA}) can be derived dependent on the population size. Given the sum of branch lengths that need to be traced back to arrive at the MRCA,

$$T_{\text{MRCA}} = T_N + T_{N-1} + \cdots + T_2$$

the expected value can be expressed as

$$\mathbb{E}[T_{\text{MRCA}} | N] = \sum_{n=2}^N \mathbb{E}[T_n] = \sum_{n=2}^N \frac{2}{n(n-1)} = 2 \left(1 - \frac{1}{N}\right). \quad (1.18)$$

Therefore, $\mathbb{E}[T_{\text{MRCA}}] \approx 2$ as $N \rightarrow \infty$, which implies that on average the number of generations until the entire sample has coalesced into a single ancestral lineage is equal to about twice the population size.

Effective population size

Natural populations rarely adhere to the assumptions made by mathematical models. One such example is the rather unrealistic assumption that the population size remains constant over time. The rate at which coalescent events occur in the genealogy of a sample is conditional on the size of the population in each generation, which in reality is often highly variable. Statistical models in population genetics may therefore resort to the concept of an effective population size, denoted by N_e , which substitutes the census population size, N , to account for departures from model assumptions. Note that the biological meaning and the mathematical definition of N_e may vary depending on the properties of the biological system under consideration. To account for variations in population size in the standard coalescent, N_e can be defined as the *variance effective size* and is estimated such that the coalescent process would result in the same shape of genetic variation as expected in a population of constant size.

Note that N_e may differ from the census size of a population by several magnitudes. For example, the human population currently counts several billion individuals globally, whereas the long-term, diploid effective size is commonly defined in the order of

$N_e \approx 10,000$, based on estimates from DNA polymorphism data (*e.g.* Takahata, 1993; Yu *et al.*, 2001).

Suppose the size of a population is known at each generation back time, where N_i denotes the census size in generation i over a period of t discrete generations. The effective size can be computed as

$$N_e = \frac{t}{\sum_{i=1}^t \frac{1}{N_i}} \quad (1.19)$$

which is the harmonic mean of N_i . However, because past population sizes are typically difficult to assess, N_e can be estimated from the genetic diversity observed in a population. The measure of genetic diversity is dependent on the rate of mutation in the genome, which is described in the following section. For consistency with the definitions provided so far, the following sections in this chapter keep N to denote the population size, but this is substituted by N_e in the remaining chapters.

The coalescent with mutation

Mutations are essential to generate genetic diversity and maintain genetic variation in a finite population. The standard coalescent relies on the assumption that variant alleles are selectively neutral; *i.e.* the effect of mutation is independent of the genealogical process. As such, mutation events can be superimposed on the coalescent tree by placing mutations on all branches proportional to their length. An example is illustrated in Figure 1.7 (next page), in which several mutation events are shown to give rise to the variation observed in the DNA sequence of a sample.

Given a constant rate of mutation per site per generation, μ , the expected number of mutations on a branch in the genealogical tree, *i.e.* a lineage that is t generations long, is $t\mu$. If time is scaled in units of N generations, see Equation (1.10) on page 19, the corresponding value is expressed by $\tau N\mu$, such that the rate of mutation per site per unit of time is equal to $N\mu$. However, for historical reasons (*e.g.*, see Wakeley, 2008), the

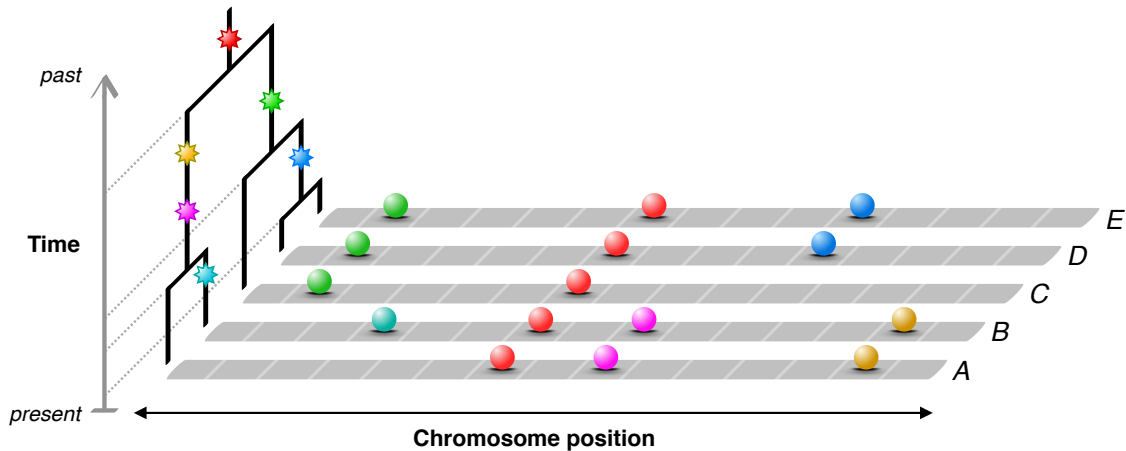


Figure 1.7: Mutation events on a genealogical tree in the coalescent. The genealogy of a sample of five haploid individuals ($A - E$) is shown on the left. The time of each coalescent event is indicated by a *dotted* line. Mutation events (*stars*) are placed along the branches of the tree. Each mutation event alters the allelic state at a random position on the chromosome, giving rise to a new allele, which is inherited by all descendants of the ancestral individual in which the mutation occurred. Horizontal lanes (*grey*) represent the chromosome sequence of the individuals, on which the derived alleles are depicted as *marbles*; colours correspond to the mutation event from which the alleles derive.

population-scaled mutation rate is given by the compound parameter

$$\theta = 2N\mu \quad (1.20)$$

where θ is assumed to be constant in the limit $N \rightarrow \infty$. Note that the factor of 2 relates to the formulation of the expected number of pairwise differences between two haploid sequences, which is equal to θ (Tajima, 1993). Thus, θ describes the amount of genetic diversity in a population.

Because mutations effectively count events that occur independently, the probability distribution of mutation is described by a Poisson process with rate parameter $\theta/2$ (Wakeley, 2008). It follows that the probability of observing K mutations on a branch of length L is itself Poisson distributed with parameter $\theta L/2$;

$$P(K = k | L) = \left(\frac{\theta L}{2}\right)^k \frac{1}{k!} e^{-\frac{\theta L}{2}} \quad (1.21)$$

where $L = t$ if measured in discrete generations or $L = N\tau$ if measured on a continuous time scale. It follows from the Poisson distribution that $\mathbb{E}[K | L] = \text{Var}[K | L] = \theta L/2$.

Suppose that each mutation event creates a new allele and that each site can only mutate once in the history of the sample; such a setting is generally referred to as the infinite sites model (Kimura, 1969; Watterson, 1975). Under this assumption, the number of segregating sites (or *variant* sites) observed in sequence data in a sample of size n , is equal to the sum of mutation events that occurred in the history of the sample. The total branch length of the tree thereby determines the expected value of the number of segregating sites, denoted by S_n . From the sum of all branch lengths, *i.e.*

$$T_{\text{total}} = i T_i + (i-1) T_{i-1} + (i-2) T_{i-2} + \dots + 2 T_2$$

where i is the number of distinct lineages during a given time interval, the expected value of the total branch length can be computed as

$$\mathbb{E}[T_{\text{total}}] = \sum_{i=2}^n i \mathbb{E}[T_i] = \sum_{i=2}^n i \frac{2}{i(i-1)} \quad (1.22)$$

where $\mathbb{E}[T_i]$ is given by Equation (1.16) on page 20. From the above, the expected value of S_n can be derived as follows.

$$\mathbb{E}[S_n] = \frac{\theta}{2} \mathbb{E}[T_{\text{total}}] = \frac{\theta}{2} \sum_{i=2}^n i \frac{2}{i(i-1)} = \theta \sum_{i=1}^{n-1} \frac{1}{i} \quad (1.23)$$

By rearrangement, the following equation can be obtained;

$$\hat{\theta}_W = \frac{S_n}{\sum_{i=1}^{n-1} \frac{1}{i}} \quad (1.24)$$

which is an unbiased estimator of the genetic diversity in sample of sequence data; also known as Watterson's θ (Watterson, 1975). With regard to the calculation of the effective population size as described in the previous section (page 22), it can be seen that an estimate for the value of N_e can be obtained, for example, from Equations (1.20) and (1.24) given an estimate of the mutation rate.

The coalescent with recombination

Recombination is ubiquitous in nature and crucially involved in the spread of genetic variability in populations of sexually reproducing organisms. Hudson (1983) showed that the genealogical process in the coalescent can be extended to model recombination along the sequence of a sample. In contrast to mutation events, which do not affect the topology of a tree under the standard coalescent, recombination events have a considerable effect on the structure of the genealogy.

Consider the sequence of one of the chromosomes present in a diploid individual. Due to recombination, different sections of the chromosome can be traced back to the ancestral material in two parents in the immediately previous generation, and further to four grandparents in the second previous generation, and so on. It becomes clear that the ancestral origin of the chromosomal sequence is distributed over many parallel lineages back in time. For example, a useful (but limited) representation of this process is seen in family trees (*pedigrees*) in which ancestral lineages *branch* back in time such that the number of ancestors appears to double in each generation. Obviously, this progression cannot go on indefinitely because in a finite population any individual will be to some degree related to any other individual (their pedigrees may partially share the same ancestors). As shown by Wiuf and Hein (1997), all chromosomal lineages will eventually coalesce back onto a single lineage which is the *ultimate* MRCA of the chromosomal sequence.

The coalescent with recombination includes coalescent events as well as branching events, but where the genealogy of a sample of sequences cannot be represented by a single tree. This is because recombination alters the genealogical relation between different segments of the ancestral material such that two chromosomes may be closely related at a particular segment, but distantly related at another segment. The chromosomal sequence is superimposed by a sequence of *marginal* trees of different topology. This tree sequence can be represented in a graph structure. The most common way to represent the genealogy of a sample of sequences is the ancestral recombination graph (ARG)

which was first described by Griffiths (1991) in a two-locus model, but which was later generalised by Griffiths and Marjoram (1996, 1997b) in regards to the infinite sites model. Figure 1.8 (this page) illustrates a minimal example of an ARG for a sample of four chromosomes, in which mutation events are included to emphasise the pattern of allelic variation resulting from recombination between two loci. In the following, the basic properties of the generalised ARG are presented.

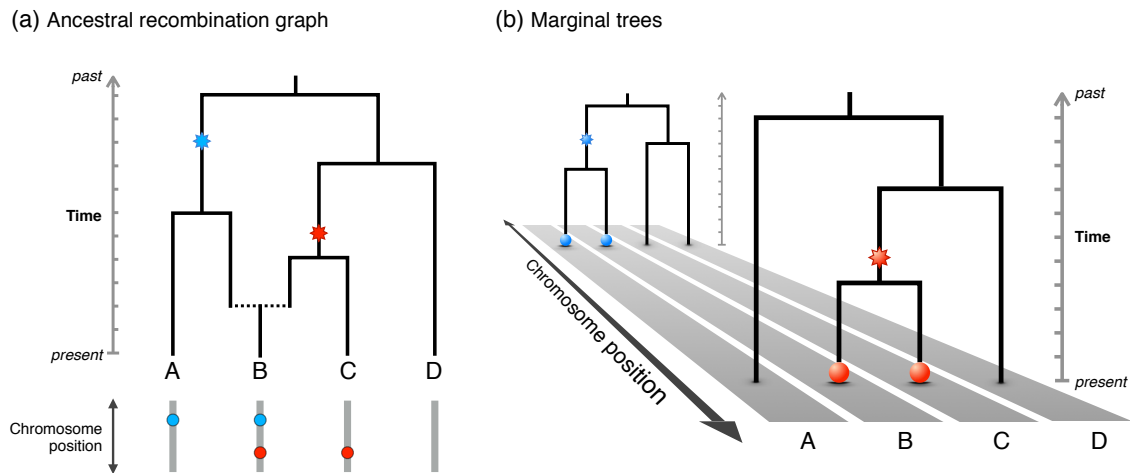


Figure 1.8: Illustration of the ancestral recombination graph. Panel (a) shows the ARG for a sample of four chromosomes, labelled by A , B , C , and D . The dotted horizontal line denotes the time of a recombination event between chromosomal lineages. Mutation events are shown as stars. The chromosomal positions of derived alleles are indicated below the ARG. The corresponding marginal trees are shown in Panel (b), where each lane (grey) represents the chromosomal sequence on which the derived alleles sit (shown as marbles).

Given the rate of recombination per site per generation, ρ , the population-scaled recombination rate is given by the compound parameter

$$\phi = 4N\rho \quad (1.25)$$

which is assumed to be constant in the limit $N \rightarrow \infty$.* The factor of 4 results from time being scaled in units of $2N$ generations, accounting for the fact that the population is diploid. Note that this adjustment permeates the coalescent and implies similar changes

* Note that in the literature r is often used to denote the per-generation recombination rate and ρ to denote the population-scaled recombination rate.

in other equations. For example, the scaled mutation rate given in Equation (1.20) on page 23 needs to be written as $\theta = 4N\mu$ if considered in a diploid population.

Given a sample of n chromosomes, the number of chromosomal lineages, k , may increase (due to recombination) or decrease (due to coalescence) back in time. First, consider the event of no recombination and no coalescence; *i.e.* the value of k remains the same in the previous generation (*e.g.*, see Tavaré, 2004). The probability of this event is

$$(1 - \rho)^k \times \left(1 - \frac{1}{N}\right) \times \left(1 - \frac{2}{N}\right) \times \cdots \times \left(1 - \frac{k-1}{N}\right) \quad (1.26)$$

where $(1 - \rho)^k$ corresponds to the probability that none of the lineages recombine; the other terms refer to the probability of no coalescence, which was already defined in Equation (1.12) on page 19. Now, because the rate at which one lineage branches into two lineages back in time is equal to $\phi/2$, Equation (1.26) can be written as

$$1 - \frac{k\phi}{2N} - 1 - \binom{k}{2} \frac{1}{N} + \mathcal{O}\left(\frac{1}{N^2}\right). \quad (1.27)$$

For the event $k \rightarrow k + 1$, which can only be facilitated through recombination, it follows that the probability of a recombination event in the previous generation is given by

$$\frac{k\phi}{2N} + \mathcal{O}\left(\frac{1}{N^2}\right). \quad (1.28)$$

The term $\mathcal{O}(N^{-2})$ is the diffusion limit of the function and corresponds to the probability that more than one recombination event occurs at a given unit of time, which can be ignored for larger population sizes; *i.e.* as N tends to infinity. Similarly, a coalescent event in the previous generation means that $k \rightarrow k - 1$, for which the probability has already been described in Equation (1.14) on page 20. Also, as shown in Equation (1.15) on page 20, the probability of coalescent events, in the limit $N \rightarrow \infty$, is exponentially distributed with rate

$$\binom{k}{2} = \frac{k(k-1)}{2}. \quad (1.29)$$

Likewise, in the limit, recombination follows the same distribution in the coalescent at rate

$$\frac{k\phi}{2}. \quad (1.30)$$

It follows that the coalescent with recombination can be described as a continuous-time Markov chain with a *birth-death* process. Lineages are “born” through recombination or “die” due to coalescence backward in time (*e.g.*, see Tavaré, 2004; Wakeley, 2008). The state space is delimited by $k = n$ at present and $k = 1$ at an MRCA. The transition rates can be summarised as follows.

$$k \rightarrow \begin{cases} k - 1 & \text{at rate } k(k - 1)/2 \quad \text{if lineages coalesce} \\ k + 1 & \text{at rate } k\phi/2 \quad \text{if lineages recombine} \end{cases} \quad (1.31)$$

Importantly, because the rate of coalescence is quadratic in the number of lineages and the rate of recombination is at most linear, the number of lineages cannot increase indefinitely (Wiuf and Hein, 1997). As a result, the ancestry of all chromosomal segments are eventually traced back to a single ancestral chromosome in the ultimate MRCA.

1.4 Advances in high-throughput genomic technologies

In this section, I provide a brief review of the developments in high-throughput genomic technologies that have been achieved over the past 40 years. I further highlight some of the milestone projects that have contributed substantially to our understanding of the human genome, namely the Human Genome Project (HGP), the International HapMap Project (HapMap), and the 1000 Genomes Project (1000G). Data from HapMap and 1000G have been used extensively in this thesis. Note that a detailed presentation of the history and biochemistry of available technologies, as well as a comprehensive list of human sequencing projects, is beyond the scope of this chapter (for review, *e.g.* see Metzker, 2009; Naidoo *et al.*, 2011; Liu *et al.*, 2012; Mardis, 2017).

1.4.1 Next-generation sequencing

The first DNA-based organism to have its genome fully sequenced was the bacteriophage ΦX174 (5,386 basepairs), which was undertaken by Sanger *et al.* (1977) based on the previously developed chain-termination sequencing method (Sanger and Coulson, 1975). This technology formed the backbone of the coming era of whole-genome sequencing (WGS), which has dominated the field since 1977 and was the main method employed to sequence the human genome (International Human Genome Sequencing Consortium, 2001; Venter *et al.*, 2001).

Following the initialisation of the Human Genome Project (HGP) in 1990, and the publication of the draft sequence of the human genome in 2001, it was proclaimed in 2004 that the sequence of the human genome was “essentially complete” (International Human Genome Sequencing Consortium, 2004). However, it became clear that available technologies could not realistically be applied to generate sequence data for larger samples due to the significant requirements in labour, cost, and time. The National Human Genome Research Institute (NHGRI), United States, therefore announced an initiative with the aim of developing novel DNA sequencing methods (awarding more than \$38 million in grants).^{*} Ultimately, it was hoped to decrease the cost of sequencing to \$1,000 or less per genome (Mardis, 2006). As a result, major advances have been made in the development of commercially available sequencing and genotyping technologies, which fostered a groundbreaking synergistic relationship between research and industry, and several large-scale international projects have been initiated; see Figure 1.9 (next page).

Sanger sequencing is now regarded as the “first-generation” of sequencing technologies, while more recently developed techniques are commonly referred to as “next-generation” sequencing (NGS), which allow higher volumes of samples to be processed in shorter time and reduced cost (Metzker, 2009). The first next-generation sequencer was the *Roche GS 20 System* by *Roche 454*, so called *pyrosequencing*, which became commercially available in 2004. Novel and diverse NGS instruments rapidly became available over the past

* <https://www.genome.gov/12513210/2004-release-nhgri-seeks-next-generation-of-sequencing-technologies/>
[Date accessed: 2017-03-15]

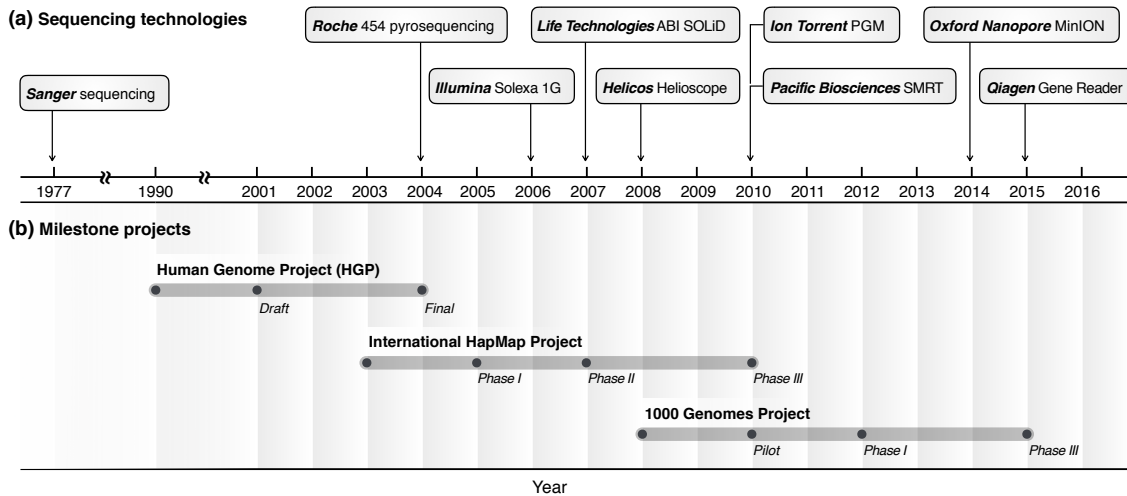


Figure 1.9: Timeline of sequencing technologies and milestone projects. Panel (a) shows the year of commercial introduction of successfully established next-generation sequencing (NGS) platforms until 2016, following the introduction of the Sanger *et al.* (1977) sequencing method. Panel (b) illustrates the timeline of three major projects that were undertaken to sequence (or genotype) the human genome. Figure modified from Mardis (2017, Figure 1) and Naidoo *et al.* (2011, Table 1).

decade; notable examples include companies such as *Illumina*, *Pacific Biosciences*, and recently *Oxford Nanopore*, to name a few. The NGS platforms shown in Figure 1.9 follow Mardis (2017).

The arrival and commodification of NGS technologies have made it feasible to sequence a whole human genome within days or weeks, rather than months or years. There is an ongoing reduction in labour and cost, while speed and accuracy of data generation is improving. Interestingly, the rate at which the cost per genome is decreasing has outpaced Moore's Law, which originally predicted that the number of transistors in a dense integrated circuit would double approximately every two years (Moore, 1965). This conjecture has been used to evaluate the rate of improvement in many technological fields, where a technology is commonly regarded to progress well if it can 'keep track' with this expectation. For example, the cost of the Human Genome Project (HGP) sequencing the first human genome has been estimated at more than \$3 billion. The first human diploid genome (James Watson) was sequenced for less than \$1 million (Wheeler *et al.*, 2008). Currently, the goal of the \$1,000 genome is surprisingly close; see Figure 1.10 (next page).

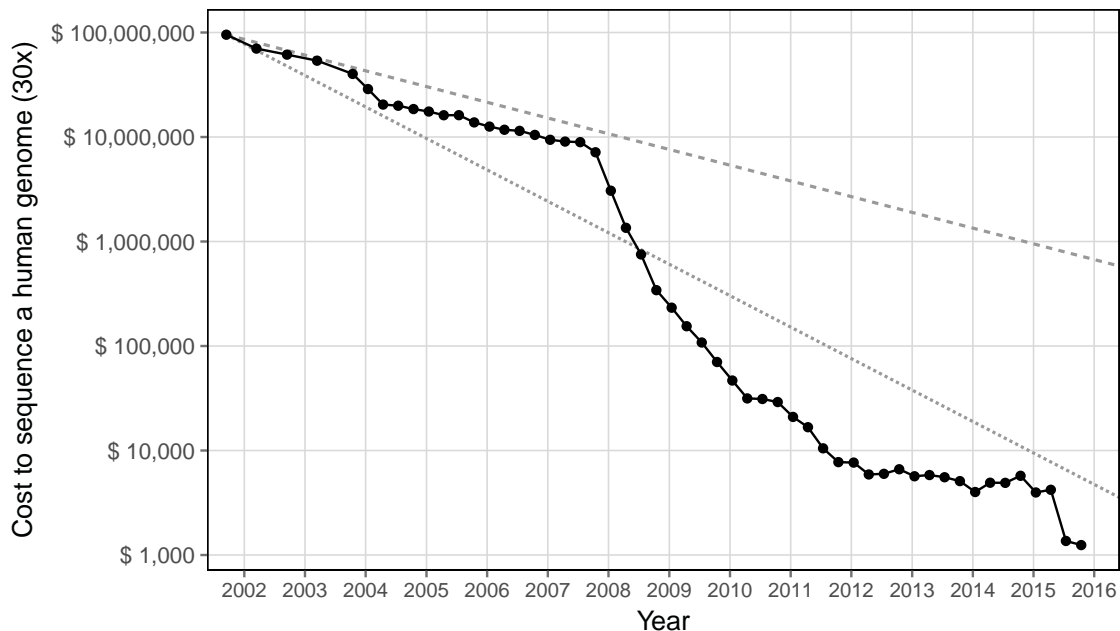


Figure 1.10: Timeline of cost reduction in DNA sequencing. Technological improvements in whole-genome sequencing have led to a drastic reductions in cost while simultaneously improving accuracy and speed of data generation. The plot shows the development of price per human-sized genome sequenced at 30x depth (price given in US dollars) since the publication of the first draft sequence of the human genome in 2001. The costs shown between 2001 and 2007 are based on the Sanger sequencing method (*first-generation* methods); since 2008, costs are based on *next-generation* technologies. The hypothetically expected rate of cost reduction per genome is indicated according to Moore's law (Moore, 1965); the price halves every two years (*dashed*) or every year (*dotted*). Data provided by the National Human Genome Research Institute (NHGRI): <https://www.genome.gov/sequencingcostsdata/> [Date accessed: 2017-03-15].

1.4.2 Exploration of the human genome

Our understanding of genetic information and the forces that shape variation in a population has grown substantially since the early breeding experiments on pea plants conducted by Mendel (1866), who formulated the fundamental laws of genetic inheritance, rediscovered more than 30 years later (Correns, 1899; De Vries, 1900; Tschermak, 1900). Yet, our patience to wait for such important insights has been decreasing exponentially.

Before the HGP was planned, an initial human genetic linkage map had been established using restriction fragment length polymorphisms (RFLPs) in 1980 (Botstein *et al.*, 1980). A second-generation linkage map of the human genome had been constructed by 1993, using microsatellite markers (Weissenbach, 1993). In 2001, linkage disequilibrium (LD) patterns had been documented for parts of the genome, using a

combination of early sequencing methods and genotyping (Daly *et al.*, 2001; Reich *et al.*, 2001).

The release of the draft sequence of the human genome in 2001 led to numerous large-scale projects. For example, GWA analyses of complex diseases required the identification of genetic markers prior to interrogation; to this end, the International HapMap Project (HapMap) was initiated to validate several million SNP markers and to examine LD patterns within different populations, eventually providing haplotype information for a representative global sample. In addition, a central aspect of the HapMap effort was to develop methods enabling GWA analysis.

The HapMap Project consisted of several phases of data acquisition and release. Phase I involved the genotyping of 1.3 million SNPs in 270 individuals from four global populations (International HapMap Consortium, 2003). Subsequently, Phase II aimed to increase the genotyping density in these same individuals to further improve the ability to map associations, supplementing the Phase I release with another 2.1 million SNPs (International HapMap Consortium *et al.*, 2007). In conjunction with the Human Genome Project and the SNP Consortium (McCarroll *et al.*, 2008), approximately 11 million common SNPs had now been identified. Finally, Phase III focussed on the coverage of additional populations, culminating in a total of 1,397 samples from 11 populations (Release 3), of which 692 individuals had been additionally sequenced at selected regions (International HapMap 3 Consortium *et al.*, 2010).

With the advantage of new NGS technologies, the 1000 Genomes Project was launched in 2008, with the aim of sequencing the genomes of at least 1,000 individuals across different populations, in order to provide a comprehensive resource of observed human genetic variation that could be leveraged by GWA studies and research in population genetics. The pilot phase described approximately 15 million SNPs, most of which had not been identified previously (Altshuler *et al.*, 2010). Several pilot projects were undertaken, including low-coverage WGS of 179 individuals from four populations, high-depth sequencing of two trios (parents and child), and targeted exome-sequencing of 697 individuals from seven different populations.

The variants discovered in the pilot stage were common (> 5% minor allele frequency); that is, low-frequency variants were underrepresented. It had been recognised that rare and low-frequency variants are candidates for functional mutations under weak purifying selection and therefore could further our understanding of complex disease (Marth *et al.*, 2011; Tennessen *et al.*, 2012). To capture variants that occur at lower frequencies per population sample, it was necessary to sequence hundreds or thousands of genomes (Kaiser, 2008).

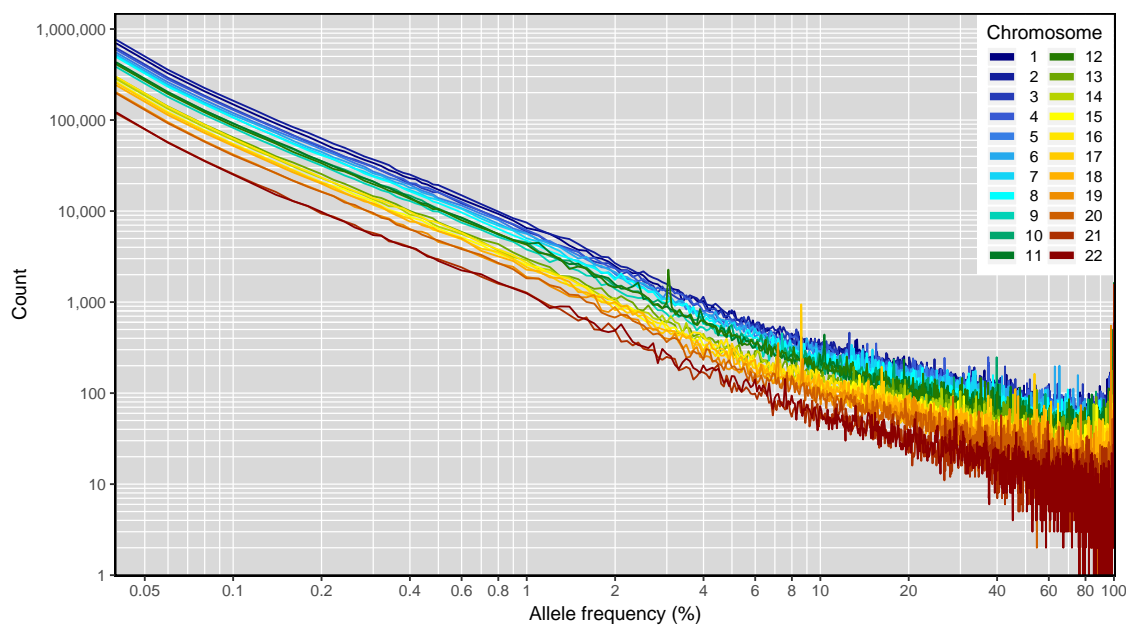


Figure 1.11: Allele frequency spectrum in the 1000 Genomes Project. The allele frequency distribution is shown per chromosome (1–22) for all variants contained in the final release dataset of 1000G Phase III. Singletons (private mutations observed only once in the sample) were excluded. Note that data are shown on log-log scale.

This led to Phase I of the 1000 Genomes Project, carried out on 1,029 individuals from 14 populations, and comprising a combination of low-coverage WGS, targeted exome sequencing, and genotyping by microarray. This resulted in the profiling of 38 million SNPs in total, with the majority being rare (1000 Genomes Project Consortium *et al.*, 2012). Phase II of the project focussed on methods development, while increasing the sample size to 1,700 individuals; these methods were applied to a total of 2,504 samples from 26 populations in Phase III, leading to a final release dataset of 84.7 million

SNPs and the completion of the project (1000 Genomes Project Consortium *et al.*, 2015). Figure 1.11 (page 33) illustrates the allele frequency spectrum of all variants identified through the 1000 Genomes Project (final release, Phase III); shown per chromosome after removal of private mutations (singletons).

1.5 Genome-wide association studies

The International HapMap Project was instrumental to the design of GWA studies by validating millions of SNPs in the human genome and revealing the structure of genetic variation through patterns of LD in different populations. Due to the non-independence of markers, association analyses may only interrogate a modest subset of variants to detect common risk alleles. It was shown that the efficiency of GWA studies could be maximised by scanning only a fraction ($\approx 1\%$) of the 11 million SNPs that were known at that time (de Bakker *et al.*, 2005; Pe'er *et al.*, 2006). The availability of HapMap data was used to guide the development of genotyping arrays, to tag SNPs markers that are informative to capture most of the variation between individuals.

The first proper GWA study was undertaken by Klein *et al.* (2005), who successfully identified a common variant of large effect size to be significantly associated with age-related macular degeneration. The number of subsequent GWA studies rapidly increased; by 2007, more than 100 studies had been published, which was considered as the “breakthrough of the year” by *Science* (Pennisi, 2007). Currently, the GWAS Catalogue maintained by the National Human Genome Research Institute (NHGRI) and the European Bioinformatics Institute (EBI) lists 2,324 publications and reports more than 30,000 unique SNP associations of which more than 8,000 are significant at p -value $\leq 5 \times 10^{-8}$ for approximately 1,000 traits (Burdett *et al.*, 2016).* The bulk of these results is summarised in Figure 1.12 (next page), in which I show the relation between risk effect size and allele frequency for identified risk-associated variants at p -value $\leq 5 \times 10^{-8}$.

In contrast to traditional linkage approaches, which have high power to locate low-frequency variants of large effect size (*e.g.* Mendelian diseases), genome-wide association

* NHGRI-EBI GWAS Catalogue: <http://www.ebi.ac.uk/gwas/> [Date accessed: 2017-01-20]

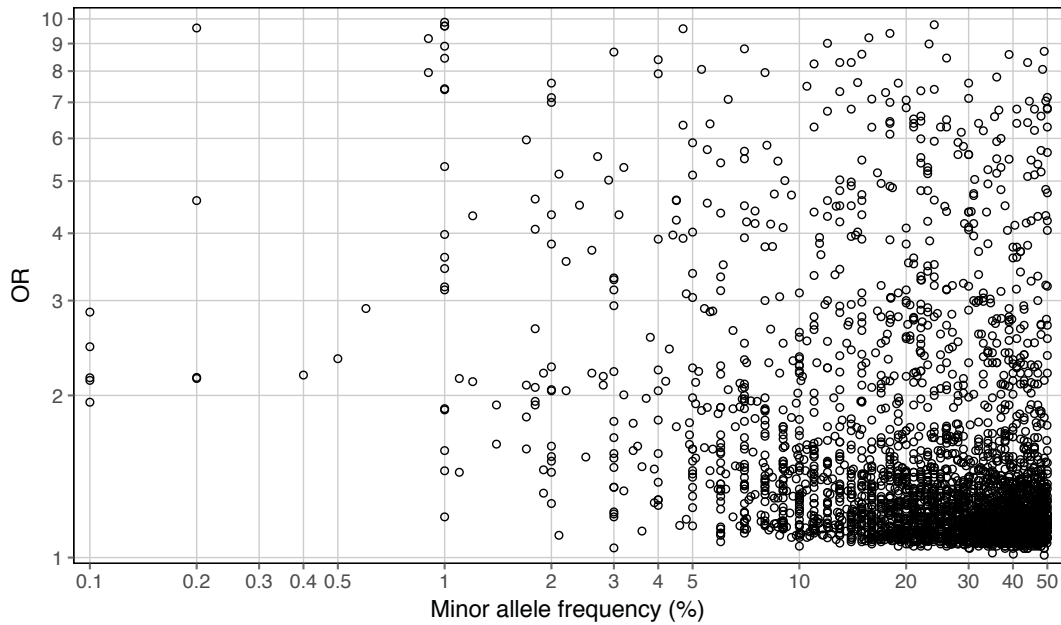


Figure 1.12: Significant risk-associated variants listed in the NHGRI-EBI Catalogue. Results are shown for 3,186 unique variants which were reported as being significant at $p\text{-value} \leq 5 \times 10^{-8}$ and for which odds ratio (OR) values were available in the database. Note that different studies may report different minor allele frequency (MAF) and OR. Duplicate entries (variants reported in more than one study) were removed, after calculating the median value of MAF and OR across duplicates; frequencies were then rounded to three decimal places. Data were taken from <http://www.ebi.ac.uk/gwas/> [Date accessed: 2017-01-20].

was designed and has proven to be powerful for interrogating common variants with modest effects. This disparity is illustrated in Figure 1.13 (next page), which outlines a seemingly categorical distinction between rare, low-frequency, and common variants based on expected penetrance and the ability to detect effects resulting from such genetic factors. The limitations of both approaches lie at the extremes (outside the band indicated in Figure 1.13).

Notably, rare variants with modest or low penetrance are difficult to detect by either linkage or GWA analysis. Since it became apparent that the human genome harbours an abundance of rare and low-frequency variants, it has been suggested that there might be unexpectedly large amounts of deleterious rare variants with low to modest effects (Coventry *et al.*, 2010; Keinan and Clark, 2012; Tennessen *et al.*, 2012). Using GWA methods, the interrogation of alleles observed at very low (rare) frequencies may represent

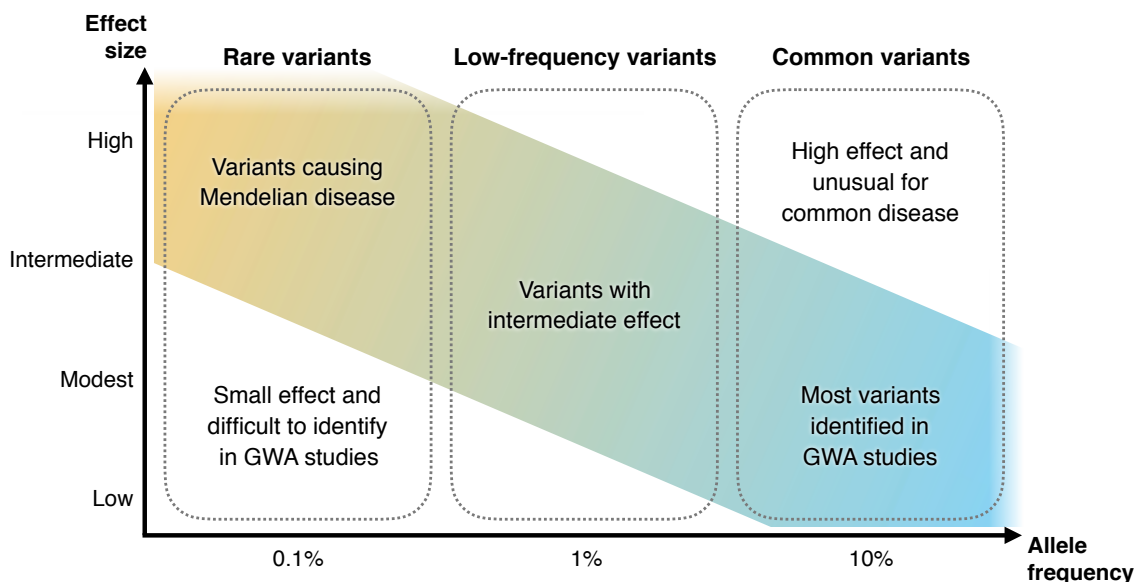


Figure 1.13: Risk-related variants by allele frequency and effect size. Rare, low-frequency, and common variants are distinguished by (minor) allele frequency. Note that frequency values are only indicated as approximate guides. Figure adapted from McCarthy *et al.* (2008, Box 7) and Manolio *et al.* (2009, Figure 1).

a conceptual limitation, however, it is hoped that the detection of low-frequency variants with intermediate effect can be improved.

1.6 Identity by descent

Relatedness among individuals is a natural property of genetic inheritance. Although this observation may seem trivial as we all inherit our DNA from somebody,* knowledge about the genetic relationship between individuals is crucial to many applications in genetic research. The validation of individual relationships is of particular interest in family-based methods such as linkage analysis (Purcell *et al.*, 2007; Albrechtsen *et al.*, 2009), or to exclude pedigree errors that would influence statistical power in linkage studies (Boehnke and Cox, 1997), but also in population-based (case-control) association studies of purportedly unrelated individuals, where unreported relatedness may lead to spurious results due to population stratification, *i.e.* systematic differences in the ancestry of individuals (Freedman *et al.*, 2004; Voight and Pritchard, 2005).

* Until CRISPR/Cas9 genome editing has been established (*e.g.* see Cai *et al.*, 2016); in reference to the term *identity by descent* (IBD) I propose the term *identity by modification*, or IBM. [*Castigat ridendo mores*]

The relationship between individuals is indicated by the alleles they have in common, where two alleles are said to be *identical by descent* if they have been co-inherited from a common ancestor (Thompson, 1974, 1975). The concept of identity by descent (IBD) was introduced by Cotterman (1940) and extended by Malécot (1948) who provided probability formulations of IBD in related individuals; the term “identity by descent” was coined by Crow (1954). Notably, Malécot (1948) defined IBD as the probability that no mutation occurred since the common ancestor; see also Slatkin (2008a). In contrast, identity by state (IBS) refers to alleles that are observed to be the “same”, but which may not be shared by descent.

1.6.1 Single-locus concept

Traditional measures of relatedness define IBD as the gametic relationship at a single locus, for which in particular the inbreeding coefficient and the kinship coefficient introduced by Wright (1921, 1922) have been relevant. For example, the probability that two homologous alleles are identical by descent in the same diploid individual is given by the inbreeding coefficient. However, such traditional approaches often assume that the relationship status of the individuals is known or can be derived from possible pedigree relationships, where ancestors are defined with respect to the founders of a pedigree. It has been argued that ancestry defined in reference to a founder sample is “something arbitrary” (Maynard Smith, 1989, p 141); see Rousset (2002). Moreover, this definition of IBD (in particular the distinction between IBD and IBS) seems to be in conflict with coalescent theory, which postulates that every allele is technically identical by descent in the individuals which carry them, because all shared mutations in the genome can be traced back to a common ancestor at different times in the past (Powell *et al.*, 2010).

1.6.2 Genealogical concept

Given the recent advances in genomic technologies, single-locus concepts of IBD have become less common and are supplanted by genealogically defined concepts of *haplotype sharing by descent* in large samples of unrelated individuals (Thompson, 2013; Wakeley

and Wilton, 2016). For example, the inference of IBD sharing has been useful to provide information about historical migration events and to reconstruct the demographic history of a population (Palamara *et al.*, 2012; Palamara and Pe'er, 2013; Harris and Nielsen, 2013).

If an allele at a given locus has been co-inherited (recently) by two or more individuals, it is likely that alleles at the surrounding loci on the same chromosome were also derived from the same ancestral lineage in those individuals. The definition of IBD is therefore extended to refer to homologous chromosomal *segments* that are identical by descent if they have been co-inherited without intervening recombination from a common ancestor (Hayes *et al.*, 2003; Powell *et al.*, 2010), such that the genealogical relationship between two haplotypes is the same along the shared region. Consequently, meiotic recombination is seen as the driving force that shapes the patterns of relatedness among individuals. The length of a shared IBD segment is delimited by recombination events that occurred independently in each lineage; IBD therefore results from the unique pairwise relationship between two gametes. To illustrate the genealogical concept of IBD, consider the example shown in Figure 1.14 (next page).

Note that recombination events may not always result in the termination of an IBD segment. This is because a coalescent event may join the two lineages broken up by recombination back together (back in time), forming a ‘closed loop’ in the ARG (see Griffiths and Marjoram, 1997a, Theorem 2.4). Further, haplotype segments that are identical by descent may not actually be “identical”, because the alleles observed along the shared sequence may differ. This is because mutations accumulate along each lineage independently, such that IBD segments separated by many meioses carry an increasing number of pairwise mutational differences. Likewise, it is expected that the length of the shared segment is decreasing over time due to recombination. As such, the “signal” of IBD might be lost for relatively old relationships, which can be described as the genetic “event horizon”. In practice, the detection of IBD segments is therefore often limited to recently inherited shared haplotypes (*e.g.* < 100 generations); see Browning (2008).

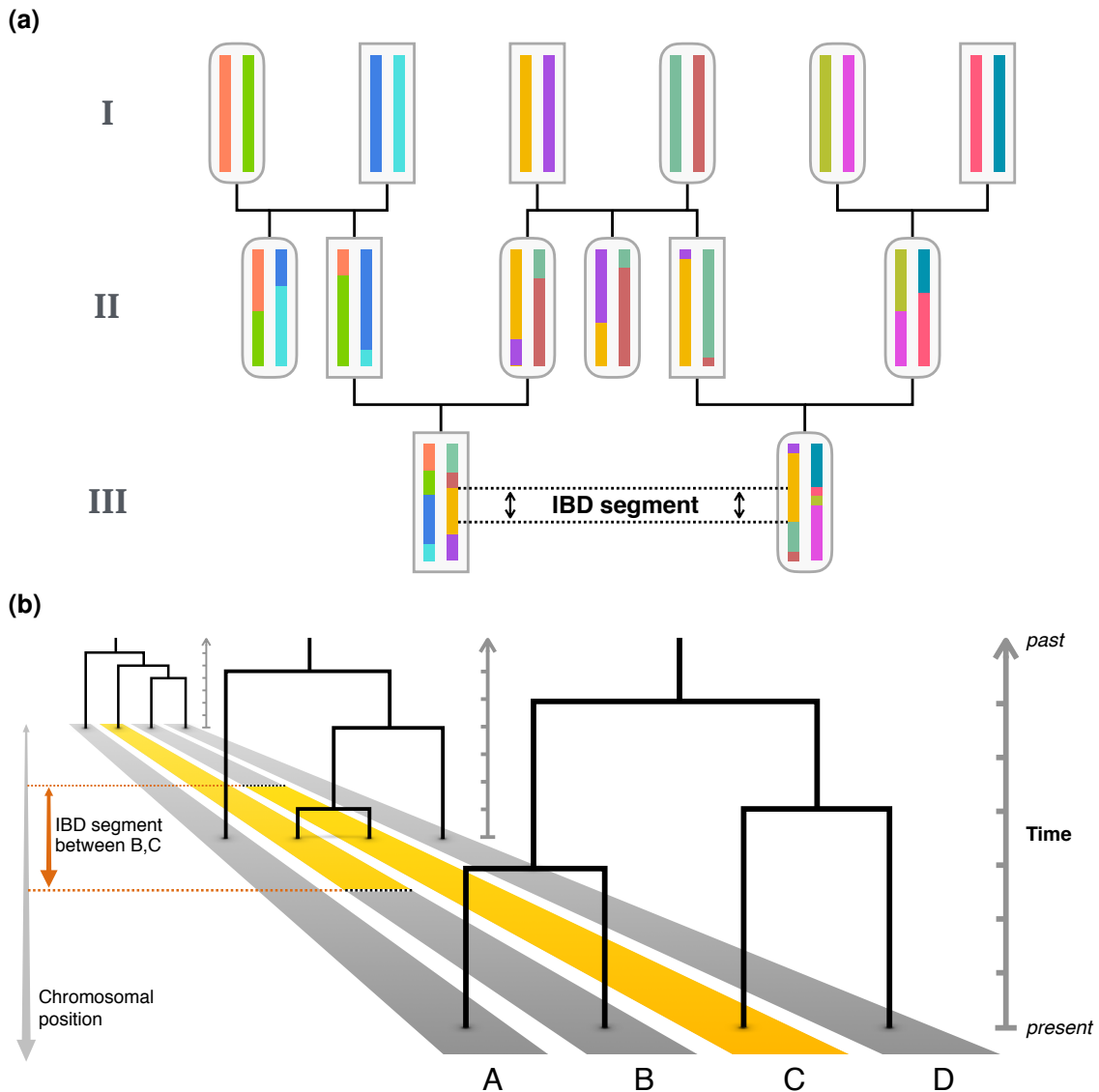


Figure 1.14: Illustration of haplotype sharing by descent. Panel (a) shows a three-generation pedigree; generation I consists of the founders of the pedigree. The two individuals shown in generation III are first-degree cousins. Male and female individuals are distinguished by square and round shapes, respectively. Each individual carries a diploid genome, shown as two large homologous chromosomes. The colour of each chromosome indicates the “identity” of the shared ancestral haplotype, which is shuffled with the other haplotype present in the same individual due to meiotic recombination in each generation, such that the offspring receives a unique arrangement of haplotype segments per chromosome from each parent. The “shared” haplotype refers to the overlapping region of haplotypes that are identical by descent; *i.e.* the IBD segment shared by the two individuals in generation III, indicated by the orange ancestral haplotype. For simplicity, all founders are shown with the same colour. Panel (b) illustrates the different genealogies along the length of the sequence of four chromosomes (A, B, C, and D), indicated by three marginal trees. The IBD segment co-inherited by chromosomes B and C is found at the overlapping region of the shared ancestral haplotype of the MRCA (orange). Note that the four chromosomes given in Panel (b) show a simpler arrangement of haplotypes than shown in Panel (a).

1.7 Allele age estimation

There has been growing interest in being able to estimate the age of alleles that segregate in contemporary human populations; that is, the time since an allele was introduced into a population through a mutation event. The age of an allele, in conjunction with patterns of allele sharing, would allow us to better understand human evolutionary history and past demographic events and processes. It has been suggested that by knowing the age of alleles, geneticists will be able to build a “time machine” to explore our past (Slatkin and Rannala, 2000).

A number of mechanisms can affect the frequency at which an allele that emerged at some unknown point in the past is observed in a population. For example, an allele might be under purifying selection and hence on its way to becoming extinct. Conversely, it might endow a selective advantage and is therefore increasing in frequency. If the allele is neutral it could be subject to random genetic drift or simply be present due to a founder effect. Finally, the heterozygous state might have a selective advantage, meaning that the allele is held at a steady frequency in the population despite being “old” (Colombo, 2007).

1.7.1 Theoretical results

The field of population genetics has been fascinated with the possibility of estimating the time of mutation events. Early and often purely theoretical approaches had been conceived prior to the discovery of the coalescent. For example, Kimura and Ota (1973) found that the frequency of a allele can be used as an estimator for its age, which they derived in a diffusion process. The expected age of a neutral allele in a constant population is given by

$$\mathbb{E}[t_m] = \frac{-2x}{1-x} \log(x) \quad (1.32)$$

where x denotes the frequency of an allele observed in a sample; the age, here denoted by t_m , is scaled in units of $2N$. Notably, this and other contributions to the field by Kimura were deserving of a dedicated review (Watterson, 1996).

Related results were provided by Maruyama (1974) and Li (1975), who considered allele age as a random variable for which the probability of reaching fixation or extinction is regarded in presence of selection (*i.e.* assuming that the allele is beneficial or deleterious, respectively). Using diffusion methods, they have shown that (purifying) selection reduces the average age of an allele, whereas mutations that increase fitness also increase the average age. Watterson (1976) further developed the theory to provide the probability distribution of allele age conditional on its frequency; see review by Slatkin (2000) and Slatkin and Rannala (2000).

An alternate approach was proposed by Thompson (1976), who considered the age of an allele as a fixed parameter to derive the likelihood function for the age using a discrete branching process model, given the number of allele copies found in a sample. Notably, Thompson (1976) has shown that it is unrealistic to arrive at an exact point estimate for the age of a given variant in a sample, due to the stochastic nature of genetic evolution in natural populations. However, it is possible to derive a confidence interval to delimit the period during which a mutation event is likely to have occurred.

Later, Griffiths and Tavaré (1998) extended these earlier results in context of the coalescent. For example, the following formulation describes the expected age of an allele under a constant population size and the assumption of the infinite sites model (Kimura, 1969; Watterson, 1975);

$$\mathbb{E}[t_m] = 2 \binom{n-1}{b}^{-1} \sum_{j=2}^n \binom{n-j}{b-1} \frac{n-j+1}{n(j-1)} \quad (1.33)$$

which is equivalent to Equation (1.32) and provides conform estimates based on allele frequency alone. Nonetheless, a general conclusion reached by the field was that the distribution of allele age based on its frequency alone is too broad to provide reliable age estimates, which meant that there was only little practical utility (see Slatkin, 2000).

However, due to the growing interest in exploring the genetic and genealogical basis of human disease, several other methods have been developed, most of which based on *intra-allelic variability*, which is defined as the extent of variability observed at closely

linked markers (Slatkin and Rannala, 2000; Slatkin and Bertorelle, 2001). Note that this idea can be seen as a progenitor to the genealogical IBD concept presented in the previous section (page 37); that is, before recombination had been first mentioned in the definition of IBD (Hayes *et al.*, 2003).^{*} These methods have been applied to numerous cases, some of which are summarised in the following section.

1.7.2 Application in human disease research

I provide three examples of studies in which the age of an allele has been estimated. The first two studies below represent early examples that have been conducted in context of a specific disease on limited data; *i.e.* prior to the high-throughput sequencing era. The third and more recent study was conducted “blindly”, in a hypothesis-generating approach on more than a million protein-coding variants using exome-sequencing data, without targeting specific loci of known disease association.

Serre *et al.* (1990) analysed the $\Delta F508$ mutation of the *CFTR* gene, which had been identified as causing cystic fibrosis, and is higher in frequency in European populations compared to other populations. They used restriction fragment length polymorphism (RFLP) data from 240 French families, estimating the age from the variation observed at two linked loci. As a result, they estimated this mutation to have occurred 3,000 to 6,000 years ago, which was consistent with an estimate of approximately 3,000 years found by Slatkin and Rannala (2000), who replicated the study on intronic microsatellite data provided by Morral *et al.* (1994).

Risch *et al.* (1995) examined six closely linked microsatellite markers in data from 59 Ashkenazi Jewish families with idiopathic torsion dystonia (ITD), a rare disorder involving involuntary and sustained muscle contractions. They showed that cases with early-onset ITD (Oppenheim’s dystonia) are due to a single founder-mutation, which they estimated to have emerged around 350 years ago, during a period when the population was geographically restricted to historic Jewish settlements in northeastern Europe.

* Note that the connection between identity by descent, linkage, and recombination had been anticipated long before (*e.g.* see Donnelly, 1983).

More recently, Fu *et al.* (2012) used exome data from 6,515 individuals and estimated the age of more than 1 million protein-coding SNPs, using a simulation-based approach under several established demographic models. In addition, they predicted whether variants were deleterious using a range of different methods. Interestingly, they found that the probability that a variant was predicted to be deleterious was strongly related to estimated allele age. Fu *et al.* (2012) found that some of the genes surveyed, among those which had been associated with human diseases, showed a significant excess of putative deleterious variants which were estimated to have a relatively recent origin through mutation. For example, several of those genes had been implicated in coronary artery atherosclerosis (*CPE*), hereditary spastic paraplegia (*KIAA0196*), premature ovarian failure (*LAMC1*), and Alzheimer's disease (*LRP1*). In fact, the majority of identified deleterious variants within gene-coding regions were rare in frequency, enriched for mutations of large effect size, and indicated to have emerged relatively recently, within in the last 5,000 to 10,000 years.

In general, it has been argued that the observed excess of deleterious rare variants in the human genome is due to a recent, explosive population growth, following a bottleneck population size after the expansion out of Africa, 50,000 to 100,000 years ago, and the advent of agriculture, approximately 10,000 years ago (Coventry *et al.*, 2010; Keinan and Clark, 2012; Tennessen *et al.*, 2012). For example, the effects of (weak) purifying selection can be considered as being too slow to purge young alleles with disadvantageous phenotypic consequences from the population, such that there might be an unrecognised large abundance of rare variants in the human genome which could influence disease risk in yet unaccounted ways. An argument to the contrary, however, suggests that recent demographic changes such as population growth may have had negligible impact on the mutational load carried by an individual on average (Simons *et al.*, 2014). As such, the amount of ascertained rare variants may not necessarily contribute to complex disease risk unless they exert strongly deleterious effects on fitness. Thus, it remains to be seen whether rare variants play an important or an inconsequential role with regard to complex disease susceptibility; to that end, knowledge about their age may lead to

a better understanding of disease aetiology. Regardless, the estimation of allele age still remains a matter of curiosity.

We chose it because we deal with huge amounts of data.
Besides, it sounds really cool.

— Larry Page, co-founder of Google Inc.

2

Meta-imputation of reference data to increase accuracy and power in association analysis

Contents

2.1	Introduction	45
2.2	Approach	48
2.2.1	Description of the method	49
2.2.2	Score metrics	51
2.2.3	Merge operations	53
2.3	Generation of reference datasets	54
2.4	Accuracy of estimated genotypes	56
2.4.1	Methods	57
2.4.2	Results	59
2.5	Power to detect significant risk signals	70
2.5.1	Methods	70
2.5.2	Results	74
2.6	Discussion	79

2.1 Introduction

Genome-wide association (GWA) studies have identified thousands of genetic risk factors that influence disease susceptibility and complex disease phenotypes. A contributing factor to this success is the ability to statistically estimate, or *impute* genotypes that have not been observed in a study sample. Genotype imputation has become a standard technique in GWA studies where it is used to increase the number of variants to achieve higher power in association analysis as well as to facilitate meta-analysis of association results across different studies (Marchini *et al.*, 2007; Marchini and Howie, 2010). Methods

for genotype imputation match patterns of genetic variation observed in a study sample with a more densely typed set of haplotypes in a reference panel. The extent of shared variation is informative for estimating the most likely genotypic states at other, unobserved variant sites in the same individuals. Commonly employed imputation methods are, for example, Beagle (Browning and Browning, 2016), MACH (Li *et al.*, 2010), and IMPUTE2 (Howie *et al.*, 2009, 2011a).

Genotypes can be imputed with remarkably high accuracy, allowing researchers to assay only a modest number of markers in sampled individuals, which makes large-scale data collection feasible and cost-effective (Li *et al.*, 2009). The accuracy of imputation is dependent on several factors. These include the number of genotyped markers in the study sample, the number of individuals sampled, the size of the reference panel, and the genetic similarity between sampled and reference individuals (Howie *et al.*, 2009; Roshyara and Scholz, 2015). The coverage of the reference panel further influences the power to find significant associations. The availability and choice of reference data therefore becomes crucial in considerations of statistical power of the study design.

One of the first larger sets of publicly available reference genomes was established by the International HapMap Project (HapMap), which identified 3.1 million variants through genotyping of 270 individuals from four continental populations (International HapMap Consortium *et al.*, 2007; International HapMap 3 Consortium *et al.*, 2010). More recently, the 1000 Genomes Project (1000G) released reference data in three phases at progressively increasing sample size, currently reaching over 88 million variants from low-coverage whole-genome sequencing (WGS) of 2,504 individuals from 26 populations (1000 Genomes Project Consortium *et al.*, 2012, 2015). Due to ongoing advances in next-generation sequencing (NGS) technologies and reductions in costs, large-scale WGS studies have become routine. However, genetic variation generally shows extensive stratification dependent on geography and ethnicity. Also, disease risk factors can be segregated on a much finer scale. Therefore, any study may only capture the variation present in the population or study cohort sampled, particularly among lower frequency and rare variants.

To increase the chance of detecting significant risk variants through GWA methods, it would be desirable to combine sequencing data from different studies to generate a single, large reference panel for imputation. However, the integration of independently produced datasets is not straightforward due to differences arising from different sequencing platforms, coverage, and strategies to filter and call variant genotypes. It is not directly feasible, for example, to compile an unbiased union of variant calls across studies, because monomorphic sites cannot be distinguished from sites that were filtered or missed. Conversely, retaining the intersection of variants that are present in all panels would dispose of much information.

One solution would be to re-process raw sequence or genotype data from multiple studies together, where variants are jointly called and phased over a combined set of samples. For example, in a large-scale collaborative effort, the Haplotype Reference Consortium (HRC) has recently created a reference panel from study data of 20 participating cohorts, which included a total of 64,976 human haplotypes in its first release (McCarthy *et al.*, 2016). This dataset currently represents the largest single resource of human genetic variation, but currently only includes samples of European ancestry. Although data are not accessible publicly, an online service has been provided for imputation and phasing from the internally stored reference dataset*.

Here, I propose an alternate solution in which multiple reference panels are separately imputed into a given study sample after which the genotype datasets produced are merged. Because imputed data may only differ in variant coverage, while the sample set is identical, it is feasible to merge data and integrate genotype information at overlapping sites. The underlying intuition is that the accuracy of an imputed genotype is indicated by its posterior probability or other metrics that result from the imputation process; for example *allelic R²* in Beagle, \hat{r}^2 in Mach, and *info-score* in IMPUTE2. The presented method applies such information to select from or assign higher weights to candidate genotypes, thereby indirectly leveraging information across different reference panels.

* Haplotype Reference Consortium: <http://www.haplotype-reference-consortium.org>
[Date accessed: 2017-02-05]

The following section (2.2) describes the approach by which sets of imputed genotype data are combined to form an integrated, larger genotype dataset; the method is referred to as *meta-imputation*. I considered several strategies to combine data based on different summary metrics. To be able to efficiently evaluate this method, as well as for application to genomic datasets on a larger scale, I implemented the method as a computational tool written in C++ called `meta-impute`.^{*} For assessment of meta-imputation, I constructed multiple, smaller reference panels from a larger dataset, which enabled comparisons between meta-imputation and direct imputations from both single and whole reference data. An additional analysis was conducted using data from several independent studies. The composition of reference data is described in Section 2.3 (page 54). The performance of meta-imputation was evaluated in regards to genotype accuracy and power to detect significant association signals. An accuracy analysis was conducted in Section 2.4 (page 56). Statistical power was analysed in a series of association experiments using simulated case-control data, which is described in Section 2.5 (page 70). Results are jointly discussed in Section 2.6 (page 79).

2.2 Approach

There are several ways by which genotypes imputed from independent sources can be combined at overlapping sites. To provide the means to explore a range of possibilities, the presented solution is implemented as a two-step process. First, a *score metric* is obtained for each genotype which, second, informs a *merge operation*. The general approach of meta-imputation is based on the assumption that a given metric is informative for distinguishing candidate genotypes that are more or less likely to reflect the underlying, true genotypic state. Here, several score metrics (Section 2.2.2, page 51) and two merge operations (Section 2.2.3, page 53) were considered, which are described after introducing principal notation and the general algorithm below.

* Meta-imputation software (`meta-impute`): <https://github.com/pkalbers/meta-impute>

2.2.1 Description of the method

It is convenient to think of genotype data as being arranged in a matrix, G , of size $M \times N$ where M is the number of observed variant sites and N is the diploid sample size. Let g_{ij} denote the genotype observed at marker i in individual j , such that g_i refers to the vector of genotypes of size N at the i th site, and g_j the vector of genotypes of size M belonging to individual j . Meta-imputation combined the information contained across several such genotype matrices. Let L denote the number of available genotype datasets imputed from different reference panels, such that G_1, \dots, G_L are available, and $k \in \{1, \dots, L\}$ is used to identify a particular matrix; note that $L \geq 2$ is assumed. Because reference data were imputed into the same study sample, the number of individuals, N , is constant in each matrix but M_k may vary due to differences in coverage per reference panel.

Meta-imputation combines available genotype matrices in an aggregated matrix, A , of size $M_A \times N \times L$ where M_A is the number of variants in the combined set of sites across imputed panels. The algorithm merges genotype information at overlapping variants by gathering those that correspond to the same genomic position per chromosome. Here, the word *analogue* is used to refer to the set of available data vectors that correspond to the same variant. Let a_i denote an analogue variant, *i.e.* the set of overlapping genotype vectors at the i th site in the aggregated matrix, and a_{ij} an analogue genotype, *i.e.* the set of overlapping genotypes at this site in individual j . Note that the number of genotypes referred to by a_{ij} may vary dependent on presence in the reference panel. Let l denote the number of overlapping variants in an analogue, where $1 \leq l \leq L$, such that l_i refers to the size of a_i .

Genotype formats may differ according to the type of data available. Note that the following considers single-nucleotide polymorphisms (SNP) specifically. In generic terms, a genotype can be observed in one of three possible states; homozygous for the reference allele, heterozygous, or homozygous for the alternate allele, which can be encoded by the alternate allele count (*allele dosage*); that is 0, 1, or 2, respectively. Imputed genotypes are typically expressed by the uncertainty associated with the imputation process. Here,

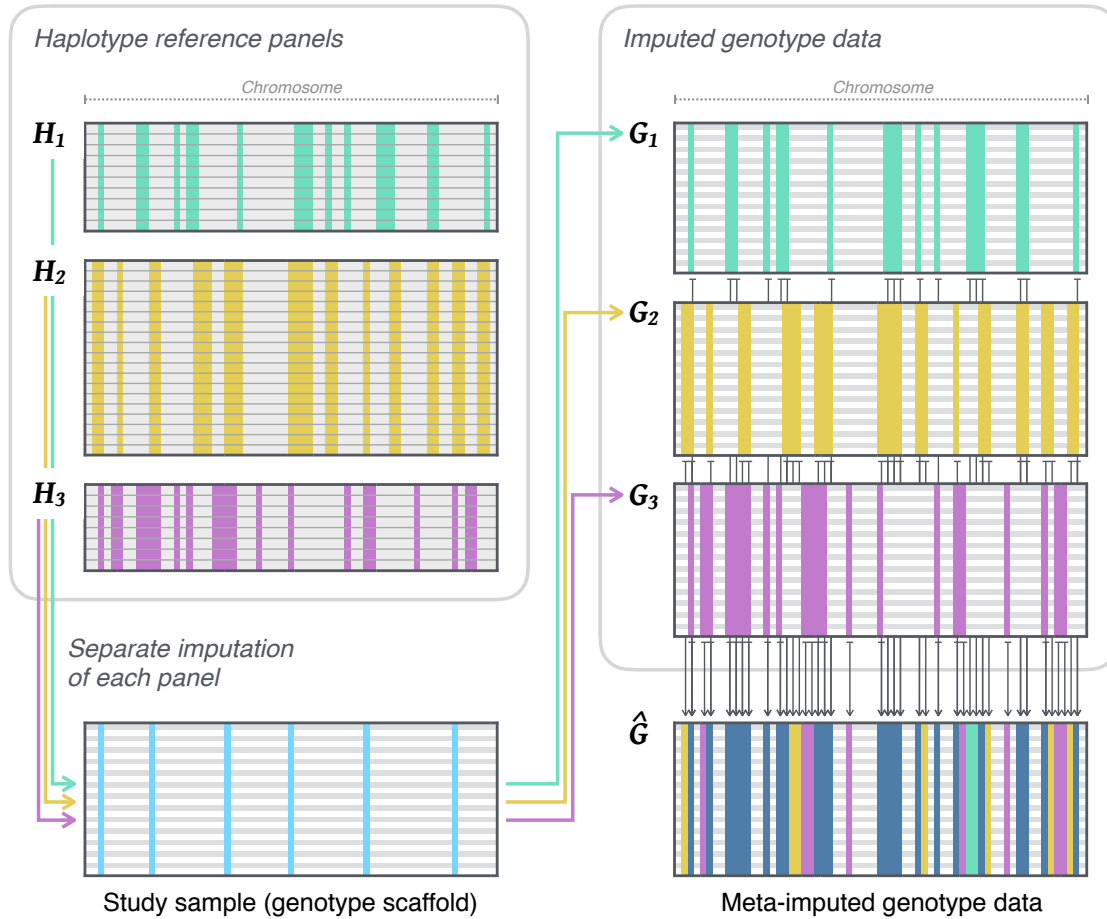


Figure 2.1: Illustration of the meta-imputation concept. An example of three haplotype reference panels is shown; denoted by H_1 , H_2 , and H_3 , where haplotypes are indicated by row (grey) and observed variant sites are indicated by column. Each panel may vary in sample size and coverage. Reference data are separately imputed into the same study sample, which is a “scaffold” of typed genotype markers, where individual genotypes are indicated by row (alternating grey-white) and observed markers by column (light-blue). Each imputation returns an imputed genotype dataset, denoted by G_1 , G_2 , and G_3 , containing marker genotypes as present in the corresponding reference panel, but where the number of individuals, N , is the same as in the study sample in each imputed dataset. Imputed data are combined through meta-imputation, such that the resulting genotype dataset, \hat{G} , contains the union of variant sites across panels. Variants merged across multiple datasets are indicated (dark-blue); the markers specific to a given panel are indicated by their corresponding colour.

an imputed genotype is considered as a tuple (p_0, p_1, p_2) of sum 1, representing the inferred posterior probability per genotypic state. Hence, a_{ijk} refers to a genotype tuple at the i th site in individual j taken from G_k .

The meta-imputation algorithm assigns a score value, s_{ijk} , to each a_{ijk} ; *i.e.* each candidate genotype per analogue variant. A *meta-imputed* genotype is formed, denoted by

\hat{g}_{ij} , by merging candidate genotype data conditional on the score assigned. At sites where $l_i = 1$, that is a given variant was imputed from only one reference panel, genotype data are retained as is, to capture as much variation as available from each separate imputation. The resulting genotype matrix, \hat{G} , contains the union of variants across input datasets. A simplified illustration of the meta-imputation concept is given in Figure 2.1 (page 50).

2.2.2 Score metrics

The score metrics considered in this work are described below; asserted 2-letter codes are used for the remainder of this chapter.

Maximum probability (MP). The mode of the probability distribution of a candidate genotype is taken as the value of the genotype's score; that is the maximum value in the tuple of posterior probabilities, which takes values in $[0, 1]$. The score is separately obtained for each candidate genotype, a_{ijk} , such that

$$s_{ijk} = \max [(p_0, p_1, p_2)_{ijk}] . \quad (2.1)$$

IMPUTE2 information score (IS). The information score (or *info-score*) is used, which is a quality metric of the difference between observed and expected information, dependent on the imputed genotype distribution and estimated allele frequency; see definition below (Marchini and Howie, 2010, S3, eq. 16; modified here to correspond to present notation).

$$I_{ik} = \begin{cases} 1 - \frac{\sum_{j=1}^N f_{ijk} e_{ijk}^2}{2N\hat{\theta}_{ik}(1-\hat{\theta}_{ik})} & \text{if } \hat{\theta}_{ik} \in (0, 1) \\ 1 & \text{if } \hat{\theta}_{ik} = 0, \hat{\theta}_{ik} = 1 \end{cases} \quad (2.2)$$

where $e_{ijk} = p_{1ijk} + 2p_{2ijk}$ is the expected allele dosage, similarly $f_{ijk} = p_{1ijk} + 4p_{2ijk}$, and $\hat{\theta}_{ik}$ is an estimate of the unknown population allele frequency, calculated as

$$\hat{\theta}_{ik} = \frac{\sum_{j=1}^N e_{ijk}}{2N} . \quad (2.3)$$

The IMPUTE2 info-score takes values in $[0, 1]$ where values close to 0 or 1 indicate low or high certainty, respectively. This and other information measures (*e.g.* Beagle R^2 or Mach r^2)

are commonly used as a filter criterion in quality control (QC) of imputed GWA data. Because meta-imputation was evaluated using IMPUTE2 for imputations (see Section 2.4.1, page 57), it is justifiable to use this information measure as a score metric. Since the info-score is calculated per imputed variant, the same score value is assigned to each candidate genotype imputed from a given reference panel at each site. Its value is assigned to each candidate genotype at a given imputed variant; that is

$$s_{ijk} = I_{ik} \forall j . \quad (2.4)$$

Sample certainty (sc). A simple measure of imputation certainty is calculated per individual, such that a score value is assigned to genotypes across variants. This metric is calculated as the proportion of an individual's genotypes which have a maximum probability that satisfies a threshold rule, defined as

$$s_{ijk} = \frac{\sum_{i=1}^M I_{ijk}}{M} \quad (2.5)$$

where

$$I_{ijk} = \begin{cases} 1 & \text{if } \max[(p_0, p_1, p_2)_{ijk}] \geq r \\ 0 & \text{otherwise} \end{cases} \quad (2.6)$$

where r is an arbitrarily defined value. In the present implementation, this threshold was set to $r = 0.9$. The intention of the sc metric is to prioritise imputations from reference haplotypes which show a closer fit to the genetic variation observed per individual in the study sample, which is assumed to be captured by the posterior probability at imputed genotypes. It must be noted that more sophisticated approaches for the estimation of genetic similarity exist, which provide summary statistics that could be used in place of the present score metric. Possible examples range from multi-locus statistics to fine-scale measures of population structure and demographic history (*e.g.* McVean *et al.*, 2004; Lawson *et al.*, 2012).

Random score (RS). In addition, the option to assign random score values to candidate genotypes was included, to be considered as a control against which the above metrics were compared. The score was explicitly calculated as

$$s_{ijk} = \frac{\text{rand}(R)}{100}, \quad R \in \{1, 2, \dots, 99\} \quad (2.7)$$

where $\text{rand}(\cdot)$ is a function which uniformly selects one value from R at random, such that $0 < s_{ijk} < 1$.

2.2.3 Merge operations

Any operation to merge the information available per analogue genotype can be divided into one of two conceptually distinct approaches; either one candidate genotype is selected and others are discarded, or a new genotype tuple is mathematically derived from available data. Accordingly, I considered the following two operations; note that the specified 3-letter codes are used henceforth.

Maximum score selection (MSS). A candidate genotype is selected by using score metrics as a ranking criterion, where the genotype tuple with the highest assigned score is selected from an analogue genotype in a_{ij} and retained as is in \hat{g}_{ij} ; see below.

$$\hat{k} = \arg \max_{k \in \{1, \dots, l_i\}} [s_{ij}] \quad \text{s.t.} \quad \hat{g}_{ij} = a_{ijk} \quad (2.8)$$

If the highest score value is equal in more than one candidate genotypes, one is selected at random from those with the highest score.

Weighted linear combination (WLS). Tuple values of the meta-imputed genotype are derived from candidate genotypes as a linear combination of their posterior probability per genotypic state. This is calculated as the weighted average over analogue genotype probabilities, using corresponding score values as weights. Each candidate genotype thereby contributes to the resulting probability distribution in \hat{g}_{ij} , except for genotypes with $s_{ijk} = 0$. Probability values in each tuple a_{ijk} are multiplied by their assigned s_{ijk}

after normalising scores such that values in s_{ij} sum to 1. The tuple of the meta-imputed genotype is then constructed by calculating the sum over the weighted probabilities at each genotypic state; see below (the mathematical definition follows Stone (1961)).

$$\hat{g}_{ij} = (\hat{p}_0, \hat{p}_1, \hat{p}_2)_{ij} = \sum_{k=1}^{l_i} (p_0, p_1, p_2)_{ijk} s_{ijk} \quad (2.9)$$

Implicitly, the resulting probability distribution in \hat{g}_{ij} sums to 1. In contrast to MSS above, the weighted linear combination of genotype data does not discard available information. But note that tuple values may not be regarded as posterior probabilities when candidate genotypes were combined using WLS, but rather as “pseudo-probabilities”.

2.3 Generation of reference datasets

Multiple reference panels were derived from the 1000 Genomes Project (1000G) Phase I dataset, which comprises both low-coverage whole-genome sequencing and whole-exome sequencing data of 1,092 individuals from 14 populations of European, East-Asian, African, and admixed American ancestries.* This original dataset was split into non-overlapping subsets in two scenarios, A and B, reflecting situations when reference data of similar or distinct ethnic backgrounds would be available for imputation into a given study sample; see details below.

Scenario A included four panels composed of individuals belonging to European sub-populations (CEU, FIN, GBR, and TSI) as an example use case when different reference data of similar ethnic background are available.

Scenario B included four panels from different continental populations (AFR, AMR, ASN, and EUR) as an example use case when panels of distinct-ancestry samples are available.

* Note that I completed work on the *meta-imputation* project prior to the release of 1000G Phase III (1000 Genomes Project Consortium *et al.*, 2015).

Because sample sizes of the population groups considered in Scenario B differed in 1000G (more than in Scenario A), extracted individuals were randomly drawn from each group to create panels of equal size. Monomorphic sites and singletons were removed in each generated panel to more closely resemble data from independently conducted studies, where singleton or monomorphic variant calls are likely to be removed in the final dataset. In the following, the term *split panel* is used to denote subset reference data from 1000G. Throughout, analyses were limited to data from one chromosome, namely chromosome 20. This was done to allow for a larger number of replicate analyses, as will be described in Section 2.5 (page 70).

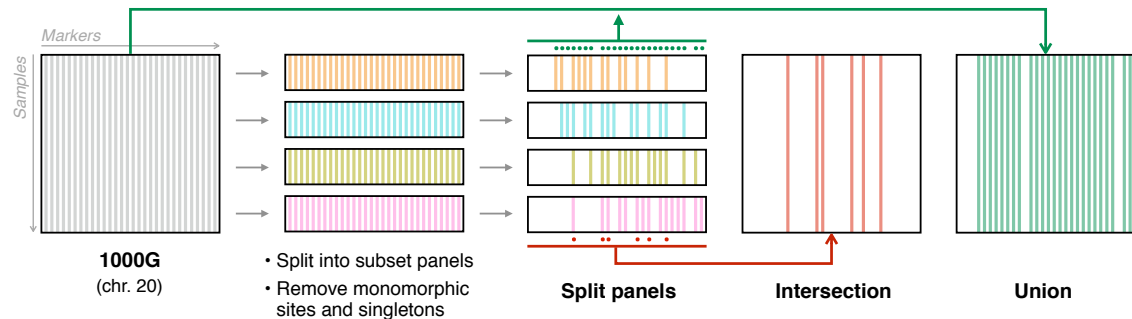


Figure 2.2: Generation of reference panels in each scenario. The original 1000 Genomes dataset (Phase I, chromosome 20) was used to generate multiple, smaller panels for imputation. This was done in two scenarios to create data of similar or distinct ethnic backgrounds. In each scenario, data were split into four *split panels* of approximately equal size. Monomorphic sites and singletons were removed in each split panel. Two additional panels were generated from the obtained split panels per scenario; one *intersection* panel and one *union* panel, both of which contained the union of individuals across split panels, but where the intersection panel only included sites if captured in all split panels, and the union panel included all sites as observed in the original dataset (except monomorphic or singleton sites as per the individuals included).

Generated split panels were used for separate imputations and subsequent integration of estimated genotype data through meta-imputation. To compare meta-imputed genotypes to those that were directly imputed from a unified panel, two additional reference datasets were generated from 1000G per scenario, which combined samples across respective split panels; referred to as the *intersection* panel and the *union* panel. The union reference contained variation as present in the original dataset, but for the individuals contained across split panels in a given scenario, and with monomorphic

and singleton variants were removed. The intersection reference contained the same set of individuals as the union panel, but with variant sites not shared across all split panels were removed. Unlike the split panels, from which imputed data were combined in meta-imputation, the genotype datasets obtained in imputations from the intersection and union panels were used in direct comparisons to meta-imputed data. The process of reference data generation is illustrated in Figure 2.2 (page 55). A summary of the final reference datasets in each scenario is given in Table 2.1 (this page).

Table 2.1: Dimensions of generated reference data used for imputations. Panels included in Scenarios A and B were generated from the 1000G Phase I dataset. These “split” panels are named after their respective population codes in 1000G. Only data from chromosome 20 were considered. Note that split panels in Scenario B were reduced to match the size of the smallest panel in that scenario. Both the *intersection* and the *union* panels were created from the combined set of individuals across panels in each scenario.

Scenario A			Scenario B		
Panel	Samples	Variants	Panel	Samples	Variants
<i>CEU</i>	85	197,252	<i>AFR</i>	181	429,088
<i>FIN</i>	93	205,093	<i>AMR</i>	181	307,454
<i>GBR</i>	89	202,707	<i>ASN</i>	181	209,209
<i>TSI</i>	98	207,583	<i>EUR</i>	181	233,527
Intersection	365	168,744	Intersection	724	144,259
Union	365	253,852	Union	724	559,172

2.4 Accuracy of estimated genotypes

Evaluation of genotype accuracy was done in two parts. First, each combination of score metric and merge operation was tested and compared to select the best performing setting for downstream analyses. Second, meta-imputed genotypes generated under the selected setting were examined in comparison to genotype data imputed from each split reference panel, as well as the intersection and union imputations. Details about the methods used are given in the section below. Results are presented in Section 2.4.2 (page 59).

2.4.1 Methods

Calculation of genotype accuracy requires that the true genotypic states at untyped variants in a study sample are known. This was done by using a larger dataset from which a subset of variants was drawn to form an imputation scaffold. Missing variants were then re-imputed from available reference panels. The generation of the genotype scaffold is described below, followed by details about imputation, quality control, and the calculation of genotype accuracy.

Generation of genotype scaffold data (study sample)

The study sample used for imputations was extracted as a scaffold from data of the Genetics of Type 2 Diabetes Project (GoT2D), consisting of 2,657 individuals of Central and Northern European descent (Fuchsberger *et al.*, 2016).^{*} The dataset is composed of data obtained on several platforms, including whole-genome sequencing, whole-exome sequencing, and exome chip data. To maintain a congruent set of markers in the genotype scaffold, variants typed on *Illumina Omni2.5 Array* were extracted from the larger GoT2D dataset, yielding 40,255 variants of in total 387,499 SNPs on chromosome 20 in GoT2D, after removing monomorphic sites and singletons. Remaining sites were masked for comparison after imputation, where imputed variants were matched to their corresponding sites in the masked dataset to calculate genotype accuracy.

Imputation and quality control

Imputations were performed using IMPUTE2 version 2.3.0 (Howie *et al.*, 2009), and executed in consecutive chunks of 5 Megabases (Mb). The GoT2D dataset comprises already phased haplotypes, so imputations were carried out on pre-phased genotypes (command line argument `-use_preparsed_g` in IMPUTE2). Because meta-imputation is indirectly based on information from more reference haplotypes than available in each separate imputation, the number of haplotypes that inform the imputation process was set to the maximum

* GoT2D Consortium: <http://www.type2diabetesgenetics.org/projects/got2d> [Date accessed: 2016-12-02]

number present in a given reference panel (command line argument `-k_hap` in IMPUTE2). This was done to minimise potential biases in comparisons between meta-imputed and imputed genotypes, but is not a requirement for general applications of this approach.

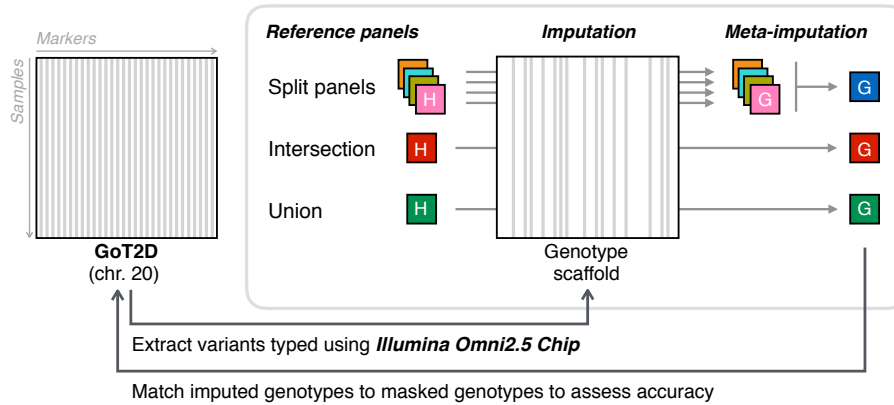


Figure 2.3: Illustration of the accuracy assessment process. Imputations were performed on the same genotype scaffold, which consisted of genetic markers obtained through genotyping using *Illumina Omni2.5 Chip*, which was part of the GoT2D dataset. This scaffold was extracted from GoT2D data, where remaining markers were masked for subsequent calculation of accuracy (squared Pearson correlation coefficient, r^2) at corresponding sites after imputation. Several reference panels were available, which were imputed into the same scaffold. Meta-imputation was applied to the imputed datasets obtained from split panels, which were generated as distinct subsets from the 1000G dataset. The intersection and union panels were separately imputed into the scaffold and subsequently compared to meta-imputed data on corresponding variant sets.

Imputed and meta-imputed genotype data were filtered in QC, removing variants at IMPUTE2 info-score < 0.4 and at deviations from Hardy-Weinberg equilibrium (HWE) at $p\text{-value} < 1 \times 10^{-4}$. Imputed data were filtered before the assessment of imputation accuracy, but not before integration through meta-imputation. The proportion of variants retained after QC was used as an indicator for data quality in comparisons between imputed and meta-imputed data. Hence, QC results were separately reported for each part of the analysis. A summary of the described analysis is illustrated in Figure 2.3 (this page).

Calculation of genotype accuracy

Genotype accuracy was calculated as the squared Pearson correlation coefficient, r^2 , as a measure for the strength of the linear relationship between imputed and masked

genotype vectors, such that r^2 was computed per site. This was done after conversion of genotypes to allelic dosage, calculated as $d = 0p_0 + 1p_1 + 2p_2$ where $d \in \{0, 1, 2\}$ for masked genotypes or $0 \leq d \leq 2$ when calculated from imputed genotype probabilities. Note that the Pearson correlation coefficient is defined as the covariance divided by the product of the standard deviation (SD) of two random variables. This is problematic if $SD = 0$, which is the case when variant genotypes are imputed as being monomorphic. To compensate for this loss in precision towards lower frequencies, the coefficient was set to $r^2 = 0$ for monomorphic variants. Imputed and masked genotype data were sorted into minor allele frequency (MAF) bins, based on their population frequency (MAF in the GoT2D dataset). In the following, accuracy is reported as mean r^2 calculated at corresponding variants per MAF bin.

2.4.2 Results

Accuracy of meta-imputed genotypes was explored for each combination of score metric and merge operation. The best performing setting was then chosen for comparison to direct imputations, as well as further analysis in Section 2.5 (page 70).

Comparison of meta-imputation settings

Each combination of score metric and merge operation produced an identical set of variants; that is, the combined set of variants across imputed panels. In total, 253,852 variants were returned from each meta-imputation in Scenario A (European sub-populations) and 559,172 in Scenario B (continental populations); *i.e.* the same number as captured by the union panel. Meta-imputed datasets were further reduced to the set of variants that matched to masked variants in the original GoT2D dataset. Variants contained in the genotype scaffold were removed, as these were not imputed. This retained 181,561 and 196,300 variants in Scenarios A and B, respectively.

The number of variants retained after QC differed among meta-imputation settings; see Table 2.2 (next page). Merge operations had a higher impact on the quality of meta-imputed genotypes than score metrics. In Scenario A, on average 92.6 % (± 0.431 % SE)

Table 2.2: Variants retained after quality control per meta-imputation setting. The number of variants retained after QC, n , per meta-imputation setting (combination of score metric and merge operation) in Scenario A and B. The percentage is given relative to the set of sites matched to masked variants in the GoT2D dataset and after removing sites contained in the imputation scaffold; 181,561 and 196,300 in A and B, respectively. Variants were removed at IMPUTE2 info-score < 0.4 and at deviations from HWE at p-value $< 1 \times 10^{-4}$.

Merge	Score	Scenario A		Scenario B	
		n retained	(%)	n retained	(%)
MSS	MP	168,595	(92.9)	178,034	(90.7)
	IS	169,455	(93.3)	179,677	(91.5)
	SC	168,686	(92.9)	179,449	(91.4)
	RS	165,877	(91.4)	171,517	(87.4)
WLC	MP	161,079	(88.7)	166,458	(84.8)
	IS	162,511	(89.5)	169,860	(86.5)
	SC	160,464	(88.4)	165,907	(84.5)
	RS	160,369	(88.3)	165,787	(84.5)

of variants were retained when **MSS** (maximum score selection) was used as the merge operation, with fewer retained using **WLC** (weighted linear combination), where 88.7 % (± 0.272 % SE) were retained on average. This was similar in Scenario B, where 90.3 % (± 0.977 % SE) and 85.1 % (± 0.491 % SE) were retained on average under **MSS** and **WLC**, respectively. Most of the variants removed in either setting were low in frequency. For instance at $MAF \leq 1\%$, 74.6 % (± 0.705 % SE) and 68.3 % (± 0.495 % SE) passed QC in Scenario A when using **MSS** and **WLC**, respectively, as well as 72.2 % (± 1.73 % SE) and 61.7 % (± 0.962 % SE) in Scenario B, respectively. Among score metrics, the number of variants that passed QC was lowest for **RS** (random scores) in each comparison; for example, 67.5 % and 60.5 % at $MAF \leq 1\%$ in A and B, respectively.

Although **MSS** overall preserved a relatively large proportion of markers after QC, the accuracy of retained genotypes was overall lower compared to data produced under **WLC**. Imputation accuracy improved after QC as illustrated in Figure 2.4 (next page), which shows mean r^2 calculated in MAF bins of equal size on log-scale. The differences among settings were small, in particular among score metrics when **WLC** was used, but where differences in accuracy become more pronounced after QC, which highlighted a clear distinction between merge operations. Throughout, mean r^2 was higher for genotype data produced under **WLC**. In Scenario A, for example, mean r^2 at $MAF \leq 1\%$ before

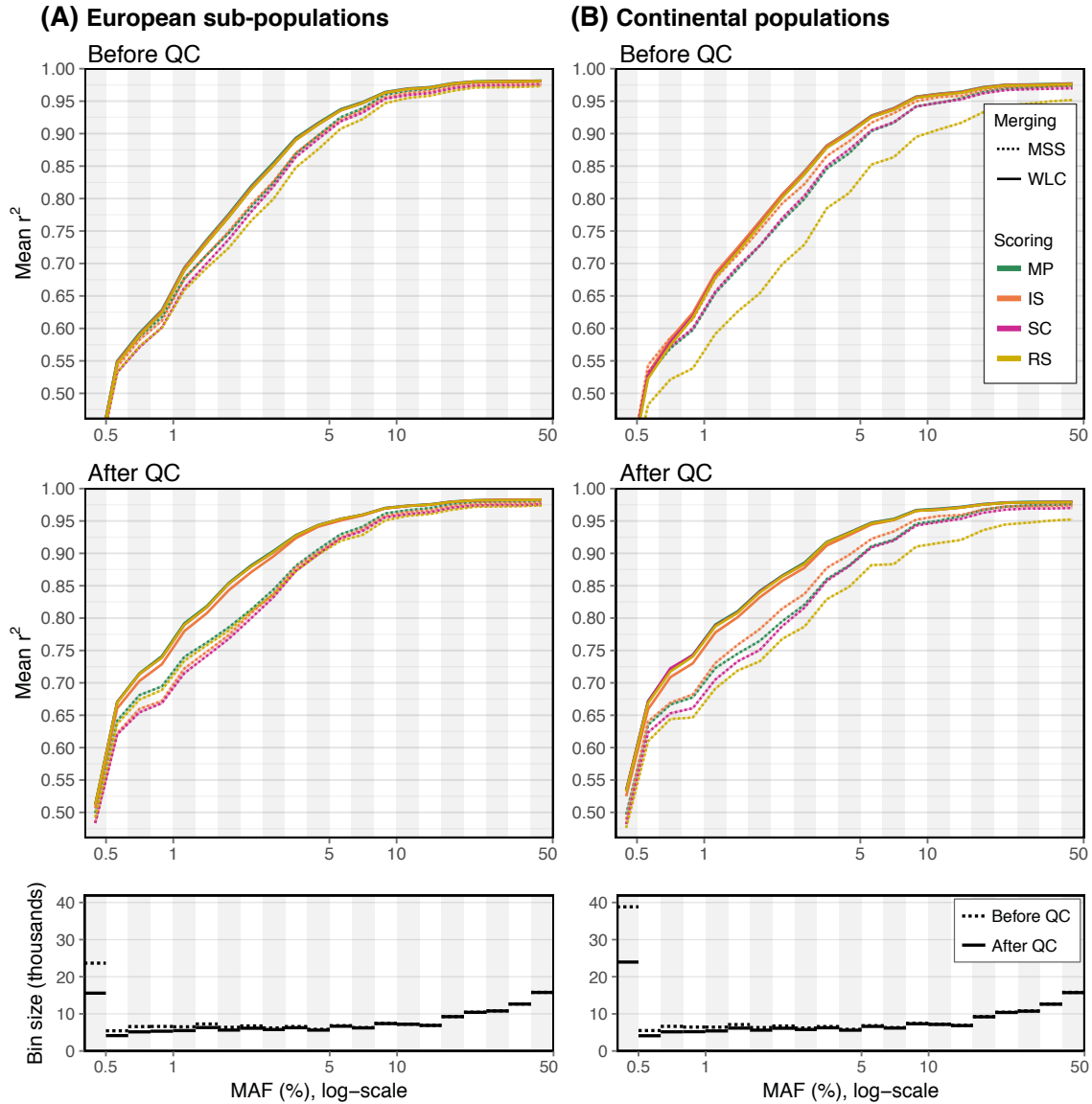


Figure 2.4: Accuracy comparison of score metrics and merge operations in meta-imputation. Each combination of merge operation (MSS and WLC) and score metric (MP, IS, SC, and RS) was examined in Scenarios A and B. Accuracy was measured as mean r^2 calculated between meta-imputed variants and variants masked in the GoT2D dataset. Results are shown both before and after QC. Bin sizes were defined on log-scale where grey-white bars indicate boundaries. The panels at the bottom indicate the number of variants per bin before QC (dotted) and the average number of variants per bin after QC (solid).

QC was $0.472 (\pm 0.886 \times 10^{-3} \text{ SE})$ in WLC and $0.464 (\pm 0.894 \times 10^{-3} \text{ SE})$ in MSS, but showed a larger difference after QC, namely $0.605 (\pm 1.01 \times 10^{-3} \text{ SE})$ and $0.472 (\pm 0.886 \times 10^{-3} \text{ SE})$ in WLC and MSS, respectively. This was also seen in Scenario B, where mean r^2 at $\text{MAF} \leq 1\%$ was $0.428 (\pm 0.796 \times 10^{-3} \text{ SE})$ and $0.418 (\pm 0.811 \times 10^{-3} \text{ SE})$ before QC in WLC and MSS, respectively, as well as $0.600 (\pm 0.951 \times 10^{-3} \text{ SE})$ in WLC and $0.548 (\pm 0.914 \times 10^{-3} \text{ SE})$ in

MSS after QC. Accuracy differences between merge operations were more pronounced at higher MAF; as seen in Figure 2.4. For example, at $\text{MAF} \leq 5\%$ after QC, mean r^2 was 0.873 ($\pm 0.442 \times 10^{-3}$ SE) and 0.811 ($\pm 0.580 \times 10^{-3}$ SE) in Scenario A for WLC and MSS, respectively, as well as 0.862 ($\pm 0.472 \times 10^{-3}$ SE) and 0.793 ($\pm 0.649 \times 10^{-3}$ SE) in Scenario B, respectively.

Table 2.3: Accuracy measured for each meta-imputation setting. Accuracy was measured as mean r^2 ($\pm \text{SE}$) per MAF bin; defined to reflect average levels of accuracy measured at rare, low-frequency, and common variants. Reported values were measured after QC for each meta-imputation setting (combination of merge operation and score metric), in Scenarios A and B. The setting with the highest accuracy per MAF bin and per scenario is highlighted (**bold**).

MAF bin	Merge	Score	Scenario A		Scenario B	
			Mean r^2 ($\pm \text{SE}^*$)	n	Mean r^2 ($\pm \text{SE}^*$)	n
[0.00, 0.01]	MSS	MP	0.585 (1.947)	31,694	0.557 (1.823)	42,101
		IS	0.567 (1.968)	32,099	0.554 (1.819)	42,769
		SC	0.565 (1.952)	31,646	0.544 (1.769)	42,335
		RS	0.578 (1.989)	30,693	0.536 (1.901)	38,468
	WLC	MP	0.608 (2.019)	28,818	0.603 (1.912)	35,020
		IS	0.600 (2.004)	29,461	0.592 (1.870)	37,049
		SC	0.606 (2.027)	28,607	0.603 (1.911)	34,793
		RS	0.606 (2.031)	28,545	0.601 (1.918)	34,748
(0.01, 0.05]	MSS	MP	0.818 (1.169)	43,330	0.799 (1.325)	42,865
		IS	0.809 (1.168)	43,787	0.814 (1.220)	43,341
		SC	0.804 (1.146)	43,499	0.790 (1.231)	43,570
		RS	0.813 (1.157)	41,848	0.769 (1.416)	40,173
	WLC	MP	0.876 (0.871)	39,309	0.865 (0.936)	39,240
		IS	0.867 (0.903)	40,107	0.856 (0.962)	40,376
		SC	0.874 (0.878)	39,000	0.863 (0.936)	38,992
		RS	0.874 (0.879)	38,972	0.863 (0.941)	38,943
(0.05, 0.50]	MSS	MP	0.970 (0.280)	93,571	0.960 (0.372)	93,068
		IS	0.967 (0.287)	93,569	0.962 (0.344)	93,567
		SC	0.964 (0.288)	93,541	0.956 (0.342)	93,544
		RS	0.962 (0.301)	93,336	0.931 (0.488)	92,876
	WLC	MP	0.977 (0.181)	92,952	0.973 (0.193)	92,198
		IS	0.976 (0.183)	92,943	0.972 (0.196)	92,435
		SC	0.976 (0.179)	92,857	0.972 (0.191)	92,122
		RS	0.976 (0.179)	92,852	0.972 (0.191)	92,096

* Standard error (SE) $\times 10^{-3}$

Accuracy as measured for each setting after QC is given in Table 2.3 (this page), which shows mean r^2 computed in three broader MAF bins to summarise accuracy levels at rare variants (here defined at $\text{MAF} \in [0.00, 0.01]$), low-frequency ($\text{MAF} \in (0.01, 0.05]$),

and common variants ($\text{MAF} \in (0.05, 0.50]$). The **RS** score metric overall resulted in less accurate genotype data compared to other metrics, in particular in Scenario B where **RS** was least accurate in all comparisons. This was not the case in Scenario A, where it showed a higher accuracy than **IS** and **SC** at rare and low-frequency variants. However, note that accuracy differences among score metrics were low overall in Scenario A (see Table 2.3), due to the presumed higher genetic similarity between sample individuals and reference haplotypes (recall that the GoT2D sample is composed of individuals of Central and Northern European descent).

Regardless, **MP** (maximum probability) outperformed other score metrics in most comparisons; except in Scenario B, for low-frequency variants under **MSS**, where it was outperformed by **IS**. The **MP** score metric was found to further improve accuracy under **WLC**, such that the combination of **MP** and **WLC** was seen to yield the highest accuracy in each MAF bin and in both scenarios (as highlighted in Table 2.3). Therefore, in the following, **WLC** was chosen as merge operation and **MP** as score metric; hence, the combination of **MP** and **WLC** is implied when referring to meta-imputation below.

Improvements of accuracy in comparison to direct imputations

Available split panels were imputed into the generated study sample and imputed genotype data were then combined through meta-imputation. The union and intersection panels were separately imputed for subsequent comparison to meta-imputed genotypes. Before accuracy was measured, all data were subjected to QC and variants were removed when not matched to masked variants or when contained in the imputation scaffold. For simplicity, imputed datasets are referred to by the panel from which they were estimated.

Comparisons were based on mean r^2 calculated at corresponding (meta-)imputed and masked variants pooled by MAF bin. In addition, significant differences in the MAF distribution of imputed and corresponding meta-imputed variants were determined using the two-sample Kolmogorov—Smirnov (KS) test. However, significance was determined from the median of the KS test statistic, here denoted by \widetilde{D} , calculated at $n = 500$ randomly selected sites over 1,000 repeated draws. This was done to account for varying subset sizes

retained in each comparison, and to avoid potential biases due to correlations of linkage disequilibrium (LD) at nearby markers. MAF distributions were significantly different if

$$\tilde{D}_n > c(\alpha) \sqrt{\frac{2n}{n^2}} \quad (2.10)$$

for significance levels $c(0.05) = 1.36$ and $c(0.01) = 1.63$. A similar approach was applied by Pasaniuc *et al.* (2014) to compare signatures of functional enrichment in imputed data.

Table 2.4: Effect of quality control on imputed genotype data. The number (percent) of variants retained after QC for direct imputations (*i.e.* four split panels, intersection panel, and union panel) and meta-imputation. Numbers refer to variants retained after removing unmatched sites and those contained in the imputation scaffold.

Panel	Scenario A			Scenario B		
	Split	n retained	(%)	Split	n retained	(%)
Split panel (1)	CEU	135,218	(95.4)	AFR	123,662	(91.8)
Split panel (2)	FIN	141,017	(96.6)	AMR	155,266	(93.6)
Split panel (3)	GBR	137,277	(95.0)	ASN	99,531	(94.3)
Split panel (4)	TSI	138,613	(94.0)	EUR	161,364	(95.3)
Meta-imputed (1–4)	–	161,079	(88.7)	–	166,458	(84.8)
Intersection panel	–	116,980	(99.8)	–	92,312	(99.8)
Union panel	–	174,229	(96.0)	–	184,158	(93.8)

The numbers of retained variants for each panel are given in Table 2.4 (this page). Meta-imputed data showed the highest proportion of variants removed through QC. In Scenario A, 11.3 % of meta-imputed variants were removed, whereas only 0.197 % of variants in the intersection and 4.04 % in the union panel were removed, compared to an average of 4.74 % (± 0.536 % SE) among split panels. Note that only 3.40 % of markers did not pass QC after imputation from the FIN sub-population. The proportion of meta-imputed genotypes removed after QC was also highest in Scenario B (15.2 %) which is compared to only 0.163 % in the intersection and 6.19 % in the union panel, as well as 6.23 % (± 0.735 % SE) on average in split panels, where the lowest proportion of removed variants was seen for the EUR panel (4.66 %). However, the number of retained variants in meta-imputed data (161,076 and 166,458 in A and B, respectively) exceeded those retained in any split panel or the intersection panel; see Table 2.4.

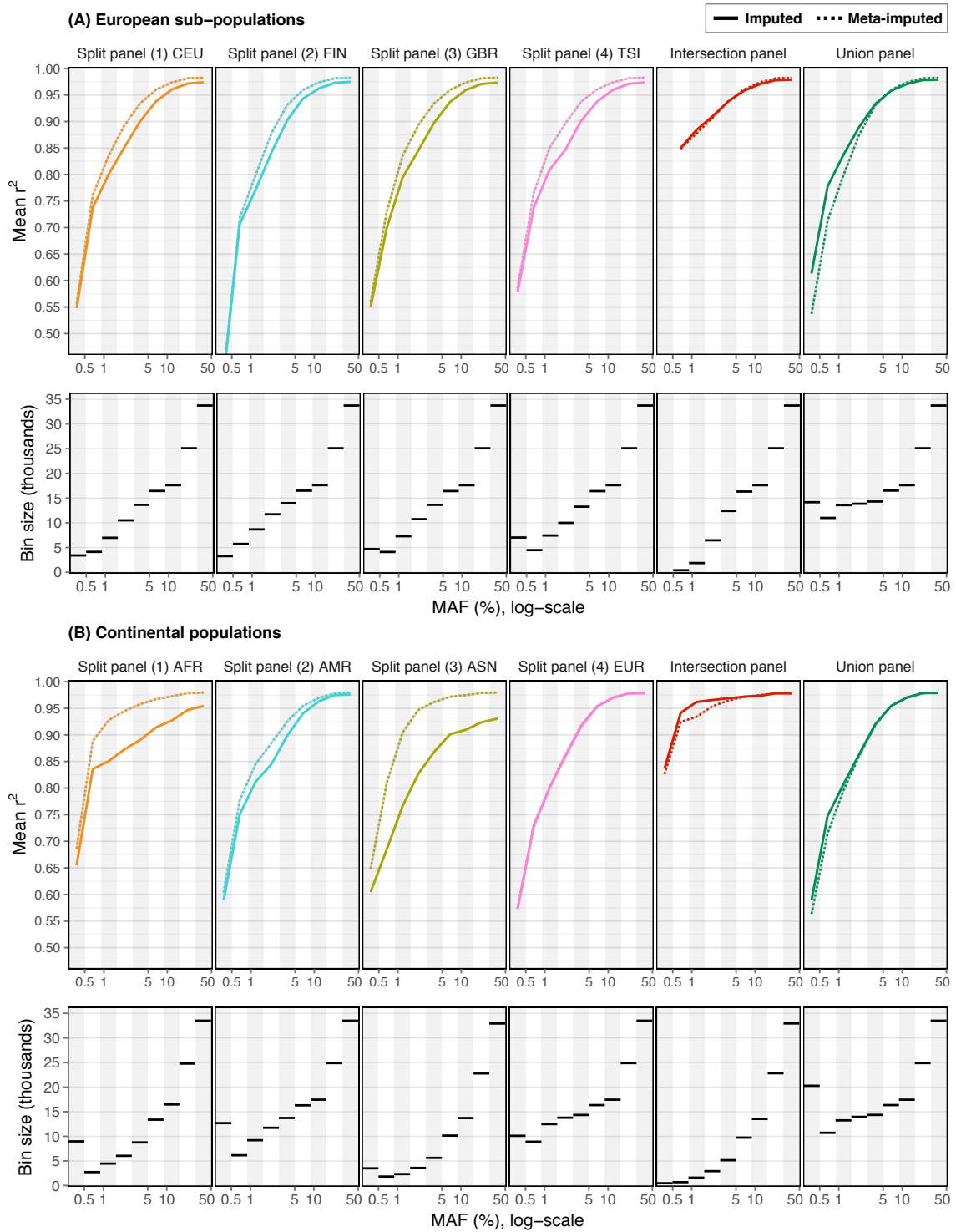


Figure 2.5: Accuracy comparison between meta-imputation and direct imputations. Accuracy was measured as mean r^2 per MAF bin, defined on log-scale where grey-white bars indicate boundaries. Each imputed panel (imputations from the four split panels, the intersection panel, and the union panel) was separately compared to meta-imputation on the same set of variants per bin; shown for variants retained after QC, in Scenarios A and B. MAF bins were defined on the actual allele frequencies as determined by the GoT2D dataset. Note that mean r^2 is not shown if the number of markers dropped below 50 per MAF bin. Panels at the bottom show the number of variants compared per bin.

Each of the imputed datasets was compared separately to meta-imputation, on the same set of variants retained after QC. The distribution of accuracy (mean r^2) measured by MAF is shown in Figure 2.5 (page 65); average accuracy measured for each imputation strategy in comparison to meta-imputation is given in Table 2.5 (next page), where accuracy was measured by MAF to distinguish rare variants ($MAF \in [0.00, 0.01]$), low-frequency ($MAF \in (0.01, 0.05]$), and common variants ($MAF \in (0.05, 0.50]$).

In Scenario A, meta-imputation showed an improvement in accuracy over imputations from split panels. For example, for rare variants, the highest improvement among split panel comparisons was seen with the GBR sample, where mean r^2 was $0.637 (\pm 3.37 \times 10^{-3} SE)$ for GBR and $0.659 (\pm 3.30 \times 10^{-3} SE)$ for meta-imputed data. Differences were larger at low-frequency, where the highest improvement was seen in comparison with the TSI sample; $0.865 (\pm 1.16 \times 10^{-3} SE)$ and $0.907 (\pm 0.808 \times 10^{-3} SE)$ for TSI and meta-imputation, respectively. Only the union panel was higher in accuracy than meta-imputation; *e.g.* $0.697 (\pm 1.87 \times 10^{-3} SE)$ and $0.627 (\pm 2.00 \times 10^{-3} SE)$ for rare variants, respectively, and $0.893 (\pm 0.801 \times 10^{-3} SE)$ and $0.877 (\pm 0.859 \times 10^{-3} SE)$ at low-frequency variants, respectively. Meta-imputation showed approximately equal levels of accuracy as the union panel at common variants, where the difference in mean r^2 was $0.00318 (\pm 0.811 \times 10^{-4} SE)$.

Genotype accuracy showed higher differences in Scenario B, where meta-imputation improved accuracy in most split panel comparisons. For rare variants, the highest difference was seen to genotype data imputed from the AFR split panel, where mean r^2 was $0.703 (\pm 3.24 \times 10^{-3} SE)$, compared to $0.745 (\pm 3.07 \times 10^{-3} SE)$ for meta-imputed genotypes. However, meta-imputation showed similar accuracy as the imputation from the EUR sample, where the difference in mean r^2 was $0.00208 (\pm 0.716 \times 10^{-4} SE)$. Likewise, at low-frequency, mean r^2 was $0.879 (\pm 1.63 \times 10^{-3} SE)$ for AFR and $0.948 (\pm 0.767 \times 10^{-3} SE)$ for meta-imputation, and the difference in accuracy was $0.00249 (\pm 0.367 \times 10^{-3} SE)$ with regard to the EUR split panel. As in Scenario A, differences were smaller for common variants, such that the difference in mean r^2 was below 0.001 in comparisons to imputations from the AFR, AMR, and EUR panels, but where the ASN sample

Table 2.5: Accuracy of imputation strategies at rare, low-frequency, and common variants.

Accuracy was calculated as mean r^2 per MAF bin on the same set of variants retained after QC in each comparison between meta-imputation and direct imputation, where n denotes the number of variants compared. The imputation strategy with the highest accuracy is highlighted (**bold**). The median of KS test statistic, \tilde{D}_{500} , determined whether imputed and meta-imputed MAF distributions were significantly different; see Equation (2.10) on page 64.

MAF bin	Panel	<i>n</i>	Imputation		Meta-imputation	KS test [†] \tilde{D}_{500}
			Mean r^2 (\pm SE*)	Mean r^2 (\pm SE [‡])		
Scenario A (European sub-populations)						
[0.00, 0.01]	Split panel, CEU	8,636	0.665 (3.491)	0.683 (3.402)	0.046	
	Split panel, FIN	10,416	0.619 (3.292)	0.630 (3.255)	0.024	
	Split panel, GBR	10,023	0.637 (3.371)	0.659 (3.296)	0.034	
	Split panel, TSI	12,763	0.654 (2.974)	0.670 (2.909)	0.098*	
	<i>Intersection panel</i>	546	0.823 (9.901)	0.824 (9.832)	0.028	
	<i>Union panel</i>	27,712	0.697 (1.873)	0.627 (2.001)	0.264**	
(0.01, 0.05]	Split panel, CEU	30,012	0.866 (1.092)	0.902 (0.813)	0.040	
	Split panel, FIN	32,969	0.853 (1.076)	0.885 (0.887)	0.032	
	Split panel, GBR	30,442	0.860 (1.119)	0.901 (0.813)	0.036	
	Split panel, TSI	29,445	0.865 (1.164)	0.907 (0.808)	0.036	
	<i>Intersection panel</i>	20,604	0.925 (0.850)	0.923 (0.803)	0.034	
	<i>Union panel</i>	39,213	0.893 (0.801)	0.877 (0.859)	0.088*	
(0.05, 0.50]	Split panel, CEU	92,885	0.964 (0.269)	0.977 (0.180)	0.014	
	Split panel, FIN	92,936	0.966 (0.250)	0.977 (0.181)	0.012	
	Split panel, GBR	92,845	0.964 (0.273)	0.977 (0.181)	0.012	
	Split panel, TSI	92,840	0.964 (0.283)	0.977 (0.180)	0.012	
	<i>Intersection panel</i>	92,751	0.973 (0.212)	0.977 (0.180)	0.012	
	<i>Union panel</i>	92,938	0.973 (0.212)	0.977 (0.181)	0.012	
Scenario B (Continental populations)						
[0.00, 0.01]	Split panel, AFR	12,495	0.703 (3.238)	0.745 (3.070)	0.030	
	Split panel, AMR	20,416	0.653 (2.480)	0.672 (2.388)	0.040	
	Split panel, ASN	5,661	0.640 (4.972)	0.714 (4.586)	0.082	
	Split panel, EUR	21,223	0.658 (2.227)	0.656 (2.207)	0.048	
	<i>Intersection panel</i>	1,364	0.907 (4.420)	0.892 (4.430)	0.172**	
	<i>Union panel</i>	33,430	0.653 (1.871)	0.626 (1.894)	0.148**	
(0.01, 0.05]	Split panel, AFR	18,468	0.879 (1.631)	0.948 (0.767)	0.048	
	Split panel, AMR	33,093	0.861 (1.158)	0.894 (0.855)	0.036	
	Split panel, ASN	11,181	0.837 (2.414)	0.948 (0.954)	0.114**	
	Split panel, EUR	38,417	0.867 (0.969)	0.870 (0.910)	0.032	
	<i>Intersection panel</i>	9,443	0.967 (0.811)	0.957 (0.816)	0.062	
	<i>Union panel</i>	39,140	0.871 (0.949)	0.866 (0.924)	0.058	
(0.05, 0.50]	Split panel, AFR	88,152	0.941 (0.426)	0.976 (0.172)	0.022	
	Split panel, AMR	92,144	0.967 (0.263)	0.973 (0.191)	0.016	
	Split panel, ASN	79,581	0.921 (0.519)	0.978 (0.165)	0.024	
	Split panel, EUR	92,188	0.972 (0.218)	0.973 (0.193)	0.016	
	<i>Intersection panel</i>	79,051	0.976 (0.201)	0.977 (0.168)	0.016	
	<i>Union panel</i>	92,187	0.973 (0.214)	0.973 (0.193)	0.016	

[†] Median of the Kolmogorov–Smirnov (KS) test statistic, \tilde{D} ; empirical CDF of imputed and meta-imputed MAF tested at $\alpha = 0.05$ (*) and $\alpha = 0.01$ (**).

[‡] Standard error (SE) $\times 10^{-3}$.

showed the highest difference; mean r^2 was 0.921 ($\pm 0.519 \times 10^{-3}$ SE) for ASN and 0.978 ($\pm 0.165 \times 10^{-3}$ SE) for meta-imputation. The union panel was similar in accuracy as meta-imputation, where the overall difference in mean r^2 was 0.0106 ($\pm 8.47 \times 10^{-3}$ SE).

Imputations from the intersection panel in Scenario A and B showed approximately equal levels of accuracy to meta-imputation. The difference in mean r^2 averaged to 0.000811 ($\pm 1.43 \times 10^{-4}$ SE) across MAF in Scenario A, and 0.00824 ($\pm 4.82 \times 10^{-3}$ SE) in Scenario B. However, note that the number of variants in the intersection panel was the lowest among available panel data in both scenarios (Table 2.4), and was further reduced as accuracy was measured on the same sets of variants retained in both the intersection and the meta-imputed datasets. For example, the comparison between the intersection panel and meta-imputation included only 546 variants at $MAF \leq 1\%$ in Scenario A and 1,364 variants in Scenario B, whereas each split panel and the union panel were compared on several thousands of variants at this frequency range. The high accuracy of genotypes imputed from the intersection panel may result from retaining only those variants that are “cosmopolitan” within the scope of the present evaluation.

Further, the empirical cumulative distribution function (CDF) of MAF at imputed and meta-imputed variants was compared per MAF bin. Differences are illustrated in Figure 2.6 (next page), which shows the CDF of compared variants in relation to the known population frequencies at masked variants in the GoT2D dataset; calculated by subtracting (meta-)imputed frequencies from masked frequencies (ΔMAF) at the same set of markers. Notably, meta-imputed frequencies showed high consistency with imputed frequencies at rare variants ($MAF \in [0.00, 0.01]$) across split panel imputations, but were skewed in comparison to imputations from the union panel in both scenarios. Significant differences were found for rare variant imputations from the TSI sample ($\tilde{D} = 0.098$) in Scenario A, as well as for the union panel at rare and low-frequency variants (0.264 and 0.088, respectively). In Scenario B, imputed and meta-imputed differences were significantly different for rare variant imputations from the intersection panel and the union panel (0.172 and 0.148, respectively) and for the union panel at low-frequency variants (0.114). These results suggested that meta-imputation was able to correctly reproduce realistic

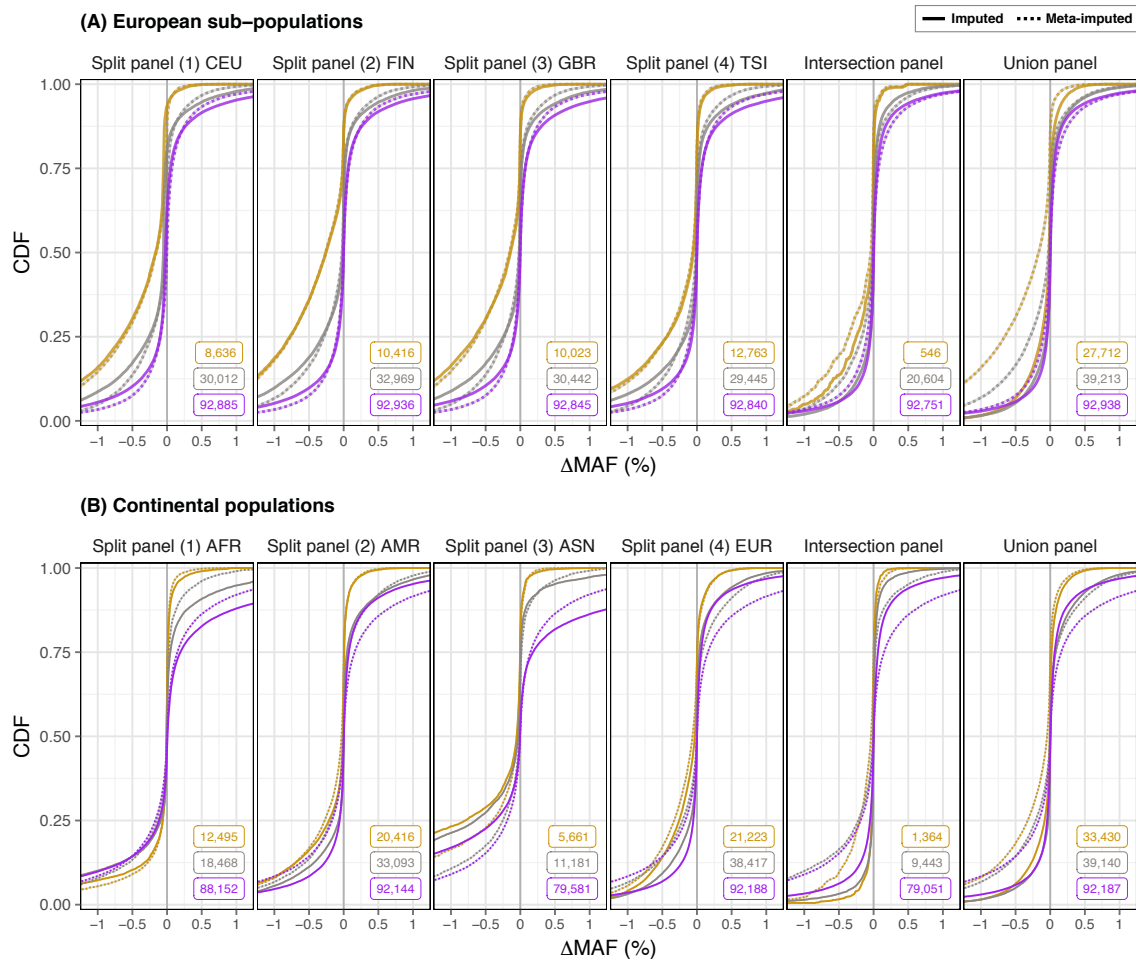


Figure 2.6: Difference between imputed and masked minor allele frequency. Comparison of imputed and meta-imputed MAF in relation to known population frequencies, compared on the same set as retained after QC in each comparison. Frequency difference, ΔMAF , was calculated as the MAF observed at a masked variant minus MAF at the corresponding (meta-)imputed variant, pooled in three MAF bins; rare variants ($\text{MAF} \in [0.00, 0.01]$; yellow), low-frequency ($\text{MAF} \in (0.01, 0.05]$; grey), and common variants ($\text{MAF} \in (0.05, 0.50]$; purple). Numbers per MAF bin per comparison are given in each panel (colour-coded).

allele frequency distributions from the combination of imputed genotypes from different sources, while achieving higher or similar accuracy compared to direct imputations from split panels. Results of KS tests in each comparison are given in Table 2.5 (page 67).

In summary, split panel imputations were either outperformed or similar levels of accuracy were achieved in direct comparisons to meta-imputed data; see Table 2.5 for a complete summary of genotype accuracy measured in each comparison. Although imputations from the union panel outperformed meta-imputation, such differences may be expected given that the union panel contained all the information which meta-imputation

had to leverage indirectly from several data sources. Nonetheless, the present evaluation of genotype accuracy was limited with regard to coverage; for instance, genotype data imputed from the intersection panel was found to be relatively high in accuracy and similar with regard to meta-imputed data, but the low number of variants present in the intersection panel may not yield similar improvements under realistic conditions in association analyses. Therefore, to provide a comprehensive assessment of the meta-imputation method and to account for a potential tradeoff between accuracy and coverage, I conducted a more extensive power analysis in the following section.

2.5 Power to detect significant risk signals

The power of meta-imputation to detect disease risk factors in association tests was evaluated using simulated sample data. This was done in consideration of expected power when causal risk factors vary in their allele frequency as well as risk effect size. In particular, a series of simulated case-control association experiments was conducted, from which the power to detect significant association signals was determined, at specified allele frequencies and effect size of simulated risk factors. The description of the methods used is provided below (Section 2.5.1, this page), followed by the presentation of results (Section 2.5.2, page 74).

2.5.1 Methods

The same regime to carry out imputation and QC was followed as described in Section 2.4.1 (page 57). An additional set of haplotype reference data was available from four independent sequencing studies, which were included here as Scenario C; see below.

Finns. A Finnish cohort composed of data from the Sequencing Initiative Suomi Project (*SISu*) and the *Finrisk* Project (Vartiainen *et al.*, 2010; Pajunen *et al.*, 2010; Lim *et al.*, 2014; Borodulin *et al.*, 2015); 4x depth; sample size and number of SNPs considered here were $N = 1,941$ and $M = 283,654$, respectively.

GoNL. The Genome of the Netherlands Project (Boomsma *et al.*, 2013; Deelen *et al.*, 2014; Genome of the Netherlands Consortium, 2014); 12x depth, consisting of a representative sample of 250 trio-families; $N = 748$, $M = 362,694$.

ORCADES. The Orkney Complex Disease Study of genetic epidemiology of an isolated population in northern Scotland (McQuillan *et al.*, 2008); 4x depth, family-based data; $N = 399$, $M = 236,755$.

UK10K. The *UK10K* Genome Sequencing Project (UK10K Consortium *et al.*, 2015); 6.5x depth; $N = 3,642$, $M = 527,199$.

Also, an intersection panel was prepared from these four datasets, but no union panel. As before, only data from chromosome 20 were considered. Note that the above datasets were part of the early stage HRC testing phase (McCarthy *et al.*, 2016).*

Simulation of study sample data

Simulations were performed using *HAPGEN* version 2.2.0 (Su *et al.*, 2011), which requires a *template* dataset of haplotypes to reproduce realistic variant data in HWE, such that LD patterns in the simulated dataset are consistent with the haplotype sample. Individual sites can be simulated to independently act as causal disease variants with specified relative risk. The simulation generates two GWA samples of individuals that are affected (*cases*) or not affected (*controls*) by a disease phenotype. Data are identical in coverage as the template dataset.

Here, simulations were performed using GoT2D data (chromosome 20) to serve as the template dataset. The size of simulated case and control samples was fixed to 2,500 individuals each. Although a larger sample would have been beneficial in terms of signal detection through association testing, exceeding the size of the template dataset ($N = 2,657$) was expected to result in factitious allele frequency changes. For example, an iterative re-sampling strategy could be applied to introduce new low-frequency variants

* Acknowledgement: Data provided by Professor Jonathan Marchini, Department of Statistics, University of Oxford; prior to the release of the HRC dataset.

(e.g. following Moutsianas *et al.*, 2015). However, this was not done here because the effect size of risk variants (as defined during simulation) would likely be affected by such a sampling process.

A series of simulation experiments was conducted in which one variant was selected per simulation to act as a causal risk factor. Its relative risk (RR) was defined for heterozygous genotypes (RR_{het}) in a log-additive disease model (*i.e.* multiplicative on linear scale); the following three risk categories were defined.

$$\text{Low risk : } RR_{het} = 1.2 \quad (RR_{hom} = 1.44)$$

$$\text{Modest risk : } RR_{het} = 1.6 \quad (RR_{hom} = 2.56)$$

$$\text{High risk : } RR_{het} = 2.0 \quad (RR_{hom} = 4.00)$$

The analysis was performed by conducting 300 replicate simulations per risk category, where variants occurring at different frequencies were selected in three defined MAF intervals; very low frequency ($MAF \in [0.5, 1]$ %), low frequency ($MAF \in (1, 5]$ %), and high frequency ($MAF \in (5, 50]$ %), such that 100 variants were drawn from each interval and simulated as risk variants.

Note that variant selection was done at random, regardless of presence or absence of the selected variant in any of the available reference panels, so as to mirror conditions encountered under realistic GWA settings; *i.e.* when a causal variant itself is absent in an imputation reference, its risk effects may be detectable through LD at neighbouring sites.

To generate a study sample for imputations, a variant scaffold was extracted from each simulation replicate. Because the set of simulated variants mirrored those in the GoT2D dataset, sites that matched with variants typed on *Illumina Omni2.5 Array* were identified and extracted. A scaffold thus contained 40,255 variants into which available reference panels were imputed. Note that simulations produced two datasets; one case and one corresponding control dataset. These were concatenated before imputation to ensure consistency in the imputation analysis. Imputed data were again separated into case and control samples prior to association analysis (described below). Because HAPGEN2 produces

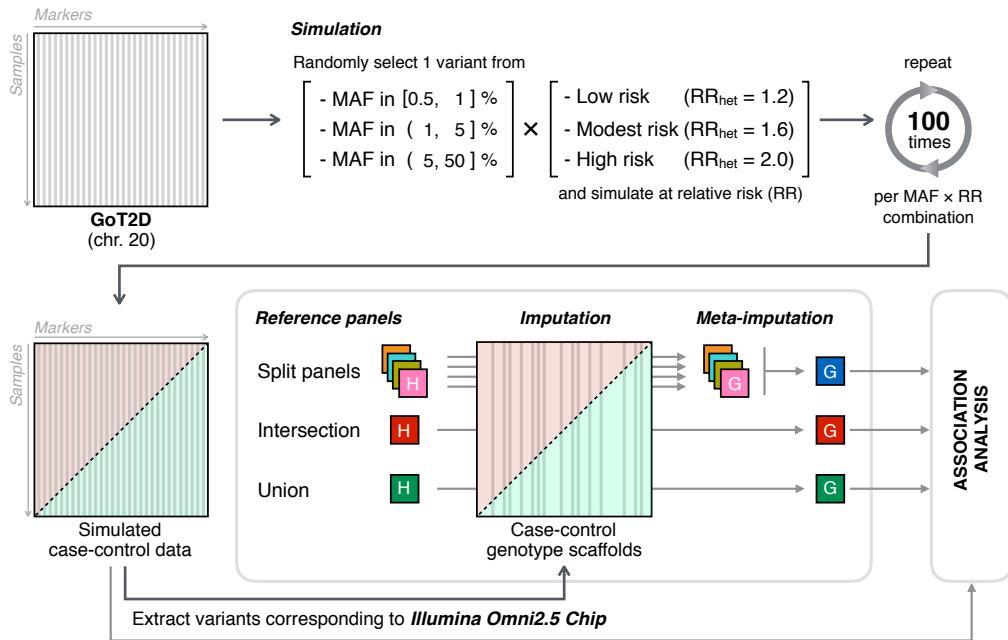


Figure 2.7: Illustration of the simulation process. Meta-imputation was assessed in terms of statistical power to detect significant risk association signals in a series of simulated case-control experiments. The GoT2D datasets was used as a template for simulations using HAPGEN (Su *et al.*, 2011), where one variant was randomly selected within one of three defined MAF intervals. The selected variant was then simulated to act as a causal disease variant in the simulated case-control dataset, where relative risk (RR_{het}) was defined according to one of three defined risk categories. In total, 100 replicate simulations were conducted per combination of MAF interval and risk category (per scenario). Simulated data were used to extract a genotype scaffold into which available reference panels were imputed, followed by meta-imputation of imputed datasets. Imputed and meta-imputed datasets were then subjected to association analysis, including the simulated (not imputed) datasets for comparison.

haplotype data, imputations were executed on pre-phased genotypes. A summary of the simulation process is illustrated in Figure 2.7 (this page).

Association analysis in imputed genotype data

Imputed case and control datasets were analysed using a frequentist score test under an additive model of association, implemented in SNPTEST version 2.5 (Marchini *et al.*, 2007). In contrast to the previous analysis (Section 2.4 on page 56), in which the variants not included in the extracted scaffold were masked to measure accuracy after imputation, here, the simulated case-control dataset was retained and separately examined in association analysis. This was done to enable comparisons of meta-imputed and imputed data to a non-imputed benchmark result for each simulation replicate.

The genomic control inflation factor, λ_{GC} , was calculated to investigate if systematic biases are present in association results, which is defined as the median of χ^2 test statistics resulting from case-control association tests divided by the expected median of the χ^2 distribution (Devlin *et al.*, 2001). Because the frequentist score test was used, λ_{GC} was calculated on basis of the resulting *p*-values from which the χ^2 statistic was calculated with one degree of freedom.

Calculation of power in replicate simulation experiments

Significant association signals were identified in each simulation and pooled by MAF interval and risk category, according to which variants were selected and simulated. The proportion of datasets in which significance was reached at the known risk variant was taken as a simple estimate for the statistical power to detect genetic risk effects. Note that the position of the simulated risk variant was known through simulation, but the variant itself may not be retained after imputation or QC. Therefore, signal detection was performed within a 1 Mb region around the position of the simulated risk variant, for any site reaching significance with this region.

Significance was defined at a nominal threshold of *p*-value $\leq 1 \times 10^{-6}$. Note that this threshold is higher (thus, less conservative) than commonly applied genome-wide thresholds, *e.g.* at 5×10^{-8} (*e.g.*, see Risch and Merikangas, 1996), because analyses were conducted on data from chromosome 20 only. However, to provide additional detail, power was estimated under a moving significance threshold; between *p*-value $\leq 1 \times 10^{-8}$ and *p*-value $\leq 1 \times 10^{-4}$. As a comparative measure between association results produced from the different imputation strategies, the difference in power between the non-imputed simulation dataset and a given (meta-)imputed dataset is reported, denoted by Δ_P , which is calculated as the average difference along the moving significance threshold.

2.5.2 Results

A number of 100 variants were selected per MAF interval such that there were 300 variants in total. Each was then simulated at the three defined risk categories such that 900

simulations were conducted from which a genotype scaffold was extracted for imputation. Given the four split panels, the intersection panel, and the union panel available per Scenario A and B, as well as the four independent reference datasets and the generated intersection panel in Scenario C, a total of 15,300 imputation analyses were performed. Imputed data were then combined in meta-imputation (except the intersection and union panels), resulting in 900 additional genotype datasets. Each dataset was then subjected to association analysis, including the non-imputed simulated case-control sample, which was used as a benchmark for comparisons. Hence, a total of 17,100 association analyses were conducted, where each was treated as an independent GWA study. All analyses were performed on whole-chromosome data (chromosome 20).

Association results were inspected with regard to inflation before and after QC; the difference is shown in Figure 2.8 (next page) where λ_{GC} is shown as the average per MAF interval. Inflation was slightly increased at higher frequencies; for example, association results using the non-imputed simulation dataset were at $\lambda_{GC} \approx 1$ on average in each scenario when the simulated risk variant was very low in frequency ($MAF \in [0.5, 1] \%$), but increased to $\lambda_{GC} \approx 1.05$ for risk variants at higher frequencies ($MAF \in [5, 50] \%$). The impact of QC was largest in Scenario B, where association results of split panel imputed data were deflated ($\lambda_{GC} < 1$) when seen in comparison to the simulated dataset or the intersection and union panels. Notably, inflation was lowest for association results obtained from meta-imputed data in Scenarios A and B. The difference between λ_{GC} calculated before and after QC was negligible in Scenario C.

Association results for each imputation strategy (referring to results obtained on genotype data imputed from available reference panels and meta-imputation) were separately evaluated with regard to each combination of risk category and the MAF interval from which simulated risk variants were selected. The distribution of power measured under a moving significance threshold (between $p\text{-value} \leq 1 \times 10^{-8}$ and $p\text{-value} \leq 1 \times 10^{-4}$) is shown in Figure 2.9; for Scenario A (page 77), B (page 78), and C (page 79). The results are summarised in Table 2.6, for power measured at the nominal significance threshold ($p\text{-value} \leq 1 \times 10^{-6}$) and the average difference to the

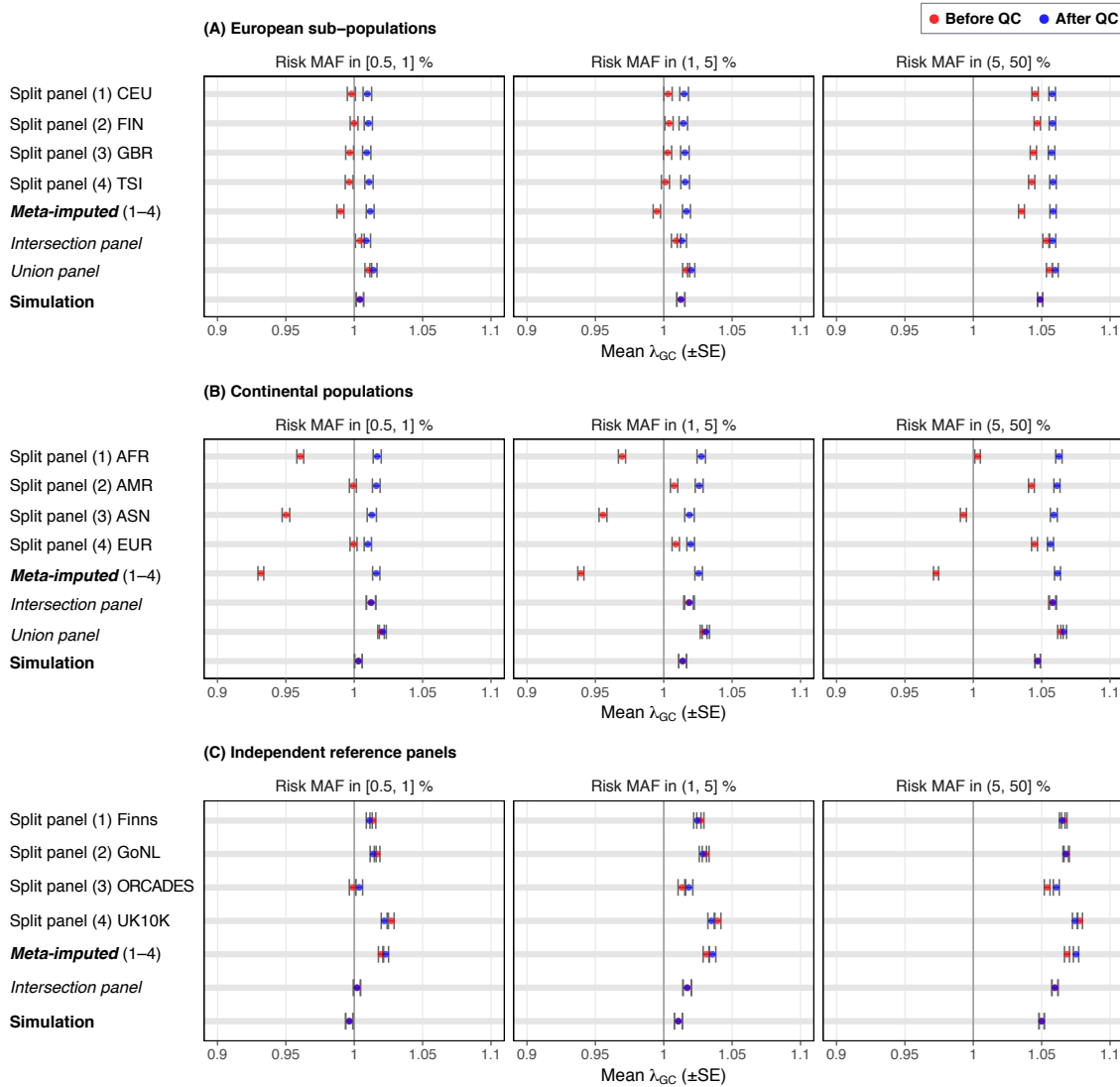


Figure 2.8: Inflation observed in simulated case-control experiments. Genomic control inflation factor calculated before (red) and after (blue) variants were filtered in QC, reported as mean λ_{GC} over replicate association results by MAF of the simulated risk variants.

non-imputed simulation benchmark (Δ_P) along the moving threshold, averaged per MAF interval of simulated risk variants; for Scenario A (page 80), B (page 81), and C (page 82).

The union panel was seen with the lowest average difference in power at very low frequencies of the simulated risk variant ($MAF \in [0.5, 1] \%$) in Scenario A, where Δ_P was $1.05 (\pm 0.206 \text{ SE})$. Meta-imputation showed the lowest average difference at very low MAF in Scenario B, $\Delta_P = 1.23 \% (\pm 0.247 \% \text{ SE})$, as well as Scenario C, $\Delta_P = 1.32 \% (\pm 0.248 \% \text{ SE})$; but recall that Scenario C (independent reference panels) did not contain a union panel. However, even in the high risk category in each scenario,

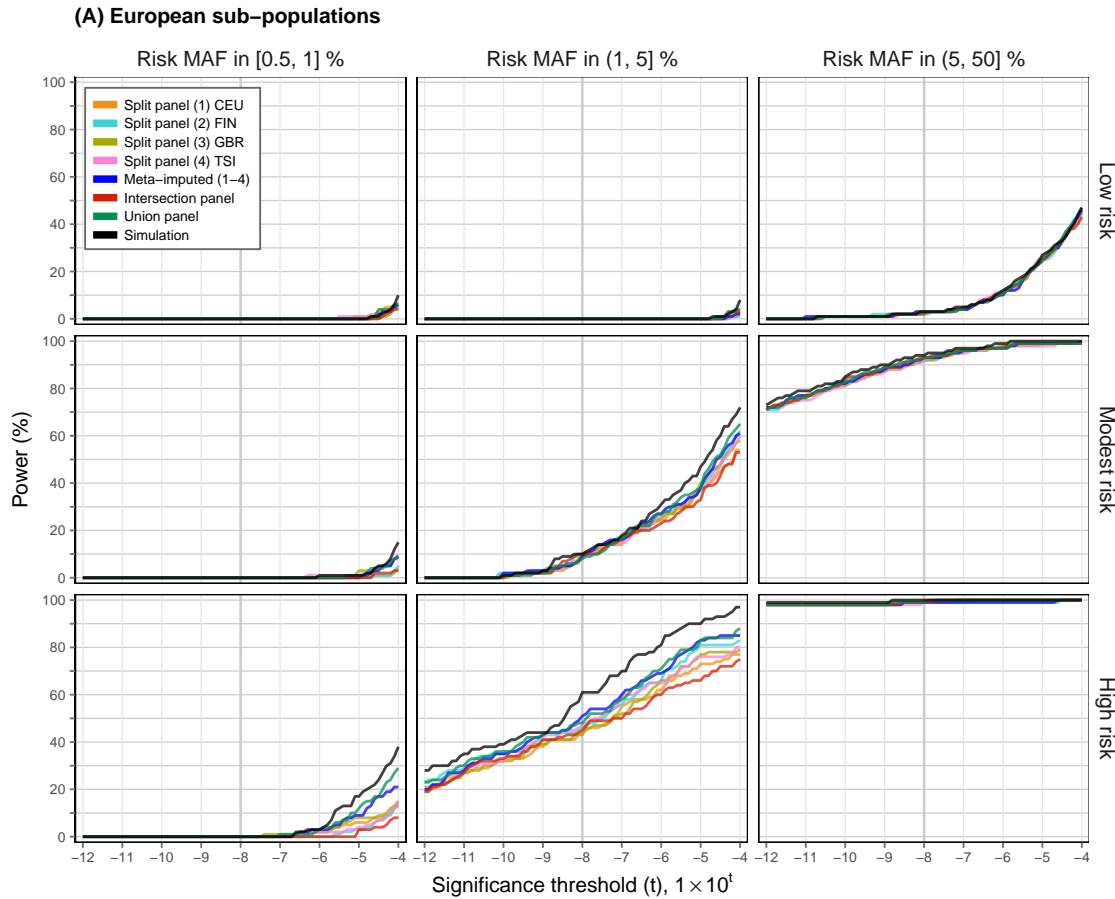


Figure 2.9: Power measured under a moving significance threshold. Power was calculated as the proportion of replicate association analyses ($n = 100$, per combination of risk category and MAF interval) in which any signal reached significance within 1 Mb around the position of a simulated risk variant. A moving significance threshold between $p\text{-value} \leq 1 \times 10^{-8}$ and $p\text{-value} \leq 1 \times 10^{-4}$ was applied to each association dataset.

estimated power did not exceed 3% for any imputation strategy when the simulated risk variant was very low in frequency, such that observed differences were negligible as these could be attributed to stochastic noise. Similarly, observed differences were small in each risk category when causal variants were selected from the high frequency interval ($\text{MAF} \in [5, 50]\%$), where the lowest average difference in power was recorded for the union panel in Scenario A, $\Delta_P = 0.537\% (\pm 0.067,6\% \text{ SE})$, the EUR split panel in B, $0.650\% (\pm 0.072,1\% \text{ SE})$, and the intersection panel in C, $0.545\% (\pm 0.091,8\% \text{ SE})$. However, note that $\Delta_P < 1\%$ in each strategy at high risk MAF in Scenarios A and C, but where some of the strategies showed larger differences in Scenario B, *e.g.* the ASN

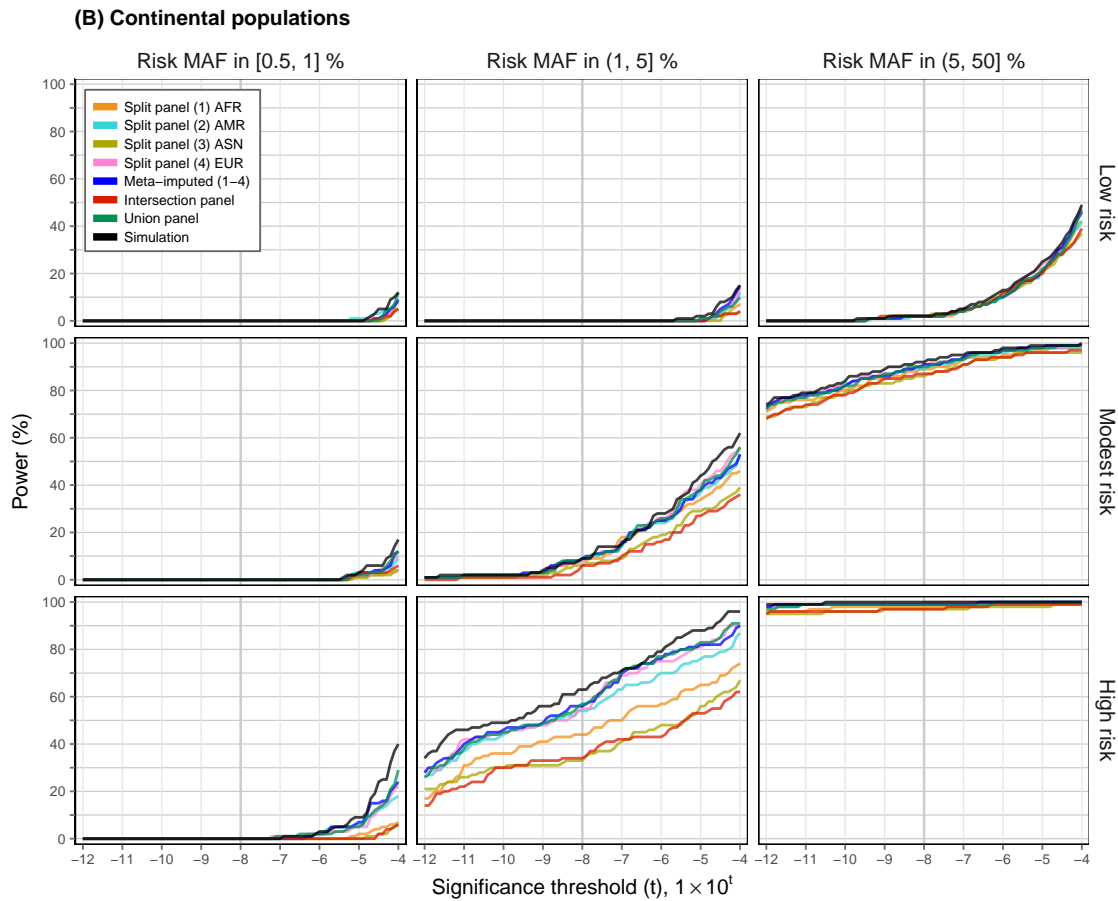


Figure 2.9: Continued.

split panel and the intersection panel; 2.83 % ($\pm 0.177\%$ SE) and 2.56 % ($\pm 0.173\%$ SE), respectively.

Noticeable differences were seen among imputation strategies for simulated risk variants selected at low frequency ($\text{MAF} \in [1, 5]\%$). The union panel was recorded with the lowest difference in power relative to the non-imputed simulation benchmark in Scenarios A and B, 4.85 % ($\pm 0.416\%$ SE) and 2.65 % ($\pm 0.248\%$ SE), respectively, whereas the intersection panel had the highest difference, 9.56 % ($\pm 0.846\%$ SE) and 15.5 % ($\pm 1.25\%$ SE), respectively. Notably, meta-imputation was similarly close as the union panel and outperformed the other imputation strategies in Scenario A, 4.96 % ($\pm 0.431\%$ SE). For example, at a nominal threshold ($p\text{-value} \leq 1 \times 10^{-6}$), the union panel reached 71% power and meta-imputation 69% in the high risk category. In Scenario B, the power observed for meta-imputed data was high by comparison,

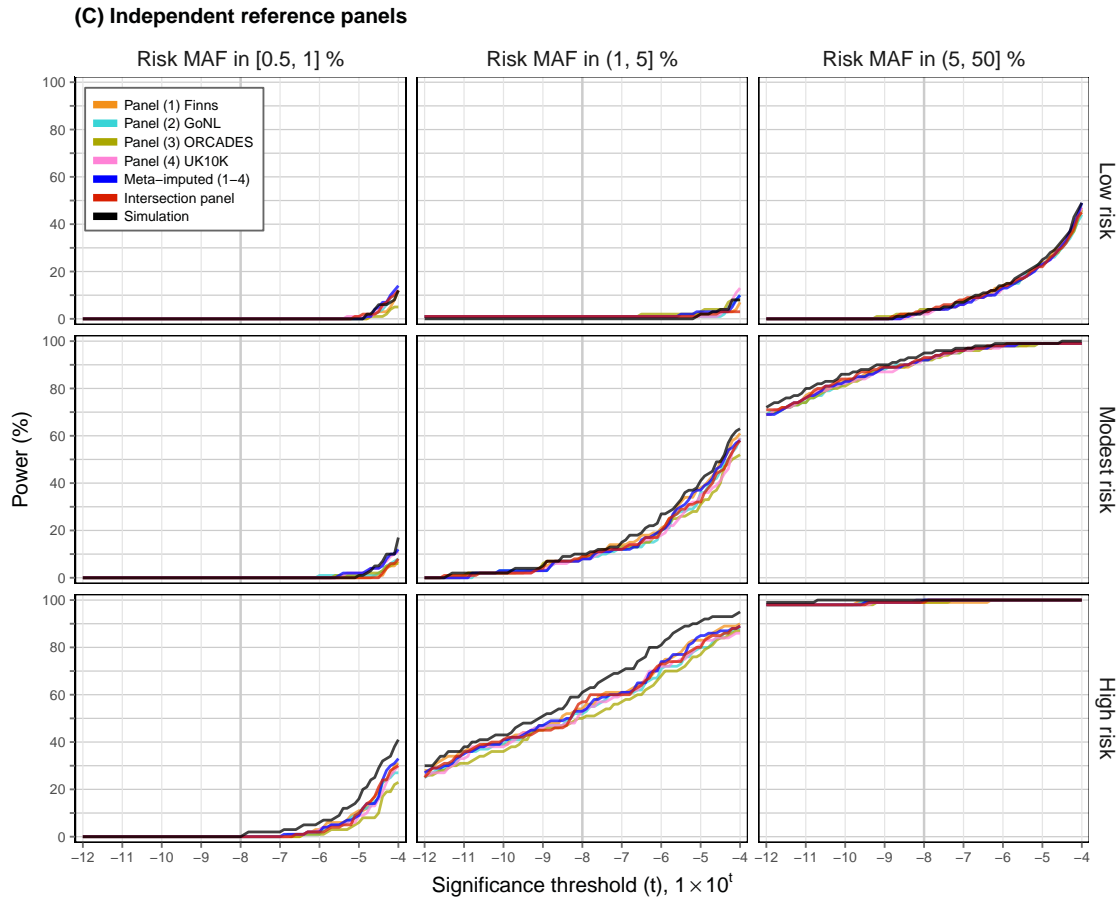


Figure 2.9: Continued.

e.g. 76% power at high risk, compared to 77% for the union panel and 43% for the intersection panel; however, Δ_P measured for meta-imputation was 3.07 % (± 0.295 % SE), which was lower in the EUR split panel, 2.72 % (± 0.259 % SE), reaching 76% in the high risk category. In Scenario C, the *Finns* panel showed the lowest difference in power, 3.11 % (± 0.343 % SE), and the *ORCADES* panel the highest, 5.76 % (± 0.572 % SE); yet, meta-imputation ranked 2nd best among the strategies compared, 3.51 % (± 0.357 % SE), but 1st in the high risk category with 74% power (compared to 73% and 68% for *Finns* and *ORCADES*, respectively).

2.6 Discussion

Meta-imputation was presented as a novel approach to integrate reference data after imputation into a common study sample, but the idea of combining genotype data imputed

Table 2.6: Estimated power per imputation strategy. Power was estimated as the proportion of significant association signals found among replicate simulation experiments, for which one variant per simulation was selected at random from three MAF intervals (as specified in the table). Each of the selected variants was simulated to act as a causal risk factor, where relative risk was simulated in three categories; low ($RR_{het} = 1.2$), modest ($RR_{het} = 1.6$), and high risk ($RR_{het} = 2.0$). Power at a nominal significance threshold ($p\text{-value} \leq 1 \times 10^{-6}$) is reported at each combination of MAF interval and risk category. The average difference (Δ_P) in relation to the non-imputed simulation benchmark is given per MAF interval for each imputation strategy; the lowest average difference is highlighted (**bold**). This table shows the results obtained for imputed and meta-imputed data in Scenario A; results for Scenario B (next page) and Scenario C (page 82) are shown separately.

(A) European sub-populations

Risk MAF (%)	Panel	Power (%), $p\text{-value} \leq 1 \times 10^{-6}$			Δ_P (%) [*]	
		Low	Modest	High	Mean	(\pm SE)
[0.5, 1]	Split panel (1) CEU	0	0	2	2.537	(0.487)
	Split panel (2) FIN	0	0	0	3.041	(0.520)
	Split panel (3) GBR	0	0	2	2.098	(0.444)
	Split panel (4) TSI	0	1	2	2.309	(0.509)
	Meta-imputed (1-4)	0	0	3	1.553	(0.289)
	<i>Intersection panel</i>	0	0	0	3.366	(0.593)
	<i>Union panel</i>	0	0	3	1.049	(0.206)
	Split panel (1) CEU	0	24	62	8.561	(0.729)
	Split panel (2) FIN	0	25	66	6.374	(0.543)
(1, 5]	Split panel (3) GBR	0	25	66	7.431	(0.670)
	Split panel (4) TSI	0	26	65	7.122	(0.605)
	Meta-imputed (1-4)	0	27	69	4.959	(0.431)
	<i>Intersection panel</i>	0	23	60	9.561	(0.846)
	<i>Union panel</i>	0	27	71	4.846	(0.416)
	Split panel (1) CEU	11	98	100	0.780	(0.068)
	Split panel (2) FIN	12	98	99	0.894	(0.070)
	Split panel (3) GBR	11	98	100	0.821	(0.083)
	Split panel (4) TSI	11	97	100	0.748	(0.090)
(5, 50]	Meta-imputed (1-4)	10	97	99	0.959	(0.069)
	<i>Intersection panel</i>	11	97	100	0.634	(0.073)
	<i>Union panel</i>	11	97	100	0.537	(0.068)

* Average difference in power between simulated and (meta-)imputed association results (Δ_P); averaged over risk category (low, modest, and high risk) and association signals detected at a moving significance threshold; between $p\text{-value} \leq 1 \times 10^{-8}$ and $p\text{-value} \leq 1 \times 10^{-4}$.

from different reference panels has been investigated before. Chen *et al.* (2013) used low to high-depth sequencing data as references for imputations into a given study sample, where imputed data have been matched and combined at overlapping sites, but such that variant genotypes imputed from the high-quality panel were included preferentially. They have shown that this approach improved overall accuracy compared to each separately

Table 2.6: Continued.**(B) Continental populations**

Risk MAF (%)	Panel	Power (%), p -value $\leq 1 \times 10^{-6}$			Δ_P (%) [*]	
		Low	Modest	High	Mean	(\pm SE)
[0.5, 1]	Split panel (1) AFR	0	0	0	3.000	(0.541)
	Split panel (2) AMR	0	0	3	1.488	(0.337)
	Split panel (3) ASN	0	0	0	3.203	(0.583)
	Split panel (4) EUR	0	0	2	1.553	(0.296)
	Meta-imputed (1-4)	0	0	2	1.228	(0.247)
	<i>Intersection panel</i>	0	0	0	3.049	(0.579)
	<i>Union panel</i>	0	0	2	1.301	(0.247)
	Split panel (1) AFR	0	25	57	9.366	(0.866)
	Split panel (2) AMR	0	24	70	5.220	(0.442)
(1, 5]	Split panel (3) ASN	0	19	48	14.618	(1.197)
	Split panel (4) EUR	0	26	75	2.715	(0.259)
	Meta-imputed (1-4)	0	25	76	3.065	(0.295)
	<i>Intersection panel</i>	0	16	43	15.545	(1.248)
	<i>Union panel</i>	0	26	77	2.650	(0.248)
	Split panel (1) AFR	11	95	99	1.984	(0.104)
(5, 50]	Split panel (2) AMR	10	96	99	1.407	(0.109)
	Split panel (3) ASN	12	94	98	2.829	(0.177)
	Split panel (4) EUR	11	97	100	0.650	(0.072)
	Meta-imputed (1-4)	10	97	100	0.951	(0.089)
	<i>Intersection panel</i>	12	94	99	2.561	(0.173)
	<i>Union panel</i>	10	97	100	1.138	(0.093)

* See Table 2.6A (page 80).

imputed dataset. Here, I considered several variations of this approach which I evaluated using several reference datasets as available in different use case scenarios. Notably, the meta-imputation method does not require prior knowledge to guide the merging process (such as high or low quality of each dataset considered), which instead is determined by summary information derived directly from imputed genotype data.

The results I presented in this chapter showed that the combination of genotype data may indeed result in an increase of accuracy across the allele frequency spectrum, but where the largest improvements were seen for low-frequency variants (*e.g.* 1–5% MAF). I showed that meta-imputation improved genotype accuracy such that single-reference imputations were outperformed (*e.g.* in Scenario A), but also that meta-imputed genotype data may not further increase accuracy if a reference is highly accurate by itself (*e.g.* the EUR sample in Scenario B). Nonetheless, the inclusion of other, more distantly related

Table 2.6: Continued.**(C) Independent reference panels**

Risk MAF (%)	Panel	Power (%), p -value $\leq 1 \times 10^{-6}$			Δ_P (%) [*]	
		Low	Modest	High	Mean	(\pm SE)
[0.5, 1]	Panel (1) Finns	0	0	3	1.919 (0.249)	
	Panel (2) GoNL	0	1	1	1.862 (0.290)	
	Panel (3) ORCADES	0	0	1	2.805 (0.416)	
	Panel (4) UK10K	0	0	3	1.683 (0.305)	
	Meta-imputed (1-4)	0	0	2	1.317 (0.248)	
	<i>Intersection panel</i>	0	0	2	1.854 (0.258)	
(1, 5]	Panel (1) Finns	1	21	73	3.114 (0.343)	
	Panel (2) GoNL	1	20	71	4.943 (0.436)	
	Panel (3) ORCADES	2	20	68	5.764 (0.572)	
	Panel (4) UK10K	1	18	72	4.789 (0.428)	
	Meta-imputed (1-4)	1	20	74	3.512 (0.357)	
	<i>Intersection panel</i>	1	20	73	4.195 (0.387)	
(5, 50]	Panel (1) Finns	14	98	100	0.683 (0.067)	
	Panel (2) GoNL	13	98	100	0.821 (0.103)	
	Panel (3) ORCADES	14	98	100	0.911 (0.096)	
	Panel (4) UK10K	13	98	100	0.780 (0.079)	
	Meta-imputed (1-4)	13	98	100	0.748 (0.079)	
	<i>Intersection panel</i>	14	98	100	0.545 (0.092)	

* See Table 2.6A (page 80).

reference haplotypes may not affect the accuracy of the resulting meta-imputed dataset (e.g. the AFR or ASN samples for imputation into the European sample in Scenario B).

Meta-imputed genotype data were contrasted with data obtained in imputations from corresponding, larger datasets, which contained the unified sample across the datasets considered in meta-imputation; *i.e.* the intersection and the union of variants present across the other reference datasets, respectively. Although meta-imputation did not perform markedly better in terms of accuracy (measured at the same variant sites), I showed that meta-imputation generally outperformed the intersection panel, in terms of power to detect significant association signals, due to the low coverage retained at the intersection of variants across available reference data. However, note that meta-imputation combined data such that the resulting coverage was identical to the coverage of the union panel; meta-imputed data was overall similar to using the union reference for imputation, with regard to both accuracy and power.

In conclusion, these results suggest that meta-imputation is a viable approach to combine genotype data such that a larger, unified dataset of imputed genotypes is available for association analysis. However, it is unlikely to increase accuracy and power further than possible with imputation from a large, canonical reference; *e.g.* the reference dataset provided by the Haplotype Reference Consortium (HRC). Yet, future GWA studies may benefit from meta-imputation, for example, in situations when researchers have to choose from a collection of available reference datasets, or to increase the coverage of imputed data in general. The meta-imputation algorithm, as presented in this chapter, is available as a computational tool which I implemented in C++.*

* Meta-imputation software (`meta-impute`): <https://github.com/pkalbers/meta-impute>

"Begin at the beginning," the King said gravely,
"and go on till you come to the end: then stop."

— Lewis Carroll, *Alice in Wonderland*

3

Using rare variants to detect haplotype sharing and identity by descent

Contents

3.1	Introduction	84
3.2	Rare variants as indicators of haplotype sharing by descent	87
3.3	IBD detection around rare variants	89
3.3.1	Inference of historical recombination events	91
3.3.2	Description of the algorithm	93
3.3.3	Anticipated limitations	95
3.4	Genotype phasing by inference of the shared haplotype	98
3.4.1	Genealogical constraints arising from IBD	99
3.5	Evaluation	101
3.5.1	Data generation	101
3.5.2	Accuracy analysis	104
3.6	Results	105
3.7	Discussion	123

3.1 Introduction

Identity by descent (IBD) is a fundamental concept in genetics that describes the genealogical relation between individuals (Malécot, 1948). Two chromosomes are said to be identical by descent, or rather to share a haplotype by descent, if they have inherited the same genetic material from a common ancestor (e.g., see Browning and Browning, 2012; Thompson, 2013). Over generations, the length of an ancestral haplotype is broken down through meiotic recombination, as the genetic material is blended with haplotypes that derive from different ancestral lineages. Consequently, any random sample of two

different chromosomes carries a unique pattern of relatedness, with different ancestries at different loci, arising as the result of historical recombination events. The underlying structure of pairwise relatedness can be thought of as a mosaic of segments at which two chromosomes share a haplotype by descent, but where each of these IBD segments traces back to a different most recent common ancestor (MRCA).

In general, knowledge about relatedness, haplotype sharing by descent, or the recombination history of a sample is of importance in a variety of statistical operations that are used in both population and medical genetics research (Milligan, 2003; Albrechtsen *et al.*, 2009; Gusev *et al.*, 2009); for example, to provide insights into the demographic history of a population (Harris and Nielsen, 2013), to inform methods for genotype phasing and imputation (Kong *et al.*, 2008), to map disease loci using linkage analysis (Purcell *et al.*, 2007; Albrechtsen *et al.*, 2009), as well as to reveal patterns of population stratification and to identify unreported relatedness among individuals in disease association analysis (Freedman *et al.*, 2004; Price *et al.*, 2006; Choi *et al.*, 2009; Mathieson and McVean, 2012).

The entire IBD structure of a sample can be represented by the ancestral recombination graph (ARG) (Griffiths, 1991; Griffiths and Marjoram, 1996, 1997b), which is straightforward to generate in coalescent simulations, but inference from observed data is limited (Rasmussen *et al.*, 2014). This is because even complete data is unlikely to provide sufficient information to explicitly infer the ARG, in addition to the problem that inference becomes computationally expensive for larger sample sizes. Most methods for IBD discovery operate on summary statistics to make inference computationally tractable.

In practice, IBD discovery is largely dependent on the length of a shared haplotype and the genetic similarity between compared sequences. Co-inherited haplotypes that are separated by only a few meioses are expected to cover relatively long tracts, because recombination had less time to break down the length of the region shared between the two chromosomes (Thompson, 2008, 2013). Likewise, as mutations are accumulated along different genealogical lineages, the similarity between shared segments is expected to

decrease over time. Thus, for most purposes, the detection of *recent* IBD is of primary interest (Browning and Browning, 2010).

Numerous approaches for the detection of IBD segments have been proposed, most of which attempt to infer IBD based on measures of genetic similarity or through use of statistical models to determine salient patterns of linkage disequilibrium (LD). Commonly employed tools are PLINK (Purcell *et al.*, 2007), GERMLINE (Gusev *et al.*, 2009), fastIBD (Browning and Browning, 2011a), and Refined IBD (Browning and Browning, 2013), to name a few. The methodological diversity of existing approaches emphasises the central role of IBD in genetics, but also indicates that there is a need for an accurate as well as efficient method to detect IBD in larger samples of purportedly unrelated individuals.

Due to the growing magnitude of available genomic datasets, IBD discovery is becoming more computationally expensive. Note that alternate approaches exist, for example methods to perform long range phasing (LRP) implicitly harness long IBD regions among related individuals (Kong *et al.*, 2008; Palin *et al.*, 2011; Loh *et al.*, 2016a), which employ computationally efficient methods to match relatively long (*e.g.* >10 cM) haplotypes even in very large datasets. But in a general context, as IBD describes a pairwise relationship between two haplotypes, a search algorithm may visit each of the possible pairs of chromosomes in a sample to determine IBD status from patterns of shared genetic variation observed along the full length of the chromosome. For instance, in a sample of n chromosomes, there are $\binom{n}{2} = n(n - 1)/2$ possible pairs that need to be scanned to resolve IBD status if done in an exhaustive manner. To reduce this search space, it would be convenient if a pairwise approach could be targeted to regions and individuals for whom it is more likely to find recent haplotype sharing by descent.

In this chapter, I present a non-probabilistic method to detect IBD segments in pairs of diploid individuals, which utilises rare variants as indicators of recent relatedness. The computational burden of IBD detection is thereby reduced due to the relative low number of individuals that share a given rare or low-frequency allele. In each pair, the regions to each side of a focal allele are scanned, so as to infer the “breakpoints” of historical recombination events that delimit the underlying IBD segment. The inference

of recombination is based on the *four-gamete test* by Hudson and Kaplan (1985), for which haplotype information is required, but which is extended, following Mathieson and McVean (2014), such that recombination breakpoints can be inferred in genotype data.

In the following section, I highlight the genealogical properties of rare variants which make them useful for the inference of recent and relatively long haplotypes by descent. I then describe the method by which IBD segments are detected, conditional on variation observed at a focal rare variant. In addition, I present a simple approach to infer the shared haplotype sequence from genotype data. For the evaluation of the methodology presented, I generated a large dataset using coalescent simulations, so as to measure the accuracy of the IBD detection method in comparison to the true IBD structure (determined from simulation records). These results are also compared to IBD detected using an alternate method. Lastly, I apply the method presented in this chapter to data from the 1000 Genomes Project (1000G).

3.2 Rare variants as indicators of haplotype sharing by descent

One of the properties of rare variants is their presumed young age, as a low frequency is indicative of a recent origin through mutation; *i.e.* the frequency of an allele is assumed to be a proxy to its age (Kimura and Ota, 1973; Griffiths and Tavaré, 1998). Individuals that share a rare allele are therefore likely to have a relatively long chromosomal segment co-inherited from a common ancestor. For example, genetic markers tend to be in high LD with alleles at lower frequencies, because the alleles near a rare variant site are likely to segregate together on the same haplotype (Kruglyak, 1999; Slatkin, 2008b).

To explain the relation between IBD length and age, consider a focal site at which two haplotypes are shared by descent. The length of the IBD segment is defined by the nearest ancestral recombination events that have occurred to either side of the focal position; *i.e.* haplotype sharing is broken down by recombination on both sides independently. The expected length of the IBD segment is determined by the number of meioses that separate two haplotypes in relation to the MRCA who lived t generations in the past;

hence, the pair is separated by $2t$ meioses. In each meiosis, recombination is modelled as a Poisson process with rate of 1 per unit of genetic distance (*Morgan*). It follows that the recombination process over $2t$ meioses is Poisson distributed with rate equal to $2t$. The expected length can be expressed as the sum of two independent random variables that are exponentially distributed, and which describes the distance to either side of the focal position (see Wakeley and Wilton, 2016); *i.e.* the length, L , is gamma-distributed with shape 2 and rate $2t$, namely $L \propto \Gamma(2, 2t)$.

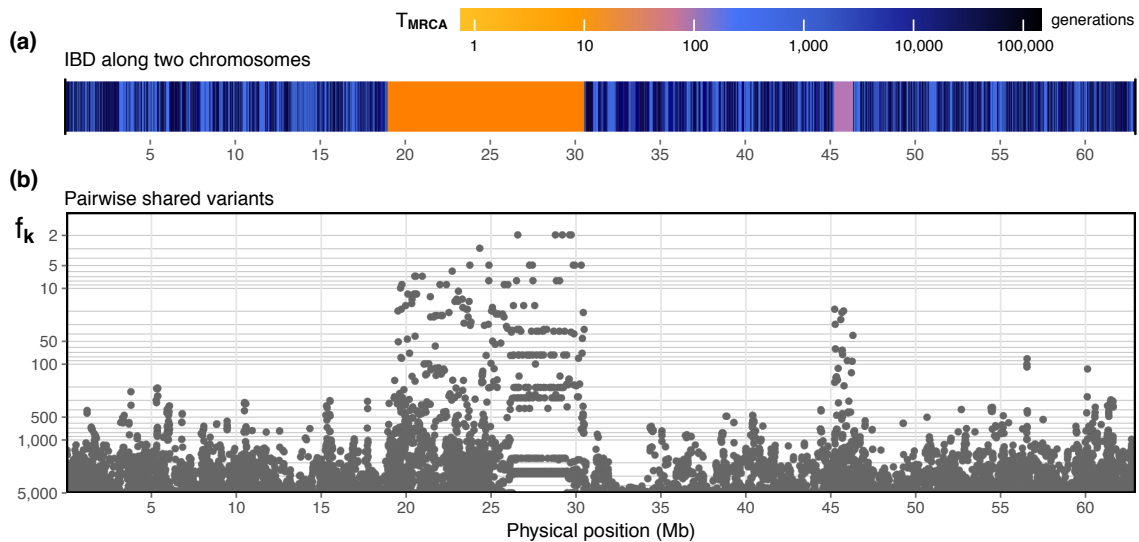


Figure 3.1: IBD structure and pairwise variant sharing. A dataset of $N = 5,000$ haplotypes was simulated under the coalescent using `msprime` (Kelleher *et al.*, 2016). IBD status was determined from simulated genealogies for a pair of chromosomes selected at random from the set of chromosomes that shared a rare allele (frequency $\leq 0.5\%$). Panel (a) shows the “mosaic” of IBD segments along the full length of the simulated region for the two selected chromosomes. The length of a given IBD segment is defined by the chromosomal interval over which the MRCA of the selected pair does not change. The colour of each segment indicates the time to the most recent common ancestor (T_{MRCA}) for the selected pair. Panel (b) shows the physical position of f_k variants shared by the two chromosomes, ranging from very low allele frequency at the top (f_2) to very high frequency at the bottom (*e.g.* $f_{>500}$). Note that the simulation was carried out under variable recombination rates using the genetic map for human chromosome 20 from the International HapMap Project (HapMap) Phase II Build 37. The pattern of extended shared variation seen at positions around 25–30 Megabase (Mb) arises from a low recombination rate at the region of the centromere.

Given this exponential “decay” of IBD length over time, rare or low-frequency variants are useful for identifying genomic regions in which individuals are likely to share recent

and relatively long IBD tracts. For example, Mathieson and McVean (2014) selected doubletons (alleles that are present only twice in a sample), which they refer to as f_2 variants, to identify the shared haplotype in the two individuals sharing the allele. To borrow from this notation, henceforth, f_k is used to denote a variant at which k allele copies are found in a sample.

To emphasise the utility of rare variants, see the example shown in Figure 3.1. Using coalescent simulations, a sample of $N = 5,000$ chromosomes was generated.* A rare variant was randomly selected (frequency $\leq 0.5\%$), as well as two of the chromosomes which share the focal allele. The underlying IBD structure for the given pair of chromosomes was determined from simulation records and shown in Figure 3.1a. IBD segments are distinguished by the time to the most recent common ancestor (T_{MRCA}) at each position along the sequence. To illustrate pairwise allele sharing, The frequency of each allele shared by the two haplotypes is shown by chromosomal position in alignment with the IBD structure above; see Figure 3.1b. As suggested in the figure, the majority of low-frequency variants align with IBD segments that are more recent.

The majority of variants observed in the human genome are low in frequency or rare. For example, there are 84.7 million single-nucleotide polymorphisms (SNP) in the final release dataset of the 1000 Genomes Project (1000G) Phase III ($N = 2,504$), of which 71.9 % are below 1% allele frequency and 64.2 % are below 0.5% (after removing singletons and monomorphic sites), suggesting that there are ample opportunities to find rare allele sharing. This is illustrated in Figure 3.2 (next page), which indicates the number of alleles shared between each pair in the dataset (chromosomes 1–22), at allele frequency $\leq 0.5\%$. Notably, the sharing pattern highlights population structure, as the number of shared alleles is generally larger within a sub-population.

3.3 IBD detection around rare variants

In the following sections, I describe the methodology by which IBD segments are detected around rare variant sites. I then describe the implementation of each of the two tests for

* See Section 3.5.1 (page 101) for a description of how data were simulated.

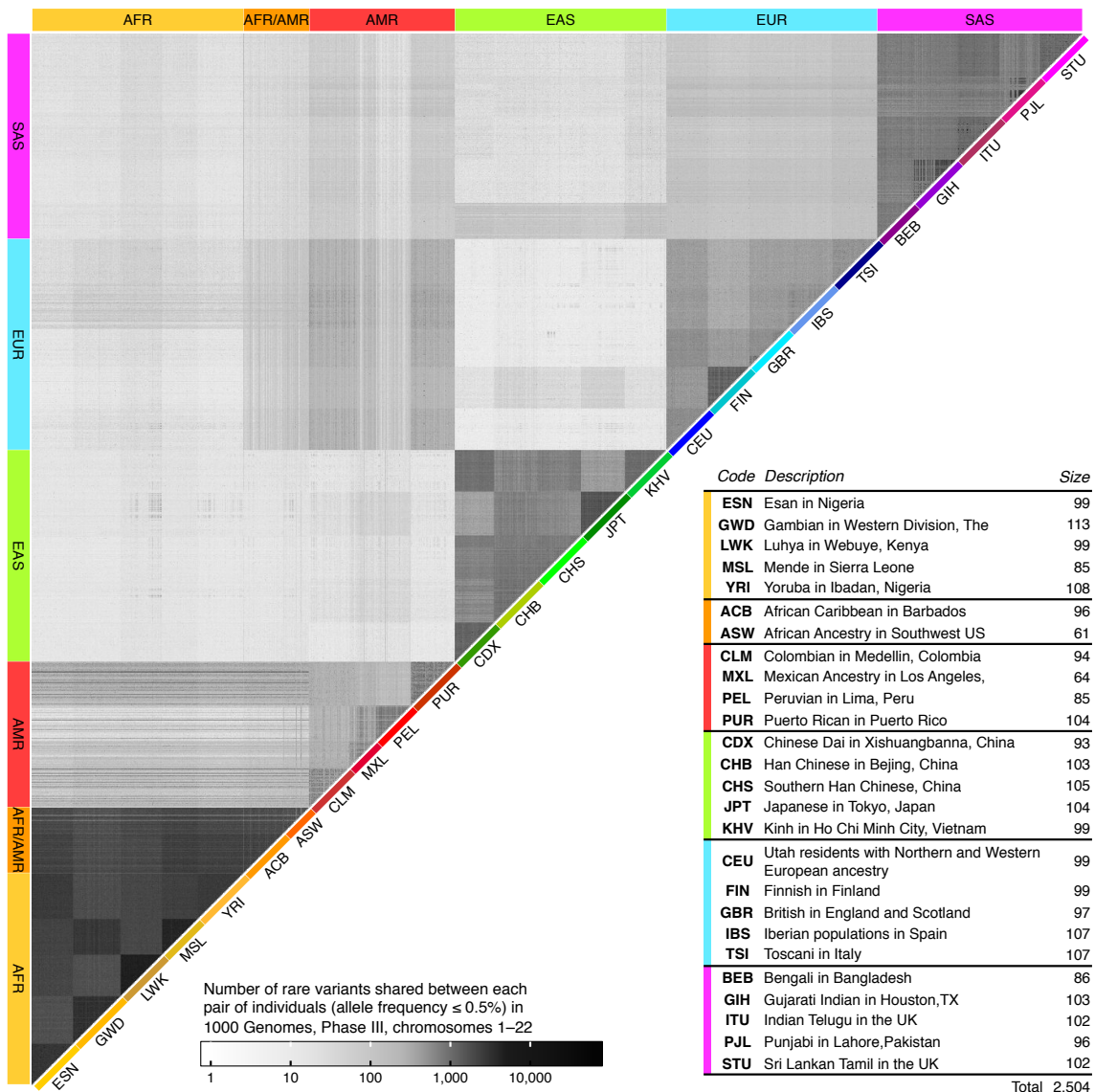


Figure 3.2: Rare variant sharing in the 1000 Genomes dataset. The plot shows the upper triangle of a pairwise sharing matrix in which the number of variants shared in each pair of individuals is indicated by tones of grey (log-scaled), ranging from *light* (low number) to *dark* (high number); see legend. Pairwise rare variant sharing was determined for all shared alleles observed at frequency $\leq 0.5\%$, across chromosomes 1–22, and in each pair of the 2,504 individuals present in the final release dataset of the 1000 Genomes Project Phase III. The dataset comprises sample data from six continental populations (or *super-populations*) which are further subdivided in 26 populations of different ethnic background. Each group is abbreviated using a three-letter code. The six continental populations are defined as follows; African (AFR), African-American (AFR/AMR), American (AMR), East Asian (EAS), European (EUR), and South Asian (SAS). The table in the lower right corner shows the code and description of each population sample, as well as the number of individuals in each group.

the detection of IBD segments in large sample data. Lastly, I conclude this section by highlighting certain caveats of the implemented method before its evaluation using simulated data.

3.3.1 Inference of historical recombination events

Two approaches for a non-probabilistic inference of recombination events are described below; these are the *four-gamete test* (Hudson and Kaplan, 1985), which requires haplotype information, and the criterion of *inconsistent homozygote genotypes* (see Mathieson and McVean, 2014), which requires genotype data; henceforth referred to as the *discordant genotype test*.

Four-gamete test (FGT). Given four haplotypes in two diploid individuals, a recombination event is inferred between two loci if all four possible gametes are observed. This holds true under the infinite sites model (Kimura, 1969), where mutation events may only occur once per site in the history of a sample, such that at most two allelic states can be observed at a given site. It follows that for a pair of sites there are four possible allelic state configurations; $(0, 0)$, $(0, 1)$, $(1, 0)$, and $(1, 1)$, where 0 and 1 denote the ancestral and derived type, respectively. If all four configurations are observed, genealogies at the two sites are incompatible and the observation can only be explained by a recombination event that occurred in the history of the sample. Because recurring mutations or back mutations are assumed to have zero probability, at least one recombination event must have occurred in the interval between the two sites. An example configuration is shown in Figure 3.3 (next page). Notably, private or *de novo* mutations appearing as singletons in the sample cannot lead to the observation of the four required configurations. Although the exact location of chromosomal crossover cannot be retrieved from the data, the FGT can be used to find the smallest interval in which recombination occurred. In the following, the term *breakpoint* is used for either of the two sites that together delimit the interval.

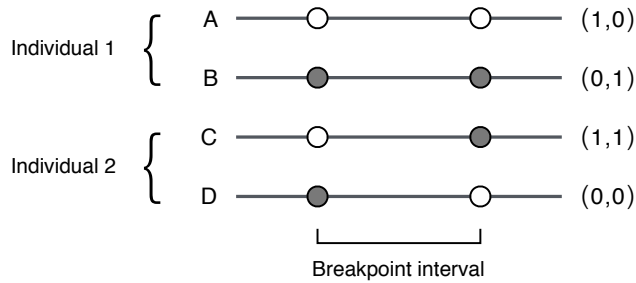


Figure 3.3: Breakpoint detection using the four-gamete test (FGT). The four haplotypes (gametes) in a pair of two diploid individuals are shown (*horizontal lines*). A breakpoint interval is detected if all four possible allelic state configurations are observed at two variant sites along the sequence. The interval delimits the region in which at least one recombination event must have occurred in the history of the sample (given the assumptions of the infinite sites model). The four allelic state configurations are shown on the *right*. The alleles are shown at the two breakpoint sites; indicated as ancestral (*hollow circle*) and derived state (*solid*). Note that the order of gametes is ignored.

Discordant genotype test (DGT). In absence of haplotype information, data are represented as genotypes, where genotypic states are encoded as 0, 1, and 2, for variants that are homozygous for the ancestral allele, heterozygous, and homozygous for the derived allele, respectively. Given the genotype sequences of two diploid individuals, recombination is inferred between two sites; one being heterozygous in both individuals (*i.e.* the genotypes 1 and 1) and another with opposite homozygous genotypes (0 and 2). In the latter case, it follows that the two individuals cannot share a haplotype at that locus.

The DGT is a special case of the FGT, as the same composition of alleles is implied. For example, if the allelic configurations (0, 1) and (0, 0) are seen in individual 1, and configurations (1, 0) and (1, 1) in individual 2, the corresponding genotypic configurations are (0, 1) and (2, 1), respectively, which satisfies the breakpoint condition in both the FGT and DGT. However, because genotype data result from haplotype occurrence in individuals, not all breakpoints detectable under the FGT can be found using the DGT. At sites where the FGT detects a breakpoint interval, the DGT cannot if both sites are heterozygous in the same individual. As a consequence, it can be expected that the DGT is more restrictive than the FGT; *e.g.* if breakpoints are found, they are likely to sit farther apart. This is further exemplified in Figure 3.4 (next page), which highlights the difference to the FGT by comparison to the example shown in Figure 3.3 (this page).

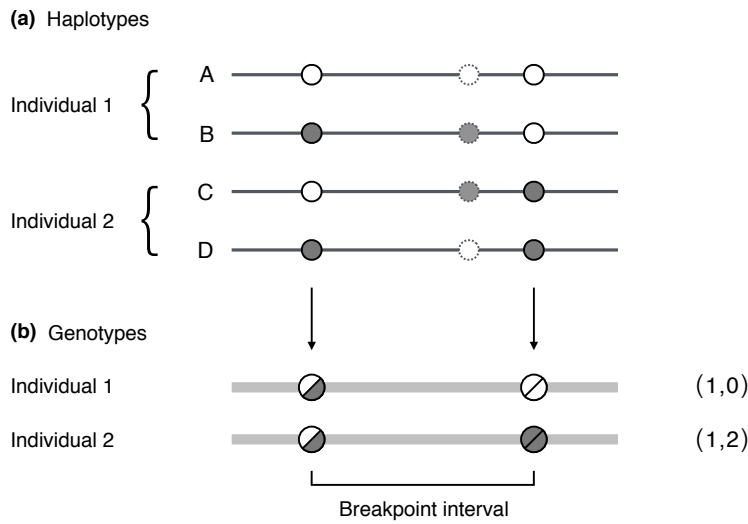


Figure 3.4: Breakpoint detection using the discordant genotype test (DGT). Unlike the FGT, which requires haplotype information, the DGT identifies a breakpoint interval using genotype data. For comparison, Panel (a) shows the four gametes of the two individuals involved; see Figure 3.3 (page 92). To highlight the difference to the FGT, an additional variant is shown in between both sites; alleles indicated by a *dotted* edge. This site would satisfy the breakpoint condition under the FGT, but is missed under the DGT. Panel (b) shows the two genotype sequences per individual (thick horizontal lines) from which a breakpoint interval is inferred using the DGT. The genotypic states of the breakpoint sites are given on the *right*. Genotypes can either be homozygous for the ancestral allele (*hollow circle*), heterozygous (*semi-solid*), or homozygous for the derived allele (*solid*).

3.3.2 Description of the algorithm

The FGT and DGT provide the means for non-probabilistic inference of recombination breakpoints from either haplotype or genotype data, respectively. This methodology is implemented such that the full length of an IBD segment can be found around a given target site in a pair of diploid individuals. The allele at a target site serves as an indicator for haplotype sharing by descent; hence, to detect recent IBD, rare variants are used as primary targets. The aim of this method is to infer breakpoint intervals independently on both sides of the target position along the sequence, so as to infer the two recombination events that delimit the underlying IBD segment. As such, the target variant is set as the *focal* breakpoint. The algorithm is described below; a more intuitive example is illustrated in Figure 3.5 (next page).

Let M be the number of variant sites observed in a sample of N diploid individuals. At the target site, b_i , where $i \in \{1, 2, \dots, M\}$, the subset of individuals sharing the derived

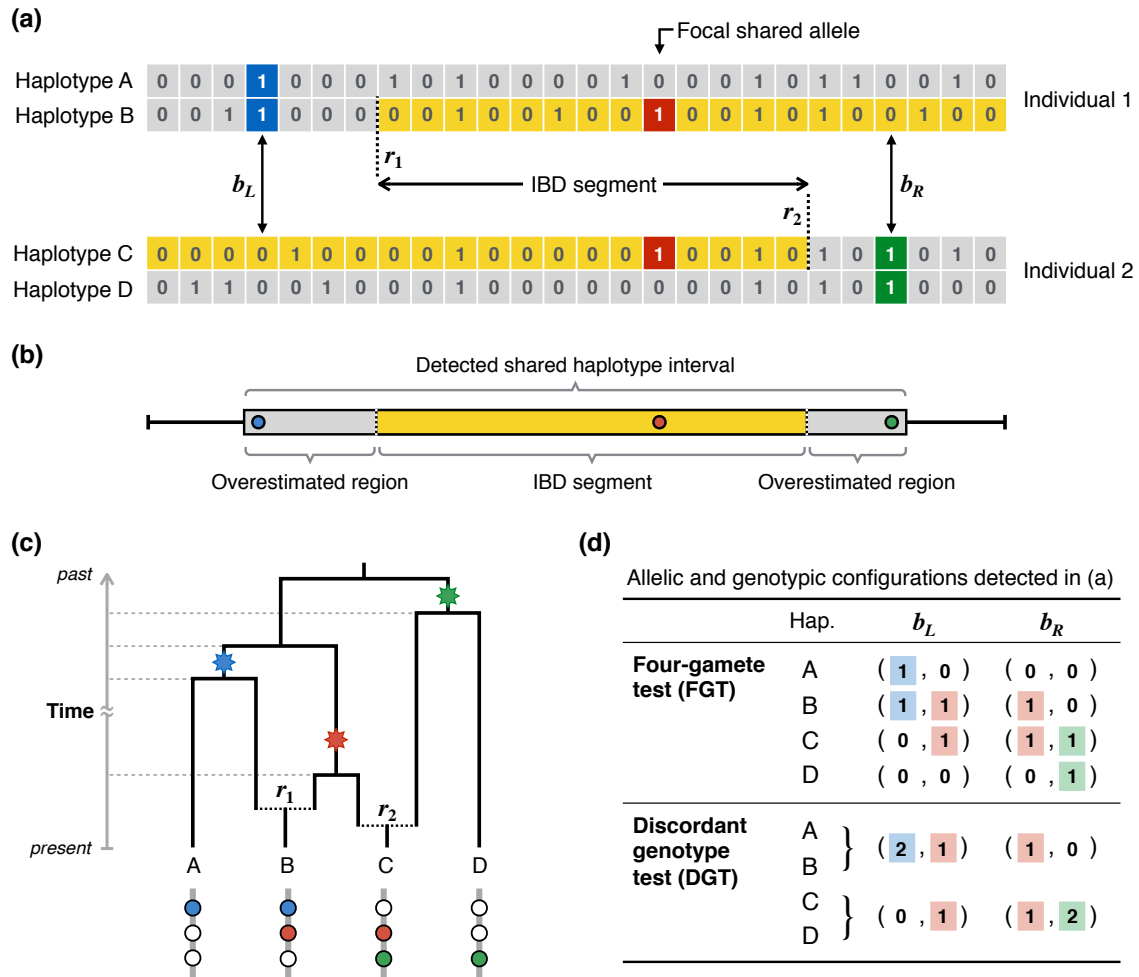


Figure 3.5: Illustration of shared haplotype detection in a pair of diploid individuals. Panel (a) shows two individuals composed of haplotypes A and B, and haplotypes C and D, respectively. Each haplotype is represented as a sequence of observed allelic states, where 0 and 1 denote the ancestral and derived allele, respectively. Breakpoints are detected by independently scanning to the left and right-hand side from the target position. The two individuals share a haplotype by descent (highlighted in yellow) which is tagged by the focal allele (red), for which the two individuals are heterozygous. Two sites (blue and green) mark the first sites at which a breakpoint condition is satisfied, such that b_L and b_R are detected. The IBD segment shared by both individuals is indicated by r_1 and r_2 (dashed lines). Panel (b) shows the detected breakpoint interval, delimited by b_L and b_R (inclusive). Note that detected breakpoints are only the first indication of recombination found distal to the focal site, but may not mark the points of the actual crossover events; thus, it is expected that the length of the detected segment is overestimated, dependent on available data. Panel (c) represents the history of the sample as an ancestral recombination graph (ARG). Mutation events are indicated on the tree (stars) and gave rise to the alleles highlighted in (a); blue, red, and green. The dotted grey lines indicate the time of coalescent events in the history of the sample; dotted black lines indicate recombination events. Panel (d) provides a table outlining the configurations of allelic and genotypic states at breakpoint sites as considered in the FGT and DGT, respectively. Notably, in the example shown, both the FGT and DGT detect breakpoints at indicated sites. But, for example, if individual 1 was composed of haplotypes A and C, and individual 2 of haplotypes B and D, the breakpoints would be detected as shown under the FGT, but not the DGT.

allele is identified and compared in a pairwise fashion. Importantly, the allele at this site is used as an identifier for haplotype sharing, on which inference is conditioned in either the FGT or DGT. Thus, individuals are only considered if they are heterozygous for the focal allele, as the breakpoint condition in either test cannot be satisfied otherwise. However, note that this restriction arises from the variant-centric focus on a given rare allele; *e.g.* the condition of the FGT could be satisfied for individuals homozygous for a given allele, but without that the allele is shared by the other individual (hence, defying the purpose of this implementation). In each pair, chromosomes are scanned to the left and right-hand side from the target site until the first site is found that, together with the allelic or genotypic states observed at b_i , satisfies the breakpoint condition, which is done independently on each side. Detected breakpoints are labelled as b_L and b_R on the left and right-hand side, respectively, such that the intervals $[b_L, b_i]$ and $[b_i, b_R]$ delimit the chromosomal regions in which recombination events occurred, respectively; where $L, R \in \{1, 2, \dots, M\}$. Hence, the underlying IBD segment is enclosed in $[b_L, b_R]$.

The allelic or genotypic states at b_L or b_R provide only the first indication of recombination found along the sequence on either side of the focal allele, but may not mark the points of the actual crossover events. The detected interval is therefore inclusive of the breakpoints such that the full length of the underlying IBD segment is covered. In cases where the end of a chromosome is reached without detecting any evidence of recombination, the terminal site is recorded to capture the length of the segment; this is hereafter referred to as a *boundary case*. Further, note that a recombination event can occur with chromosomes outside the sub-tree of the lineages deriving from the focal mutation, such that a breakpoint may be falsely inferred; however, such cases are sufficiently rare to be negligible.

3.3.3 Anticipated limitations

As noted by Hudson and Kaplan (1985), not all recombination events in the history of a sample are found by the FGT, and are therefore also missed by the DGT. In the implementation presented, a breakpoint is found by performing a scan along the sequence

away from a target position. Given that the neighbouring haplotype regions derive from different ancestral lineages, in the general case, it is likely that a breakpoint will be found eventually (or the boundary of the chromosome is reached).

The main limitation to the accuracy of the detected breakpoints is the overestimation of the interval, in relation to the underlying true IBD length; as shown in Figure 3.5b. While the underlying IBD segment is enclosed in the interval, it can be expected that breakpoints are detected at sites some distance away from where recombination occurred, thus overestimating the true length of the underlying IBD tract. The extent of overestimation is dependent on the number and density of observed variant sites in the sample. This suggests that the method may become more accurate with larger samples. Likewise, because the rate of mutation is directly proportional to the expected number of segregating sites (Watterson, 1975), a higher mutation rate can generally be expected to decrease the overestimation of segment length.

Conversely, it is also possible that segment length is underestimated. Given the four chromosomes required, there are $\binom{4}{2} = 6$ possible pairs of chromosomes which may share extended regions by descent. For example, if two individuals share multiple IBD tracts at different pairs of their chromosomes, these tracts may overlap. In such cases, breakpoint detection cannot distinguish between overlapping segments. This is illustrated in Figure 3.6 (next page), which shows two examples generated using coalescent simulations.

In Example 1 (3.6a), a rare allele target site was randomly selected, as well as the two individuals sharing the this allele. The true IBD structure was determined from simulation records for each pair of the four chromosomes in the two individuals. Each pair is represented by a mosaic of IBD segments along the sequence, where each segment is distinguished by time to the most recent common ancestor (T_{MRCA}). Both the FGT and DGT were applied, but where all consecutive breakpoints after the first detection were also recorded along the sequence on both sides of the focal variant. The innermost interval delimits the detected shared haplotype segment around the target site. Example 1 illustrates the general case in which a rare allele identifies the underlying

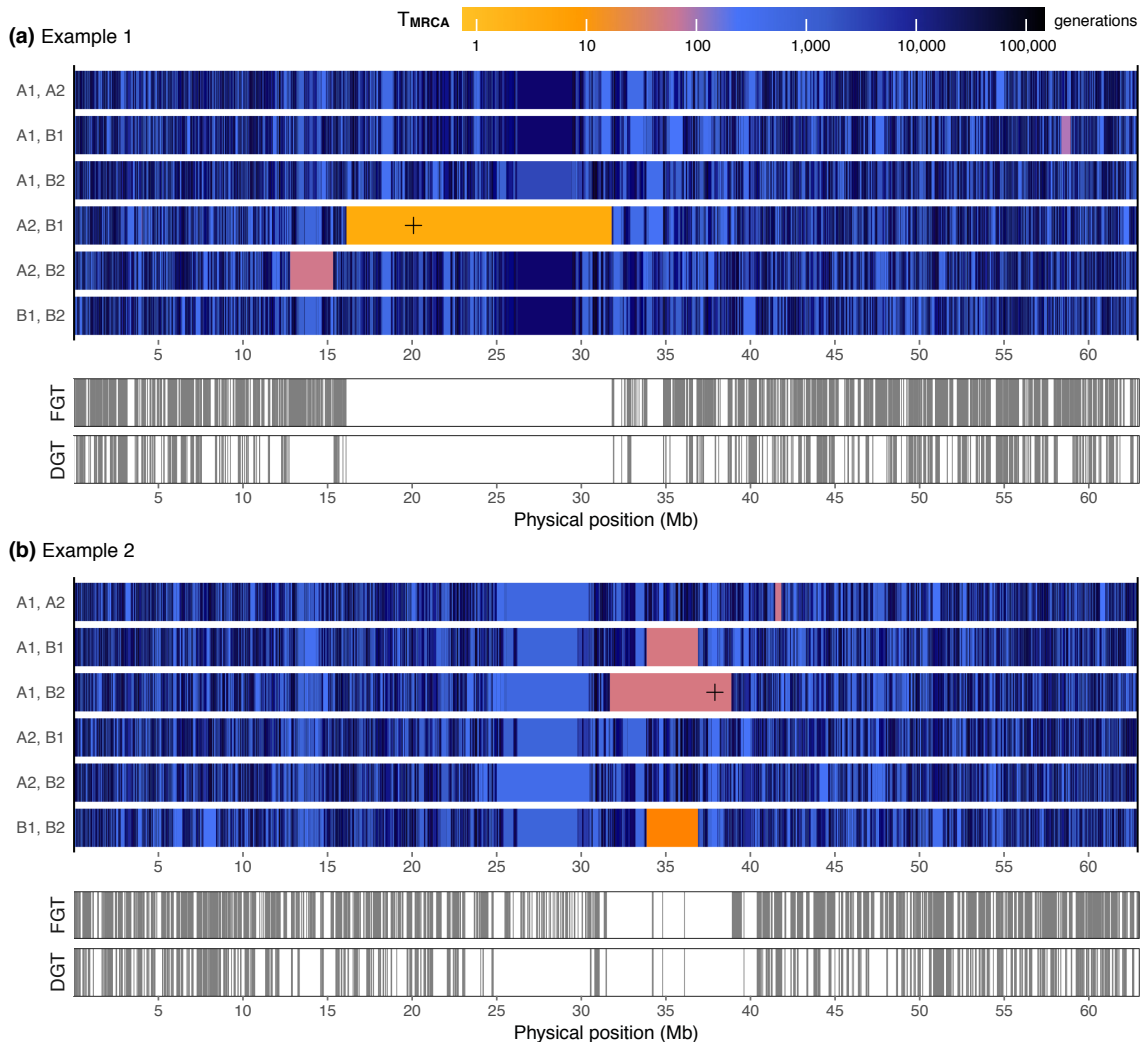


Figure 3.6: Examples of the underlying IBD structure in each pair of four chromosomes. The true, underlying IBD structure is shown for each possible pair among four chromosomes in two diploid individuals; two examples are shown. Each chromosome is labelled by its occurrence in individuals A and B, where chromosomes 1 and 2 are distinguished. The “mosaic” of IBD segments per pair was determined from coalescent records produced in simulations using `msprime` (Kelleher *et al.*, 2016); see Section 3.5.1 (page 101). Each segment defines the region that was co-inherited from a most recent common ancestor (MRCA), and is colour-coded by the number of generations separating the two chromosomes from their shared MRCA in that region. The *cross* marks the position of the focal allele in the pair that shares it. Below, all breakpoints detected relative to the focal variant along the simulated region are indicated, using the FGT (*top*) and DGT (*bottom*). Panel (a) shows that the innermost breakpoint intervals (relative to the target position) detected in the FGT or DGT align closely with the true termini of the IBD segment. The extent of overestimation appears to be negligible in relation to the length of the detected segment. Panel (b) shows that the innermost intervals are underestimated, due to an overlap of recently co-inherited haplotypes on different chromosome pairs.

co-inherited haplotype segment, which may stand out as being much younger due to recent shared ancestry.

The same was done in Example 2 (3.6b), but here the target site and the pair of individuals was chosen because it was found that the length of the detected IBD segment was underestimated. As can be seen, this underestimation is due to an overlap of multiple pairwise shared IBD tracts in other chromosome pairs within the same pair of individuals. Such a result may be expected in cases of inbreeding, where the maternal and paternal chromosomes in an individual are more closely related to each other than to other chromosomes in the population. Note that in the simulations conducted, the generated haplotypes were randomly paired to form diploid individuals.

3.4 Genotype phasing by inference of the shared haplotype

In this section, I extend the IBD detection method such that the allelic sequence of the shared haplotype can be deduced. Since it is assumed that a breakpoint interval covers a region in which two individuals share a haplotype recently co-inherited from a common ancestor, in principle it is possible to infer the shared haplotype sequence based on genealogical constraints. By knowing the sequence of the shared haplotype, it follows that the sequences of the “unshared” haplotypes in both individuals can be derived. The approach presented can therefore be seen as an application to genotype *phasing*, *i.e.* the inference of haplotypes from genotype data, which has become a fundamental problem in genetic research (Browning and Browning, 2011b).

Currently, the most accurate and widely employed phasing algorithms are designed to infer haplotype sharing using Hidden Markov Models (HMMs), which typically operate under a probabilistic model of coalescence with recombination (Stephens *et al.*, 2001; Delaneau *et al.*, 2008). Notable examples include computational tools such as SHAPEIT (Delaneau *et al.*, 2011, 2013) and EAGLE (Loh *et al.*, 2016a,b). The basic phasing process can be described in context of the influential Li and Stephens (2003) model, where haplotypes are reconstructed from genotype data as “imperfect mosaics” of other haplotypes (*e.g.*

using a reference panel). Existing phasing methods typically show high levels of accuracy. However, the phase at low-frequency variants is often problematic to resolve because patterns of allelic variation or linkage disequilibrium (LD) may be too rare to allow correlation with available haplotype information.

Here, I explore the feasibility of phasing genotypes at sites within a given breakpoint interval using the IBD detection method presented in the previous section; haplotypes are therefore inferred *locally* and are limited to the region covered by the interval. In the following, I explain the genealogical constraints that determine the possible haplotype allocation of alleles in genotype data. I then describe the general phasing approach as implemented here.

3.4.1 Genealogical constraints arising from IBD

At a given site, the genotypic states observed at two diploid individuals represent the sum of alleles, where each allele derives from a mutation event on some branch of the genealogical tree of the sample. By knowing that two haplotypes were co-inherited from a recent MRCA, a part of this unseen genealogy is resolved, such that certain genotypes can only be formed if mutation events occurred on certain branches of the tree. This can be seen as being analogous to having partial pedigree information; *i.e.* the two individuals are implicitly treated as the “offspring” of their ancestral “parent”. By following the line of descent, the ancestral haplotype can be inferred if consistent with observed genotypes. However, here, the assumed pedigree is incomplete, because ancestral relations of the two unshared haplotypes are not known from available IBD information. There is nonetheless sufficient information to deduce the allelic states given certain genotypic arrangements.

As a result, a set of rules can be formulated which define the state of the shared allele if a certain genotype pair is observed in the two individuals considered. As before, the infinite sites model is assumed. If both genotypes are homozygous for the same allele, the deduction of the shared allele is trivial. If they are homozygous for different alleles, they cannot share an allele. Importantly, because this is seen at breakpoint sites detected using the DGT, which mark the limits of the underlying IBD segment, breakpoints are excluded

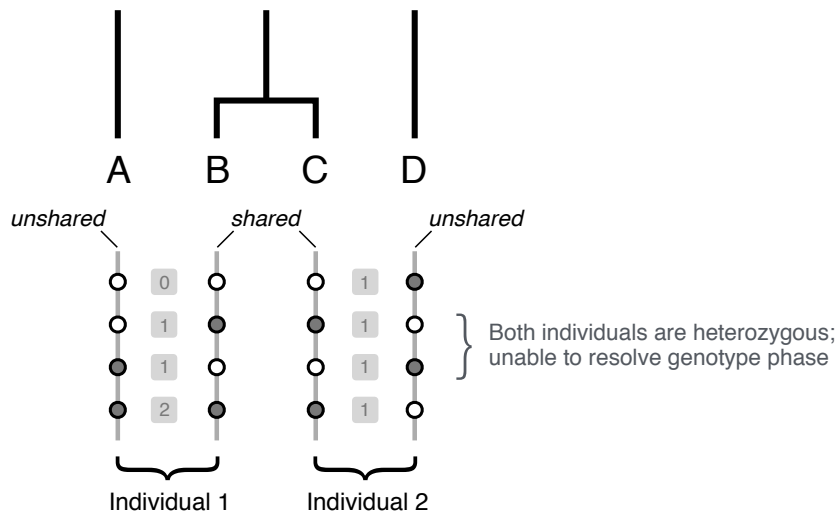


Figure 3.7: Genealogical constraints from haplotype sharing. The top graph indicates the genealogy of four haplotypes (A, B, C, and D) as seen in two individuals (1 and 2), which can be resolved partially if two haplotypes are shared by descent. Below, the allelic states are shown at four positions along the sequence for each haplotype; ancestral and derived states are indicated by *hollow* and *solid* circles. Only the genotypic state is seen in each individual as indicated between individual haplotypes; *i.e.* homozygous for the ancestral allele (0), heterozygous (1), and homozygous for the derived allele (2). The phase of a genotype can be resolved at sites with one homozygous genotype (phasing is redundant if both genotypes are homozygous). Genotype phase cannot be determined if both individuals are heterozygous.

from this analysis; recall that the FGT cannot be used with genotype data. A caveat of this analysis, however, is that haplotypes cannot be distinguished if both individuals are heterozygous, as it is not known whether the the allele is shared or not. This conflict arises because an unshared haplotype may be more closely related to either the shared or the other unshared haplotype. Thus, haplotype inference is restricted to sites at which *heterozygous-homozygous* genotype pairs are found. This is further illustrated in Figure 3.7.

A complete definition of these rules is given in Table 3.1. The table gives the inferred allelic state of the shared haplotype for each of the possible combinations of two genotypes. Note that the alleles at *heterozygous-heterozygous* sites are likely to be shared if three conditions are met; first, if the allele frequency at that site is lower than the frequency at the target position, second, if the allele only segregates within the subsample sharing the focal allele and, third, if the genealogy does not change along the sequence within an inferred interval. An allele that is lower in frequency is likely to be younger than the focal allele and, thus, to segregate on the same haplotype. However, this may only

Table 3.1: Shared haplotype inference from genotype pairs. Given the two genotypes observed at a pair of individuals (A and B), there are nine possible ordered combinations of alleles. The corresponding haplotypes are shown for both individuals (unordered). Note that genotype phase cannot be resolved for individuals that are both heterozygous; *i.e.* the corresponding certainty score is equal to $1/2$. If a pair is homozygous for different alleles, they do not share a haplotype.

Genotype Individual A	Genotype Individual B	Haplotypes Individual A	Haplotypes Individual B	Shared haplotype
0	0	(0, 0)	(0, 0)	0
0	1	(0, 0)	(0, 1)	0
0	2	(0, 0)	(1, 1)	–
1	0	(0, 1)	(0, 0)	0
1	1	(0, 1)	(0, 1)	–
1	2	(0, 1)	(1, 1)	1
2	0	(1, 1)	(0, 0)	–
2	1	(1, 1)	(0, 1)	1
2	2	(1, 1)	(1, 1)	1

be the case under the infinite sites model, *e.g.* because recurrent or back mutation may otherwise suggest a different genealogical order of descent.

3.5 Evaluation

The IBD detection method presented in this chapter was evaluated using simulated data. This allowed assessment of the accuracy of detected breakpoint intervals in relation to the known genealogy of the simulated sample. For comparison, an alternate IBD detection method was applied to the same data. Lastly, the method presented was applied to data from the 1000 Genomes Project.

3.5.1 Data generation

The coalescent simulator used to generate data was `msprime` (version 0.4.0), which simulates the exact coalescent with recombination, and where mutations are generated under the infinite sites model (Kelleher *et al.*, 2016).* The software is a reimplementation of the classic `ms` algorithm by Hudson (2002), but allows efficient simulation of extended chromosomal regions for very large sample sizes, where the entire history of the simulated

* Coalescent simulator `msprime`: <https://github.com/jeromekelleher/msprime> [Date accessed: 2016-11-12]

sample can be stored and queried for further analysis. Notably, `msprime` allows simulation under variable recombination rates, for example by using established recombination maps of the human genome.

Demographic model

A demographic model was defined following Gutenkunst *et al.* (2009), who used intergenic data from four global populations to estimate parameters from diffusion approximations of expected allele frequency spectra. Accordingly, here, data were simulated with an ancestral population size of $N_e = 7,300$ (denoted by N_A in the model) and under the assumption of a generation time of 25 years. The mutation rate was set to a constant $\mu = 2.35 \times 10^{-8}$ per site per generation, which was estimated from the human-chimp divergence in Gutenkunst *et al.* (2009). Note that recent studies have estimated the human mutation rate to be slightly lower; for example, Scally and Durbin (2012) have estimated $\mu \approx 1.2 \times 10^{-8}$ from analyses of genome-wide *de novo* mutations using recent sequencing technologies, but which is in the same order as the mutation rate used here.

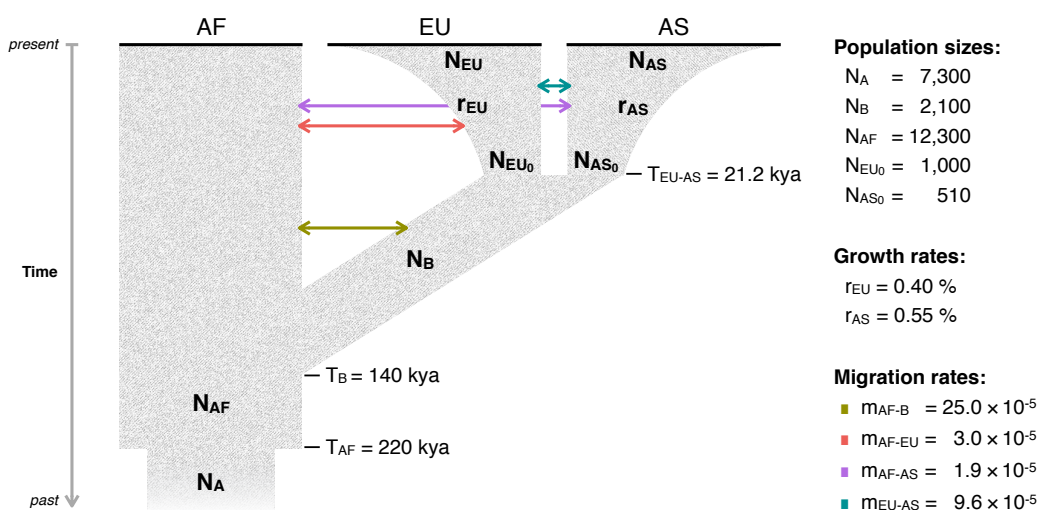


Figure 3.8: Demographic model used in simulations. Three populations were modelled, African (AF), European (EU), and Asian (AS), which derive from an ancestral population (A). Both EU and AS experienced a bottleneck with subsequent exponential growth following the out-of-Africa expansion of a founder population (B) that split from the ancestral population. Modified from Gutenkunst *et al.* (2009), Figure 2 (see [doi:10.1371/journal.pgen.1000695.g002](https://doi.org/10.1371/journal.pgen.1000695.g002)), with parameter values taken from Table 1 (see [doi:10.1371/journal.pgen.1000695.t001](https://doi.org/10.1371/journal.pgen.1000695.t001)).

The demographic history as defined in the simulation model is illustrated in Figure 3.8 (page 102); parameter values of the model are specified therein. The model recapitulates the human expansion out of Africa, for which three populations were considered; African (AF), European (EU), and Asian (AS). The African population was included with a constant population size, while EU and AS experienced exponential growth after divergence and split from an ancestral African population. Population sizes of EU and AS were calculated as $N = N_0/e^{-rt}$, where N is the size at present, N_0 the initial size at EU-AS divergence, r the growth rate, and t the time since divergence (in years).

Simulated dataset

A sample of 5,000 haplotypes was simulated, where the set of generated chromosomes represented a sample taken from the EU population. To reproduce realistic distributions of recombination variability along the simulated sequence, the simulation was performed using recombination rates from human chromosome 20, as provided in Build 37 of the International HapMap Project (HapMap) Phase II (International HapMap Consortium *et al.*, 2007; International HapMap 3 Consortium *et al.*, 2010).* The resulting dataset consisted of 0.673 million segregating sites observed over a chromosomal length of 62.949 Mb (108.267 cM). The history of the simulated sample was stored separately to derive genealogical information in subsequent analyses.

The simulated chromosomes were used to generate three datasets. In the first, haplotypes were randomly paired to construct a sample of 2,500 diploid individuals. From this, second, a corresponding genotype dataset was generated by forming genotypes (encoded as 0, 1, and 2) as the sum of alleles (encoded as 0 and 1) along the sequence in each individual. This dataset was then used to generate a third dataset in which haplotypes were estimated from genotype data; *i.e.* resulting data consisted of phased haplotypes. Phasing was conducted using SHAPEIT version 2 (Delaneau *et al.*, 2008, 2013), using default parameters without a reference panel.[†]

* HapMap recombination map: ftp://ftp.ncbi.nlm.nih.gov/hapmap/recombination/2011-01_phaseII_B37/genetic_map_HapMapII_GRCh37.tar.gz [Date accessed: 2016-11-12]

[†] Phasing software SHAPEIT: https://mathgen.stats.ox.ac.uk/genetics_software/shapeit/shapeit.html [Date accessed: 2016-11-12]

3.5.2 Accuracy analysis

The detection of IBD was evaluated in relation to the underlying true IBD structure of the sample, which was determined from the stored simulation records. Given a target site and the two haplotypes sharing the focal allele, the genealogy was scanned along the sequence of variant sites observed in the sample, in both directions from the target position. The MRCA of the pair was identified at each variant site and a breakpoint was defined as the first site at which a different MRCA was found. This returned the smallest interval detectable from available data around the nearest recombination events that delimit an IBD segment.

Accuracy was measured in terms of the distance between a given breakpoint site and the focal position of the segment. Two measurements were considered; the squared Pearson correlation coefficient, r^2 , which measures the strength of the linear relation between detected and true distance, and the root mean squared logarithmic error (RMSLE);

$$\text{RMSLE} = \sqrt{\frac{1}{n} \sum_{i=1}^n \left[\log_{10} \left(\frac{\hat{d}_i + 1}{d_i + 1} \right) \right]^2} \quad (3.1)$$

where d_i and \hat{d}_i are the distances of the true and detected breakpoints, respectively, and n is the overall number of comparisons. The RMSLE is similar to the root mean squared error (RMSE), which measures the variance and bias in the set of compared values, and is equal to the standard deviation when there is no bias. As such, the RMSLE can be interpreted as a score metric for the magnitude of error. Here, this is useful because larger departures from the actual values are penalised more than smaller ones. A lower score value indicates a lower magnitude of error, where $\text{RMSLE} = 0$ indicates that true and inferred values are identical. Also, note that the RMSLE is usually defined using the natural logarithm; here, \log_{10} was used as a more intuitive representation of error magnitude.

The performance of the proposed IBD detection method was assessed for the described haplotype and genotype-based tests on the three datasets derived from coalescent simulations. The following approaches were distinguished:

- (a) FGT on haplotype data as simulated; *i.e.* *true* haplotypes,
- (b) FGT on *phased* haplotypes, and
- (c) DGT on genotype data.

3.6 Results

IBD detection was carried out on a large set of target sites, for which all f_k variants found at $k \in \{2, \dots, 25\}$ were selected, *i.e.* alleles shared at frequency $\leq 0.5\%$. This threshold was chosen arbitrarily, but such that the considered frequency range was expected to be sufficiently low to identify recent IBD given the size of the sample. The set of target sites comprised 0.317 million SNPs that were heterozygous in the individuals sharing a focal allele. This resulted in 11.598 million pairwise analyses and an equal number of IBD segments detected using the FGT on the true and phased haplotypes in Approaches (a) and (b), respectively, and the DGT on genotype data in Approach (c).

Because the same IBD segment may be inferred from multiple target sites, the analysis was reduced to the set of uniquely detected breakpoint intervals per pair of individuals in each approach. Duplicate segments were removed after the corresponding target variants were sorted by allele frequency, with lower frequencies at the top and removing duplicate segments below. Detected segments were thereby tagged by the presumably youngest shared alleles within the intervals. The number of uniquely identified segments differed slightly in Approaches (a), (b), and (c); 2.983 million (25.723 %), 3.091 million (26.654 %), and 2.978 million (25.679 %), respectively. For the corresponding true IBD segments, the number of unique segments was 3.001 million (25.876 %). These data were further reduced to the intersection of retained target sites across approaches, so as to enable direct comparisons on the same set of targets, which resulted in 2.978 million (25.679 %) unique intervals. The results obtained from these data are summarised in Table 3.2 (next page).

The proportion of breakpoints that were overestimated (in relation to the corresponding true IBD breakpoints) was noticeably high overall; using the FGT, 97.390 % and 95.666 % were overestimated in Approaches (a) and (b), respectively. However,

Table 3.2: Accuracy of detected breakpoints per f_k category. The accuracy of detected IBD breakpoints was measured using the squared Pearson correlation coefficient, r^2 , and the RMSLE in relation to the true IBD segments determined from simulation records; measured in terms of the distance between breakpoint site and the corresponding focal position per segment. The analysis included of 317,020 target sites around which IBD was detected in Approaches (a), (b), and (c). In each, accuracy was computed after data were reduced to identical sets of unique IBD segments ($n = 2,978,220$). The table specifies the allele frequency (%) corresponding to each f_k category, as well as the number of target sites identified.

f_k	Freq. %	Targets	r^2			RMSLE		
			FGT*	FGT**	DGT†	FGT*	FGT**	DGT†
2	0.04	76,515	0.998	0.895	0.995	0.219	0.598	0.317
3	0.06	46,138	0.989	0.957	0.978	0.243	0.516	0.359
4	0.08	31,658	0.963	0.959	0.941	0.256	0.463	0.379
5	0.10	23,581	0.975	0.963	0.929	0.276	0.429	0.408
6	0.12	19,241	0.954	0.938	0.904	0.281	0.409	0.421
7	0.14	15,869	0.955	0.944	0.892	0.298	0.403	0.447
8	0.16	13,175	0.898	0.918	0.813	0.320	0.398	0.469
9	0.18	10,966	0.932	0.927	0.827	0.314	0.375	0.467
10	0.20	11,142	0.879	0.887	0.773	0.332	0.387	0.494
11	0.22	9,392	0.895	0.892	0.758	0.344	0.401	0.513
12	0.24	7,751	0.835	0.848	0.733	0.358	0.398	0.526
13	0.26	6,933	0.842	0.835	0.721	0.361	0.405	0.532
14	0.28	5,767	0.816	0.816	0.679	0.367	0.391	0.540
15	0.30	5,062	0.871	0.860	0.712	0.381	0.406	0.556
16	0.32	4,711	0.839	0.830	0.701	0.373	0.395	0.546
17	0.34	4,210	0.829	0.832	0.681	0.387	0.410	0.566
18	0.36	3,913	0.813	0.832	0.670	0.380	0.397	0.561
19	0.38	3,684	0.801	0.798	0.642	0.381	0.401	0.566
20	0.40	3,214	0.831	0.837	0.685	0.401	0.416	0.587
21	0.42	3,333	0.773	0.778	0.603	0.399	0.413	0.584
22	0.44	2,863	0.753	0.795	0.571	0.399	0.406	0.586
23	0.46	2,595	0.732	0.745	0.596	0.414	0.425	0.599
24	0.48	2,653	0.784	0.780	0.581	0.396	0.406	0.583
25	0.50	2,654	0.701	0.730	0.560	0.400	0.408	0.585

* Approach (a), using the FGT with true haplotypes

** Approach (b), using the FGT with phased haplotypes

† Approach (c), using the DGT with genotype data

overestimation was highest when the DGT was used (98.362 %) in Approach (c). Conversely, the proportion of underestimated breakpoints was lowest in (c), 1.543 %, and highest when haplotypes were phased in (b), 4.147 %; in (a), 2.418 % of breakpoints were underestimated. The proportion of detected breakpoints that coincided with the corresponding true breakpoints was 0.192 %, 0.188 %, and 0.095 % in (a), (b), and (c), respectively.

The highest overall accuracy was found for the FGT on true haplotypes, followed by the analysis on phased haplotypes, which had $r^2 = 0.926$ and $r^2 = 0.892$ in Approaches (a) and (b), respectively. The accuracy achieved by the DGT was lower, but still considerably high with $r^2 = 0.847$ in Approach (c). This was also reflected in the measured magnitude of error (RMSLE), which was 0.400, 0.434, and 0.569 in (a), (b), and (c), respectively. The measurement of accuracy was further broken down by the allele frequency of target variants (f_k category); results are shown in Table 3.2 (page 106). Accuracy decreased towards higher allele frequency in each approach. For example, for f_2 variants, r^2 was 0.998, 0.985, and 0.995 in (a), (b), and (c), respectively, which was reduced for f_{25} variants where $r^2 = 0.701$ in (a) and $r^2 = 0.730$ in (b), but where (c) was seen to decrease more rapidly by comparison ($r^2 = 0.560$). Notably, when haplotype data were phased in (b), accuracy was highest at f_5 variants ($r^2 = 0.963$), indicating that accuracy was decreased at lower frequencies. Similarly, RMSLE scores reflected the same general pattern, but where the magnitude of error in (b) was at a maximum at f_2 variants.

A more intuitive representation of results is provided in Figure 3.9 (next page), which compares true and detected breakpoint distances in two ways. First, in Figure 3.9A, breakpoint densities are shown in separate scatterplots for breakpoints detected on the left and right-hand side of focal positions. For example, a clear difference in the proportion of underestimated breakpoints can be seen between Approaches (a) and (b), *i.e.* where the FGT was used on true and phased haplotypes, respectively. In Approach (c), where the DGT was used on genotype data, breakpoint densities indicate a higher proportion of overestimated distances compared to (a) or (b). Second, in Figure 3.9B, the relative distance was calculated as $x = \hat{d}_i/d_i$, where \hat{d} and d denote detected and true distances, respectively. By doing so, detected breakpoint distances were “mapped” relative to the corresponding true distances, such that $0 < x < 1$ indicates underestimation and $x > 1$ indicates overestimation. The cumulative distribution function (CDF) of the relative distance is shown separately per f_k category. For example, it can be seen that a larger proportion of f_2 variants (15.215 %) contributed to the overall underestimation found in Approach (b), *e.g.* compared to f_5 (5.544 %) and f_{25} variants (0.755 %).

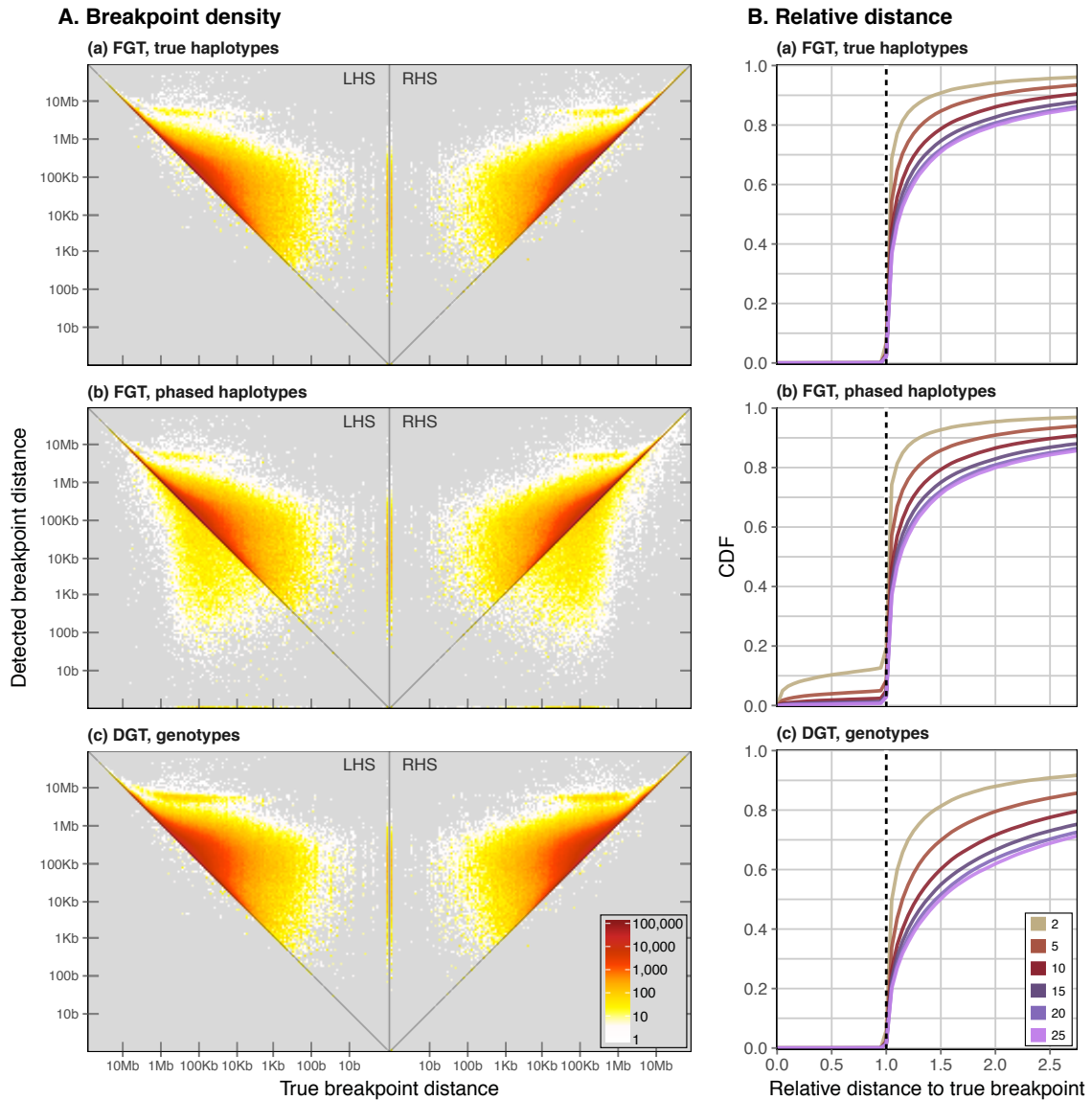


Figure 3.9: Accuracy of breakpoint detection in simulated data. Breakpoints detected in f_k pairs at $k \in \{2, \dots, 25\}$ are compared to true IBD breakpoint sites, after removing boundary cases in either the detected or true dataset. Segments were inferred using the FGT on true haplotypes (a) and phased haplotypes (b), as well as the DGT on genotype data (c). Panel (A) shows the density of detected breakpoints in relative distance to the focal and true breakpoint sites. The physical distance between detected breakpoint and focal position was divided by the distance between true breakpoint and focal position, such that values < 1 indicate underestimation and > 1 overestimation relative to the true distance (dashed line). Panel (B) illustrates the relationship between each detected breakpoint and the corresponding true breakpoint, measured as the physical distance to the focal site. Along each axis, distances were pooled into 200 bins (on log scale) and cells in the resulting 200^2 grid were colour-coded for the number of intersecting true and detected breakpoints, where grey indicates zero. Segment breakpoints to the left (LHS) and right-and side (RHS) of the focal position are shown separately.

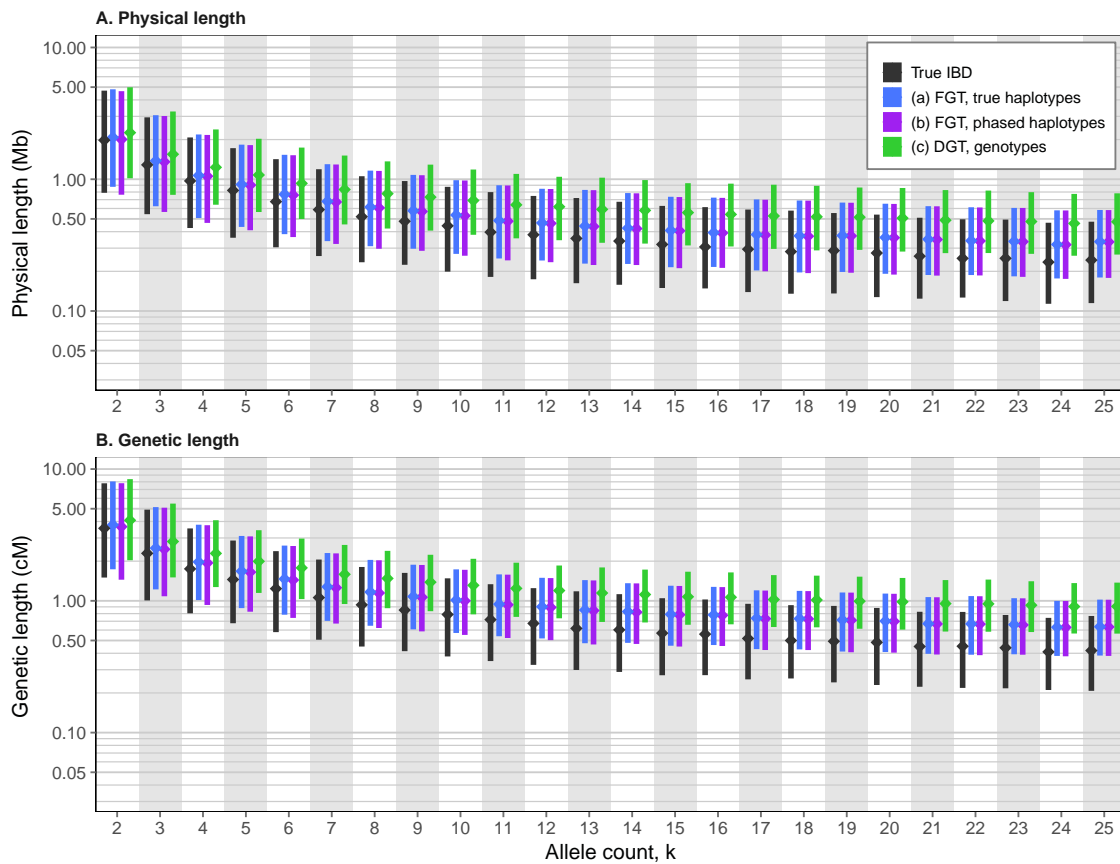


Figure 3.10: IBD segment lengths inferred in simulated data. The distribution of median physical and genetic length of detected IBD segments is shown by allele frequency of the focal variant ($f_{[2,25]}$). IBD detection was performed using the FGT on true and phased haplotypes, as well as the DGT on genotype data; Approaches (a), (b), and (c), respectively. The true IBD length is shown for comparison. Bottom and top of each bar indicate 1st and 3rd quartiles, respectively, between which the median (2nd quartile) is marked (diamonds).

The distribution of physical and genetic IBD length is shown in Figure 3.10 (this page). These results were obtained after boundary cases were removed in each approach (*i.e.* discarding segments where the end of a chromosome was reached without detecting a breakpoint), so as to ensure that observed IBD length was delimited by recombination on both sides of a segment; 1.449 %, 1.400 %, and 1.637 % was removed in (a), (b), and (c), respectively, and 1.340 % in the set of true IBD segments. Data were then intersected again to retain the same set of target sites in each approach; as a result, 2.929 million unique segments were retained (98.363 %).

Median physical length (and median genetic length) over the set of retained segments was computed for each approach. A small difference was seen for the FGT, where

median length was 0.417 Mb (0.800 cM) on true haplotypes in Approach (a), and 0.413 Mb (0.791 cM) on phased haplotypes in Approach (b). For the DGT on genotype data, median length was longer by comparison, 0.570 Mb (1.094 cM). The median of true IBD length was 0.328 Mb (1.573 cM), which was shorter than detected in each approach. But as seen in Figure 3.10, the distribution of IBD lengths in (a), (b), and (c) closely followed the true lengths along the allele frequency range. However, the gap between true and detected lengths increased towards higher allele frequencies. For example, for f_2 variants, median length of true IBD segments was 1.978 Mb (3.551 cM), which is only marginally shorter compared to 2.079 Mb (3.773 cM), 2.005 Mb (3.652 cM), and 2.256 Mb (4.085 cM) in (a), (b), and (c), respectively. For f_{25} variants the difference was more pronounced; *i.e.* median length of true IBD segments was 0.243 Mb (0.419 cM), compared to 0.336 Mb (0.636 cM), 0.335 Mb (0.634 cM), and 0.475 Mb (0.907 cM) in (a), (b), and (c), respectively.

In summary, the FGT on true haplotype data in Approach (a) overall achieved the highest levels of accuracy while maintaining low error. This was particularly seen in comparison to Approach (b), which differed only in the additionally included phasing step. Since genomic datasets were typically composed of phased haplotypes, Approach (b) can be seen as being the realistic approach. However, the higher rate or error at lower frequency variants may pose a problem for analysis for rare variants. As an alternative, the DGT on genotype data, Approach (c), can be used to detect IBD with high accuracy and comparatively low error rates. However, the larger proportion of overestimated IBD breakpoints may result in additional error, *e.g.* if it is assumed that the genealogy is consistent along the sequence of inferred IBD segments.

IBD detection using the *Refined IBD* algorithm

Simulated data were additionally analysed using the Refined IBD algorithm implemented in Beagle version 4.1 (Browning and Browning, 2013).* The method is based on the non-probabilistic GERMLINE algorithm (Gusev *et al.*, 2009), which identifies putative IBD segments from short exact matches between haplotype pairs; candidate segments are

* Beagle 4.1: <https://faculty.washington.edu/browning/beagle/beagle.html> [Date accessed: 2016-11-22]

found by extending identified regions to longer inexact matches. In Refined IBD, an additional probabilistic approach is included to assess candidate segments conditional on the likelihood ratio (LR) of the data, calculated under IBD and non-IBD models. A logarithm of odds (LOD) score is calculated as $\log_{10}(\text{LR})$, and segments are reported as IBD if the LOD score is above a specified threshold. This approach has been found to achieve greater accuracy than GERMLINE alone or fastIBD, which is a non-probabilistic method that detects IBD based on haplotype frequency (Browning and Browning, 2011a, 2013).

The analysis was performed using default parameters in Refined IBD (retaining candidate segments at $\text{LOD} > 3.0$) and after conversion of simulated data into Variant Call Format (VCF)*. Note that haplotype data are required; therefore only the FGT was evaluated using true and phased haplotype data in Approaches (a) and (b), respectively. The analysis returned 13.689 million IBD segments in (a), of which 0.248 % were duplicated, and 13.647 million in (b), of which 0.249 % were duplicated. The median length of all detected segments was 0.191 Mb and 0.191 Mb in (a) and (b), respectively (after removal of duplicates).

The accuracy of detected IBD segments was measured in relation to the true IBD intervals, which were already determined for the set of previously analysed target sites; *i.e.* all $f_{[2,25]}$ variants found in the data (allele frequency $\leq 0.5\%$). Note that the detection approach employed by Refined IBD reports all segments inferred for a given pair of haplotypes, such that detected and true intervals cannot be matched by direct reference to a particular target site. Hence, for a given pair of haplotypes, true and detected segments were matched if the focal allele associated with a true segment fell within the interval of the detected segment, which was discarded if none of the pairwise shared target alleles were found within the detected interval. This matching process resulted in a set of 2.166 million unique segments in the analysis conducted on true haplotypes, Approach (a). For the phased dataset, Approach (b), 0.528 million unique segments were matched. The lower number of segments retained in Approach (b) is likely to be the consequence of mismatched haplotypes in original and phased data.

* Variant Call Format: <http://vcftools.sourceforge.net/VCF-poster.pdf> [Date accessed: 2016-11-22]

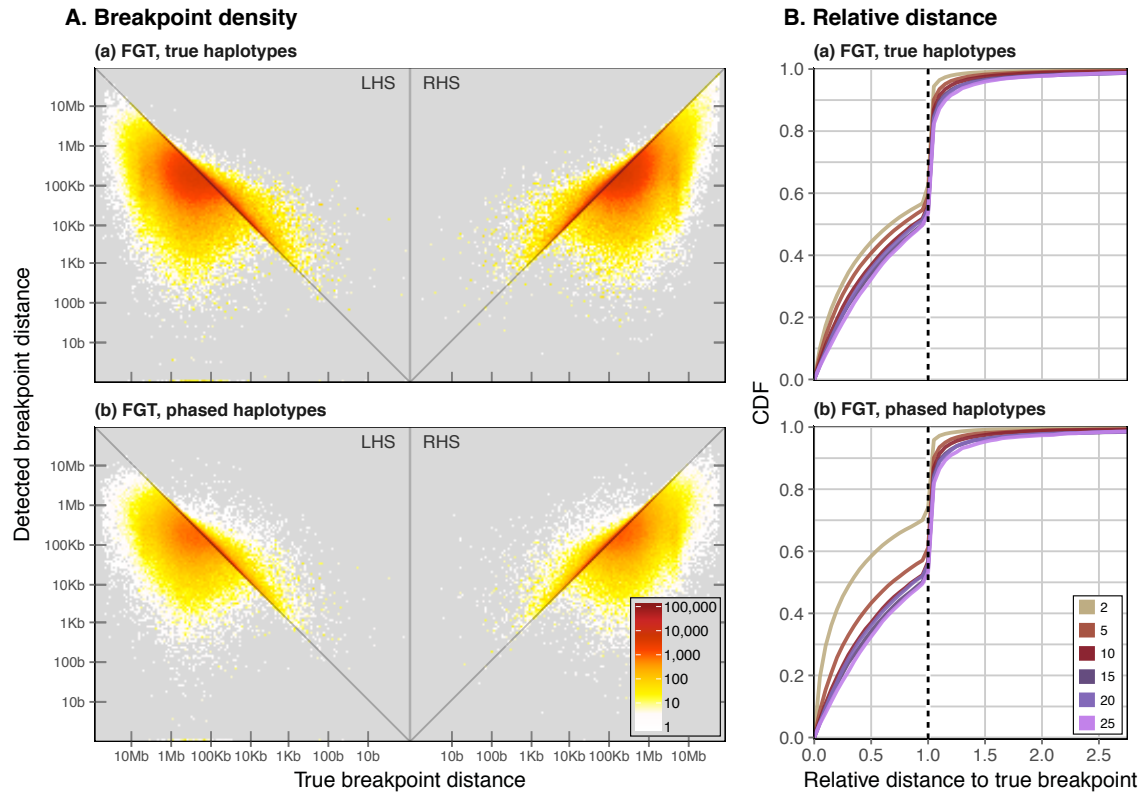


Figure 3.11: Accuracy of breakpoint detection in simulated data using Refined IBD in Beagle 4.1. Results are shown for one million randomly selected shared haplotype segments, after removing boundary cases in either the detected or true segments. Segments were inferred using the FGT on true haplotypes (a) and phased haplotypes (b), as well as the DGT on genotype data (c). Panel (A) shows the density of detected breakpoints in relative distance to the focal and true breakpoint sites. For each detected breakpoint, its physical distance to the focal site was divided by the distance between the corresponding true breakpoint and the focal site, such that values < 1 indicate underestimation and > 1 overestimation of the true distance (dashed line). Panel (B) provides a heatmap representation of a scatter plot, comparing physical distances between focal site and true breakpoint (x-axis) and detected breakpoint (y-axis). Along each axis, distances were pooled into 200 bins (on log scale) and the resulting 200^2 squares were colour-coded for the number of intersecting true and detected breakpoints, where grey indicates zero. Segment breakpoints to the left (LHS) and right-and side (RHS) of the focal position are shown separately.

After the removal of segments at which haplotype pairs did not share any of the alleles in $f_{[2,25]}$, median lengths were longer in comparison to the original datasets; 0.255 Mb and 0.256 Mb in (a) and (b), respectively. This can be seen as the result of both the removal of falsely identified segments, as well as segments that were older and thereby expected to be shorter.

The majority of retained breakpoints was underestimated in both Approaches (a) and (b); 55.356 % and 56.606 %, respectively. In Approach (a), 44.385 % were overestimated and 0.259 % coincided with true breakpoint positions. This was similar in Approach (b), where 43.155 % were overestimated and 0.238 % coincided. Accuracy was measured in terms of the physical distance between breakpoint position and the corresponding focal site. Because the latter was not specified in the results obtained from Refined IBD, the same focal position as associated with the matched true IBD segment was assumed. Data were not reduced to the intersection of segments retained across datasets, due to the low number of consistent matches. These results are illustrated in Figure 3.11 (page 112).

The distance distribution of true and detected breakpoints (Figure 3.11A) suggests that detected breakpoints were closely distributed around the corresponding true breakpoints. However, overall accuracy was low in both (a) and (b), reaching $r^2 = 0.287$ and $r^2 = 0.171$, respectively. The magnitude of error, RMSLE, was lower in (a) compared to (b); 0.595 and 0.616, respectively. When true haplotypes were analysed, Approach (a), accuracy decreased steadily towards higher allele frequencies. For example, accuracy was highest for f_2 variants ($r^2 = 0.346$) but lowest for f_{25} variants ($r^2 = 0.074$). However, the magnitude of error was highest for f_2 variants (RMSLE = 0.750) and lowest for f_{25} variants (RMSLE = 0.543). When haplotypes were phased, Approach (b), error was further increased at f_2 variants (RMSLE = 0.999) in comparison to f_{25} variants (RMSLE = 0.546). The higher error at lower allele frequencies was also reflected in r^2 values; e.g. accuracy was low at f_2 ($r^2 = 0.087$), higher at f_5 ($r^2 = 0.132$), but lowest at f_{25} ($r^2 = 0.048$). The difference between true and phased datasets is further highlighted in Figure 3.11B, where a higher proportion of f_2 variants is seen to be underestimated in (b).

The distribution of physical and genetic lengths for the segments retained in Approaches (a) and (b) are shown in Figure 3.12 (next page), in relation to the true IBD lengths at each f_k category. Because (a) and (b) were compared on different sets of detected segments, the reported lengths of true segments were computed from the set matched

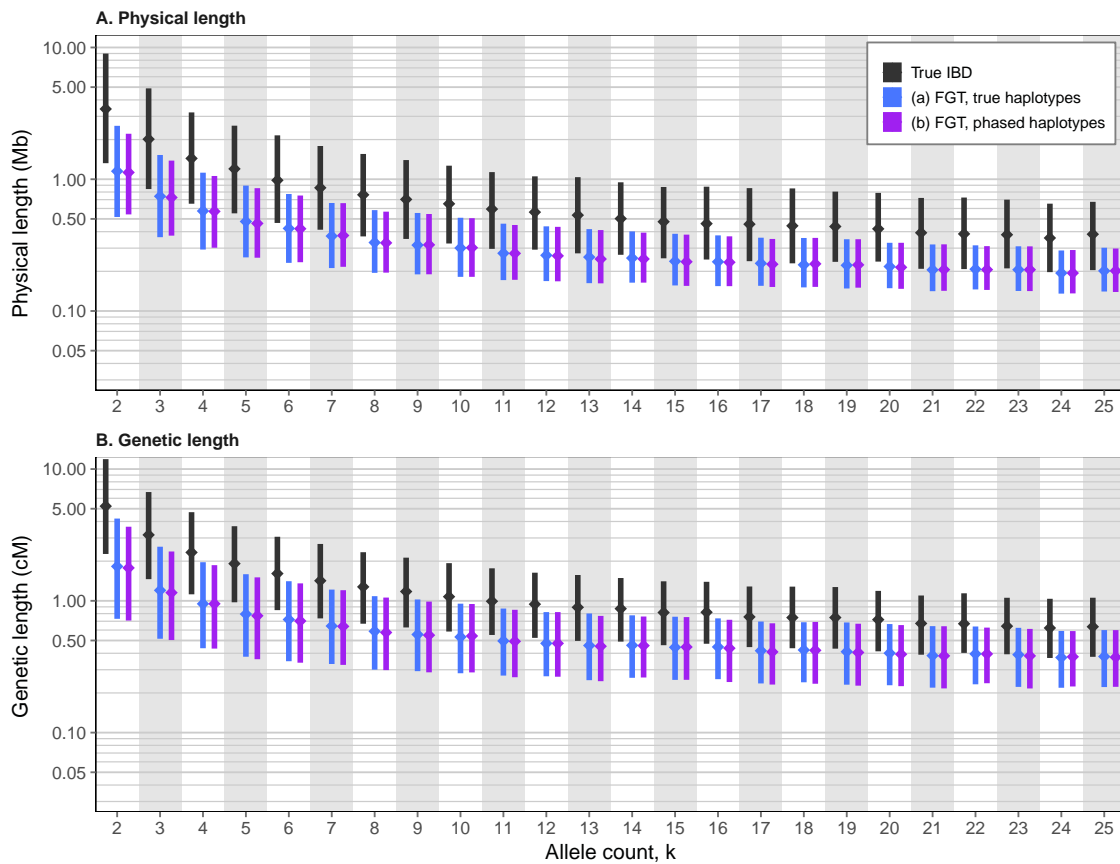


Figure 3.12: IBD segment lengths inferred using *Refined IBD* in Beagle 4.1. The distribution of median physical and genetic segment length is shown by allele count (f_k category). IBD segments were estimated using the *Refined IBD* algorithm implemented in Beagle 4.1. Because the method requires haplotype data, only the FGT was evaluated using true haplotypes, Approach (a), and phased haplotypes, Approach (b). These are compared to the true lengths of corresponding IBD tracts. Bottom and top of each bar indicate 1st and 3rd quartiles, respectively, between which the median (2nd quartile) is marked (*diamonds*).

to (a). Boundary cases were removed to avoid potential bias in length comparisons; 1.012 % and 0.893 % in (a) and (b), respectively.

Overall median physical length (and median genetic length) was 0.185 Mb (0.621 cM) in (a) and 0.192 Mb (0.429 cM) in (b), but both were shorter in comparison to true IBD segments at 0.260 Mb (0.912 cM). At f_2 variants, the median length of IBD segments inferred in (a) was 1.150 Mb (1.825 cM), which was longer compared to (b), where median length was 1.126 Mb (1.777 cM). However, both were considerably shorter in comparison to the true segments, 3.413 Mb (5.229 cM). This difference persisted towards higher allele frequencies; e.g. for f_{25} variants, where the median of true lengths was

0.383 Mb (0.636 cM), which was longer compared to 0.202 Mb (0.378 cM) in (a) and 0.202 Mb (0.373 cM) in (b).

While this analysis does not permit to make statements about falsely identified IBD segments, as these were among the segments removed in the matching process, the results presented showed that the lengths of inferred breakpoint intervals are likely to be shorter than the underlying haplotype region shared by descent. Thus, the Refined IBD algorithm is less accurate with regard to the inference of the recombination events that delimit the underlying IBD tract.

IBD detection in real data: 1000 Genomes, chromosome 20

The IBD detection method presented was applied to the final release dataset of the 1000 Genomes Project Phase III (1000 Genomes Project Consortium *et al.*, 2012, 2015), which included $N = 2,504$ individuals. IBD detection was performed for each autosome (chromosomes 1–22), where selected target sites comprised all shared rare variants at allele frequency $\leq 0.5\%$; *i.e.* f_k where $k \in \{2, \dots, 25\}$. However, to enable a closer comparison to the results obtained on the simulated dataset (which simulated variable recombination rates as inferred for chromosome 20), the following results are presented for chromosome 20 only. A summary of the IBD detection results for chromosomes 1–22 is given in Table 3.3 (next page).

Data were available as phased haplotypes, which enabled the analysis using both the FGT and DGT; *i.e.* the results produced can therefore be seen as being analogous to Approach (b) and Approach (c), respectively. In each, 18.0 million IBD segments were inferred, of which 43.2 % were unique for the FGT, and 39.4 % for the DGT. After removal of boundary cases (0.194 % and 0.285 % for the FGT and DGT, respectively), data were intersected to retain a common set of target sites in the analysis, which retained 7.069 million unique segments.

As there is no “truth” dataset that could serve as a reference to measure accuracy, the following analysis was limited to the quantitative description of the inferred IBD lengths. These results are shown in Figure 3.13 (page 117). Median physical length

Table 3.3: Inferred IBD length per chromosome in 1000 Genomes. Shared haplotype segments in 1000G Phase III were inferred using the FGT and DGT, on data from 2,504 individuals across all autosomes. Pairwise shared segments were identified from rare variants at allele frequency $\leq 0.5\%$ ($f_{[2,25]}$). Median genetic and physical lengths over all inferred segments were calculated per chromosome, after removing boundary cases and retaining unique segments only.

Chr.	SNPs	Targets	Segments	Unique (%)		Length (Mb)		Length (cM)	
				FGT*	DGT**	FGT*	DGT**	FGT*	DGT**
1	6,196,151	2,126,720	64,449,399	40.3	35.9	0.125	0.237	0.150	0.300
2	6,786,300	2,323,889	70,274,554	38.1	33.8	0.136	0.248	0.143	0.280
3	5,584,397	1,893,872	57,220,884	37.1	33.2	0.138	0.243	0.154	0.290
4	5,480,936	1,847,521	57,598,118	36.6	32.8	0.138	0.247	0.150	0.283
5	5,037,955	1,716,580	53,055,802	36.4	32.8	0.139	0.245	0.158	0.293
6	4,800,101	1,625,828	50,544,859	37.0	33.0	0.133	0.238	0.148	0.280
7	4,517,734	1,546,940	47,303,666	39.2	34.8	0.119	0.218	0.139	0.270
8	4,417,368	1,519,028	46,250,487	37.3	33.4	0.119	0.212	0.140	0.268
9	3,414,848	1,171,960	35,718,922	40.6	36.6	0.110	0.203	0.156	0.296
10	3,823,786	1,313,699	40,488,078	39.6	35.3	0.114	0.210	0.154	0.299
11	3,877,543	1,318,559	39,668,383	38.3	34.2	0.128	0.228	0.148	0.283
12	3,698,098	1,255,880	38,116,079	39.4	35.3	0.124	0.221	0.164	0.311
13	2,727,881	919,222	28,252,993	38.9	35.2	0.126	0.222	0.166	0.305
14	2,539,149	861,549	25,955,712	39.5	35.6	0.119	0.214	0.157	0.299
15	2,320,474	795,882	23,977,630	42.6	38.2	0.100	0.183	0.153	0.304
16	2,596,072	901,185	26,907,909	43.5	38.3	0.081	0.153	0.140	0.286
17	2,227,080	775,133	22,914,233	44.5	39.8	0.096	0.175	0.150	0.300
18	2,171,378	739,822	22,405,301	41.5	37.7	0.109	0.193	0.169	0.311
19	1,751,878	607,451	18,033,860	46.1	41.3	0.079	0.146	0.147	0.293
20	1,739,315	599,065	18,040,053	43.2	39.4	0.102	0.180	0.182	0.339
21	1,054,447	365,330	11,051,666	44.7	40.4	0.090	0.172	0.162	0.312
22	1,055,454	363,748	10,748,355	47.2	42.5	0.070	0.133	0.145	0.291
<i>Total</i>		77,818,345	26,588,863	808,976,943					

* 1000G data are available as phased haplotypes; hence, results are analogous to Approach (b).

** Conducted on genotype data; hence, results are analogous to Approach (c).

(and median genetic length) over the whole set of retained IBD segments was 0.101 Mb (0.188 cM) using the FGT and 0.180 Mb (0.339 cM) using the DGT. As was seen in the analysis of simulated data, the DGT generally is more likely to overestimate breakpoint distance, leading to the discovery of longer intervals. This discrepancy in length was more pronounced for f_2 variants, for which median length was 0.124 Mb (0.195 cM) using the FGT and 0.253 Mb (0.428 cM) using the DGT. Notably, IBD lengths were more than twice as long in half of the detected segments using the DGT, compared to the FGT. The length of segments identified at lower frequencies was longer in comparison to higher frequencies; e.g. for f_{25} variants, median length was 0.084 Mb (0.165 cM) and 0.149 Mb

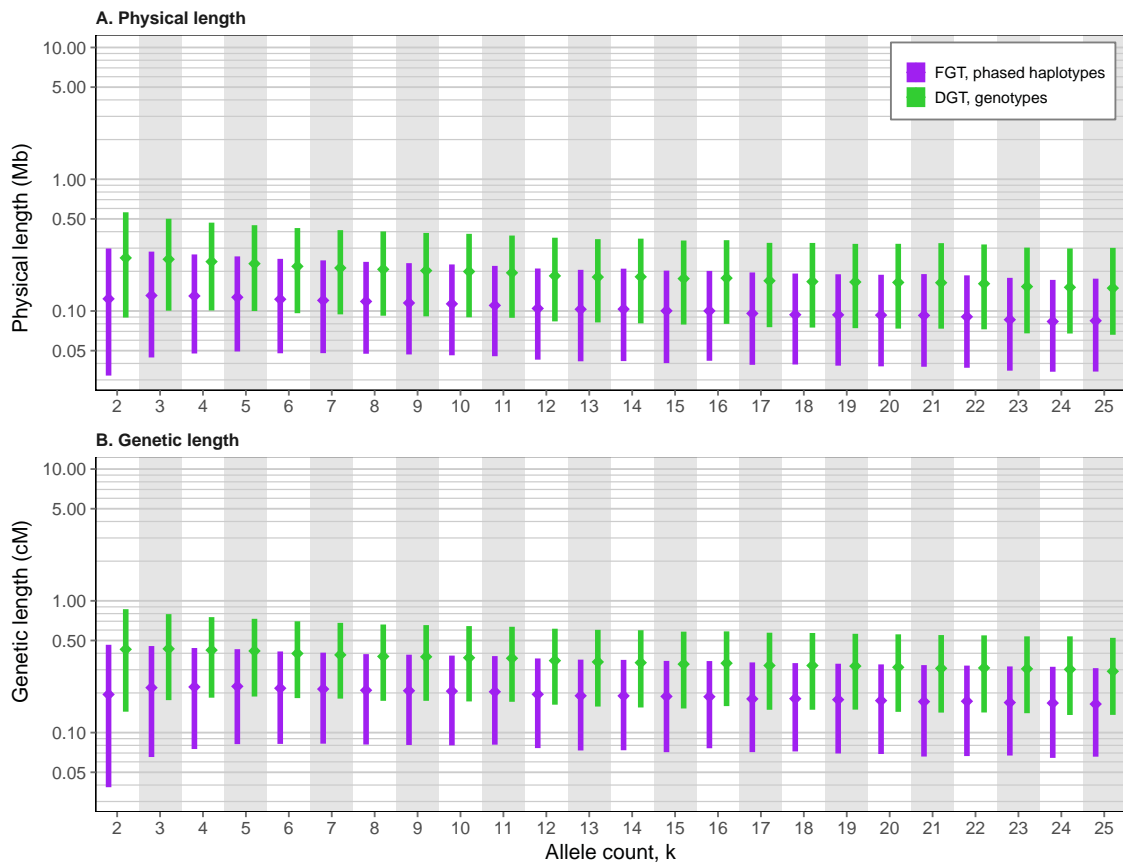


Figure 3.13: Distribution of inferred IBD lengths in 1000 Genomes data, chromosome 20. Results are shown for the detected physical and genetic lengths of shared haplotype segments by f_k , using chromosome 20 in the final release dataset of 1000 Genomes Project Phase III, including $N = 2,504$ individuals. IBD segments were detected using the FGT (on phased haplotypes) and the DGT (on genotype data). Bottom and top of each bar represent the 1st and 3rd quartile, respectively, between which the median (2nd quartile) is marked (*diamonds*).

(0.292 cM) using the FGT and DGT, respectively. However, the IBD lengths were highest at $f_{[3,5]}$ when the FGT was used, but which was not the case for the DGT.

Inference of the shared haplotype sequence

The IBD-based phasing concept described in Section 3.4 (page 98) was explored in this section. Given the genealogical constraints that follow from the assumption that the genealogy does not change along the sequence within a given breakpoint interval, it is straightforward to derive the sequence of the shared haplotype. This applies to sites where exactly one genotype is heterozygous and one is homozygous in a pair of individuals. In the following, such heterozygous-homozygous sites are referred to as being *informative*, as

opposed to sites where both genotypes are heterozygous, which are referred to as being *indeterminate*. At sites where both genotypes are homozygous, phasing is trivial. Hence, phasing is attempted at heterozygous sites along the sequence.

The analysis was performed on the full set of IBD segments detected using the DGT in the simulated dataset; recall that the FGT requires (phased) haplotypes and cannot be used on genotype data. Also, note that breakpoint sites delimit the interval enclosing a haplotype that is shared by descent, but they themselves represent the first positions along the sequence at which haplotype sharing was broken through recombination; hence, breakpoint sites were excluded from the inference. The purpose of this evaluation was to determine the proportions of correctly and incorrectly phased sites, as well as the proportion of indeterminate sites. This was then compared to the same haplotypes inferred using the set of true IBD segments.

In the following, two approaches were explored; first, haplotype inference was performed separately per IBD segment and, second, the segments identified by the same shared allele were grouped and a majority-rule was applied to determine the shared haplotype sequence (referred to as *consensus* approach). The latter represents an attempt to increase the number of informative sites, as these may differ if more pairs of individuals are considered. Since they share the same focal allele, it is assumed that this allele identifies the same haplotype in all pairs.

A random subset of 10,000 IBD segments was drawn for each f_k category from the full set of detected intervals using the DGT in which the shared haplotype was inferred. Similarly, for the consensus approach, target sites were randomly drawn for the set of identified targets for each f_k category, such that the total number of identified segments did not exceed 10,000 per f_k category. Haplotypes were then inferred and combined in each focal group by applying a majority-rule to estimate the sequence of the shared haplotype. For each segment, the proportions of correctly inferred, incorrectly inferred, or indeterminate alleles was then determined per f_k category. Additionally, to compare these results to the “truth”, the same subsets of IBD segments was analysed in each approach, but where estimated haplotype length was delimited by the corresponding true IBD segments.

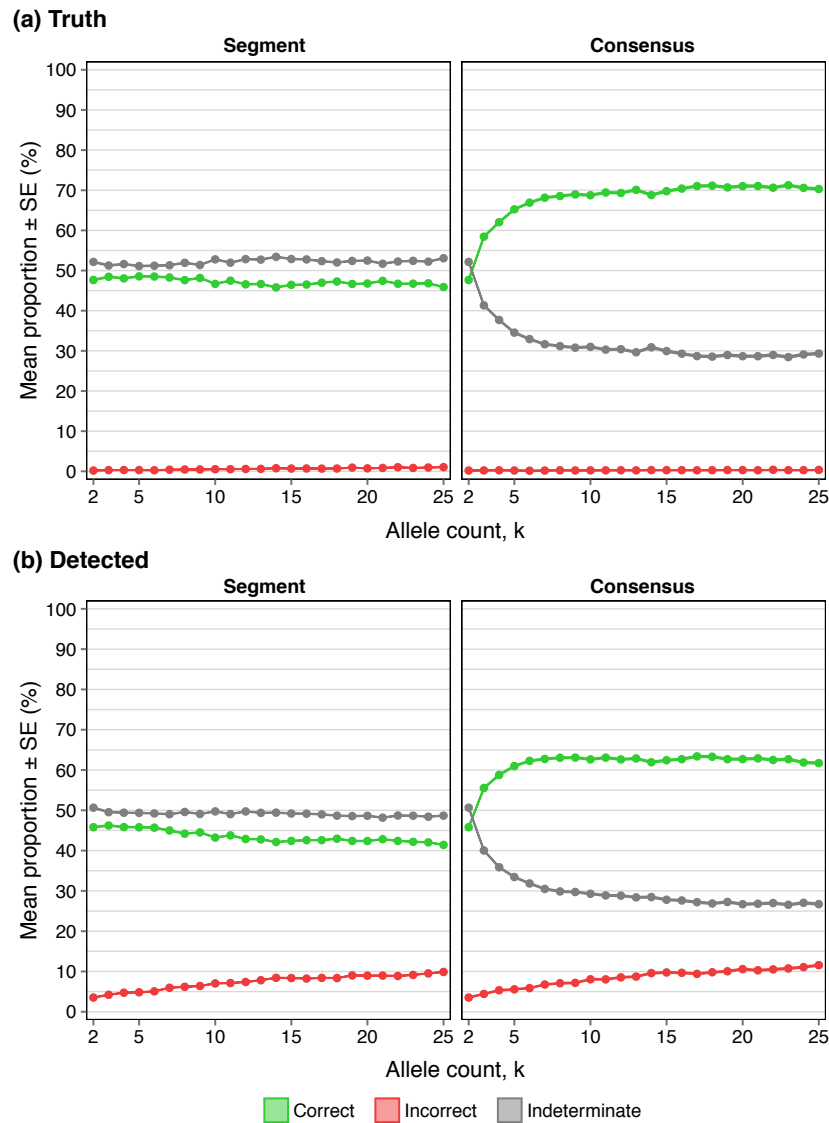


Figure 3.14: Accuracy of alleles inferred through IBD-based phasing by focal allele frequency. IBD segments were randomly selected; 10,000 per f_k category. Genotypes within each segment were phased and the relative proportions of correct, incorrect, and indeterminate alleles were recorded and averaged ($\pm \text{SE}$) per f_k category. This was done separately per segment (left) and using the consensus approach (right). The results shown in Panel (a) correspond to the “truth”, where the true IBD segments were used to delimit the extent of the inferred shared haplotype sequence. This is compared to Panel (b), where the DGT was used to detect IBD breakpoints in genotype data.

The same was done for both approaches, but using the set of true IBD segments to delimit the haplotype sequence. The results of this analysis are shown in Figure 3.14 (this page).

When true IBD segments were used, Figure 3.14a, the proportion of incorrectly phased sites was consistently low along the allele frequency range; however, note that

this proportion was not equal to zero. In comparison, the proportion of error increased towards higher allele frequencies when IBD was detected using the DGT, Figure 3.14b, which was seen in both the segment-based approach and the consensus approach. Notably, the proportion of indeterminate sites was consistently close to 50% in the segment-based approach using both true and detected data. However, the proportion of correctly phased genotypes decreased towards higher allele frequencies; from 46.173 % at f_2 variants to 42.330 % at f_{25} variants. In the consensus approach, the proportion of correctly phased genotypes showed a rapid increase but then reached a plateau around 70% in when true IBD segments were used, and between 60% and 65% when detected segments were used.

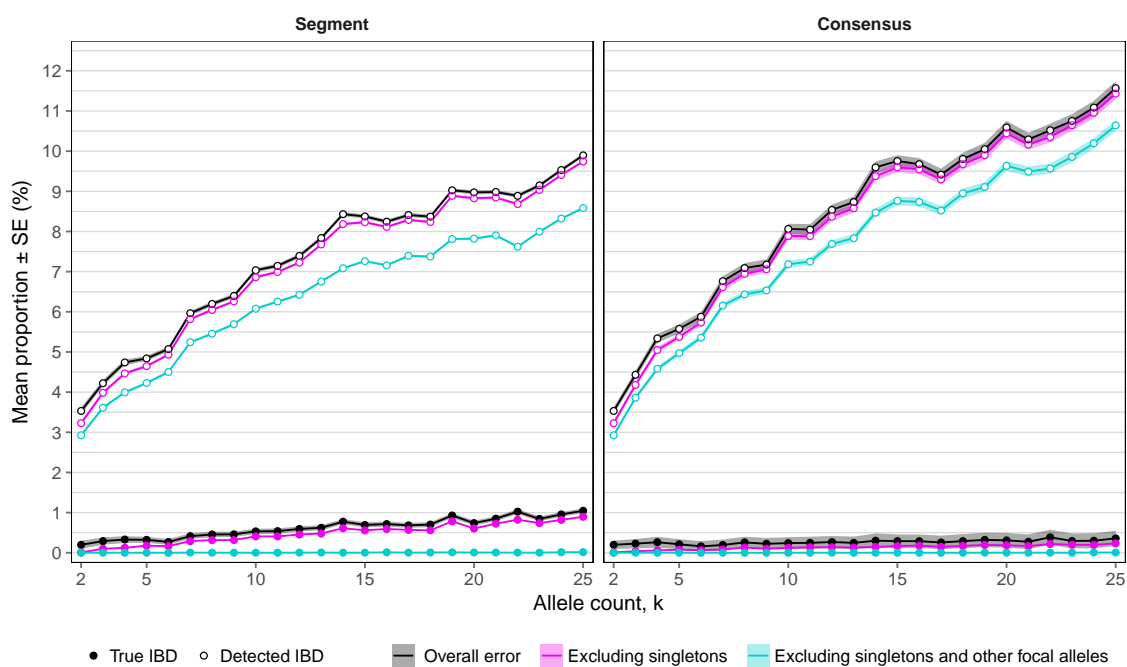


Figure 3.15: Error distribution of alleles inferred through IBD-based phasing. The same results are shown as in Figure 3.14, but with focus on incorrectly inferred alleles only; *i.e.* the proportion of overall error corresponds to the proportion of incorrect alleles in Figure 3.14. The source of error was further

The distribution of incorrectly phased genotypes was further analysed to distinguish error due to singletons and other focal alleles that fell within the intervals of the segments analysed. These results are shown in Figure 3.15 (this page). Note that in both, the exclusion of singletons did not markedly reduce the overall proportion of

incorrectly phased genotypes. In both the segment-based approach and the consensus approach, error was noticeably reduced if genotypes at other focal variants were excluded. Importantly, by excluding singletons and other focal alleles that fell within the interval of the segments analysed, error was reduced to zero when true IBD segments were used. In fact, incorrectly phased genotypes only occurred within the overestimated regions of detected IBD segments; *i.e.* using the DGT.

This finding is important as it suggests that haplotypes could be determined correctly if overestimation in the detection of breakpoints could be reduced or excluded. For example, instead of considering the full length of the segments detected, genotype phase could be determined from a narrow interval around a given target site.

Phasing coverage of pairwise shared haplotypes per individual

Although the presented IBD-based phasing approach attempted to only determine genotype phase locally, it may nonetheless be of interest to explore the possibility to phase individuals “globally”; that is, to distinguish haplotypes from genotype data along the full length of a chromosome per individual. To this end, it is relevant to determine the coverage of shared haplotypes along a chromosome per individual. Since simulated data may not be suited to derive expectations that would apply to reality, the following analysis was conducted on data from the 1000 Genomes Project Phase III, chromosome 20.

I randomly selected 500 of the 2,504 individuals and, for each individual, I identified all other individuals (in the whole sample of 2,504 individuals) which shared any rare allele at $f_{[2,25]}$ with a given individual. The average number of rare alleles shared between a given individual and any other individual was 15200 (± 455 SE), and the average number of unique individuals who shared any rare allele with a given individual was 1400 (± 9.65 SE), which ranged between 888 and 1,978. The DGT was used to detect segment breakpoints per pairwise shared focal allele; for comparison, the same was done using the FGT, although only the DGT would be applied in the context of genotype phasing.

Each set of detected segments was then reduced to include only unique IBD intervals; again after sorting by focal allele frequency such that the focal allele is the one with

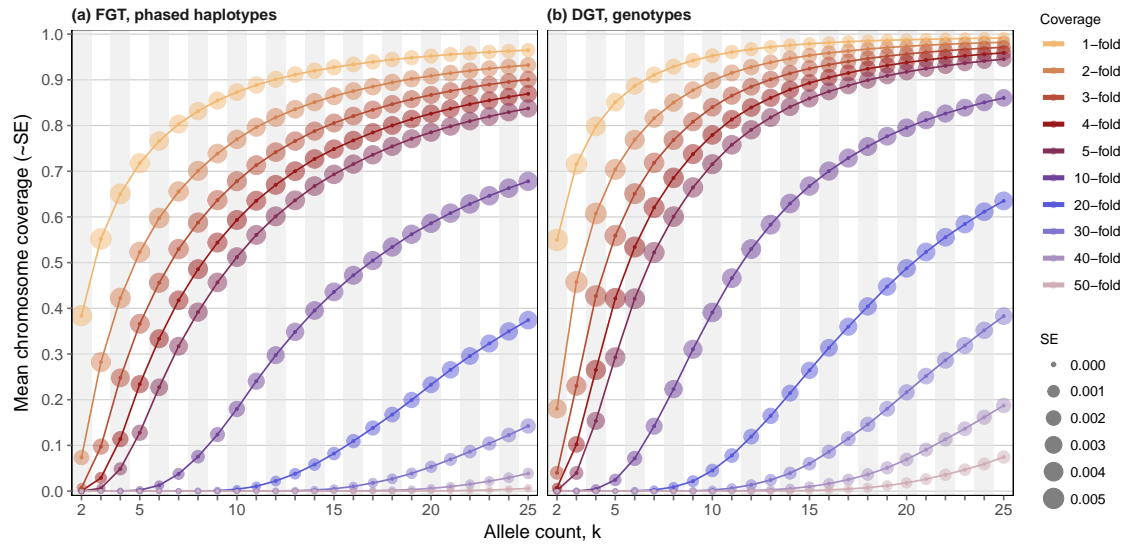


Figure 3.16: Cumulative shared haplotype coverage by focal allele count in 1000 Genomes data. Results are shown for 500 randomly selected individuals, among $N = 2,504$ in the 1000G dataset. Segments detected using the FGT (a, left) are compared to the segments detected using the DGT (b, right). Coverage was defined as the proportion of chromosome length covered by inferred and aligned shared haplotypes, where n -fold indicates that the chromosome was covered n -times by all segments up to a given f_k category (hence, cumulative). Standard error (SE) is indicated by the size of dots (see figure legend).

lowest frequency within a given segment. Recall that duplicate segments refer to IBD intervals that are tagged by multiple f_k variants, which are assumed to sit on the same underlying shared haplotype. The average number of unique segments retained per individual was 5070 (± 80.0 SE) for the DGT and 5460 (± 85.3 SE) for the FGT; note that haplotype data were phased. Retained haplotype segments were aligned by position along the chromosome to measure coverage, *i.e.* the proportion of the chromosome covered. Mean coverage across all 500 randomly selected individuals is given in Figure 3.16 (this page), which indicates the n -fold cumulative coverage by f_k category; shown for true IBD segments (Figure 3.16a) and segments detected using the DGT (Figure 3.16b).

Coverage was overall higher for the DGT compared to the FGT, due to overestimating IBD lengths. Notably, neither the DGT nor the FGT reached full coverage on average. However, a steady increase was seen when f_k variants at higher frequency were included. Considering f_2 variants alone, the DGT reached $> 50\%$ 1-fold coverage, which was higher compared to the FGT with $< 40\%$ 1-fold coverage. Considering focal alleles occurring at

higher frequencies, the DGT was at $\approx 99\%$ 1-fold cumulative coverage at $f_{\leq 20}$, whereas the FGT slowly approached $\approx 95\%$ 1-fold cumulative coverage at $f_{\leq 25}$.

These results indicate that a “global” phasing approach using inferred IBD information alone would not be able to fully determine haplotypes in sample data of unrelated individuals. However, note that similar approaches have been applied to sets of related individuals, for which it can be expected that there are more and longer pairwise shared haplotypes; *i.e.* long range phasing (LRP) methods (Kong *et al.*, 2008; Palin *et al.*, 2011; Loh *et al.*, 2016a).

3.7 Discussion

In this chapter, I presented a novel IBD detection method which is able to infer recombination events in both haplotype and genotype data. To be able to apply this method on a larger scale, I implemented the IBD detection algorithm described in this chapter as a computational tool written in C++; called **tidy** (targeted IBD detection done thoroughly).*

Although the FGT showed overall high levels of accuracy, phasing error was identified as a problem. Current phasing methods such as SHAPEIT2 typically show very low error rates (O’Connell *et al.*, 2014). However, occasionally, alleles are placed on the wrong haplotype. This may happen at single loci (*flip errors*) or such that longer haplotype stretches are exchanged (*switch errors*). Both types of error can affect breakpoint detection under the FGT as both flip and switch errors may change the configuration of alleles observed in relation to a given focal variant. As an alternate solution to using phased haplotypes, the DGT can be used on genotype data, which is therefore not affected by phasing error. However, the lengths of detected IBD segments tend to be overestimated.

Notably, the IBD results obtained from analysis of the 1000G dataset suggests that the FGT was similarly affected by phasing error as seen in the simulation analysis. However, the DGT was also affected by other sources of error. One consideration is that both the FGT

* Targeted IBD detection done thoroughly, tidy: <https://github.com/pkalbers/tidy>

and DGT assume the infinite sites model, but this is only an approximation of conditions observable in nature. In particular, back mutations and recurrent mutations are excluded in the model, but these are prevalent in the (human) genome. For instance, recurrent mutations can produce patterns of variation that would otherwise only be observable if recombination had occurred (McVean *et al.*, 2002). Thus, false positive breakpoints may be inferred, such that IBD length is underestimated. Nonetheless, the infinite sites model is usually seen as a reasonable approximation to reality, as the number of variant sites in a sample is typically much smaller than the number of nucleotides in the chromosomal sequence (Hein *et al.*, 2004). However, the presence of genotype error cannot be ruled out and therefore requires further consideration.

Lastly, the IBD-based phasing concept showed that it is possible to derive the shared allelic state sequence in pairs of individuals that share a haplotype by descent. This approach, in its current implementation, is only able to phase genotype data over locally shared segments. However, a potential utility of such a local phasing approach may arise considering that rare variants can be used to identify recent relatedness patterns in large datasets. Because a given rare allele identifies the underlying shared haplotype, the inferred sequence is likely to correctly distinguish the haplotypes of an individual within a shorter region around the target position. For example, this information may serve as a *post-hoc* correction to haplotype data produced using existing phasing methods.

*The first principle is that you must not fool yourself –
and you are the easiest person to fool.*

— Richard Feynman

4

Consideration of genotype error in the inference of haplotype sharing by descent

Contents

4.1	Introduction	125
4.1.1	Probability of genotype error	127
4.2	Generation of platform-specific genotype error profiles	129
4.2.1	High-confidence genome data as benchmark for comparisons	130
4.2.2	Selection and preparation of datasets from different platforms	131
4.2.3	Penetrance of genotype error in sequencing and genotyping data	134
4.3	Impact of genotype error on IBD detection	140
4.3.1	Integration of empirical error distributions in simulated data	141
4.3.2	Results	142
4.3.3	Discussion	150
4.4	A Hidden Markov Model for IBD inference	151
4.4.1	The algorithm for probabilistic IBD inference	153
4.4.2	Description of the model	154
4.4.3	Integration of empirically determined genotype error rates	162
4.4.4	Inference of IBD segments	167
4.4.5	Results	170
4.4.6	Discussion	174

4.1 Introduction

Recent advancements in genotyping and next-generation sequencing (NGS) technologies have enabled us to study the human genome in unprecedented detail and scale. The availability of high-throughput methods to survey large samples has led to successful identification of thousands of disease causing risk factors, which in particular was driven

by genome-wide association (GWA) studies. This explosion of human genetic data has further enabled collaboration initiatives through the setup of genetic databases, which can be queried by research groups worldwide. However, because no technology is perfect, acquired data are likely to contain undetected amounts of error, which may affect statistical inference in many ways.

Statistical tests often rely on the assumption that genotype data (retained after quality control) are correct, or that error quantities are negligible. Yet, the effects of misclassification in genotype data are well documented. For example, it has been shown that even minor amounts of genotype error can distort estimated distances in linkage mapping studies (Buetow, 1991; Shields *et al.*, 1991; Sobel *et al.*, 2002), result in a substantial loss of linkage information in quantitative trait analyses (Douglas *et al.*, 2000; Abecasis *et al.*, 2001), decrease power in association studies (Kang *et al.*, 2004), and can substantially increase type I (false positive) error in haplotype-based case-control analyses (Moskvina *et al.*, 2005).

Identification of incorrectly typed or called genotypes remains a difficult problem, which becomes more challenging as the magnitude of data increases. But, for example, as shown by Cox and Kraft (2006) and independently by Moskvina and Schmidt (2006), genotype error does not always affect the distributions of genotypes to the extent that Hardy-Weinberg equilibrium (HWE) can be violated, which is disturbing given the circumstance that departures from HWE are often used as a simple and quick method to test for and thereby exclude presumably incorrect genotypes.

In this chapter, I explore the impact of genotype error on the detection of identity by descent (IBD) segments and, based on these results, I implement a new approach for targeted IBD inference using a Hidden Markov Model (HMM). First, I introduce a generic model for genotype error; see section below. The remainder of this chapter is then divided into two main parts. In the first part (Section 4.2), I characterise the distribution of genotype error in data obtained on different genotyping and sequencing platforms, to construct empirical error profiles. I use this information to integrate realistic error rates in simulated data, such that the effects of error can be observed in practice. In particular, I

evaluate the non-probabilistic IBD detection method presented in Chapter 3. The insights gained from this analysis enabled a probabilistic extension of the targeted IBD detection method, which I implemented using a HMM; I present this new method in the second part of this chapter (Section 4.4). This HMM-based method is incorporated in the previously presented `tidy` algorithm for the targeted detection of IBD segments (see Chapter 3).

4.1.1 Probability of genotype error

Consider a biallelic locus with alleles a or b , which respectively occur at frequency p and $q = 1 - p$ in a population. Genotypes are formed by combination of two alleles in diploid organisms (therefore sometimes referred to as *diplotypes*). There are four possible combinations of alleles, *i.e.* aa , ab , ba , and bb , but of which genotypes ab and ba are indistinguishable. It is convenient to recode the two alleles as 0 and 1 to denote the reference and alternate allele, respectively. By introducing k to count the number of alternate alleles, let g_k denote a genotype, where $k \in \{0, 1, 2\}$. If all combinations of the two alleles are statistically independent, *e.g.* in a randomly mating population, sample genotype frequencies, $f_g(k)$, are multinomially distributed with expectations given by HWE proportions (Hardy, 1908; Weinberg, 1908); *i.e.* such that $(p + q)^2 = p^2 + 2pq + q^2 = 1$. The general form of the expected genotype frequency is given in Equation (4.1), where n refers to the number of chromosome copies (ploidy); *e.g.* $n = 2$ for diploid organisms.

$$f_g(k) = \binom{n}{k} p^{n-k} q^k \quad (4.1)$$

In presence of genotype error, the actual, *true* genotype is distinguished from the *observed* genotype, \tilde{g}_k , and the observed frequency, $f_{\tilde{g}}(k)$, is different from the true (but unknown) genotype frequency, dependent on the rate of error. More precisely, let the rate at which genotype g_j is classified as \tilde{g}_i be denoted by ε_{ij} , where $i, j \in \{0, 1, 2\}$. The value of ε_{ij} is often referred to as the *penetrance* of a genotype and represents the probability of observing genotype \tilde{g}_i given the true genotype g_j (Ott, 1999; Gordon

et al., 2002). For convenience, penetrance parameters can be represented in a 3×3 confusion matrix, \mathcal{E} , below.

$$\mathcal{E} = \begin{bmatrix} \varepsilon_{00} & \varepsilon_{01} & \varepsilon_{02} \\ \varepsilon_{10} & \varepsilon_{11} & \varepsilon_{12} \\ \varepsilon_{20} & \varepsilon_{21} & \varepsilon_{22} \end{bmatrix} \quad (4.2)$$

Considering the relation $\sum_{i=0}^2 \varepsilon_{ij} = 1 \forall j$, where $0 \leq \varepsilon_{ij} \leq 1$, it follows that the expected observation frequency of a genotype is

$$f_{\tilde{g}}(k) = \begin{cases} f_g(0) \varepsilon_{00} + f_g(1) \varepsilon_{01} + f_g(2) \varepsilon_{02} & \text{if } k = 0 \\ f_g(0) \varepsilon_{10} + f_g(1) \varepsilon_{11} + f_g(2) \varepsilon_{12} & \text{if } k = 1 \\ f_g(0) \varepsilon_{20} + f_g(1) \varepsilon_{21} + f_g(2) \varepsilon_{22} & \text{if } k = 2 \end{cases} \quad (4.3)$$

where $i = j$ indicates correct classification and $i \neq j$ misclassification of the true genotype; see Moskvina and Schmidt (2006).

Genotype penetrance models

Equations (4.2) and (4.3) provide a generic framework for the penetrance of genotypes and the calculation of genotype frequencies after error. Two penetrance models are presented below which provide formulations for the calculation of model parameters ε_{ij} .

Douglas *et al.* (2002) introduced a genotype-based model with parameters γ and η , denoting the probability of a homozygous genotype to be misclassified as a heterozygous genotype and vice-versa, respectively. The intuition behind this model is based on technical error in the polymerase chain reaction (PCR) amplification process, which is used in both genotyping and sequencing methods for the replication of DNA fragments. However, note that observed genotypes \tilde{g}_0 and \tilde{g}_2 both have equal probability to arise from misclassification of g_1 , and the probability that a homozygous genotype appears as the opposite homozygote, g_0 as \tilde{g}_2 or g_2 as \tilde{g}_0 , is zero.

As an alternative, misclassification of genotypes can be modelled as a consequence of errors that occur at random and independently in each of the two alleles. An explicit formulation of an allele-based model was proposed by Gordon *et al.* (2001), where ε_0 was defined as the probability that allele 0 (h_0) was observed as allele 1 (h_1), and ε_1 the

Table 4.1: Penetrance functions in genotype and allele-based error models. Error probability (or *penetrance*) is denoted by ϵ_{ij} , which is the probability of observing genotype i given the true genotype j . Two models are presented which are genotype-based and allele-based, respectively. In each model, equations refer to the probability that a true genotype, g_j , was observed as any of the possible genotypes, \tilde{g}_i , such that ϵ_{ij} is calculated from the corresponding row-by-column expression.

Model	Observed genotype	True genotype		
		g_0	g_1	g_2
Genotype-based¹	\tilde{g}_0	$1 - \gamma$	$\frac{1}{2}\eta$	0
	\tilde{g}_1	γ	$1 - \eta$	γ
	\tilde{g}_2	0	$\frac{1}{2}\eta$	$1 - \gamma$
Allele-based²	\tilde{g}_0	$(1 - \epsilon_0)^2$	$\epsilon_1(1 - \epsilon_0)$	ϵ_1^2
	\tilde{g}_1	$2\epsilon_0(1 - \epsilon_0)$	$\epsilon_0\epsilon_1 + (1 - \epsilon_0)(1 - \epsilon_1)$	$2\epsilon_1(1 - \epsilon_1)$
	\tilde{g}_2	ϵ_0^2	$\epsilon_0(1 - \epsilon_1)$	$(1 - \epsilon_1)^2$

¹ Douglas *et al.* (2002); $\gamma = P(\text{hom.} \rightarrow \text{het.})$, $\eta = P(\text{het.} \rightarrow \text{hom.})$

² Gordon *et al.* (2001); $\epsilon_0 = P(h_0 \rightarrow h_1)$, $\epsilon_1 = P(h_1 \rightarrow h_0)$

Table modified from Gordon *et al.* (2002), Table 2.

probability that h_1 was observed as h_0 . Penetrance functions for both models are given in Table 4.1 (this page); note that these are arranged as in error matrix \mathcal{E} in Equation (4.2).

In the following section, I estimated the genotype penetrance rates in different datasets. In each, error was computed from the proportions of correctly and incorrectly classified genotypes, such that error parameters were estimated for each model.

4.2 Generation of platform-specific genotype error profiles

Assessment of genotype accuracy requires the existence of an error-free “gold standard” dataset against which data generated on other platforms can be compared; provided that data were obtained on the same biological sample. In reality, however, the possibility of undetected genotype error cannot be excluded, but it can be reduced, for example, based on pedigree information and the laws of Mendelian inheritance. In the section below, I describe the dataset which I used as a reference for high-confidence genotype data. These were compared to several publicly available datasets generated using different genotyping and sequencing technologies, which included individuals also present in the reference dataset.

4.2.1 High-confidence genome data as benchmark for comparisons

The analysis was based on data from the Illumina Platinum Genomes Project (IPG),*, which comprises a 17-member, three-generation family of European ancestry; CEPH pedigree 1463.† This dataset has been generated using recent state-of-the-art sequencing technologies and methods for variant calling, where a total of 5.43 million variants were identified genome-wide (Eberle *et al.*, 2016); this included 4.73 million single-nucleotide polymorphisms (SNP). Individuals had been sequenced to a depth of 50x on Illumina HiSeq 2000, and variants were called in concordance to several variant calling methods. Notably, due to the availability of pedigree information, artefacts such as genotype errors had been excluded based on deviations from Mendelian inheritance. The dataset comprises 11 children from two parents, who themselves are the children of the four founders of the pedigree; see Figure 4.1. Thus, inheritance constraints were most informative for the two parents, labelled NA12877 and NA12878 (Coriell ID), which were additionally sequenced to 200x depth, and for which high-confidence variant calls were made available.

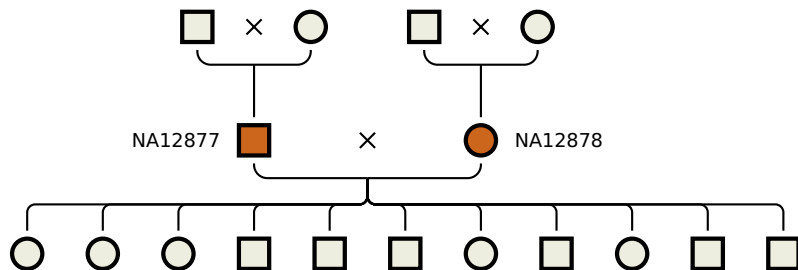


Figure 4.1: CEPH pedigree 1463. The pedigree of the family sequenced in the Illumina Platinum Genomes Project. Genotype data of individuals NA12877 and NA12878 (indicated) were used as reference against which data obtained on other genotyping or sequencing platforms were compared. Figure modified from Eberle *et al.* (2016), Figure 1.

Genotype (SNP) data from IPG for individuals NA12877 and NA12878 were used as reference or *truth* for comparison to concordant data obtained on other platforms.

* Illumina Platinum Genomes: <http://www.illumina.com/platinumgenomes/> [Date accessed: 2016-11-16]

† Centre d'Etude du Polymorphisme Humain (CEPH), Utah family pedigree 1463:

<https://catalog.coriell.org/0/Sections/Collections/NIGMS/CEPHFamiliesDetail.aspx?fam=1463>
[Date accessed: 2016-11-16]

Although the possibility of genotype error in IPG data cannot be excluded, it is assumed that error rates in NA12877 and NA12878 are sufficiently low to allow proportional estimation of genotype misclassification rates based on observations over thousands of variant sites.

Due to the imperfection of even high-standard sequencing technologies, not all chromosomal regions are equally accessible, which affects the power to determine variants in the calling process along the length of the sequence. The confidence of variant calls is derived from the depth of mapped sequence reads and quality scores. To maintain high levels of confidence in the data, accessibility masks provided by IPG were applied such that only sites in high-confidence regions were retained in the analysed datasets. This retained a sum of 3.407 million and 3.605 million SNPs for NA12877 and NA12878, respectively, across chromosomes 1–22.

4.2.2 Selection and preparation of datasets from different platforms

Because cell lines from CEPH pedigree 1463 are a well-characterised model system, either NA12877 or NA12878, or both, have been assessed in several studies. For example, CEPH pedigree 1463 was genotyped in the International HapMap Project, which was one of the first large-scale catalogues of human genetic variation (International HapMap Consortium, 2003; International HapMap Consortium *et al.*, 2007; International HapMap 3 Consortium *et al.*, 2010). Considering a more recent example, the 1000 Genomes Project provides data obtained on several platforms, including whole-genome sequencing (WGS) and high-density genotyping technologies (Altshuler *et al.*, 2010; 1000 Genomes Project Consortium *et al.*, 2012, 2015).

It must be noted that the process of acquiring data is substantially different for genotyping and sequencing methods. The established approach for genotyping is to use chip or array-based methods, which are designed to target, or “type” specific molecular markers at predetermined regions and require prior knowledge about mapped locations in the genome. On the other hand, sequencing determines the contiguous nucleotide sequence, either genome-wide or for a region of the genome. Sequence data are aligned

against a reference genome and further processed. Eventually, variants are “called” at nucleotides that differ from the reference at each position along the sequence.

Genotype error profiles were generated for both sequencing and genotyping data, which were taken from available resource data of the 1000 Genomes Project. The following *test* datasets were included:

- Low-coverage sequencing data from the final release of 1000 Genomes Project Phase III (**1000G**), generated on Illumina HiSeq 2000 and HiSeq 2500 platforms (2-4x), and consisting of 78 million SNPs in total.
- Genotyping data generated on Illumina HumanOmni2.5 BeadChip (**Omni2.5**) with 2.46 million SNPs.
- Genotyping data generated on Affymetrix Genome-Wide Human SNP Array 6.0 (**Affy6.0**) with 0.91 million SNPs.

To acknowledge differences arising from the variant calling and filtering process in sequencing data, two *1000G* profiles were created; one that included all variant sites (**1000G.A**), and one containing only sites within high-confidence regions (**1000G.B**). For the latter, the “strict” accessibility mask provided by 1000 Genomes Project Phase III was used (see 1000 Genomes Project Consortium *et al.*, 2015, supplementary information 9.2).^{*} Note that the sample of the final release dataset of *1000G* included NA12878, but not NA12877. The other two datasets, *Omni2.5* and *Affy6.0*, which were part of previous releases of the 1000 Genomes Project, included both NA12877 and NA12878.[†]

Misclassification of SNP genotypes was determined by comparison of each test dataset to the truth dataset, which was done for chromosomes 1–22. Genotype data were matched by chromosome and variant position (GRCh37/hg19). As a precaution, sites where reference or alternate nucleotides did not match between test and truth datasets were

* Accessible genome masks in 1000G:

http://ftp.1000genomes.ebi.ac.uk/vol1/ftp/release/20130502/supporting/accessible_genome_masks/
[Date accessed: 2016-11-27]

† High-density genotyping data, Omni2.5 and Affy6.0 in 1000 Genomes Project (1000G):

http://ftp.1000genomes.ebi.ac.uk/vol1/ftp/release/20130502/supporting/hd_genotype_chip/
[Date accessed: 2016-11-17]

Truth dataset				Test dataset			
Position	A ₀	A ₁	NA12878	Position	A ₀	A ₁	NA12878
:				4950	C	T	1 0
5001	A	C	1 0	5001	A	C	0 0
5012	G	T	0 1	5012	G	C	0 1
:				5233	A	C	0 1
5802	T	G	1 0	5667	A	G	1 1
:				5802	T	G	1 1
6003	C	A	0 1	5993	A	T	0 0
6100	A	C	0 1	6003	A	C	0 1
6133	G	A	1 1	6100	A	C	1 0
6139	A	C	1 1	6120	A	G	1 1
:				6137	G	C	0 1
6924	C	T	1 1	6139	A	C	1 1
7017	A	C	1 0	6224	T	G	0 0
:				6955	C	A	0 0
				7017	A	G	1 1
				8578	C	G	0 0

Matched dataset				
Position	A ₀	A ₁	True genotype	Observed genotype
5001	A	C	1	0
5802	T	G	1	2
6100	A	C	1	1
6137	G	C	0	1
6139	A	C	2	2
6955	C	A	0	0

█ accepted match
█ rejected due to inconsistent alleles
█ assumed from high-confidence region

Figure 4.2: Illustration of the matching process in the generation of error profiles. Variant data were reduced to SNPs and matched per chromosome by variant position and both alleles (A_0 and A_1) as recorded for either NA12877 or NA12878. Gaps shown in the truth dataset indicate the regions removed after filtering using the accessibility mask provided by IPG, such that only high confidence variant calls were retained. Note that the truth dataset did not contain SNPs homozygous for the reference allele, but which were assumed from high-confidence regions if present in the test dataset. This is indicated by left-pointing arrows.

removed, although only genotypes were compared. Note that IPG data did not contain variants called as being homozygous for the reference allele (g_0). Therefore, the following assumption was made. If the position of a variant site in a given test dataset was within high-confidence regions (using the IPG accessibility mask), but not reported in the truth dataset, the true state was assumed to be the g_0 type. This relies on the expectation that the high-confidence intervals comprised data which would have otherwise been reported as a different type. This matching process is illustrated in Figure 4.2 (this page).

At each matched site, the population frequency was assigned as recorded in the full sample of the final 1000 Genomes Project Phase III dataset, which contained 2,504 individuals from several continental populations worldwide. Sites for which no frequency

information was available were removed. Then, the retained genotypes in the matched datasets were used to measure the rate at which a true genotype (g_0 , g_1 , or g_2) was observed as the same or another genotype (\tilde{g}_0 , \tilde{g}_1 , or \tilde{g}_2). This was done to obtain estimates for the genotype penetrance parameters ε_{ij} in error matrix \mathcal{E} .

4.2.3 Penetrance of genotype error in sequencing and genotyping data

The total number of matched variant sites was 76.859 million in *1000G.A*, but of which 73.435 million ($\approx 96\%$) were assumed as homozygous reference genotypes from high-confidence regions in IPG. A lower amount was available in *1000G.B*, where 59.234 million genotypes were retained, but of which 56.739 million ($\approx 96\%$) were assumed. This large proportion of sites at which a true g_0 genotype was assumed may not come as a surprise, because there is a high chance that a considerable fraction of the variants present in either test dataset may fall within the lengths covered by high-confidence regions. However, because g_0 genotypes were removed in IPG data, it is a necessary assumption that those genotypes can be recovered from high-confidence regions. Otherwise, error rates could not be determined for g_0 genotypes. Overall, 0.079% of genotypes were misclassified in *1000G.A*, and 0.025% in *1000G.B*. If assumed g_0 genotypes are ignored, thus only considering true genotype classes $j \in \{1, 2\}$, overall error was increased; reaching 0.538% and 0.183% in *1000G.A* and *1000G.B*, respectively.

Due to the comparatively lower number of available sites in genotyping data (*Omni2.5* and *Affy6.0*), the matched **NA12877** and **NA12878** datasets were merged. Together, the total number of sites was 4.464 million in *Omni2.5* and 1.733 million in *Affy6.0*, and where 3.087 million ($\approx 69\%$) and 0.932 million ($\approx 54\%$) were assumed, respectively. The rate of misclassified genotypes in *Omni2.5* was 1.177 %, whereas in *Affy6.0* overall error was 1.164 %. In contrast to sequencing datasets, error rates decreased if g_0 was ignored, yielding 0.113 % and 0.106 % of misclassified genotypes in *Omni2.5* and *Affy6.0*, respectively.

In the following, the penetrance of genotypes was investigated in greater detail, for which matched sites from each true genotype class were considered; first, by exploring

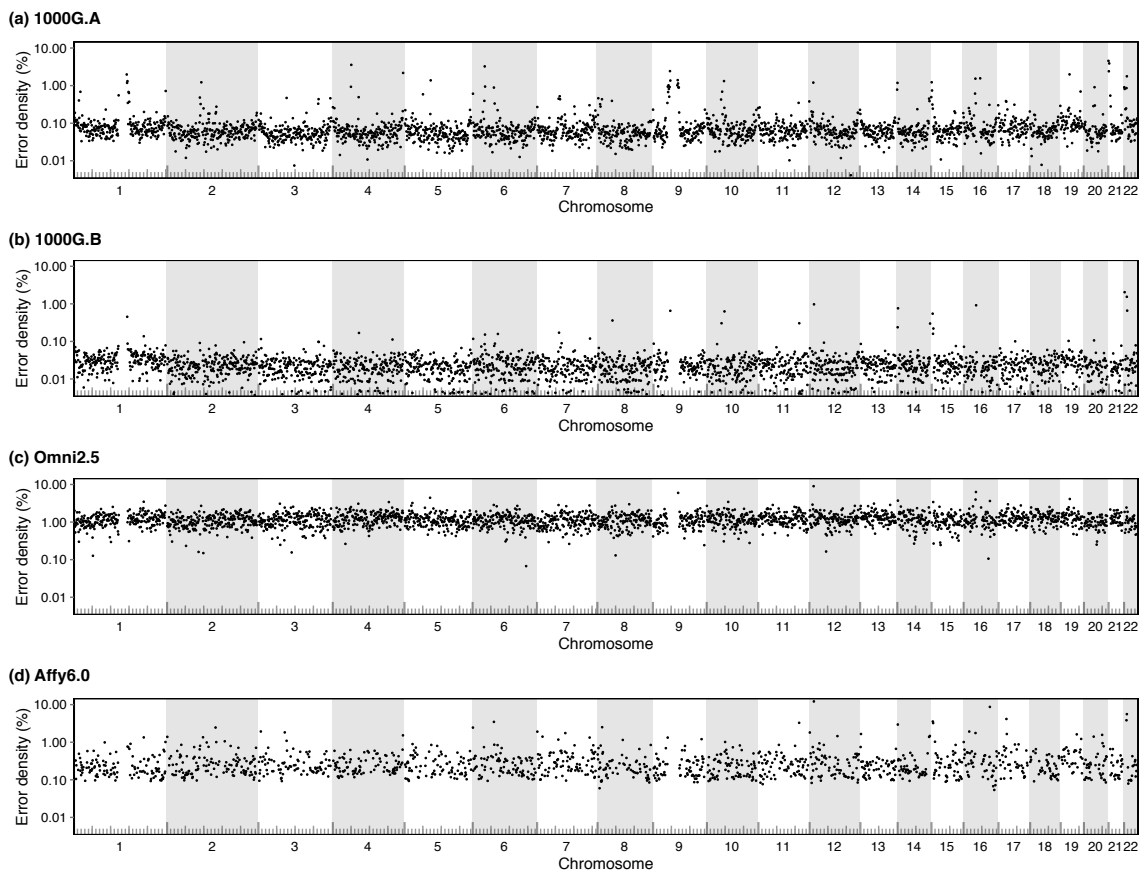


Figure 4.3: Positional genotype error density in sequencing and genotyping datasets. The density of misclassified genotypes was calculated along the length of each chromosome, which were divided into equally sized chunks of 1 Mb size. Error was calculated as the number of misclassified genotypes divided by the total number of genotypes per chunk; percent error shown on log scale. Chunks with less than 100 genotypes were removed. The ruler at the bottom edge of each panel shows physical distance per chromosome, where tick marks sit 10 Mb apart.

the distribution of error along the genome and, second, by true genotype class to obtain empirical penetrance estimates, which was then extended to generate frequency-dependent error profiles for each dataset.

Genotype accuracy by chromosomal region

Each chromosome was divided into 1 Mb long chunks to depict the rate of misclassified genotypes over the length of the genome; see Figure 4.3 (this page). Error densities were calculated by dividing the number of incorrect genotypes by the number of all genomes within each chunk, where chunks with less than 100 matched sites were removed.

The distribution of error in the *1000G.A* dataset was consistently low on average, but where error densities increased towards telomere regions and near centromeres, reaching error rates above 1% and occasionally above 5%. This is expected, because DNA in the telomeric and centromeric regions is highly repetitive and rich in GC content, which results in difficulties in the amplification process and makes sequence reads difficult to align to the genome. This pattern was less pronounced in *1000G.B*, as sites outside high-confidence regions were excluded, which resulted in a clear reduction of error along the genome. However, most chromosomes showed locally increased error rates, but where rates above 1% were rarely observed. Yet, the persistence of error hotspots indicates that not all low-confidence regions were identified from quality assessment of sequencing data.

In genotyping data, error rates showed less variability along the genome, *e.g.* in the *Omni2.5* dataset, but where error rates averaged above 1%, with a few regions of increased error above 5%. Although error was low on average in *Affy6.0*, the likewise lower number of sites resulted in sparse coverage, but which rarely increased above 1%. However, a few regions showed error rates near 10%.

Empirical estimation of genotype penetrance

Estimates for penetrance parameters in \mathcal{E} were derived by considering the proportional relation among observed types per true genotype class. For each true genotype class j , the number of genotypes observed in class i was divided by the total number in class j , which gives the empirical value of parameter ε_{ij} ; denoted by $\tilde{\varepsilon}_{ij}$. For an exact formulation, let n_{ij} be the number of observed \tilde{g}_i genotypes whose actual type belongs to the true genotype class j . The empirical value is calculated as

$$\tilde{\varepsilon}_{ij} = \frac{n_{ij}}{N_j} \quad \forall j \quad (4.4)$$

where $N_j = \sum_{i=0}^2 n_{ij}$, *i.e.* the number of all genotypes per true class j , such that $\tilde{\varepsilon}_{0j} + \tilde{\varepsilon}_{1j} + \tilde{\varepsilon}_{2j} = 1 \quad \forall j$. Results for each dataset are presented in Table 4.2 (next page).

In all four datasets, values for $\tilde{\varepsilon}_{ij}$ were highest when genotypes were classified correctly; *i.e.* $i = j$, the main diagonal in \mathcal{E} . Notably, $\tilde{\varepsilon}_{00}$ was highest in all sequencing

Table 4.2: Measured genotype penetrance in sequencing and genotyping data. Genotypes in each true genotype class (g_0 , g_1 , and g_2) were distinguished by observed genotype class (\tilde{g}_0 , \tilde{g}_1 , and \tilde{g}_2), to obtain empirical expectations for genotype penetrances ε_{ij} . Per dataset, proportions sum to 100% by column. The total number of genotypes counted per true class are given in the table.

Dataset	Observed genotype	True genotype		
		g_0	g_1	g_2
1000G.A	\tilde{g}_0	99.942%	0.550%	0.033%
	\tilde{g}_1	0.041%	99.281%	0.228%
	\tilde{g}_2	0.017%	0.169%	99.739%
	<i>Total</i>	73,435,064	2,076,115	1,347,647
1000G.B	\tilde{g}_0	99.982%	0.193%	0.003%
	\tilde{g}_1	0.013%	99.749%	0.077%
	\tilde{g}_2	0.005%	0.057%	99.920%
	<i>Total</i>	56,739,327	1,515,508	978,728
Omni2.5	\tilde{g}_0	98.349%	0.110%	0.011%
	\tilde{g}_1	0.869%	99.838%	0.021%
	\tilde{g}_2	0.782%	0.052%	99.968%
	<i>Total</i>	3,087,037	854,327	522,876
Affy6.0	\tilde{g}_0	99.786%	0.081%	0.004%
	\tilde{g}_1	0.116%	99.849%	0.040%
	\tilde{g}_2	0.098%	0.071%	99.956%
	<i>Total</i>	931,857	463,649	337,649

Note that true genotypes homozygous for the reference allele, g_0 , were not present in IPG and assumed from high-confidence regions if present in a given test dataset.

datasets, whereas ε_{22} was highest in genotyping datasets. In each dataset, true homozygous genotypes were more likely to be misclassified as heterozygotes than as the opposite homozygote, but the probability to observe opposite homozygotes was non-zero throughout. Misclassification of true heterozygous genotypes showed a preference towards genotypes that are homozygous for the reference allele; except in *Affy6.0* where misclassification rates were nearly equal for \tilde{g}_0 and \tilde{g}_2 . As formulated in Equation (4.3) on page 128, the observed genotype frequency is a function of the true allele frequency and the penetrance of genotypes. Hence, the frequency-dependent distribution of empirical genotype penetrance was assessed; see section below.

Frequency-dependent penetrance distribution

For each true genotype class, sites were pooled by their assigned population allele frequencies into 200 frequency bins of equal scope on linear scale; *i.e.* bins were separated in steps of 0.5%. Using Equation (4.4) on page 136, the proportions of observed genotypes were calculated in each bin, to obtain penetrance expectations across the frequency spectrum. Additionally, because it can be expected that N_j becomes small at lower genotype frequencies, bins where the number of genotypes dropped below a nominal threshold were marked to indicate less support for estimated penetrance values. Three nominal levels of support were distinguished;

Low support if $N_j < 100$,

Reduced support if $100 \leq N_j < 1000$,

High support if $N_j \geq 1000$.

For each dataset, the resulting penetrance distributions are shown in Figure 4.4 (next page). The most striking observation is the substantial loss of accuracy for g_0 genotypes at higher allele frequencies. For example in 1000G.A, all g_0 in the highest frequency bin were misclassified as \tilde{g}_2 , despite high support. The proportion of g_0 observed as \tilde{g}_1 was low throughout. This effect was seen in all four datasets, regardless of level of support, which was low for bins above 80% frequency in all datasets, except 1000G.A. However, this pattern should be interpreted with caution, as the set of true homozygous reference genotypes had to be assumed from high-confidence regions in IPG data.

A possible explanation for this observation may be seen in somatic mutations in the sampled biological material. Data for both NA12877 and NA12878 were generated from lymphoblastoid cell lines created from sampled B-Lymphocyte cells. For example, it has been shown that induced pluripotent stem cells may accumulate genetic modifications (Gore *et al.*, 2011). Although CEPH cell lines are often used as a renewable resource of

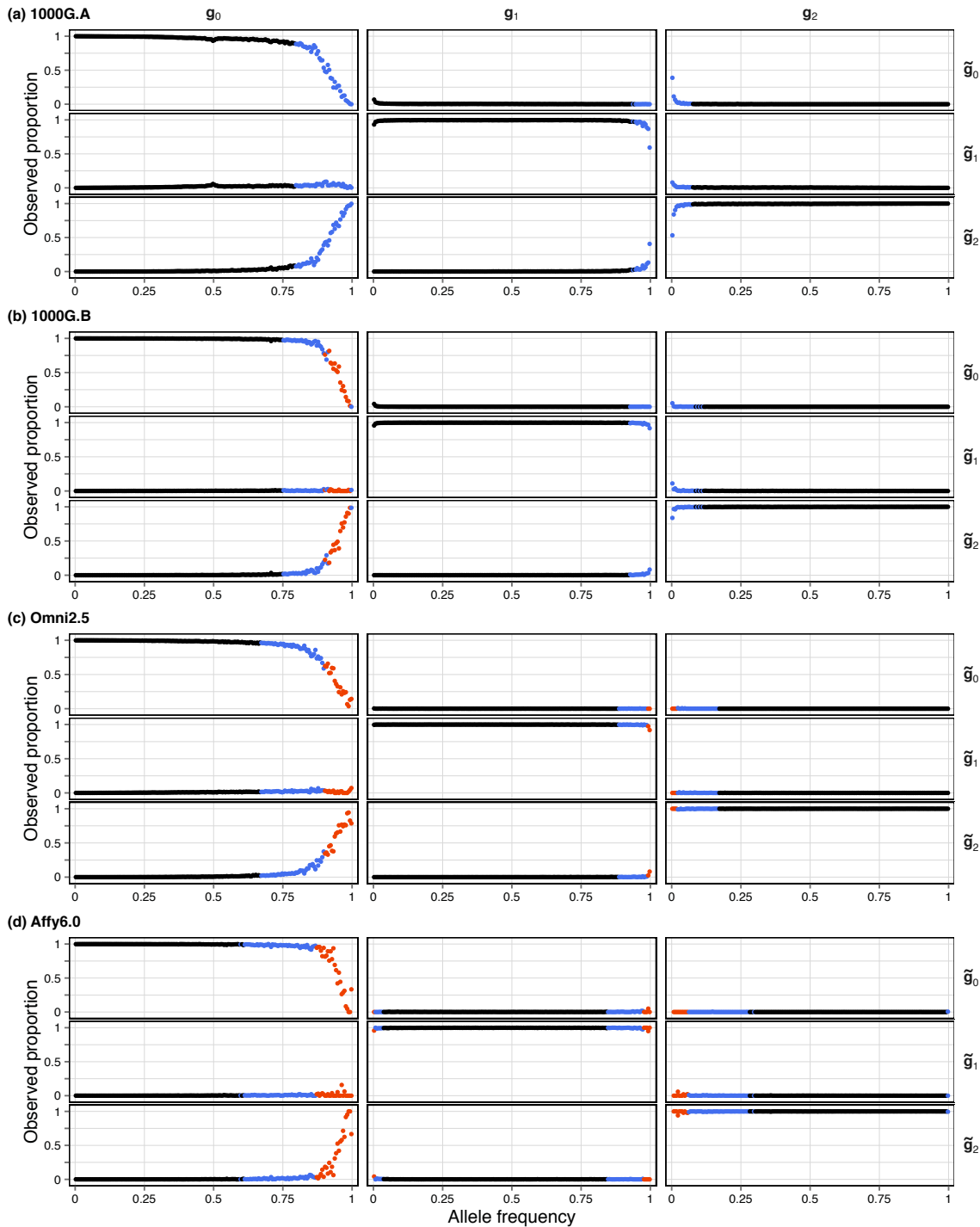


Figure 4.4: Frequency-dependent distribution of genotype penetrance in sequencing and genotyping data. For each true genotype class (columns), the fraction of g_j observed as \tilde{g}_i (rows) was calculated per allele frequency bin, to estimate the frequency-dependent distribution of genotype penetrance ε_{ij} . The set of matched genotypes per true genotype class was divided into 200 bins along the allele frequency spectrum. Allele frequency was assigned to each matched site in a given test dataset, taking the population frequency as recorded in the full sample of the 1000 Genomes Project phase 3 dataset (2,504 individuals). Colours indicate the number of genotypes per bin, n , distinguished at nominal thresholds $N_j < 100$ (red), $100 \leq N_j < 1000$ (blue), and $N_j \geq 1000$ (black). Note that true genotypes homozygous for the reference allele, g_0 , were not present in IPG and assumed from high-confidence regions if present in a given test dataset.

DNA, the possibility that cell lines undergo further genetic modifications may not be excluded. However, here, because the IPG protocol would have excluded sites that showed cell line artefacts, it is assumed that the genotypes had to be consistent with Mendelian laws. Regardless, note that salient patterns of genotype error were most apparent for the assumed subset of the data; *i.e.* at sites not actually contained in the set of reported genotypes. It is therefore possible that not all unobserved homozygous reference genotypes can be assumed from high-confidence regions when sites are only observed in other data.

In the opposite homozygote class, g_2 , observed distributions were mirrored, such that the loss of accuracy occurred at lower frequencies; yet, the proportion of misclassified genotypes was markedly lower. Under the allele-based error model, this asymmetry suggests that the probability of the alternate allele to appear as the reference allele was higher than in reverse direction, such that $\epsilon_0 < \epsilon_1$; see Table 4.1 (page 129).

The estimated error distributions were used to reproduce empirical error rates in simulated data. This was done to assess the effect of genotype misclassification on IBD detection, using the method proposed in Chapter 3; *i.e.* targeted IBD detection done thoroughly, or tidy. For comparison, an alternate IBD detection method was applied to the same data (Refined IBD in Beagle 4.1; Browning and Browning 2013).

4.3 Impact of genotype error on IBD detection

One of the genotype error profiles constructed in the previous section was used to induce realistic error patterns in simulated data. Among the four test datasets, both sequencing datasets were recorded with higher levels of support. Although *1000G.B* showed overall lower levels of genotype error, *1000G.A* can be seen as being more representative for data obtained in recent large-scale studies; hence, the integration of error was conducted according to the frequency-dependent penetrance distribution in the *1000G.A* profile. The process of error integration in simulated data is described below.

4.3.1 Integration of empirical error distributions in simulated data

The dataset simulated in Chapter 3 was re-used for integration of genotype error, so as to enable a direct comparison to previously obtained results after applying the same methodology for IBD detection; see Section 3.5.1 on page 101 for a description of the simulation process. Briefly, data were simulated using `msprime 0.4.0` (Kelleher *et al.*, 2016), with a sample size of $N = 2,500$ individuals (*i.e.* 5,000 haplotypes), resulting in 0.673 million variant sites over a length of 62.949 Mb (108.267 cM). Diploid individuals were formed by pairing haplotypes. From those, data were converted into genotypes, which were then phased, such that three datasets were generated (true haplotypes, phased haplotypes, and genotype data). The same process was followed here; however, genotype error was evoked on haplotype level before haplotype sequences were combined to form genotypes. By doing so, identically distributed proportions of error were present in both the haplotype and genotype datasets, after conversion of the former into the latter, as well as subsequent phasing.

Haplotypes were randomly assigned into fixed pairs which would later form the genotypes of individuals. Error was included by randomly replacing haplotype pairs dependent on the empirically determined misclassification rates per true genotype class j . This was done by selecting each variant site in turn and indexing each haplotype pair that would form genotype g_j before error. The index ensured that pairs would be drawn without replacement. Then, for each class j , indexed pairs were randomly drawn and assigned to each of the three observed genotype classes, in proportions equal to empirical penetrance rates, as determined for the given allele frequency of the currently selected site. Haplotype pairs were “mutated” according to their assigned class, such that they would form \tilde{g}_i after error.

These haplotype data were then converted into a corresponding genotype dataset, which was then phased using `SHAPEIT 2` (Delaneau *et al.*, 2008, 2013); see description in Section 3.5.2 (page 104). The three resulting datasets resembled the original datasets used in the evaluation of IBD inference presented in Chapter 3 (Section 3.6 on page 105), which

therefore allowed assessment in relation to the simulated genealogy and the underlying IBD structure of the sample, as well as a direct comparison to the results generated before error was included.

Accuracy analysis

The following briefly describes the analyses performed. Two IBD detection methods were applied to available data; the `tidy` method as proposed in Chapter 3 and the `Refined IBD` algorithm in `Beagle 4.1` (Browning and Browning, 2013). Recall that the `tidy` method is based on inference of recombination events in pairs of individuals to detect breakpoints distal to a given target site, which is enabled by the four-gamete test (FGT), which requires haplotype data, and the discordant genotype test (DGT), which requires genotype data; see Section 3.3 (page 89). Accuracy was measured in terms of the physical distance between breakpoints and focal target position at which IBD segments were identified; calculated using the squared Pearson correlation coefficient, r^2 , and the root mean squared logarithmic error (RMSLE) as defined in Equation (3.1) (page 104). Data were analysed in three approaches: (a) the FGT on the simulated haplotypes and (b) on phased haplotypes, and (c) the DGT on genotype data. Note that the `Refined IBD` algorithm can only be used with haplotype data and was therefore evaluated in (a) and (b). Again, f_k was used to denote the frequency of shared alleles, where k is the allele count in the sample.

4.3.2 Results

In presence of genotype error, the misclassification of alleles observed to be shared among individuals may pose a problem to the identification of haplotype sharing by descent, in particular for variants that are low in frequency or rare, see Figure 4.5 (next page); recall that the `tidy` method utilises rare allele sharing to identify regions of recent relatedness. Figure 4.5a indicates the rate at which genotype data appear at a frequency different to their true frequency due to genotype error; shown for variants below 5% allele frequency. The figure shows the change between true and observed allele count, depicted as the difference of the observed minus the true count. For example, 68.226 % of f_2 variants

remained at the same frequency, but this fraction decreased for alleles found at higher frequencies, e.g. 51.140 % for f_{10} and 28.771 % for f_{50} variants.

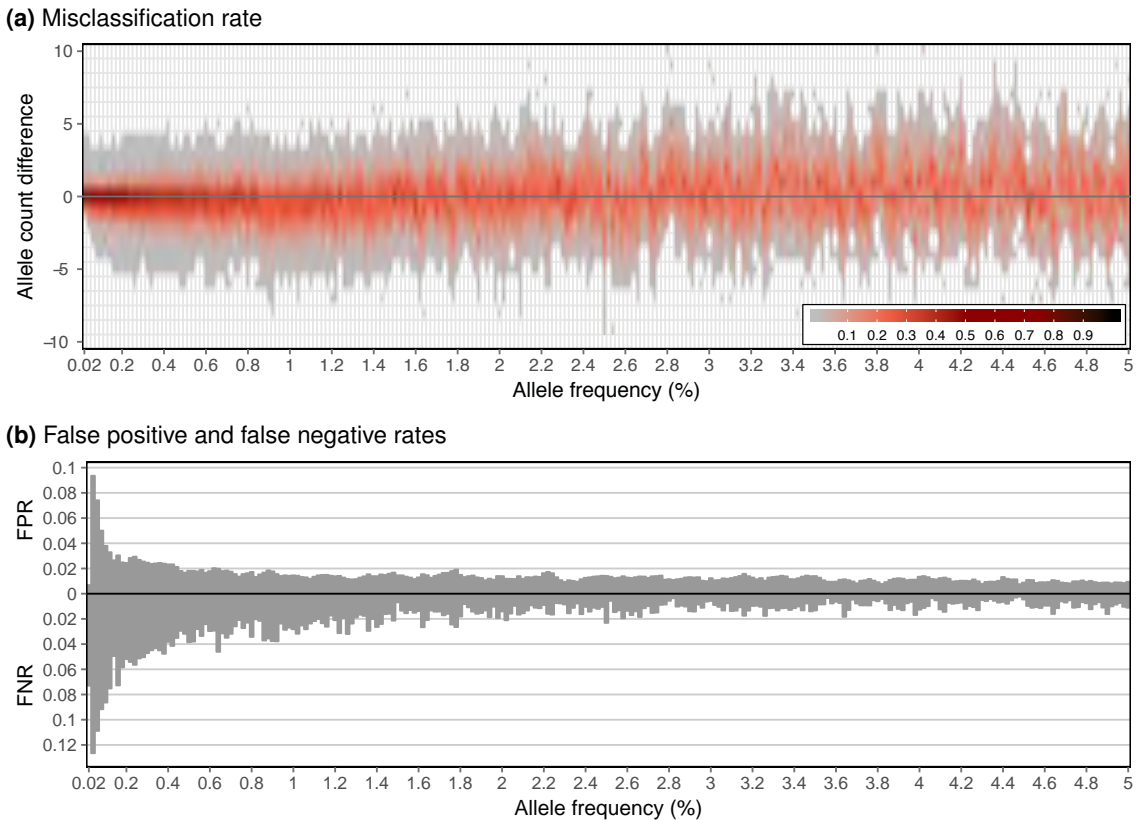


Figure 4.5: Misclassification of target sites in presence of genotype error. Simulated data were modified such that realistic distributions of genotype error were induced. Panel (a) indicates the rate at which alleles were observed at different frequencies after the inclusion of error. The proportion of misclassification is indicated by colour intensity. Panel (b) distinguishes alleles that were falsely observed (false positive) as well as alleles that were missed after the inclusion of error (false negatives).

For IBD detection using rare variants as target sites, this may not pose a problem if identified individuals indeed share a given allele. This is further explored in Figure 4.5b, where the false positive rate (FPR) indicates the proportion of alleles that were falsely identified due to g_0 or g_2 genotypes being observed as \tilde{g}_1 . Conversely, the false negative rate (FNR) indicates the proportion of shared alleles that were missed due to g_1 being observed as \tilde{g}_0 or \tilde{g}_2 . The risk for both types of error was greatest for f_2 variants, here observed at $FPR = 0.094$ and $FNR = 0.127$. On average, $FNR (0.009; \pm 0.665 \times 10^{-3} SE)$

was higher than FPR ($0.007 ; \pm 0.404 \times 10^{-3}$ SE), indicating that more shared alleles were missed than falsely observed.

IBD detection using *tidy*

The set of target sites included all f_k variants found at $k \in \{2, \dots, 25\}$ (*i.e.* alleles shared at frequency $\leq 0.5\%$). In total, 0.297 million SNPs were available in this frequency range, which represented 0.936 % of the targets previously identified before the inclusion of error. Note that sites were only considered if matched to the set of true IBD segments (as previously determined from simulation records). Hence, false positives were not considered in this analysis. The number of pairs sharing the focal alleles at available target sites was 10.362 million; *i.e.* the total number of IBD segments detected in each approach.

Duplicate segments were removed to retain unique segments after sorting segments by f_k , such that segments were associated with the presumably youngest shared allele within the detected breakpoint interval. Recall that the same IBD interval may be inferred from multiple focal alleles, as these are assumed to sit on the same shared haplotype. The proportion of uniquely identified segments was 48.035 % in Approach (a), 48.554 % in Approach (b), and 41.094 % in Approach (c), whereas 27.403 % were unique in the set of true IBD segments. These sets were then intersected to measure accuracy on the same set of unique IBD segments, which resulted in 2.824 million (27.256 %) per approach.

The proportion of breakpoints that were overestimated (in terms of the true distance between target position and actual recombination breakpoint) was 50.684 %, 49.691 %, and 63.864 % in (a), (b), and (c), respectively. Recall that before error was included, the vast majority of breakpoints ($> 95\%$) was overestimated in each approach. When the FGT was used, 49.221 % of breakpoints were underestimated and 0.095 % coincided with true breakpoints in Approach (a), which was similar in Approach (b) where 50.217 % and 0.092 % of breakpoints were underestimated and exact, respectively. When the DGT was used, 36.074 % of breakpoints were underestimated, but also only 0.061 % were exact.

Overall accuracy was low in all approaches; r^2 was 0.069, 0.072, and 0.089 in (a), (b), and (c), respectively, which was also reflected in corresponding high error scores (RMSLE),

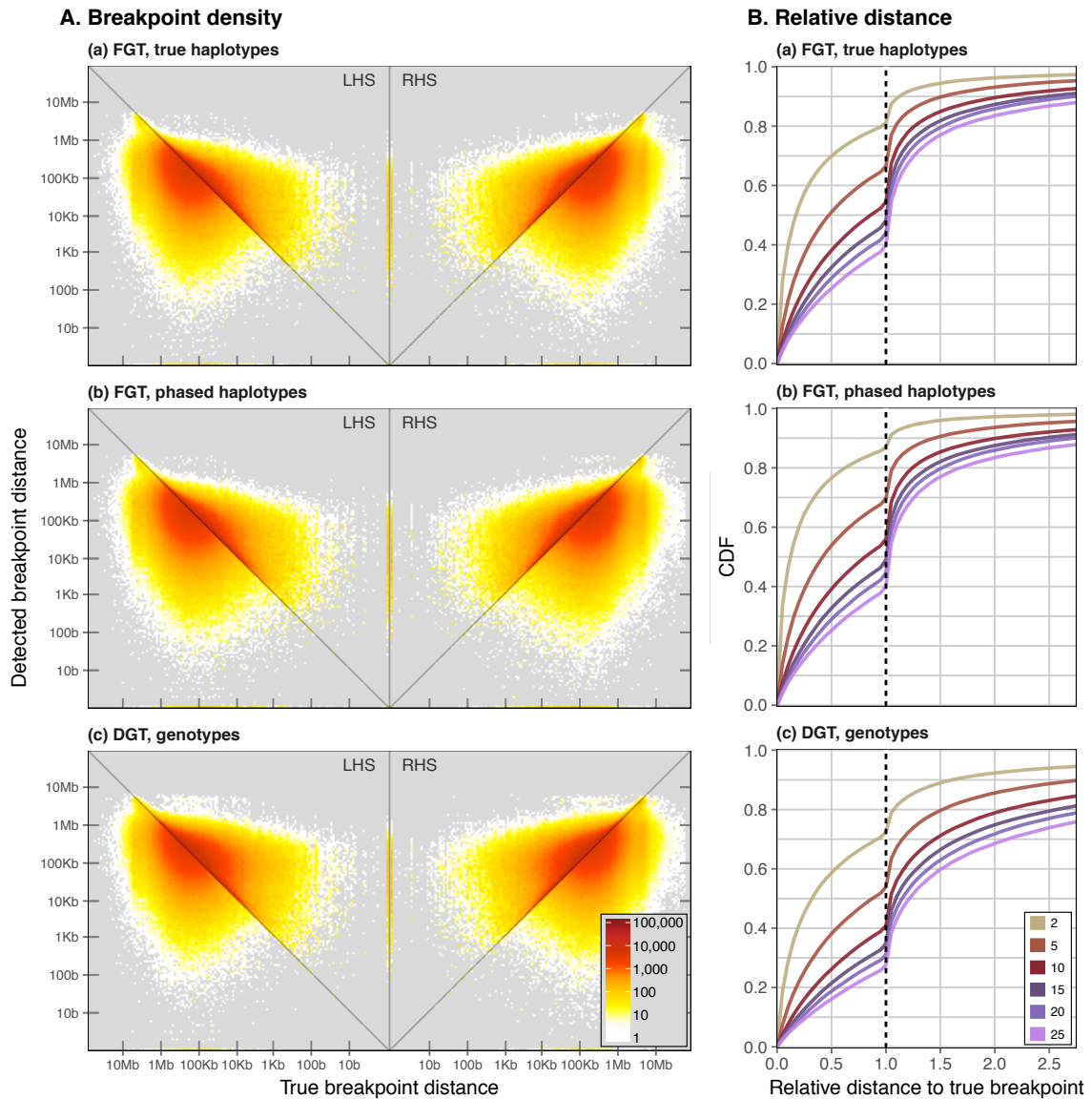


Figure 4.6: Accuracy of IBD detection using *tidy* after inclusion of genotype error. Simulated data after the inclusion of error was analysed using the FGT on true haplotypes (a), phased haplotypes (b), and the DGT on genotype data (c). Panel (A) shows the density of true and detected breakpoints in terms of the physical distance between each detected breakpoint and the corresponding focal site; shown separately for breakpoints detected on the left (LHS) and right-hand side (RHS) of a focal position. The number of detected and true breakpoints is indicated by colour intensity. Panel (B) shows the physical length in terms of the relative distance between a focal site and the detected breakpoint, \hat{d} , normalised by the distance to the true breakpoint, d ; i.e. relative distance was calculated as \hat{d}/d , such that < 1 indicates underestimation and > 1 overestimation of detected breakpoint distance. This is shown as the cumulative density per f_k variant, for $k \in \{2, 5, 10, 15, 20, 25\}$.

which were 0.714, 0.722, 0.694, respectively. For comparison, accuracy measured on the same set of segments, but without genotype error, was $r^2 > 0.85$ and RMSLE < 0.55 for each approach. When seen per f_k category, all three approaches consistently showed low correlation with true segment breakpoints ($r^2 < 0.2$) and a high magnitude of error (RMSLE > 0.6); see Table 4.4 on page 171, which is shown for comparison to results obtained using the HMM-based approach developed in the second part of this chapter.

To determine the lengths of IBD segments in each approach, boundary cases were removed to ensure that breakpoints were detected on both sides of each segment; 0.622 %, 0.621 %, and 0.924 % were removed in (a), (b), and (c), respectively, but which was noticeably lower compared to boundary cases removed in the set of true IBD segments (1.359 %). Again, sets were intersected, retaining 2.782 million (98.490 %) common segments across approaches.

Median physical length (and median genetic length) was relatively short when the FGT was used in Approaches (a) and (b), yielding 0.200 Mb (0.381 cM) and 0.198 Mb (0.378 cM), respectively. For the DGT, Approach (c), median length was closer to the true length; 0.332 Mb (0.635 cM) and 0.337 Mb (0.585 cM), respectively. However, for f_{25} variants, a clear difference was seen, where the median length was 0.311 Mb (0.527 cM) in (a) and 0.270 Mb (0.430 cM) in (b). But median length was likewise reduced in (c) compared to the true length; 0.543 Mb (0.926 cM) and 2.172 Mb (3.677 cM) respectively. This difference was not seen towards higher frequencies, e.g. at f_2 variants, reaching 0.171 Mb (0.354 cM), 0.173 Mb (0.354 cM), and 0.289 Mb (0.578 cM) in (a), (b), and (c), respectively, compared to 0.228 Mb (0.408 cM) in true segments.

The length distribution of true and detected IBD segments is shown in Figure 4.7 (next page). Note the similarity to Figure 3.13 on page 117, which was conducted using the FGT and DGT on data from 1000G (chromosome 20). This result suggests that the non-probabilistic IBD detection method implemented in tidy is likely to be biased in presence of genotype error. To illustrate the problem, consider the example given in Figure 4.8 (page 148), which highlights the effect of misclassified genotypes when seen in pairs of genotypes. The figure shows the underlying IBD structure for each pair of

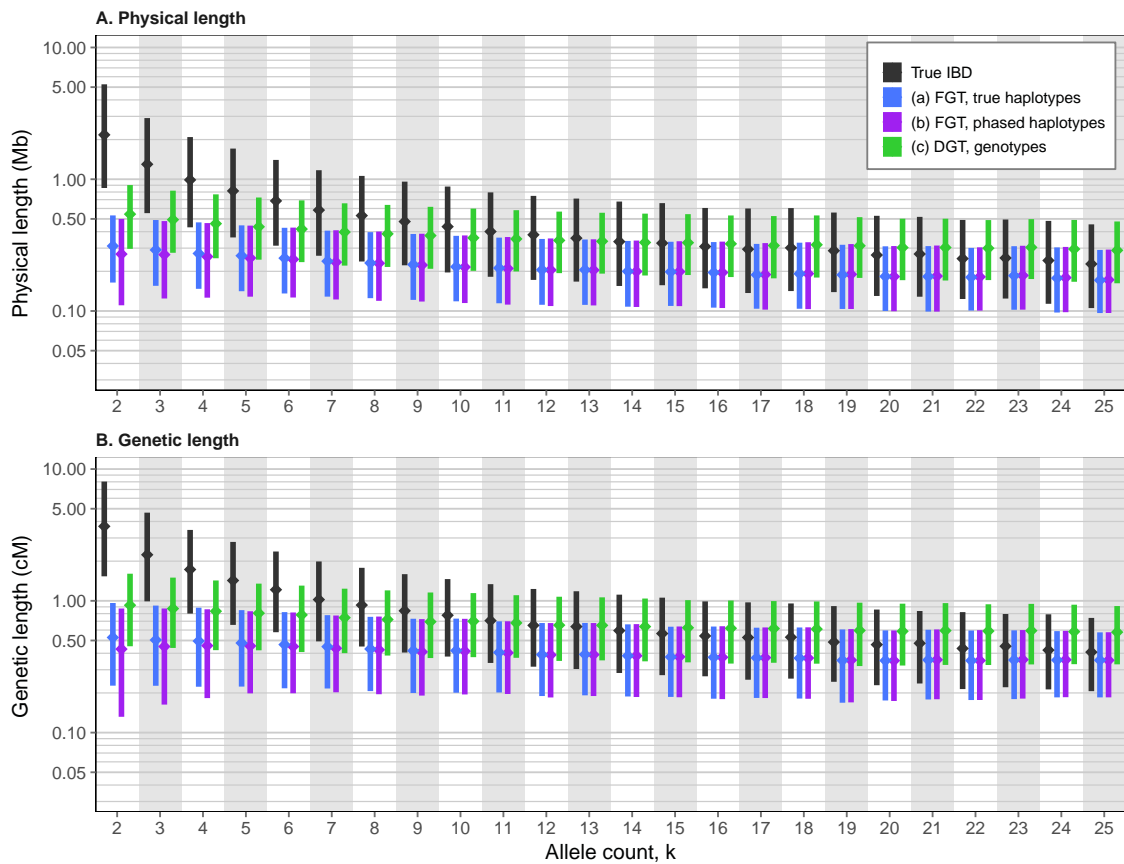


Figure 4.7: Length distribution of IBD segments using *tidy* after inclusion of genotype error. The distribution of physical (A) and genetic (B) segment length is shown by allele count (f_k category). Results are shown for three approaches; (a) FGT on true haplotypes, (b) FGT on phased haplotypes, and (c) DGT on genotype data. Corresponding true lengths are shown in for comparison. Bottom and top of each bar indicate 1st and 3rd quartiles, respectively, between which the median (2nd quartile) is marked (*diamonds*).

chromosomes in two individuals sharing a randomly picked rare allele. In Figure 4.8a, the positions of breakpoints detected using the FGT and DGT are indicated as found along the whole chromosome before the inclusion of error. In contrast, Figure 4.8b shows the same analysis but after genotype error was included. Since the innermost breakpoint interval delimits the inferred IBD segment, it can be expected that even small amounts of genotype error are likely to result in underestimation of IBD length.

IBD detection using *Refined IBD* in *Beagle 4.1*

The probabilistic *Refined IBD* method for IBD detection was applied to the data after the inclusion of error. The analysis was conducted on true and phased haplotype data,

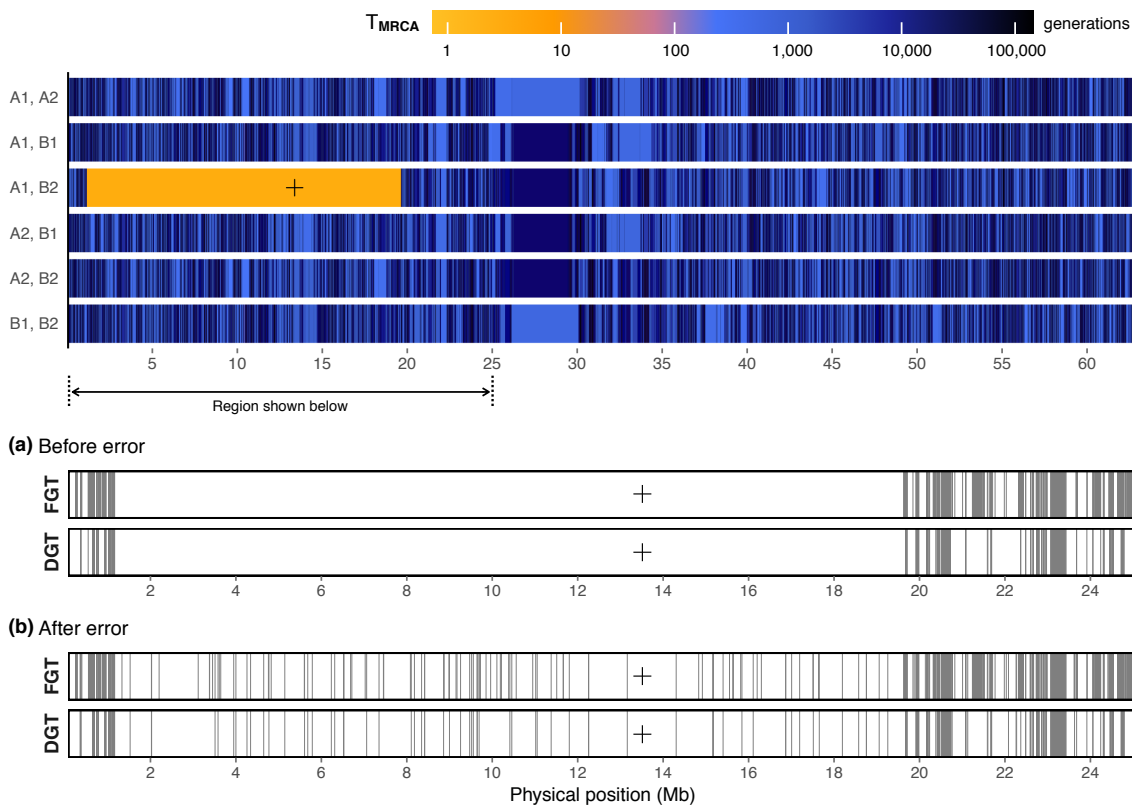


Figure 4.8: Example of the effect of genotype error on IBD detection. Using simulated data, the underlying IBD structure for all six possible pairs of the four chromosomes in two individuals is shown (*top*); determined from simulation records. The pair of individuals was randomly selected among those sharing a rare allele which identified recent haplotype sharing by descent. The figure shows the “mosaic” of IBD segments along the sequence of the simulated chromosome; distinguished by the time to the most recent common ancestor (T_{MRCA}). The focal shared allele is indicated at the pair of chromosomes sharing that allele (*cross*). Data were compared before (a) and after (b) the inclusion of empirically determined genotype error. In each dataset, the FGT and DGT were used to detect breakpoints to the left and right-hand side of the target position. The first breakpoints to each side delimit the detected IBD interval; here, all breakpoint following first detection are shown. Data were simulated using `msprime` (see Section 3.5.1 on page 101).

Approaches (a) and (b), which returned 12.195 million and 12,397,767 million segment, respectively. Because IBD is not reported in reference to a particular target site, as is done in `tidy`, the set of true IBD segments available was matched to inferred IBD segments if target positions fell within detected intervals of reported segments; see Section 3.6 (page 110). As a result, only 1.496 million segments were matched in (a) and 0.374 million in (b), of which 76.743 % and 76.512 % were unique, respectively. Data were not intersected due to the small number of segments retained in each approach.

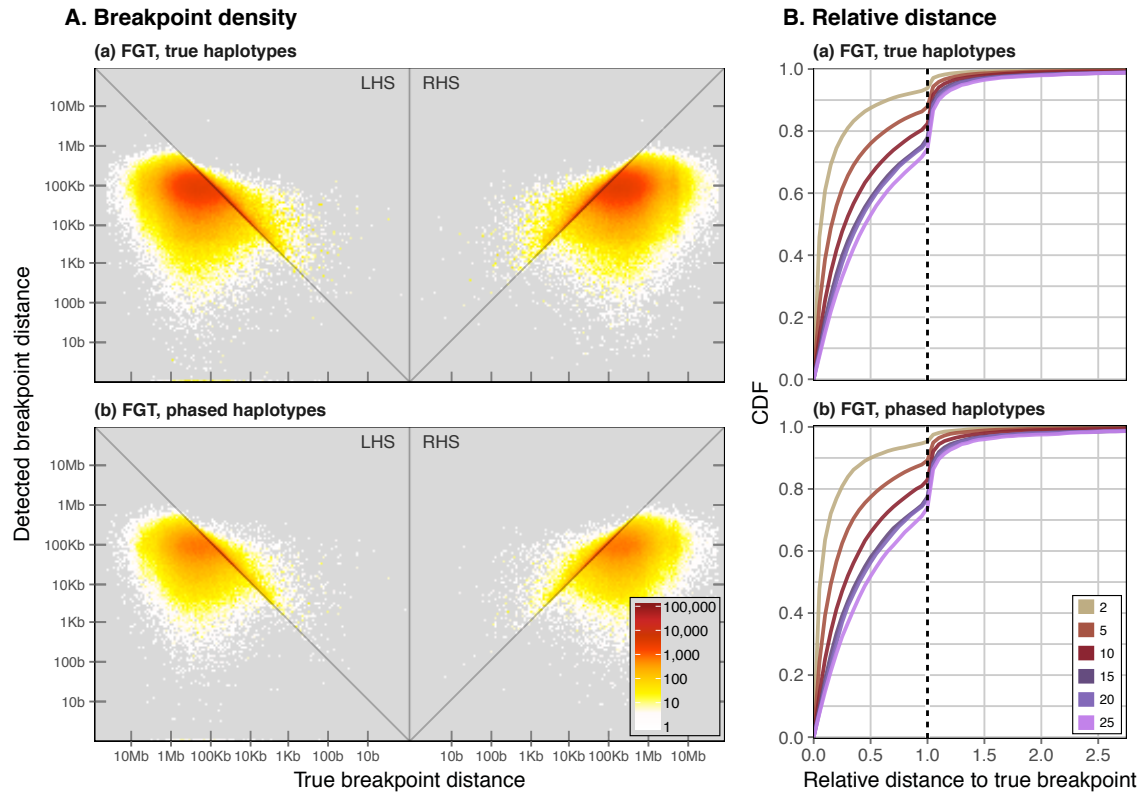


Figure 4.9: Accuracy of IBD detection using *Refined IBD* after inclusion of genotype error. Panel (A) shows the density of true and detected breakpoints; Panel (B) shows the physical length in terms of the relative distance between a focal site and the detected breakpoint. See Figure 4.6 (page 145) for a detailed description.

In Approach (a), 20.362 % of the breakpoints detected were underestimated, 79.527 % overestimated, and 0.111 % coincided with true IBD breakpoints. This distribution was similar in Approach (b), yielding 20.262 %, 79.642 %, and 0.096 %, respectively. This is also seen in Figure 4.9 (this page), where IBD breakpoints tend to be underestimated. In comparison to IBD detected using *tidy*, overall accuracy was lower, with $r^2 = 0.017126$ in (a) and $r^2 = 0.017756$ in (b), and the magnitude of error more elevated, at RMSLE = 0.8496714 and RMSLE = 0.8441583, respectively.

After removing boundary cases, 0.271 % and 0.287 % in (a) and (b) respectively, median length was further reduced in comparison to *tidy*, which was observed at 0.129 Mb (0.253 cM) in (a) and 0.131 Mb (0.256 cM) in (b); true length was noticeably longer with 0.496 Mb (0.883 cM); note that this was the median length found for the same set of segments as matched in (a). The distribution of true and detected IBD length is given in Figure 4.10 (next page).

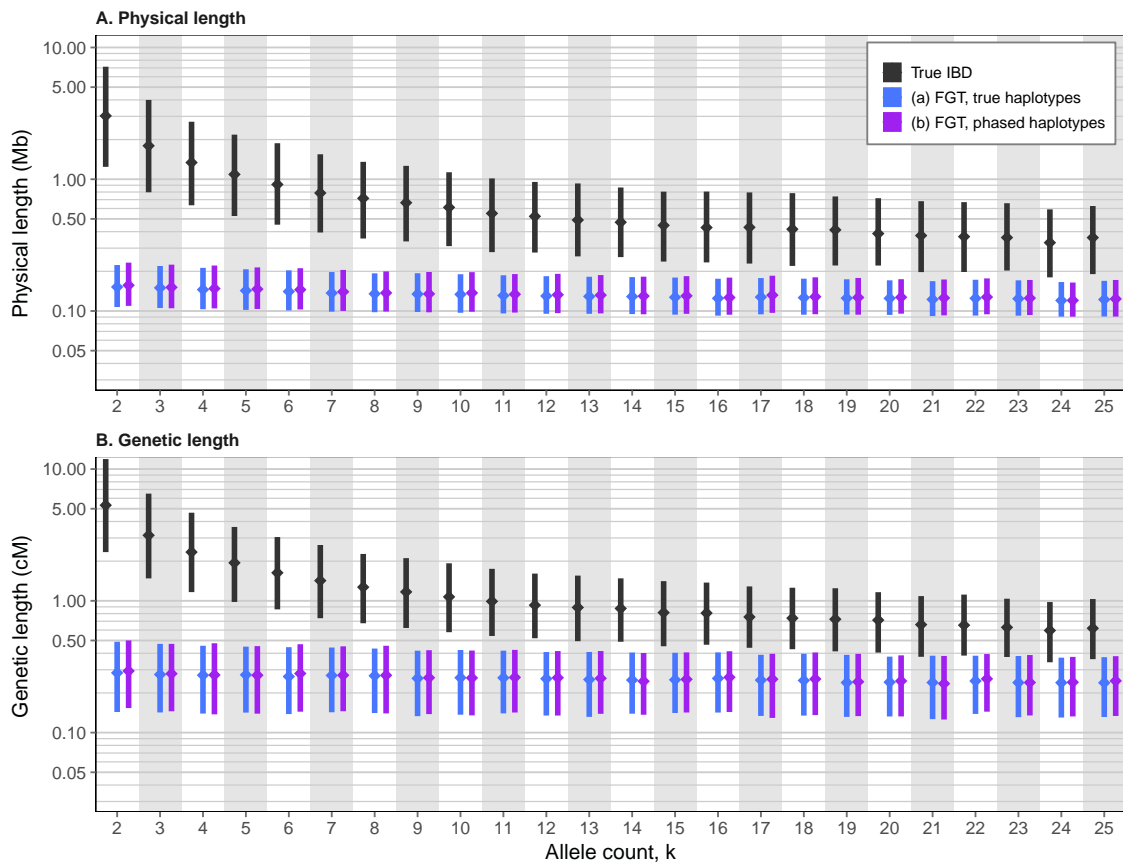


Figure 4.10: IBD length detected using *Refined IBD* after inclusion of genotype error. The distribution of physical (A) and genetic (B) segment length is shown by allele count (f_k category). Results were obtained using *Refined IBD* in Beagle 4.1, on true and phased haplotype data. Bottom and top of each bar indicate 1st and 3rd quartiles, respectively, between which the median (2nd quartile) is marked (*diamonds*).

4.3.3 Discussion

While it cannot be avoided that some rare variants are irretrievably missed, because of genotype error resulting in false negatives. The underlying IBD segment may still be retrieved from other, nearby rare variants that identify the same shared haplotype in a given pair of individuals. However, due to false positive genotypes, the assumption that haplotype sharing by descent can be identified from rare variants may turn out to be problematic in practise. For example, strict quality control may exclude certain candidate target sites, but which requires further consideration in future work.

The general insight gained from this analysis is that the impact of genotype error on the detection of IBD segments is not negligible. Given the example in shown Figure 4.8

(page 148), it is suggested that even small amounts of misclassified genotypes may disrupt the IBD detection process and is likely to result in a general underestimation of the underlying IBD length. Therefore, the analysis has provided sufficient evidence to justify the development of a more extensive method for IBD detection. In particular, I used the estimated proportions of genotype penetrance to extend the targeted IBD detection approach such that the distribution of genotype pairs can be modelled for inference under IBD and non-IBD; this is presented in the following section.

4.4 A Hidden Markov Model for IBD inference

Despite the high accuracy of the FGT and DGT to detect shared haplotype segments in simulated data, it has emerged from the previous analysis that a non-probabilistic approach may be less suitable for IBD detection if the presence of genotype error cannot be excluded. Because it cannot be assumed that real data is obtained without error, it would therefore be beneficial to devise a fully probabilistic implementation of the IBD detection algorithm, in which observed error rates can be included. Here, this was attempted by constructing a Hidden Markov Model (HMM).

An HMM is a probabilistic sequence model which is widely used in applications of machine learning, likelihood computation, and sequence classification; see Rabiner (1989). In general, a sequence of observations is assumed to be the product of an unobserved Markov process, in which a sequence of underlying, but “hidden” states determines the probability of observing the data. Each state is characterised by a probability distribution over a finite set of possible observations. Although the sequence of hidden states is not known, it can be inferred from the sequence of observations.

A wide range of statistical methods for genetic data analysis are driven by HMM-based algorithms. Notable examples are methods used for genotype phasing and imputation; e.g. SHAPEIT (Delaneau *et al.*, 2011), EAGLE (Loh *et al.*, 2016a,b), and IMPUTE (Howie *et al.*, 2009, 2011b), to name a few. It is worth to mention that many of the commonly employed methods (above included) are based on the influential Li and Stephens (2003) model, which

for a set of observed genotypes reconstructs the unobserved haplotypes as “imperfect mosaics” of known haplotypes in reference data. While this model provides the ability to solve several kinds of problems in statistical genetics, such as phasing or imputation, it is less applicable for inference of IBD.

A variety of different approaches exist for the inference of IBD segments, many of which have not fully adopted the view that observed genetic variation is the product of a genealogical process which, in principle, can be modelled as a Markov process. An example of a rule-based method is the widely implemented GERMLINE algorithm (Gusev *et al.*, 2009), which is part of the often employed Refined IBD method (Browning and Browning, 2013). This algorithm was designed as an efficient search method through which IBD status is inferred from imperfectly matched haplotypes in large sample data. In contrast, model-based implementations for inference of IBD in samples of seemingly unrelated individuals all rely on HMMs; see review by Thompson (2013). The first to assume that IBD arises from a Markov process (without specifically stating it) was Stam (1980), who extended the idea of recombination breakpoints (or “junctions”) introduced by Fisher (1949, 1954) to describe the probability distribution of the fraction of the genome that is identical by descent in a finite and randomly mating population. Later, Leutenegger *et al.* (2003) developed an HMM for inference of inbreeding coefficients from genotype data in individuals of unknown parental relationships. Equivalent models were implemented to detect IBD in phased haplotypes (*e.g.* Purcell *et al.*, 2007; Browning, 2008).

Here, a different IBD-model is proposed which is used for inference of recombination breakpoints around a target position in pairs of individuals. The approach is conceptually similar to the previously presented method for deterministic IBD detection using the FGT or DGT, see Section 3.3 (page 89), but where the detection of breakpoint intervals (*i.e.* the physical start and end points of IBD segments) are determined through sequence classification in the HMM. Notably, the presented method relies on genotype information and does not require haplotype data; it is therefore not affected by phasing error.

The following section describes the algorithm through which target sites in sample data are analysed. This is followed by a detailed description of the model, which includes the

theoretical expectations under the assumption of no error. Then, the model is extended to include the empirically determined distributions of genotype error for each of the possible genotype pairs. In the end, the presented HMM-based method for IBD detection was evaluated in the same way as was done for the FGT or DGT in the previous chapter.

4.4.1 The algorithm for probabilistic IBD inference

Consider a sample of N diploid individuals and M variant markers; in particular, SNP data are assumed. To determine the IBD structure around a focal variant site, let this site be denoted by $i \in \{1, \dots, M\}$ and its physical position by b_i . All individuals sharing the derived (alternate) allele at this site are identified and analysed in a pairwise fashion. In each pair, the breakpoint interval, $[b_L, b_R]$, is inferred, where b_L and b_R are the chromosomal positions of the most likely recombination breakpoints to the left and right-hand side of the focal position, respectively.

As before, it is convenient to refer to a target site by its frequency in the sample. Thus, f_k variants are distinguished where k is the number of allele copies in the sample, and where $k \geq 2$ must be satisfied. Note that only those individuals are considered that are heterozygous for the focal allele, which is why the subset of identified individuals may be smaller than k , but not smaller than 2 in order to form at least one pair. Also, as described in Chapter 3 (Section 3.2, page 87), rare variants are presumed to derive from relatively recent mutations and are therefore more likely to identify long IBD tracts, as recombination had less time to break down the length of the shared haplotype identity. Hence, this method is primarily intended for inference of IBD around rare variants, where $k \ll 2N$. However, note that in principle any $f_{\geq 2}$ variant can be analysed using the presented method.

The input data analysed in the HMM is the paired sequence of genotypes in both individuals sharing the focal allele. The observation sequence is composed of the paired genotypes along the chromosomes of the two individuals sharing the focal allele; as such, haplotype data is not required. Since each individual contributes a genotype at a single locus, g_k (where $k \in \{0, 1, 2\}$), to form a genotype pair, denoted by $g_{k_1 k_2}$, it follows that

there are six possible observation states; g_{00} , g_{01} , g_{02} , g_{11} , g_{12} , and g_{22} , where the order of genotypes in a pair is ignored. Further, two states are distinguished in which genotype pairs can be observed; either the two individuals share a haplotype identical by descent, or they do not, which is denoted by *ibd* and *non*, respectively. These correspond to the hidden states that are assumed to generate the data.

For a given focal site and a pair of individuals sharing the allele, the sequence of genotype pairs is analysed as two independent Markov chains; *i.e.* one to the left and one to the right-hand side of the focal variant, with the focal site at the start of both chains. For convenience, the index j is defined relative to i and follows the direction of moving from b_i to the last site in the observed sequence, either b_1 to the left or b_M to the right-hand site. Hence, $j = 0$ at the focal site and $j = m$ at the last site, where m is the number of markers to the left or right-handed sequence relative to the focal site (excluding the focal site).

Since the focal allele is assumed to identify the shared haplotype in *ibd*, the first site along the sequence that is classified in the *non* state is taken as a breakpoint, on both sides, such that the inferred IBD segment is enclosed in $[b_L, b_R]$. By definition, the smallest detectable interval around a focal variant at site i is therefore $[b_{i-1}, b_{i+1}]$. If the chain remains in *ibd* until the end of the sequence, the last position is taken as a breakpoint (referred to as a *boundary case*).

The following section describes the underlying model through which each site in the observation sequence is classified into either *ibd* or *non*.

4.4.2 Description of the model

Identity by descent is modelled as a first-order Markov process in a two-state HMM, where the observed genotypes in a pair of diploid individuals are emitted from either the *ibd* or the *non* state. Given the Markov property, the following assumptions are made. First, the probability of the hidden state at site j only depends on the previous hidden state at site $j - 1$. Second, the probability of observing a particular genotype pair at site j only depends on the hidden state at site j and not on any of the other states.

Let the hidden state space be denoted by $S = \{ibd, non\}$, and the set of observable states by $G = \{g_{00}, g_{01}, g_{02}, g_{11}, g_{12}, g_{22}\}$. The model itself is denoted by

$$\lambda = \{\Psi, \xi, \pi\} \quad (4.5)$$

where Ψ is a matrix of state *transition* probabilities and ξ corresponds to a set of vectors which store the probability of observing each of the possible genotype pairs; *i.e.* the *emission* probabilities in each state. The model is illustrated in Figure 4.11 (this page), where the probabilities of emission from *ibd* are denoted by $\delta_{k_1 k_2}$ and from *non* by $\eta_{k_1 k_2}$. The *initial* probabilities of being in either state at the start of the sequence is given by π .

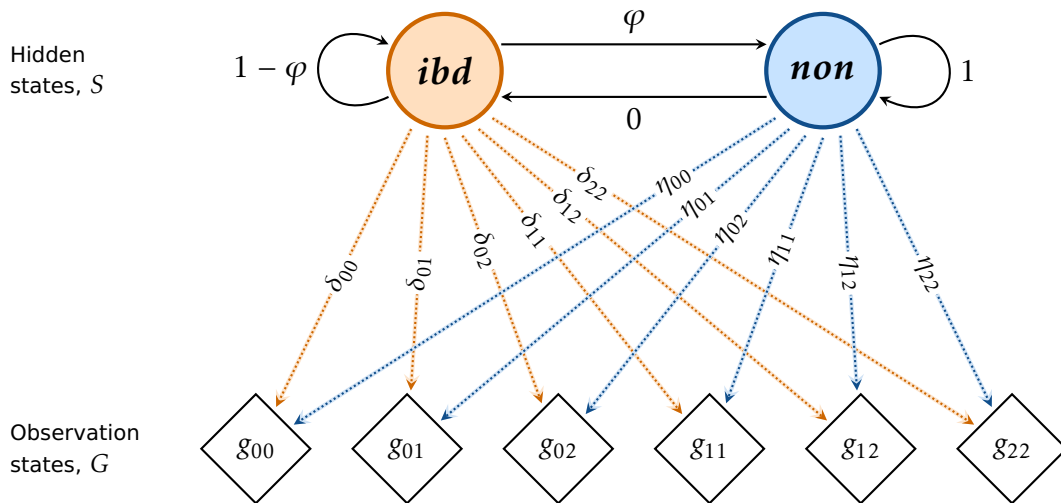


Figure 4.11: Illustration of the Hidden Markov Model for IBD inference. Two hidden states are assumed to generate the observations in a Markov process; *ibd* and *non*. Transitions from each state into any state are indicated by *solid* lines. The probability of transition from *ibd* to *non* is denoted by φ , and from *non* to *ibd* is set to zero; hence, once the Markov chain proceeds into the *non* state it cannot transition back into *ibd*. This is because the IBD process is modelled such that only the innermost IBD segment is inferred, relative to the focal position which sits at the start of the sequence. The input sequence consists of genotype data from a pair of individuals, resulting in six possible observation states; denoted by $g_{k_1 k_2}$, where $k_1, k_2 \in \{0, 1, 2\}$. The probabilities of emitting each possible genotype pair given each hidden state are denoted by $\delta_{k_1 k_2}$ and $\eta_{k_1 k_2}$ for *ibd* and *non*, respectively; indicated by the *dotted* lines. The direction of arrows indicates conditional dependence; *i.e.* the transition from one hidden state into another state, or emission of a genotype pair while being in *ibd* or *non*.

The parameters of the model are defined in two ways. First, theoretical expectations for transition, emission, and initial probabilities are derived; see next page, page 158,

and page 162, respectively. Then, in Section 4.4.3 (page 162), the model is extended to include genotype error from empirical data as obtained in Section 4.2 (page 129).

Transition probabilities

Given the two hidden states, the transition matrix Ψ is defined as a 2×2 matrix which stores the probabilities of moving from one state into another state, as well as the probabilities of remaining in the same state; see below.

$$\Psi_{j,k} = \begin{bmatrix} \psi_{j,k}(ibd | ibd) & \psi_{j,k}(non | ibd) \\ \psi_{j,k}(ibd | non) & \psi_{j,k}(non | non) \end{bmatrix} \quad (4.6)$$

In particular, the probability of transition from *ibd* to *non*, denoted by $\varphi = \psi_{j,k}(non | ibd)$, is modelled dependent on the rate of recombination between consecutive sites, in order to estimate the probability of the distance to the first recombination breakpoint along the sequence. Two variables are considered; the genetic distance between the current and the previous position, and the expected T_{MRCA} of the focal f_k variant.

Let the genetic distance between positions b_j and b_{j-1} be denoted by r_j , measured in *Morgan*, which is the product of the recombination rate per site per generation, ρ , and the physical distance of the sequence interval in basepairs. If the recombination rate varies over the length of the chromosome, that is if a genetic map is available, r_j can be obtained from map distances. Note that the model considers $2r_j$ to account for recombination occurring along either of the two lineages considered. In a population genetics setting, time is scaled in units of $2N_e$ generations for a sample of diploid individuals, where N_e is the diploid effective population size of the population under consideration. Thus, the scaled rate of recombination within the interval between consecutive sites and per time unit is equal to $4N_e r_j$.

The expected age of a focal allele, measured in scaled time units and denoted by τ_k , can be estimated directly from its frequency. For example, Kimura and Ota (1973) formulated the expected age of a selectively neutral allele in a stationary population, which was derived in a diffusion process;

$$\frac{-2x}{1-x} \log(x) \quad (4.7)$$

where x corresponds to the allele frequency in the sample; here calculated as $x = k/2N$. In context of the coalescent, Griffiths and Tavaré (1998) derived the following formulation for the T_{MRCA} under a constant population size and the assumption of the infinite sites model (Kimura, 1969; Watterson, 1975);

$$2 \binom{n-1}{b}^{-1} \sum_{j=2}^n \binom{n-j}{b-1} \frac{n-j+1}{n(j-1)} \quad (4.8)$$

where b is the number of allele copies in the sample and n the haploid sample size; here corresponding to k and $2N$, respectively. Both formulations result in approximately equal distributions for allelic age. Here, Equation (4.7) was used for computation of τ_k due to its simplicity.

The distance to a recombination event follows the geometrical distribution if measured in discrete generations. However, it can be approximated on a continuous time scale using the exponential distribution in the limit as N_e tends to infinity; that is, generally, if population size is sufficiently large (see Hein *et al.*, 2004). Thus, the probability of transition from *ibd* to *non* can be expressed as follows.

$$\varphi = \psi_{j,k}(\text{non} \mid \text{ibd}) = 1 - \left(1 - \frac{4N_e r_j}{2N_e}\right)^{2N_e \tau_k} \approx 1 - e^{-2N_e r_j \tau_k} \quad (4.9)$$

The probability of remaining in *ibd* is therefore $\psi_{j,k}(\text{ibd} \mid \text{ibd}) = 1 - \varphi$, because the probability distribution over possible states for a given state must sum to 1. For illustration, Figure 4.12 (next page) shows the probability of transition from *ibd* dependent on the genetic distance between consecutive sites along the sequence and the allele frequency of the focal allele.

Note that the model relies on the assumption that the probability of transition from *non* to *ibd* has zero probability; *i.e.*

$$\psi_{j,k}(\text{ibd} \mid \text{non}) = 0, \quad \psi_{j,k}(\text{non} \mid \text{non}) = 1.$$

Therefore, the architecture of the model is not fully connected or *ergodic*. This is typically referred to as a left-to-right or *Bakis* HMM, as transitions can only proceed in one direction.

Once the *ibd* state has been left, the chain remains in the *non* state such that only the innermost IBD segment is inferred, relative to the focal site at the start of the sequence.

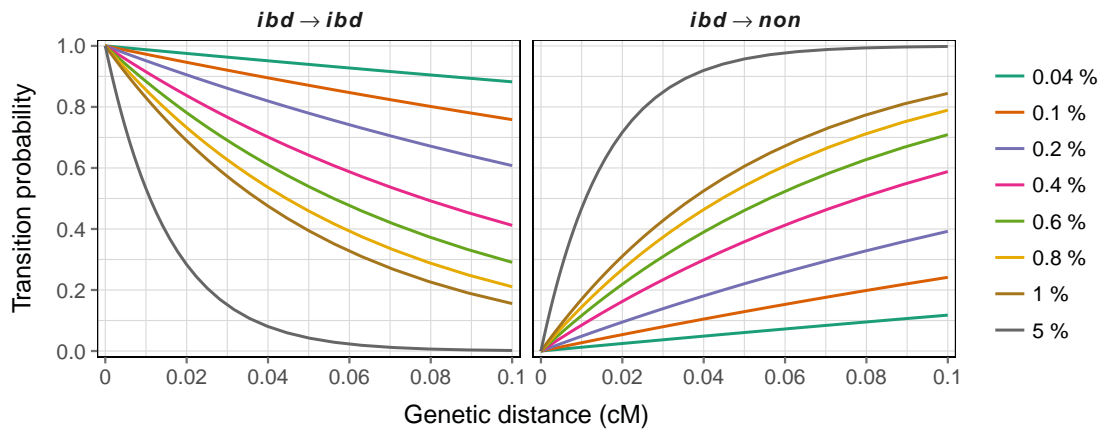


Figure 4.12: Probability distribution of transition dependent on IBD. The probability of transition was modelled dependent on the genetic distance between a particular site and the previous site and the expected age of the focal allele. The frequency of the focal allele determines its expected age, which is shown for different frequency values. An effective population size of $N_e = 10,000$ was specified. For example, the frequency of a f_2 allele in a sample of 5,000 haplotypes is equal to 0.04% (green line).

It is necessary to note that a pair of diploid individuals may share more than one recent haplotype identical by descent; *e.g.* along the same two chromosomes or any pair of the four chromosomes. Here, this possibility was not considered due to the variant-centric approach of the method. As such, inference is dependent on the properties of a given f_k variant. The focal allele serves as an indicator for haplotype sharing and transition probabilities are computed dependent on the expected time of the focal mutation event, given the allele frequency at the focal site. For example, by allowing transitions from the *non* state back to *ibd*, the IBD inference would be biased as the length of distinctly inferred segments (*i.e.* for other genealogies along the chromosome) would be conditioned on the expected age of the focal allele.

Emission probabilities

The model parameter ξ stores the emission or *output* probability vectors of the hidden states. Each vector is a probability distribution over the possible observation states

with sum 1. The probability to observe a given genotype pair in *ibd* is written as $P_{ibd}(k_1, k_2) = \delta_{k_1 k_2}$ and in *non* as $P_{non}(k_1, k_2) = \eta_{k_1 k_2}$, where $k_1, k_2 \in \{0, 1, 2\}$. In the following, the emission probabilities for the possible genotype pairs are derived from their expected proportions in both hidden states. First, the *non* state is considered. Then, the formulations are extended to derive expectations in the *ibd* state.

Emission probabilities in the *non* state. Consider $m = 2$ genotypes observed in a pair of individuals at a single locus. Each genotype can be observed in one of three possible states, which are again indexed by $k \in \{0, 1, 2\}$, where k counts the alternate alleles that compose a genotype. Similarly, let α_k count the genotypes, g_k , that compose a genotype pair, $g_{k_1 k_2}$. For example, the pair g_{00} carries two g_0 genotypes, such that $\alpha_0 = 2$, $\alpha_1 = 0$, and $\alpha_2 = 0$, the pair g_{01} carries one g_0 and one g_1 genotype, such that $\alpha_0 = 1$, $\alpha_1 = 1$, and $\alpha_2 = 0$, and so on. Expected pairwise frequencies follow a multinomial distribution. Recall that $f_g(k) = \binom{n}{k} p^{n-k} q^k$ where $n = 2$, as given in Equation (4.1) on page 127. In the general case, that is in a randomly mating population, genotypes in both individuals are assumed to be independent. It follows that the expected frequency of a given genotype pair is the joint probability of the expected genotype frequencies involved; expressed below.

$$f_{pair}(\alpha_0, \alpha_1, \alpha_2) = \binom{m}{\alpha_0, \alpha_1, \alpha_2} \prod_{k=0}^m f_g(k)^{\alpha_k} \quad (4.10)$$

The order of genotypes in a pair is ignored; e.g. the pairs g_{01} and g_{10} are identical. In the following, the order $k_1 \leq k_2$ is preferred in notation. Note that the expected frequency for a pair of diploid genotypes cannot be represented by assuming a ploidy level of $n = 4$ in Equation (4.1). For example, the frequency of genotype pair g_{02} is different to the frequency of g_{11} , despite the same number of allelic types that compose the genotypes in the pair, but which would be equal if Equation (4.1) is used. It is therefore necessary to distinguish genotypes by individual.

The probability of observing a given genotype pair in *non* can now be modelled using Equation (4.10). However, for convenience, the following function is used, which

dependents only on k_1 and k_2 ;

$$\eta_{k_1 k_2} = \begin{cases} p^4 & \text{if } k_1 = 0, k_2 = 0 \\ 4p^3q & \text{if } k_1 = 0, k_2 = 1 \\ 2p^2q^2 & \text{if } k_1 = 0, k_2 = 2 \\ 4p^2q^2 & \text{if } k_1 = 1, k_2 = 1 \\ 4pq^3 & \text{if } k_1 = 1, k_2 = 2 \\ q^4 & \text{if } k_1 = 2, k_2 = 2 \end{cases} \quad (4.11)$$

where p and $q = 1 - p$ correspond to the frequency of the reference and alternate allele, respectively, in the sample at the current site in the sequence.

Emission probabilities in the *ibd* state. The formulations derived in the previous paragraph assume a pair of unrelated individuals; that is if alleles are independently distributed in the population and haplotype occurrence in individuals is random. This assumption does not hold if the two individuals share a haplotype identical by descent. Because it is not straightforward to arrive at a similarly simple expression as given in Equation (4.10), it is more convenient to construct a function similar to Equation (4.11). For this purpose see Table 4.3 (this page), which provides a more intuitive representation

Table 4.3: Punnett squares of genotype pair partitions under non-IBD and IBD. Allele frequency contributions are itemised for each possible pair of genotypes. Rows and columns correspond to alleles in ordered haplotype combinations, (h_{c_1}, h_{c_2}) , with $f_h(c = 0) = p$ and $f_h(c = 1) = q$, where $c \in \{0, 1\}$. Expressions in cells are the product of these combinations. Genotype pairs are formed by summing over the cells corresponding to the two genotypes in a given pair (labelled on the right in each row and at the bottom of each column). Panel (a) shows the partitions of expected frequencies for genotype pairs that do not share a haplotype (*i.e.* *non* state). In Panel (b), if a haplotype is identical by descent (*i.e.* *ibd* state), one of the haplotypes is marked as shared; denoted by an asterisk, h_k^* . Note that a haplotype can only be shared, if contained in both row-by-column combinations, or frequencies are zero otherwise.

(a) *non*

	h_0, h_0	h_0, h_1	h_1, h_0	h_1, h_1	
h_0, h_0	p^4	p^3q	p^3q	p^2q^2	
h_0, h_1	p^3q	p^2q^2	p^2q^2	pq^3	
h_1, h_0	p^3q	p^2q^2	p^2q^2	pq^3	
h_1, h_1	p^2q^2	pq^3	pq^3	q^4	
	g_0	g_1	g_1	g_2	
	g_0	g_1	g_1	g_2	

(b) *ibd*

	h_0, h_0^*	h_0, h_1^*	h_1, h_0^*	h_1, h_1^*	
g_0	h_0, h_0^*				
g_1	h_0, h_1^*				
g_1	h_1, h_0^*				
g_2	h_1, h_1^*				
	g_0	g_1	g_1	g_2	
	g_0	g_1	g_1	g_2	

of the composition of haplotypes in each genotype pair, where the allelic contribution in each pair is illustrated for both *non* and *ibd*.

If a haplotype is shared by both individuals, some combinations of alleles cannot be observed under *ibd*; see Table 4.3b. For example, if individual 1 carries the genotype g_0 and individual 2 carries g_2 at a given site in the sequence, the observation of the genotype pair g_{02} has zero probability in *ibd*, as the possibility to share a haplotype is precluded. The probability of any given genotype pair in *ibd* can be expressed using the function below.

$$\delta_{k_1 k_2} = \begin{cases} p^3 & \text{if } k_1 = 0, k_2 = 0 \\ 2p^2q & \text{if } k_1 = 0, k_2 = 1 \\ 0 & \text{if } k_1 = 0, k_2 = 2 \\ p^2q + pq^2 & \text{if } k_1 = 1, k_2 = 1 \\ 2pq^2 & \text{if } k_1 = 1, k_2 = 2 \\ q^3 & \text{if } k_1 = 2, k_2 = 2 \end{cases} \quad (4.12)$$

In summary, the resulting probability distribution of emission of each possible genotype pair is shown in Figure 4.13 (this page), under both *non* and *ibd*.

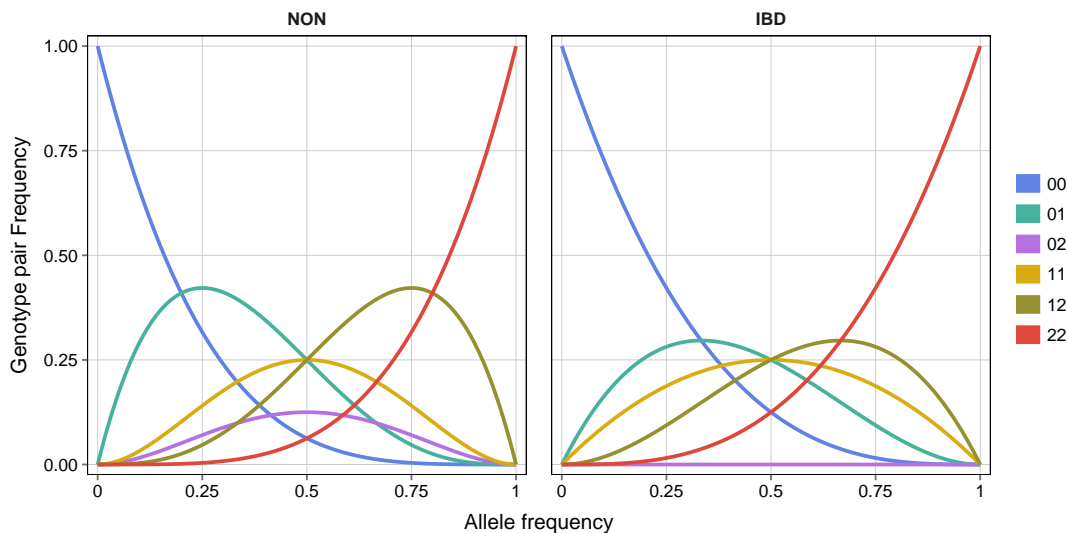


Figure 4.13: Expected frequency distribution of genotype pairs under non-IBD and IBD. Proportions were calculated using Equation (4.11) and Equation (4.12) in both hidden states, *non* and *ibd*, respectively. Colours distinguish the six possible genotype pairs, given by g_{k_1, k_2} , as indicated.

Initial state probabilities

The model parameter π stores the probabilities of being in either state at the start of the sequence. Since the focal allele is used to identify the shared haplotype in a pair of individuals, the probability of being in *ibd* is assumed to be $\pi_{ibd} = 1$, such that $\pi_{non} = 0$.

4.4.3 Integration of empirically determined genotype error rates

In this section, the data generated in Section 4.2 (page 129) were used to inform the model parameters in the HMM. This was done, first, to validate the expectations formulated in the previous sections, second, to explore variation instigated by genotype error and, third, to obtain empirical parameter values for emission and initial state probabilities in *non* and *ibd*.

Note that the effect of genotype error on state transition probabilities is not considered. The computation of transition probabilities include the expected age of a focal allele dependent on its frequency, which could be biased in presence of genotype error, but where deviations are expected to be negligibly small if sample size is large. In particular, the expected age represents an approximation to the T_{MRCA} of the focal allele, which is more likely to be affected by unconsidered demographic parameters such as selection, migration, growth, and population structure, as well as sampling bias.

Two datasets were available from previous analyses; the original genotype matrix as produced from simulated haplotypes, denoted by \mathcal{D} , and a corresponding, but modified genotype matrix, \mathcal{D}^* , in which the empirical, frequency-dependent proportions of genotype error were included in Section 4.3 (page 140). These datasets allowed analysis *before* and *after* error, respectively. Data consisted of $n = 2,500$ individuals and $m = 672,847$ variant sites.

Empirical emission probabilities

Information about IBD status was available through coalescent records obtained in the simulation. By performing scans over all coalescent trees, true IBD intervals were

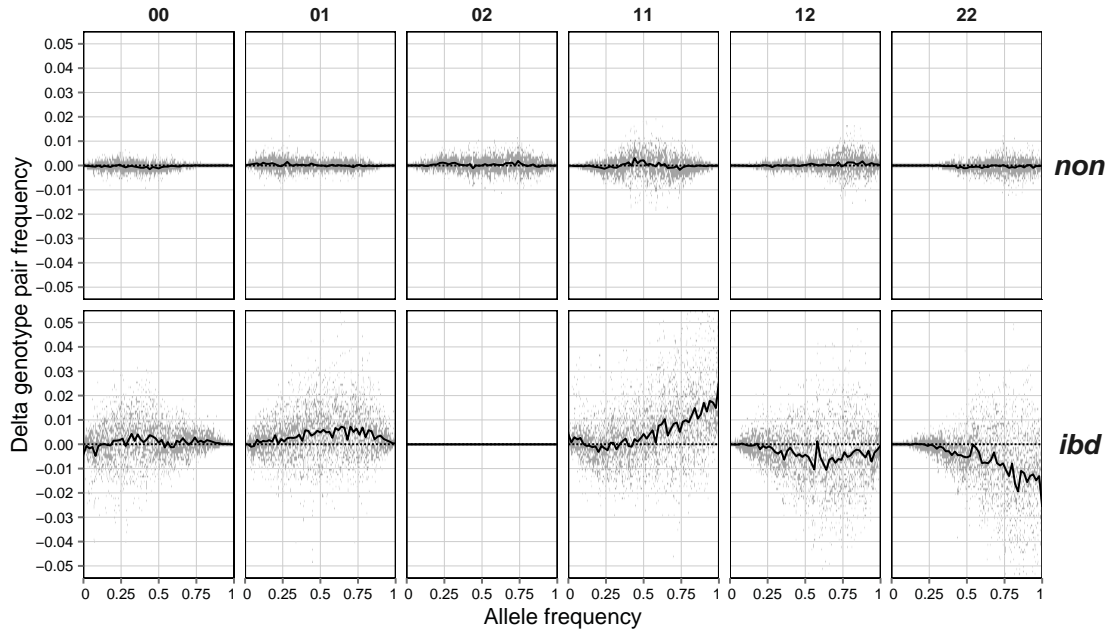
determined for f_k variants at $k \in \{2, \dots, 25\}$ (allele frequency between 0.04% and 0.5%). In total, a set of 11.598 million true IBD segments was compiled. Each segment was recorded as a tuple of two breakpoint coordinates (b_L and b_R to the left and right-hand side of a focal variant, respectively) and two individuals, *i.e.* indices for the pair of individuals who share a haplotype identical by descent within the breakpoint interval.

The set of compiled IBD segments was used to determine the empirical probability to observe a given genotype pair in *ibd*. This was done by randomly sampling 500,000 segments with replacement, for which genotype data were extracted in $[b_{L+1}, b_{R-1}]$ for the two individuals. Note that breakpoint sites were excluded to ensure IBD over the entire region. For each segment, extracted genotype sequences were paired and collected by their coordinates along the length of the chromosome. In a similar fashion, the empirical probability of observing genotype pairs in *non* was determined using the same sample of segments, but where the two individuals sharing the IBD segment were ignored. Instead, the two individuals were drawn at random from the subset of samples which did not share a haplotype IBD within $[b_{L+1}, b_{R-1}]$. After sampling was complete, genotype pairs were aggregated by allele frequency per site, such that the frequency-dependent proportion of each genotype pair could be calculated in *ibd* and *non*. In both cases, genotype data were taken separately from \mathcal{D} and \mathcal{D}^* to measure proportions before and after error.

The resulting probability distributions after error were used to define the empirical emission model in *ibd* and *non*, again denoted by $\delta_{k_1 k_2}$ and $\eta_{k_1 k_2}$, respectively. For illustration, deviations from expected genotype pair proportions are shown in Figure 4.14 (next page), both before error (4.14a) and after error (4.14b). Expectations in *ibd* and *non* were calculated according to Equations (4.11) and (4.12) on page 160 and page 161, respectively. Differences were calculated by subtracting empirical from expected genotype pair proportions, which was done in discrete allele frequency units, but also averaged per frequency bin, in 100 bins of equal size across the allele frequency spectrum.

Before error, empirical and expected proportions in *non* were equal on average, in each of the six possible genotype pairs. The variability along the allele frequency spectrum was negligibly small, where deviations per frequency unit were seen as stochastic noise

(a) Before genotype error



(b) After genotype error

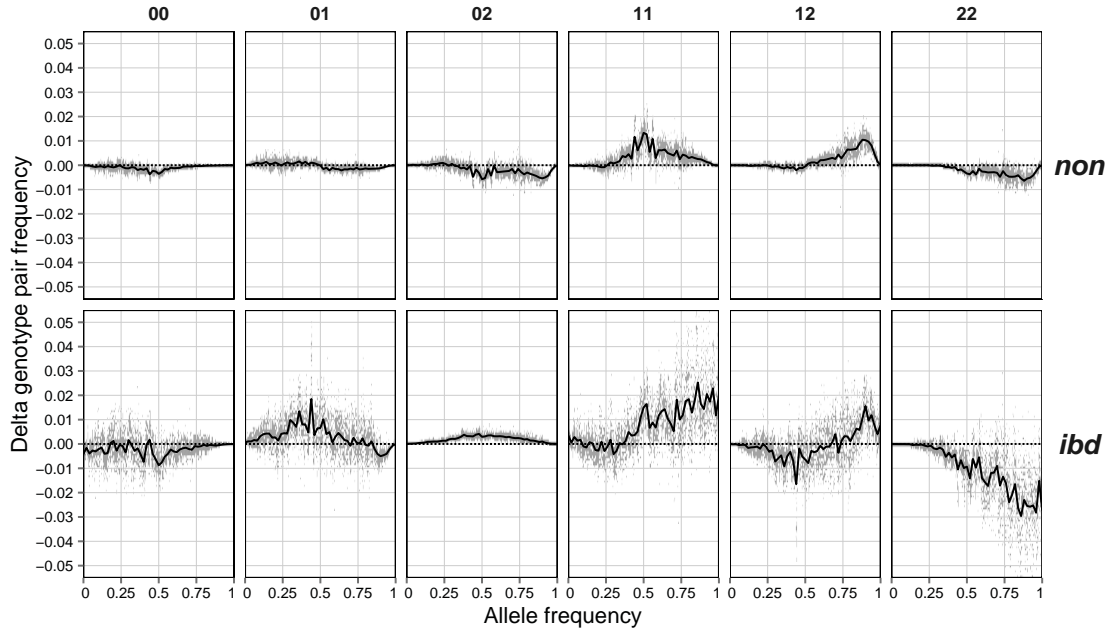


Figure 4.14: Difference between empirical and expected proportions of genotype pairs. In total, 500,000 segments were sampled in *non* and *ibd* as determined from coalescent records. Segments were aggregated by allele frequency to calculate empirical proportions for each of the six possible genotype pairs (g_{k_1, k_2} , indicated above each panel). Delta values were calculated by subtracting empirical from expected proportions; the latter were calculated using Equations (4.11) and (4.12) under *non* and *ibd*, respectively. Each panel is a scatterplot showing the deviation at each discrete step in allele frequency. The mean (\pm SE) of delta values was calculated in steps of 1% allele frequency; indicated by the *black* line. Results in Panel (a) were generated on data before the inclusion of genotype error, D , and Panel (b) on data after genotype error was included, D^* .

around the mean and ranged between -1% and $+1\%$. In contrast, the variability across frequency units was overall amplified in *ibd*. The mean proportion of g_{11} was up to 2% higher than expected towards the higher end of the frequency spectrum, whereas g_{22} was up to 2% lower than expected towards higher frequencies. Notably, g_{02} is expected to have a constant zero probability of observation in *ibd*, which was confirmed from the data.

After error, overall variability increased in each comparison. In *non*, the mean proportion of g_{11} showed deviations of up to $+1\%$ towards 50% allele frequency, which was also seen for g_{12} , but towards higher frequencies. In *ibd*, mean proportions showed as similar distribution as in comparisons before error, but where the difference between empirical and expected values was further increased. For example, deviations of g_{11} were increased up to $+2.5\%$ towards higher frequencies, which was mirrored by g_{22} but reaching up to -3% . Importantly, on average the empirical proportion of g_{02} was non-zero along the frequency spectrum, but which increased up to $+0.5\%$ towards 50% allele frequency.

Empirical initial state probabilities

Genotype error can affect the allele frequency distribution and thus bias the identification of individuals which share an allele at a given site. Some of the formed pairs may therefore be wrongly included, whereas some others may be missed. In particular, the following four cases can be distinguished:

- (a) **True positives.** The focal allele correctly identifies haplotype sharing in two individuals which are heterozygous for the allele; *i.e.* $g_1 \rightarrow g_1$.
- (b) **False positives.** The focal allele is observed in a misclassified genotype, $g_0 \rightarrow g_1$, such that IBD is wrongly assumed for a pair which does not share a haplotype. Note that the change $g_2 \rightarrow g_1$ also leads to the inclusion of an individual which actually is homozygous for the focal allele, but which is not considered in the model.
- (c) **False negatives.** The genotype of an individual was misclassified at the focal site, $g_1 \rightarrow g_0$, such that the focal allele is missed and the individual wrongly excluded.

Note that this also considers the change $g_1 \rightarrow g_2$, leading to the exclusion of the individual due to the assumptions of the model.

- (d) **True negatives.** An individual is correctly excluded due to not being heterozygous for the focal allele, *i.e.* $g_0 \rightarrow g_0$ or $g_2 \rightarrow g_2$, as well as $g_0 \rightarrow g_2$ or $g_2 \rightarrow g_0$

The inference of IBD segments in a pair where at least one individual is a false positive, Case (b), is likely to result in a disproportionately reduced segment length. In principle, such falsely identified individuals, and thereby specific false genotypes, may be exposed if segment lengths are consistently shorter than expected in each pairwise analysis. On the other hand, genotype error leading to false negatives, Case (c), is inadvertently missed, because it is not directly possible to assume that particular individuals carry the focal allele if not observed in the data.

The proportion of genotype pairs identified as true positives, Case (a), is relevant to determine the probability of the initial state at the start of the sequence. The true positive rate was determined by comparison of the data before and after error. All f_k variants at $k > 1$ were identified in \mathcal{D}^* , as well as all the individuals carrying the alternate allele at a particular variant site. This resulted in a set of matrix coordinates (marker by individual) which were pooled into site frequency bins, defined by k . Bins with less than 1,000 markers were removed. Then, for each k , all possible pairs of individuals were formed at each marker and the dataset \mathcal{D} was queried with the joint set of coordinates. This was done to extract the corresponding vector of true genotype pairs, from which the true positive rate was calculated as the proportion of pairs in which both genotypes were heterozygous.

The empirical distribution of correctly identified genotype pairs was used to define the initial state probability of being in *ibd*, given the frequency of the focal allele expressed in f_k . The resulting distribution is shown in Figure 4.15 (next page), for focal variants with k in [2, 50], corresponding to an allele frequency between 0.04% and 1%. The fraction of correctly observed genotype pairs was lowest for f_2 variants, found at 0.812, but rapidly increased to 0.913 and 0.950 for f_5 and f_{10} variants, respectively. At higher frequencies, the true positive rate stabilised around 0.975 and 0.995. At frequencies near 100%, however,

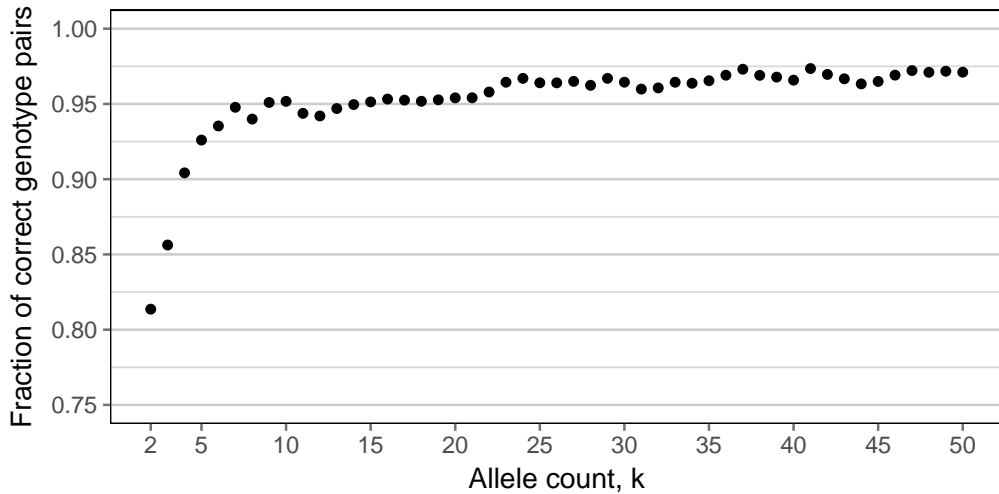


Figure 4.15: True positive rate of identified genotype pairs at focal sites. Pairwise shared genotypes at focal f_k variants with $k > 1$ were compared between datasets before and after error. The true positive rate was determined for each k . Results are shown for k in $[2, 50]$, which corresponds to an allele frequency between 0.04% and 1%.

the number of markers observed per k was too low to provide conclusive estimates. These values were stored in an array such that the initial state probability for a given k can be accessed through the functions $\pi_{ibd}(k)$ and $\pi_{non}(k) = 1 - \pi_{ibd}(k)$.

4.4.4 Inference of IBD segments

The aim of the presented IBD-model is to find the most likely position along the sequence at which the *ibd* state changes into the *non* state, which is done independently to the left and right-hand side of the focal f_k variant; *i.e.* the focal site sits at the start of both observation sequences. Recall that the IBD segment around the focal variant is defined by the interval $[b_L, b_R]$, where b_L and b_R denote the breakpoints which delimit the region in which at least one recombination event is likely to have occurred to the left and right-hand side of the focal variant site at position b_i . To infer this interval, the most likely hidden state which generated the observed genotype pair is inferred at each site along the sequence. In general, given H hidden states and an observation sequence of length m , there are H^m possible state sequences. For example, given this two-state HMM and a short region of only 100 genotype pairs, the number of possible state sequences

already exceeds the number of seconds the universe has existed*. To circumvent this problem, Rabiner (1989) formally advised the use of the *Viterbi algorithm* for sequence classification in HMMs, which scales quadratically with the number of hidden states and has a time complexity of $O(H^2 m)$.

The Viterbi algorithm is a dynamic programming technique which finds the most likely sequence of hidden states that maximises the probability of observing the data (Viterbi, 1967; Forney, 1973). Let X_j denote the hidden state at site j which generated the observed genotype pair o_j . Following Rabiner (1989), the probability of the most likely sequence of hidden states until site j and ending in state x is given by

$$v_j(x) = \max_{X_0, X_1, \dots, X_{j-1}} P(X_0, X_1, \dots, X_{j-1}, X_j = x, o_1, o_2, \dots, o_j | \lambda) \quad (4.13)$$

where λ denotes the model; see Equation (4.5) on page 155. The procedure to retrieve the actual state sequence is summarised as follows.

1. Initialisation. The probability that a given state generated the genotype pair observed at the focal site is simply the product of its initialisation and emission probabilities. If genotype error is included, the initialisation probability is defined conditionally on the frequency of the focal f_k variant. Note that emission probabilities were defined as $\delta_{k_1 k_2}$ and $\eta_{k_1 k_2}$ in *ibd* and *non*, respectively. For simplicity, these are now written as $\delta_j(o_j)$ and $\eta_j(o_j)$, where the index j refers to the position in the sequence at which the allele frequency is taken to retrieve the frequency-dependent probability of the observed genotype pair at site j .

$$\begin{aligned} v_0(ibd) &= \pi_{ibd}(k) \delta_0(o_0) \\ v_0(non) &= \pi_{non}(k) \eta_0(o_0) \end{aligned} \quad (4.14)$$

The Viterbi algorithm involves the successive multiplication of probabilities during the recursion step (see below), which may result in values too small to be

* Current age of the universe: 42×10^{16} seconds [Date accessed: 2017-02-18]

distinguishable from zero using conventional computers. To avoid this problem, a commonly implemented solution is a log-transformation of probabilities. Here, it is more convenient (and computationally less demanding) to define a weighting function to obtain a scaling factor which is stored in an additional array, w .

$$w_0 = \max_{x \in S} [v_0(x)] \quad \text{s.t.} \quad v'_0(x) = \frac{v_0(x)}{w_0} \quad \forall x \in S \quad (4.15)$$

2. Recursion. The array u is defined to keep track of the states traversed along the path; that is, $u_j(x)$ stores a back-pointer to the state at site $j - 1$ which resulted in the highest probability $v_j(x)$ at site j .

$$u_j(x) = \arg \max_{y \in S} [v'_{j-1}(x) \psi_{j,k}(y | x)] \quad \forall x \in S; j = 1, 2, \dots, m \quad (4.16)$$

Recall that $\psi_{j,k}$ refers to the transition probability from a given state to another or the same state, and is dependent on the frequency of the focal allele (k), as defined in Equation (4.9), page 157. The chain proceeds through the most likely path at each site along the sequence by following the transitions that maximise the probability of observing a given state. Given Equation (4.13), by induction on j it follows that

$$\begin{aligned} v_j(ibd) &= \delta_j(o_j) \max_{y \in S} [v'_{j-1}(ibd) \psi_{j,k}(y | ibd)], \quad j = 1, 2, \dots, m \\ v_j(non) &= \eta_j(o_j) \max_{y \in S} [v'_{j-1}(non) \psi_{j,k}(y | non)], \quad j = 1, 2, \dots, m. \end{aligned} \quad (4.17)$$

Note that the current state probability is computed conditionally on the weighted probability value at the immediate previous site, but which does not affect the outcome of the maximisation.

$$w_j = \max_{x \in S} [v_j(x)] \quad \text{s.t.} \quad v'_j(x) = \frac{v_j(x)}{w_j} \quad \forall x \in S; j = 1, 2, \dots, m \quad (4.18)$$

3. Termination. At the last site in the sequence, m , the state with the highest probability is picked to mark the final state of the most likely sequence of hidden

states (*i.e.* the “Viterbi path”), denoted by X^* .

$$X_m^* = \arg \max_{x \in S} [v'_m(x)] \quad (4.19)$$

4. Path backtracking. Given the array of back-pointers, u , the most likely path is found by tracing back from the final state until the initial site in the sequence.

$$X_j^* = u_{j+1}(X_{j+1}^*) , \quad j = m-1, m-2, \dots, 0 \quad (4.20)$$

The IBD segment is determined from the two resulting state sequences, which were obtained independently from the observation sequence to the left and right-hand side of the focal position. The Viterbi paths on the left and right-hand side are denoted by L^* and R^* , respectively. The breakpoint interval defining the segment, $[b_L, b_R]$, is found by scanning each path from its start (*i.e.* from a given target site) to the first position at which the *non* state was inferred. Note that this includes the site of the first *non* state, which is defined as a breakpoint. In boundary cases, when each site until the end of the chromosome was inferred as being in the *ibd* state, the last site in the sequence is taken as a breakpoint.

4.4.5 Results

The HMM-based method for IBD inference was evaluated on the same error-treated dataset as used in Section 4.3.2 (page 142). Because the HMM does not require haplotype information, the analysis was conducted on genotype data only, both before and after the inclusion of error. Recall the there are multiple focal alleles that may sit on the same underlying shared haplotype, such that the resulting set of segments inferred from all selected target sites may result in duplicate segments. As these do not add to the analysis below, duplicate segments were removed to retain a set of unique segments. The number of unique segments inferred was 3.179 million and 3.236 million before and after error, which corresponds to 32.250 % and 32.827 % of the reported set of IBD

Table 4.4: Accuracy comparison per f_k category after error. The accuracy of detected IBD breakpoints was measured using the squared Pearson correlation coefficient, r^2 , and the RMSLE in relation to the true IBD segments determined from simulation records; measured in terms of the distance between breakpoint site and the corresponding focal position per segment. Results were obtained on the error-treated dataset, D^* (which included the true haplotypes, phased haplotypes, and genotype data), using the FGT, DGT, and the HMM-based method for targeted IBD detection. Accuracy was measured after duplicate segments had been removed, and the same set of target sites was assessed in each approach; separately computed per f_k category. The approach with the highest accuracy (highest r^2 and lowest RMSLE) per f_k is indicated (**bold**).

f_k	Freq. (%)	r^2				RMSLE			
		FGT*	FGT**	DGT	HMM	FGT*	FGT**	DGT	HMM
2	0.04	0.011	0.015	0.018	0.982	1.208	1.362	1.029	0.390
3	0.06	0.031	0.039	0.050	0.908	1.013	1.112	0.855	0.452
4	0.08	0.049	0.060	0.079	0.832	0.924	0.993	0.792	0.490
5	0.10	0.064	0.075	0.097	0.755	0.869	0.913	0.756	0.534
6	0.12	0.084	0.093	0.120	0.682	0.832	0.863	0.730	0.555
7	0.14	0.089	0.097	0.123	0.602	0.791	0.810	0.711	0.582
8	0.16	0.094	0.106	0.135	0.575	0.767	0.784	0.692	0.588
9	0.18	0.105	0.112	0.138	0.523	0.754	0.766	0.690	0.613
10	0.20	0.113	0.123	0.147	0.492	0.733	0.740	0.682	0.635
11	0.22	0.122	0.128	0.149	0.440	0.713	0.716	0.677	0.659
12	0.24	0.139	0.144	0.173	0.424	0.718	0.721	0.691	0.654
13	0.26	0.117	0.120	0.154	0.424	0.708	0.711	0.686	0.675
14	0.28	0.149	0.157	0.178	0.386	0.699	0.696	0.683	0.678
15	0.30	0.126	0.129	0.151	0.408	0.691	0.690	0.676	0.681
16	0.32	0.146	0.150	0.175	0.379	0.676	0.675	0.669	0.689
17	0.34	0.132	0.140	0.158	0.312	0.683	0.682	0.690	0.712
18	0.36	0.143	0.158	0.175	0.334	0.669	0.667	0.669	0.702
19	0.38	0.149	0.153	0.170	0.303	0.675	0.669	0.673	0.705
20	0.40	0.173	0.179	0.192	0.327	0.664	0.665	0.681	0.716
21	0.42	0.154	0.165	0.172	0.309	0.667	0.660	0.682	0.720
22	0.44	0.151	0.154	0.160	0.257	0.659	0.657	0.684	0.725
23	0.46	0.139	0.144	0.160	0.265	0.653	0.649	0.675	0.723
24	0.48	0.153	0.153	0.168	0.247	0.663	0.655	0.690	0.746
25	0.50	0.098	0.102	0.102	0.239	0.664	0.656	0.702	0.740

* True haplotypes

** Phased haplotypes

segments, respectively. In comparison, the number of unique segments in the set of *true* IBD segments, those determined from simulation records on the same targets, was 2.721 million (27.599 %). The proportion of breakpoints overestimated was similar in for both datasets; 55.716 % before error and 54.094 % after error. Likewise, 55.716 % and 54.094 % were underestimated, respectively, and 4.328 % and 4.281 % coincided with true breakpoints, respectively. Overall accuracy was $r^2 = 0.634$ before error and $r^2 = 0.638$ after error, and RMSLE was 0.781 and 0.791, respectively. While it appears from these

results that accuracy was comparatively low, consider the results by allele frequency; see Table 4.4 (page 171), which also includes the same results obtained using the FGT on true haplotypes as well as phased haplotypes, and the DGT on genotype data. As can be seen from the table, the HMM-based approach reached highest accuracy at lower allele frequencies, but which then rapidly decreased towards higher frequencies.

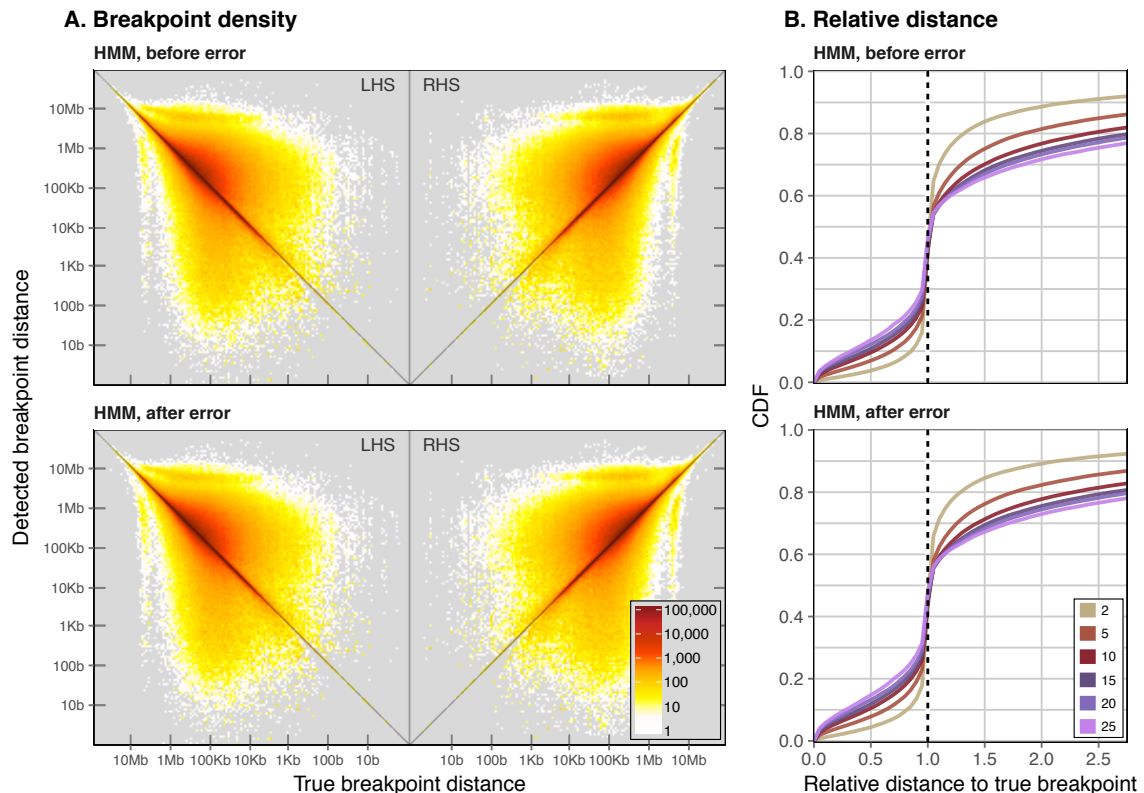


Figure 4.16: Accuracy of IBD breakpoint detection using the Hidden Markov Model on simulated data, before and after error. Panel (A) shows the density of true and detected breakpoints; Panel (B) shows the physical length in terms of the relative distance between a focal site and the detected breakpoint. See Figure 4.6 (page 145) for a detailed description.

Median length was assessed after removal of boundary cases, discarding 1.241 % the data before inclusion of error and 1.216 % after error. This proportion was similar in true IBD segments (1.377 %). Before error, overall median length was 0.526 Mb (0.884 cM), and 0.504 Mb (0.884 cM) after error; this is compared to the shorter median length found for the true dataset; 0.343 Mb (0.590 cM). The distribution of IBD length is shown in Figure 4.17 (next page), which for comparison also includes the results obtained for the FGT and DGT after error.

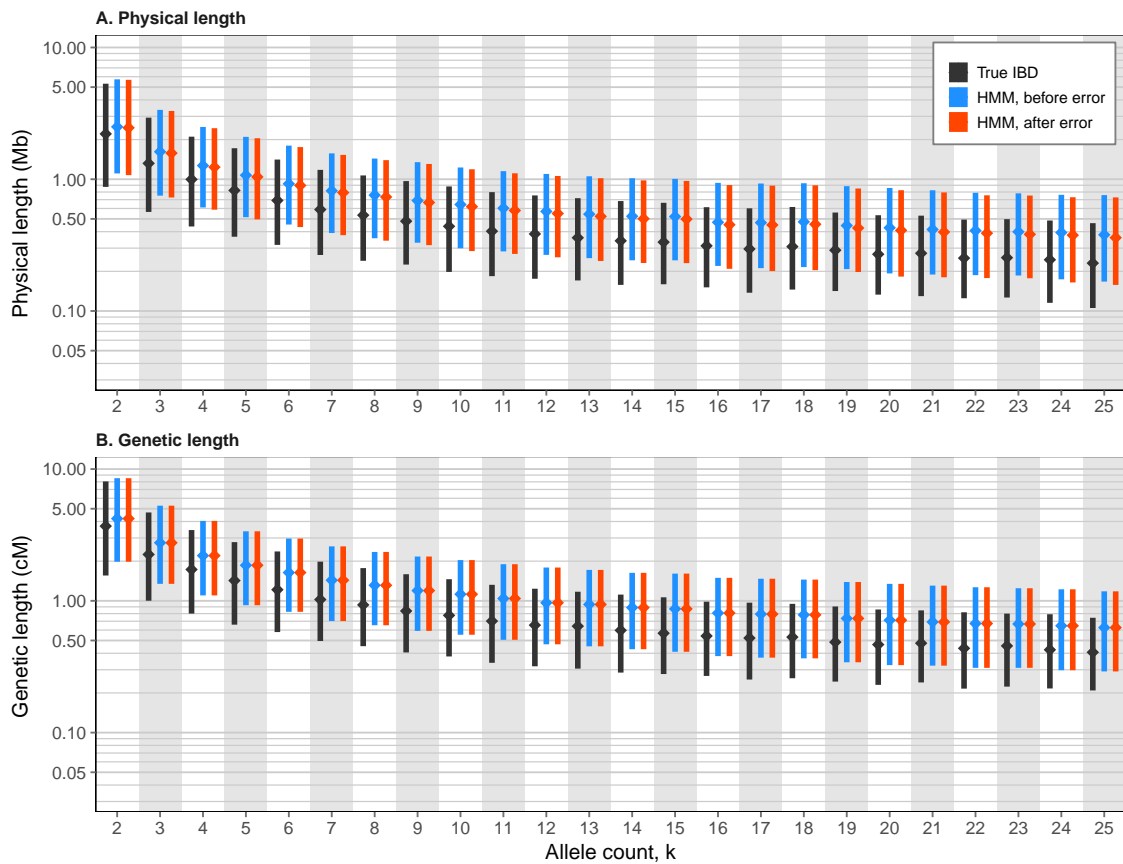


Figure 4.17: Length distribution of shared haplotype segments using the Hidden Markov Model on simulated data. The HMM-based approach for targeted IBD detection was applied to simulated data before and after the inclusion of genotype error; *i.e.* datasets D and D^* , respectively. Bottom and top of each bar indicate 1st and 3rd quartiles, respectively, between which the median (2nd quartile) is marked (diamonds).

Lastly, I applied the HMM-based method on data from the 1000 Genomes Project (1000G) Phase III (chromosome 20). These results are shown in Figure 4.18 (next page), which also includes previous results obtained for the FGT and DGT, on the same set of retained target sites (duplicate segments were again removed). The figure shows that only the HMM is able to infer longer IBD segments that are more consistent with expectations. In direct comparison to the length distribution seen in simulated data, shown in Figure 4.17 (this page), median length was consistently shorter in 1000G. Such a direct comparison, however, may not be applicable, as there are considerable differences between this and the simulated dataset. For example, the simulated dataset was generated as a sample of “European” haplotypes only (as defined in the demographic model; see Chapter 3, Section 3.5.1, page 102).

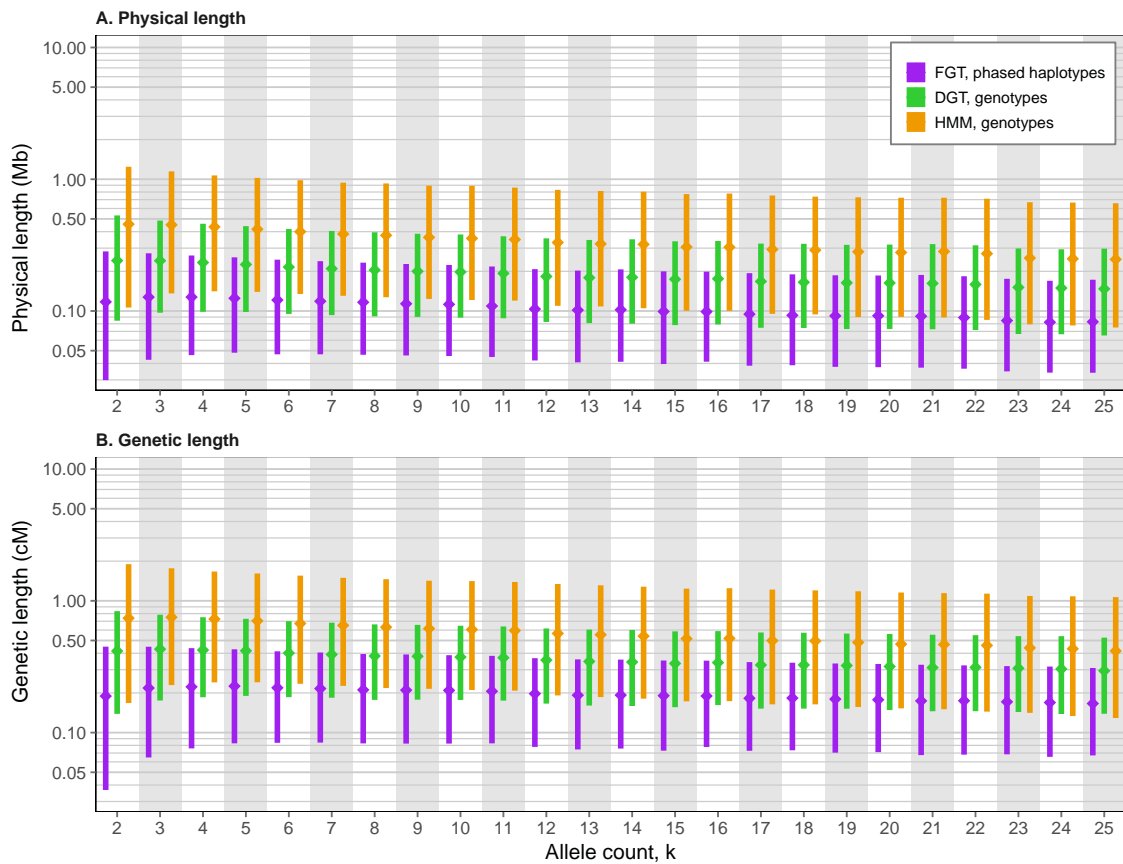


Figure 4.18: IBD inference using the Hidden Markov Model on 1000 Genomes data, chromosome 20. IBD detection using the HMM-based method was performed under the empirical error model defined on genotype data from the 1000 Genomes Project. The resulting length distribution is compared to previous results obtained on the same set of target sites using the FGT and DGT. Bottom and top of each bar indicate 1st and 3rd quartiles, respectively, between which the median (2nd quartile) is marked (*diamonds*).

4.4.6 Discussion

The analysis on simulated data has shown that the HMM-based approach to infer IBD around target sites is able to operate equally well in both absence and presence of genotype error. In particular, I showed that IBD detected using the HMM maintained high levels of accuracy when genotype error is present. However, a notable caveat is seen in the decreasing accuracy towards higher frequencies of the focal allele; for example, IBD segments identified by f_2 variants were overall higher in accuracy compared to f_{15} or higher. The emission model was generated under the assumption of recent IBD, and empirical distributions closely followed the expected genotype pair frequencies. Besides

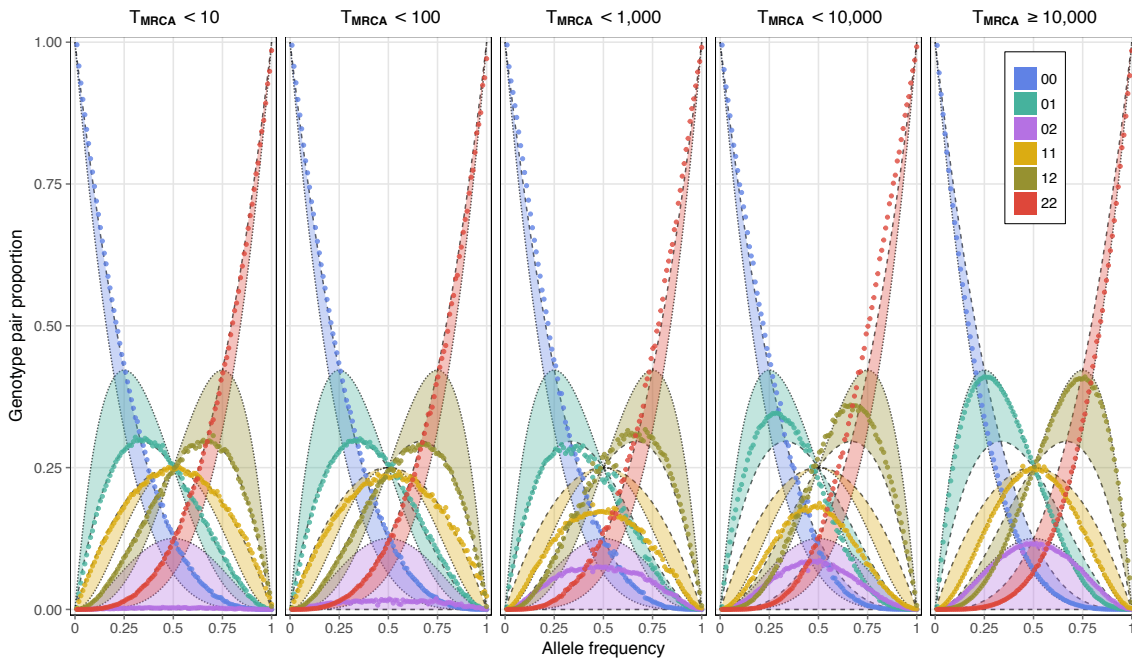


Figure 4.19: Empirical emission probabilities of genotype pairs dependent on time. The relative proportions of genotype pairs observed in IBD segments in simulated data are shown, which is distinguished by the time to the most recent common ancestor (T_{MRCA}); *i.e.* the time since a haplotype was co-inherited from a common ancestor. The dataset used to determine proportions was the original, error-free dataset (D). Dots indicate the empirical mean proportion by allele frequency bin ($n = 100$), equally spaced along the frequency spectrum. Genotype pairs are colour-coded (see legend). Shaded areas indicate the space between the expected frequency distribution under IBD and non-IBD, coloured according to the respective genotype pair, where the edges of these areas correspond to the expectation under IBD (dashed) and non-IBD (dotted).

genotype error, the accumulation of mutations over time are expected to lead to further deviations from expectations under IBD.

The difference between recent and older relationships of IBD is exemplified in Figure 4.19 (this page), where I used the same methodology I applied as in Section 4.4.3 (page 162), using the error-free dataset (D), but where I distinguished IBD segments by T_{MRCA} . The difference is shown between IBD haplotypes that were very recently co-inherited ($T_{MRCA} < 10$ generations) and those denoting older relationships ($T_{MRCA} \geq 10,000$ generations). The resulting proportions of genotype pairs, *i.e.* their observation probability dependent on age, show an interesting pattern, but one that may be difficult to model. For example, g_{00} and g_{22} genotype pairs appear to be consistent and less variable most of the time, but then show a distribution as expected under non-IBD at

very old age ($\geq 10,000$ generations). In contrast, the g_{02} genotype pair gradually increases from zero probability expected under IBD to a distribution expected under non-IBD. Interestingly, the g_{11} genotype pair varies inconsistently with regard to either expectation at intermediate time frames (*e.g.* between 1,000 and 10,000 generations). This result suggests that a static emission model may not provide sufficient leverage to distinguish IBD from non-IBD at older (*i.e.* higher-frequency) alleles, or in general when IBD is not recent. It would therefore be advantageous to device a fully probabilistic model to compute emission probabilities; *e.g.* conditional on mutation rate and expected allele age, similar to the transition model.

People assume that time is a strict progression of cause to effect, but, actually, from a non-linear, non-subjective point of view, it's more like a big ball of... wibbily-wobbly... timey-wimey... stuff.

— Doctor Who (David Tennant)

5

Estimation of rare allele age

Contents

5.1	Introduction	177
5.2	Approach	179
5.2.1	Coalescent time estimators	180
5.2.2	Cumulative coalescent function	184
5.2.3	Composite likelihood estimation of mutation time	185
5.2.4	Inference of IBD around shared and unshared alleles	188
5.3	Evaluation	192
5.3.1	Data generation	192
5.3.2	Accuracy analysis	195
5.4	Results	196
5.4.1	Validation of the method under different thresholds	197
5.4.2	Comparison of IBD detection methods	203
5.4.3	Impact of genotype error on allele age estimation	209
5.5	Age of alleles with predicted effects in 1000 Genomes data	221
5.5.1	Quality control	221
5.5.2	Error correction based on allele frequency	222
5.5.3	Results	223
5.6	Discussion	226

5.1 Introduction

The inference of the genealogical history of a sample is of interest to a myriad of applications in genetic research, both in population and medical genetics. The “age” of an allele, which simply refers to the time since the allele was created by a mutation event, is of particular interest; for example, to observe demographic processes and events,

or to better understand the effects of disease-related variants by their time of emergence in the population.

In this chapter, I propose a composite likelihood method to estimate the age of an allele, which is based on a collection of statistical models that derive from coalescent theory. Composite likelihood methods recently have gained in popularity for various applications in genetic research. The coalescent-based approach was pioneered by Hudson (2001) and has been used successfully, for example, for the fine-scale estimation of recombination rates (McVean *et al.*, 2004; Myers *et al.*, 2005). In contrast to existing methods for allele age estimation (*e.g.*, see review by Slatkin and Rannala, 2000), the method I present in this chapter does not require prior knowledge about past demographic processes or events. Although an assumption of certain population parameters is required, such as effective population size (N_e) or mutation rate (μ), these are expected to only affect the scaling of time, such that differences between age estimates for different alleles are proportionally constant.

The age estimation framework presented in this chapter is based on allele sharing at a particular variant site observed in the sample, where the underlying IBD structure is inferred locally around the chromosomal position of the variant under consideration. The methodology for targeted IBD detection presented in Chapters 3 and 4 is therefore essential for this approach; *i.e.* the `tidy` algorithm which includes the four-gamete test (FGT), discordant genotype test (DGT), and the probabilistic IBD model for inference using a Hidden Markov Model (HMM). I implemented the age estimation method as a computational tool written in C++, referred to as the **rvage** algorithm (for rare variant age estimation) which incorporates the full functionality of the previously presented `tidy` algorithm for IBD detection.*

I begin this chapter by introducing the concept of the method, which is followed by a detailed description of the statistical framework. The method is evaluated in extensive simulation studies which consider genotype error as a source of estimation bias. Although the method can be applied to single-nucleotide polymorphisms (SNP) occurring at any

* Rare variant age estimation (rvage): <https://github.com/pkalbers/rvage>

frequency, here, I focus on rare alleles in particular. Finally, I present results using real data in relation to predicted variant consequences.

5.2 Approach

Consider a set of haplotypes which share a given allele by descent from a common ancestor who lived at some point in the past. Suppose that the genealogical history of the sample is known such that the ancestral origin of the allele can be found by tracing back to the most recent common ancestor (MRCA) of the haplotypes that share the allele. In a finite population, however, the MRCA is unlikely to indicate the individual in which the allele arose through mutation; therefore the actual age of the allele is expected to be older than the time to the most recent common ancestor (T_{MRCA}) of the set of haplotypes which share the focal allele. The mutation from which the allele derived can be seen as a distinguishing event in the history of the population, immediately after which only one individual in the population carried the mutant allele. It follows that the allele is expected to be younger than the MRCA of that one individual and any of the other contemporary individuals. This insight is of particular interest as it suggests that the actual time of the mutation event lies somewhere in between those two points in time.

There are two main sources of information available from the data which relate to the T_{MRCA} . First, mutation events occur independently in each lineage and mutations accumulate along the sequence as the chromosome is passed on over generations. Second, recombination events break down the length of the shared haplotype in each generation independently in each lineage. The number of mutations which segregate in the two haplotypes as well as the genetic length of the pairwise shared haplotype segment can be used to infer the T_{MRCA} of two chromosomes; *i.e.* the time of the coalescent event at which the two lineages join.

In the following section, I derive the formulations for three estimators of the T_{MRCA} of a pair of chromosomes, two of which are the *mutation clock* and the *recombination clock* model and are denoted by \mathcal{T}_M and \mathcal{T}_R , respectively. The third estimator combines

both the number of mutations and the genetic length of the segment; referred to as the *combined clock* model, denoted by \mathcal{T}_{MR} .

5.2.1 Coalescent time estimators

The presented age estimation method is based on the computation of the posterior probability of the T_{MRCA} of a pair of haplotypes. It is assumed that no recombination has occurred along the sequence in the haplotype segment considered, such that the genealogical relationship between the two haplotypes does not change along the region. This allows analysis under a coalescent process, where the posterior probability is proportional to the prior probability of the time to coalescence multiplied by the likelihood of the time given the estimator. The derivation of the coalescent prior is described below.

Let t be the number of discrete generations that separate two haplotypes in relation to the MRCA. As shown by Tajima (1983), the probability that two haplotypes are derived from one common ancestral haplotype t generations in the past is

$$f(t) = \frac{1}{2N_e} \left(1 - \frac{1}{2N_e}\right)^{t-1} \approx \frac{1}{2N_e} e^{-\frac{t}{2N_e}} \quad (5.1)$$

where N_e is the effective population size. The expression above relates to the probability distribution of the branch length in the underlying genealogical tree. Further, the probability that the two haplotypes do not share an ancestral haplotype more recently than t generations in the past is given by

$$P(T_c \geq t) = 1 - \sum_{i=1}^{t-1} f(i) \approx e^{-\frac{t}{2N_e}} \quad (5.2)$$

where T_c is the time of the coalescent event. It is convenient to use a continuous time approximation and measure time in units of $2N_e$ generations, in the context of the coalescent, such that $\tau = t/2N_e$. Thus, the coalescent prior can be expressed as

$$\pi(t) \propto e^{-\frac{t}{2N_e}} \quad \text{or} \quad \pi(\tau) \propto e^{-\tau}. \quad (5.3)$$

The sections below describe each clock model in detail. Recall that the *breakpoints* of past recombination events are inferred for a pair of individuals, independently on the left and right-hand side of a target variant. Under this *variant-centric* approach, a given IBD segment is composed of two intervals, each delimited by the focal site and one distal breakpoint, where at least one recombination event was inferred to have occurred within each interval. If no evidence of recombination was found on either the left or the right-hand side, a *boundary case* is recorded where the chromosomal end position is taken as a breakpoint to delimit the length of the interval.

Mutation clock model (\mathcal{I}_M)

Let the physical length of the shared haplotype segment be denoted by D , measured in basepairs. The sum of mutational differences observed along the segment in the pair of haplotypes is denoted by S . The value of S refers to the number of segregating sites in a sample of $N = 2$ haplotypes, for which the infinite sites model is assumed without recombination; *e.g.* see Watterson (1975) and Tavaré *et al.* (1997). Mutations are assumed to occur only once at each site in the history of the sample (Kimura, 1969), such that S reflects the total number of mutation events that have occurred along both lineages since the split from the MRCA.

Given the time of the MRCA, mutation events are Poisson distributed, as each mutation represents an independent binomial trial over a large number of sites, where each site has a small probability of mutation. The mutation rate per site per generation is given by μ . In the coalescent, the mutation rate is scaled by population size, which is expressed by the composite mutation parameter $\theta = 4N_e\mu$. It follows that $\theta \times D$ is equal to the expected number of pairwise differences per coalescent time unit over the length of the segment. Thus, the probability of observing S over the distance D and time τ is modelled as a Poisson process, such that $S \sim \text{Pois}(\theta D \tau)$, for which the probability density function (PDF) is defined as

$$P(S | \theta, D, \tau) = \frac{(\theta D \tau)^S}{S!} e^{-\theta D \tau}. \quad (5.4)$$

Note that the equation above is the *joint* probability of observing mutational differences at each site along the sequence. The likelihood function for τ is proportional to the joint PDF, but requires only those terms that involve τ and where constant terms can be dropped, such that

$$\mathcal{L}(\tau | \theta, D, S) \propto \tau^S e^{-\theta D \tau}. \quad (5.5)$$

The posterior probability of the time to coalescence can now be written as

$$\begin{aligned} p(\tau | \theta, D, S) &\propto \pi(\tau) \times \mathcal{L}(\tau | \theta, D, S) \\ &\propto \tau^S e^{-\tau(\theta D + 1)} \end{aligned} \quad (5.6)$$

where $\pi(\tau)$ is the coalescent prior, reflecting the assumption that the expected time to a coalescent event grows exponentially back in time.

Recombination clock model (\mathcal{T}_R)

In reference to the position of a focal allele that is shared by descent in two chromosomes, the length of the shared haplotype is delimited by two recombination events between the two lineages that occurred on either side of the focal position. The recombination rate per site per generation is given by ρ ;^{*} again, the rate is rescaled by population size and the composite recombination parameter $\psi = 4N_e\rho$ is used. The interval on the left and right-hand side of the focal position is distinguished by defining the distance variable D_X , where $X \in \{L, R\}$. The genetic distance to the first recombination event is geometrically distributed along the sequence, but can be approximated by the exponential distribution if time is continuously measured and provided that N_e is large; *e.g.* see Hein *et al.* (2004). The probability of observing a recombination breakpoint can therefore be modelled such that $D_X \sim \text{Exp}(\psi\tau)$, for which the PDF is defined as

$$P(D_X | \psi, \tau) = 2\psi\tau e^{-2\psi D_X \tau} \quad (5.7)$$

* Note that the literature often specifies ρ as the population-scaled recombination rate and r as the rate per site per generation.

which is equal to the joint probability of recombination between consecutive sites along the sequence. The factor of 2 is included to consider that recombination events occur independently in the two lineages. Note that D_X may refer to the entire length of interval if recombination rate is uniform, but it is straightforward to compute a variable recombination rate over the interval (*e.g.* by using a genetic map) to derive the genetic length expressed in ψD_X .

Considering Equation (5.7), the likelihood function for τ can be written as

$$\mathcal{L}(\tau | \psi, D_X) \propto \tau^{I_X} e^{-2\psi D_X \tau} \quad (5.8)$$

where I_X is an indicator function of the detected breakpoint. Recall that an IBD segment may extend to the end of a chromosome if no recombination occurred on one or both sides of the focal position; *i.e.* a boundary case. The indicator function is therefore defined as

$$I_X = \begin{cases} 0 & \text{if boundary case on side } X \\ 1 & \text{otherwise.} \end{cases}$$

Thus, to consider the intervals on both sides simultaneously by the length of the whole IBD segment, D , the following likelihood function is defined.

$$\mathcal{L}(\tau | \psi, D) \propto \tau^{I_L + I_R} e^{-2\psi D \tau}. \quad (5.9)$$

As a result, the posterior probability of the time to coalescence under the recombination clock can be written as

$$\begin{aligned} p(\tau | \psi, D) &\propto \pi(\tau) \times \mathcal{L}(\tau | \psi, D) \\ &\propto \tau^{I_L + I_R} e^{-\tau(2\psi D + 1)}. \end{aligned} \quad (5.10)$$

Note that the inference of recombination breakpoints does not require haplotype data; thus, the recombination clock model may provide a convenient solution if only genotype data is available.

Combined clock model (\mathcal{T}_{MR})

Given the information available for both the mutation and the recombination clocks, the posterior probability of τ is readily calculated; see below.

$$\begin{aligned} p(\tau | \theta, \psi, D, S) &\propto \pi(\tau) \times \mathcal{L}(\tau | \theta, D, S) \times \mathcal{L}(\tau | \psi, D) \\ &\propto e^{-\tau} \times \tau^S e^{-\theta D \tau} \times \tau^{I_L + I_R} e^{-2\psi D \tau} \\ &\propto \tau^{S+I_L+I_R} e^{-\tau(D(\theta+2\psi)+1)} \end{aligned} \quad (5.11)$$

However, it is worth to consider the following. Both clocks, \mathcal{T}_M and \mathcal{T}_R , can be consolidated by their conjugate prior distributions which, for both, is the Gamma distribution. The PDF of the Gamma distribution in support of τ is

$$\frac{\beta^\alpha}{\Gamma(\alpha)} \tau^{\alpha-1} e^{-\beta\tau}$$

where α is the shape and β the rate parameter of the distribution. Given the variables at hand for the combined clock, and under consideration of the coalescent prior, the parameters can be defined as $\alpha = 1 + S + I_L + I_R$ and $\beta = D(\theta + 2\psi) + 1$. Note that because α is an integer, the Erlang distribution can be used instead of the Gamma distribution, e.g. to facilitate faster computation;

$$\begin{aligned} P(S, L | \theta, \psi, \tau) &= P(S | \theta, D, \tau) \times P(D | \psi, \tau) \\ &= \frac{(D(\theta + 2\psi) + 1)^{1+S+I_L+I_R}}{(S + I_L + I_R)!} \tau^{S+I_L+I_R} e^{-\tau(D(\theta+2\psi)+1)} \end{aligned} \quad (5.12)$$

for which the likelihood function for τ is identical to Equation (5.11). Note that a similar derivation has been used by Schroff (2016).

5.2.2 Cumulative coalescent function

Each clock model described above computes the posterior probability for two lineages to have coalesced at a particular point in time. This is extended such that the posterior distribution of coalescent times is calculated over a continuous time prior such that

the T_{MRCA} can be derived from the cumulative distribution function (CDF). Here, this approach is referred to as the cumulative coalescent function (CCF) which is defined as

$$\Lambda_{ij}(t | \cdot) = \int_0^t p(\tau | \cdot) d\tau \quad (5.13)$$

where t denotes the coalescent time prior and i, j denote the two haplotypes under consideration. The parameterisation of the clock model used is indicated by “ \cdot ”. In practise, the posterior probability $p(\tau | \cdot)$ is calculated from the Gamma (Erlang) distribution in each clock model, due to the conjugate relation described in the previous section.

5.2.3 Composite likelihood estimation of mutation time

Consider a sample of haplotypes and an allele shared by some of the haplotypes. The time at which this allele was created by a mutation event is bound by the times of the two coalescent events that delimit the length of the branch on which the mutation occurred in the underlying coalescent tree; see the example provided in Figure 5.1. The haplotypes which co-inherited the allele (*sharers*) are distinguished from the other haplotypes which do not carry the allele (*non-sharers*). Thus, the sample is divided into two disjoint subsamples; let X_c denote the set of chromosomes which share a given allele and X_d the set of chromosomes which do not share that allele. Importantly, all lineages in the X_c subsample coalesce before any of them can coalesce with a lineage in the X_d subsample.

It follows that any coalescent event between two lineages in X_c must have occurred *earlier* than the focal mutation event (back in time). On the other hand, any coalescent event between one lineage in X_c and one lineage in X_d must have occurred *later* than the focal mutation event. In the following, pairs of haplotypes in X_c are referred to as *concordant* pairs and pairs from X_c and X_d as *discordant* pairs. The sets Ω_c and Ω_d are defined to contain all concordant and discordant pairs, respectively.

The time of a focal mutation event is found at the “sweet spot” in between the earlier coalescent event at time t_c and the later coalescent event at time t_d . The CCF is computed for concordant pairs in Ω_c to infer the T_{MRCA} of the X_c subsample, such that the oldest

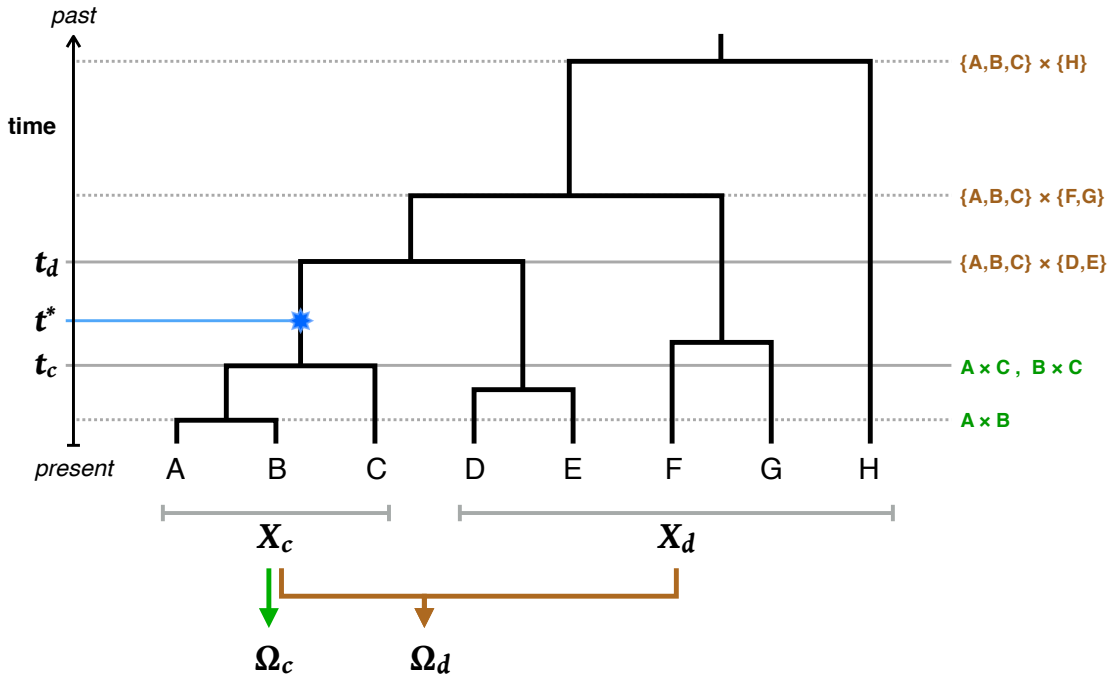


Figure 5.1: Allele age in relation to concordant and discordant pairs. The genealogy of a sample of eight haplotypes is shown of which A, B, and C share a focal allele that derived from a mutation event as indicated in the tree (star). These chromosomes constitute the set of *sharers*, denoted by X_c , which are differentiated from the set of *non-sharers*, denoted by X_d . Horizontal lines indicate the time of each coalescent event in the history of the sample within the local genealogy. The time of the focal mutation event is denoted by t^* ; the two coalescent events at time t_c and t_d define the length of the branch on which the focal mutation event occurred. In particular, t_c and t_d correspond to the time until all haplotypes in X_c have coalesced and the time at which the derived lineage joins the ancestral lineage of the most closely related haplotype in X_d , respectively.

MRCA indicates the lower bound in the estimation of the focal allele age. The upper bound is found by computing the CCF for discordant pairs in Ω_d , where the youngest MRCA is closest in time to the focal mutation event. The information provided from these pairwise CCF analyses are used in the calculation of the composite likelihood, which is defined below.

$$\Phi(\tau) \propto \prod_{i,j \in \Omega_c} \Lambda_{ij}(\tau | \cdot) \times \prod_{i,j \in \Omega_d} (1 - \Lambda_{ij}(\tau | \cdot)) \quad (5.14)$$

The lower and upper bounds on the estimated age are provided by the incomplete gamma functions

$$P_{i,j}(\tau > t) = \int_0^\tau \Phi(t | i, j) dt \quad (5.15)$$

and

$$P_{i,j}(\tau < t) = \int_\tau^\infty \Phi(t | i, j) dt. \quad (5.16)$$

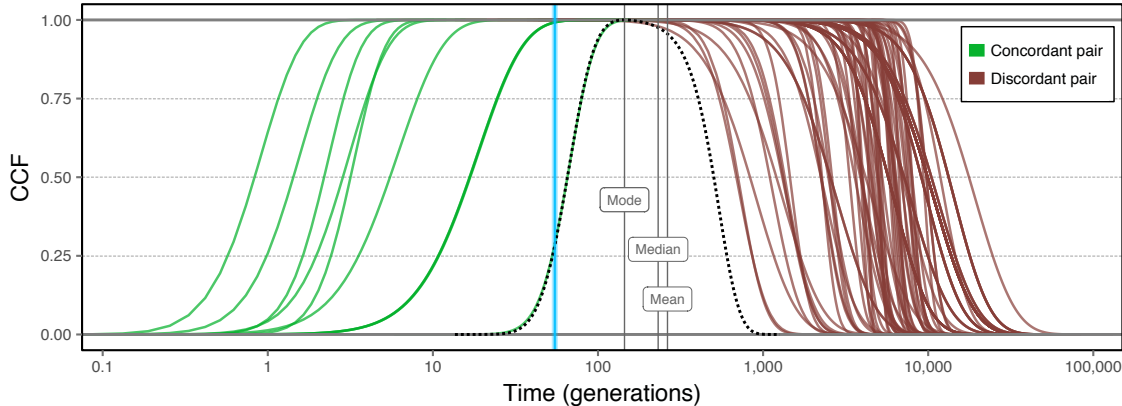


Figure 5.2: Example of the age estimation result for a focal variant. A target variant was randomly selected from simulated data. Each of the possible concordant pairs was formed and analysed using the CCF. A subset of $n_d = 100$ discordant pairs was randomly selected and analysed using the CCF. Vertical lines indicate the mode, median, and mean of the composite likelihood distribution. The *blue* line marks the true age of the mutation, as determined from simulation records.

The composite likelihood estimate of the time is scaled in units of $2N_e$. The mean, median, and mode of the posterior distribution were taken as age estimates. In the following, the estimated age is reported using the median, which is denoted by \hat{t} and expressed in units of generations. The example shown in Figure 5.2 (this page) illustrates the output produced for a single focal variant.

Reduction of the computational burden

A major caveat to the estimation of allele age is the computationally demanding analysis of each haplotype pair in Ω_c and Ω_d per target site. The numbers of concordant and

discordant pairs are denoted by n_c and n_d , respectively, and the overall number of pairwise analyses varies dependent on the observed frequency of the focal allele and the sample size. For a given f_k variant, the number of possible concordant pairs is

$$\max[n_c] = \binom{k}{2} = \frac{k(k-1)}{2} \quad (5.17)$$

where k is the number of allele copies observed in the sample; *i.e.* the size of X_c . The number of possible discordant pairs is given by

$$\max[n_d] = k(2N - k) \quad (5.18)$$

where N refers to the diploid sample size. The total number of pairwise analyses conducted per target site is the sum of n_c and n_d . However, the estimation process for a single focal allele quickly becomes intractable if the allele is observed at higher frequencies or if sample size is large, which is particularly problematic if many target sites are considered. For example, if $N = 1,000$, each f_2 variant has $n_c = 2$ and $n_d = 3,996$, whereas each f_{20} variant already has $n_c = 190$ and $n_d = 19,600$.

To make the age estimation analysis computationally tractable, a sampling regime was employed which randomly pairs individual chromosomes drawn from X_c and X_d until a nominal threshold of unique pairs in Ω_c and Ω_d is reached. Note that the rvage algorithm in its current implementation includes all possible concordant pairs in Ω_c , because $\max[n_c]$ is assumed to be reasonably small if the focal allele frequency is low, even in larger samples of thousands of individuals. Hence, the method specifies a sampling threshold as the upper limit of n_d .

5.2.4 Inference of IBD around shared and unshared alleles

The age estimation method relies on the inference of the underlying IBD structure of the sample. In particular, IBD around a given target position is detected in each pair in Ω_c and Ω_d in order to obtain the parameter values required by the clock model used. This is accomplished through the targeted IBD detection methodology incorporated from

the tidy algorithm; namely the FGT, DGT, and the HMM, which detect IBD in pairs of diploid individuals. However, these methods were originally designed to detect IBD segments in individuals sharing a focal allele. While this condition is fulfilled when considering concordant pairs, the IBD detection in discordant pairs is problematic as these are defined by not sharing the focal allele.

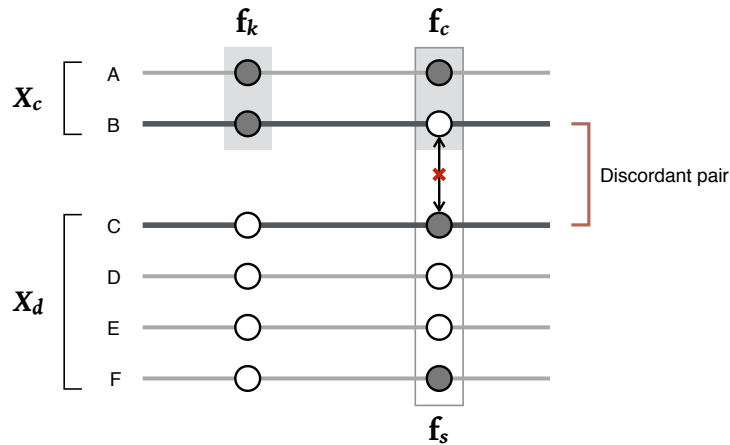


Figure 5.3: Breakpoint detection in discordant pairs. A discordant pair is formed by one haplotype from X_c (which share the focal allele) and one haplotype from X_d (which do not share the focal allele). The lines indicate the chromosomal sequence where the alleles at two sites are indicated; allelic states are distinguished as the ancestral (hollow circle) and derived state (solid). The conditions that lead to the detection of a recombination breakpoint is indicated between the focal site (*left*) and another, distal site (*right*), where f_k denotes the number of allele copies at the focal site within the subsample X_c , f_c denotes the number of allele copies observed at the distal site within the subsample X_c , and f_s denotes the number of allele copies at the distal site within the whole sample. The FGT is passed if all four allelic configurations are observed at four haplotypes in the sample.

Recall that the FGT is applied to the four haplotypes observed in two diploid individuals. A recombination event is inferred to have occurred between two variant sites if all four possible allelic configurations are observed. Let the focal site be denoted by b_i and another, distal site by b_j . In the four haplotypes, the alleles observed at (b_i, b_j) confirm a breakpoint if, for example, $(0, 0)$, $(1, 0)$, $(0, 1)$, and $(1, 1)$ are observed, where 0 denotes the ancestral allelic state and 1 the derived state. Since breakpoints are inferred on both sides of a given focal variant, the genotypes at the focal site are both heterozygous in concordant pairs. But because the two individuals considered in a discordant pair do not share the focal allele, the required configuration cannot be observed.

To maintain the variant-centric concept, breakpoints are detected in discordant pairs as follows. Let f_k denote the number of allele copies at the focal site b_i . At a distal site, b_j , let f_c denote the number of allele copies observed only within the subsample X_c , and f_s the number of allele copies in the whole sample. A recombination breakpoint is indicated at b_j if the two haplotypes carry different alleles and if $f_c < f_k$ and $f_c < f_s$; additionally $f_s > 1$ to exclude singletons and $(f_s - f_c) > (2N - f_k)$ to exclude sites that are monomorphic within X_d , where $2N$ refers to the number of haplotypes in the sample. The condition implies the existence of the four allelic configurations at any of the haplotypes in the sample but is not bound by haplotype occurrence in two diploid individuals. The FGT thereby still holds but is practically inverted. An example is illustrated in Figure 5.3 (page 189).

Note that both the DGT and the HMM-based approach may operate on genotype data alone. Importantly, if haplotype information is not available, the sets X_c and X_d are formed by assigning all individuals that are heterozygous to X_c while all others are assigned to X_d , but excluding individuals that are homozygous for the focal allele. This may reduce the information available from the sample, but the effect is expected to be negligible, in particular if the focal allele is rare. Since haplotype data are required to determine pairwise differences, S , along haplotype sequences, \mathcal{T}_M and \mathcal{T}_{MR} cannot be used with genotype data.

Recall that the DGT is a special case of the FGT which detects breakpoints at genotypic configurations that would also pass the FGT if haplotypes were available. Given the two heterozygous genotypes at the focal variant, a breakpoint is found at a distal site if opposite homozygous genotypes are observed; for example, (1, 0) and (1, 2), where 0 denotes a genotype homozygous for the ancestral allele, 1 a heterozygous genotype, and 2 a genotype homozygous for the derived allele. Again, in discordant pairs, such a configuration cannot be observed. The observation of opposite homozygous genotypes nonetheless implies that the two individuals do not share a haplotype at this site and is therefore also applied for breakpoint detection in discordant pairs.

The HMM-based approach includes a probabilistic model for observing each possible genotype pair in pairs of diploid individuals in *ibd* and *non*, which are the hidden states defined in the underlying IBD model; see Chapter 4. Both the emission and initial

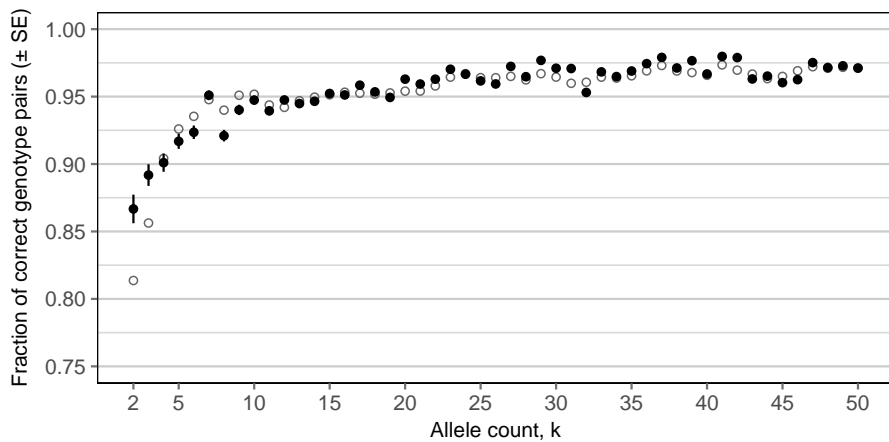


Figure 5.4: Initial state probability of discordant pairs in the Hidden Markov Model (HMM). The proportion of discordant pairs that were correctly identified by their genotypes was empirically determined from data before and after the inclusion of realistic genotype error rates. The mean per f_k was used as the initial state probability of the HMM-based approach for IBD detection around target sites. For comparison, the initial state probability of concordant pairs is shown (hollow circles).

probabilities were determined empirically, from data before and after the inclusion of realistic genotype error rates. The initial state probability corresponds to the probability of correctly observing a concordant pair by allele sharing, *i.e.* the true positive rate of observing heterozygous genotypes at a given target site where both individuals share the focal allele, which was determined per focal allele frequency (f_k). To extend the model to consider discordant pairs, here, initial state probabilities were estimated as the true positive rate of observing the focal allele as a heterozygous genotype in the X_c individual and not observing the focal allele in a homozygous genotype, g_0 , in the X_d individual; again, based on the comparison between genotype data before and after error (using the same dataset as available in Chapter 4). For each f_k category, I randomly selected 1,000 target sites in the dataset before error and randomly selected 1,000 discordant pairs per target site, which I then compared to the genotypes observed in the dataset after error to determine the true positive rate. The mean per f_k was taken as the empirical initial state probability. The resulting probability distribution is shown in Figure 5.4 (this page); the initial state probabilities used for discordant pairs are indicated for comparison. Notably, the discordant probability of initialisation is similar to the concordant one. A possible explanation is that this is particularly driven by the heterozygous status being false.

Anticipated limitations

Since the estimation of allele age is dependent on parameters inferred from the underlying IBD structure of the sample, the accuracy of IBD detection is expected to affect the accuracy of the estimated age.

Possible consequences of inaccurately inferred lengths of IBD segments are summarised in Figure 5.5 (next page), which illustrates a minimal example for the different cases possible when concordant or discordant IBD length is over or underestimated. For instance, in cases where IBD is overestimated in both concordant and discordant pairs (Figure 5.5a), both the the genetic length and the number of pairwise differences, S , may be inflated, which affects the computation of the CCF under the mutation and recombination clock differently. Notably, because the pairwise probability distributions computed by the CCF in the set of pairs are multiplied to calculate the composite likelihood in Equation (5.14), it is possible that some analyses my return invalid results, as probabilities may cancel out or become too small to be distinguishable from zero given machine limits. In the following, the term *conflict* is used to refer to sites at which the analysis returned an invalid age estimate.

5.3 Evaluation

The method was assessed using data generated in coalescent simulations. First, the validity of the method under each clock model was demonstrated based on the true IBD structure of the sample as known from simulation records. Second, the analysis was repeated for each IBD detection method. Third, each approach was then assessed with regard to genotype error, which also considered the effects of phasing error.

5.3.1 Data generation

The performance of the age estimation method was evaluated using several simulated datasets. First, sample data were simulated under a simple demographic model of constant population size ($N_e = 10,000$) with mutation rate $\mu = 1 \times 10^{-8}$ per site per generation

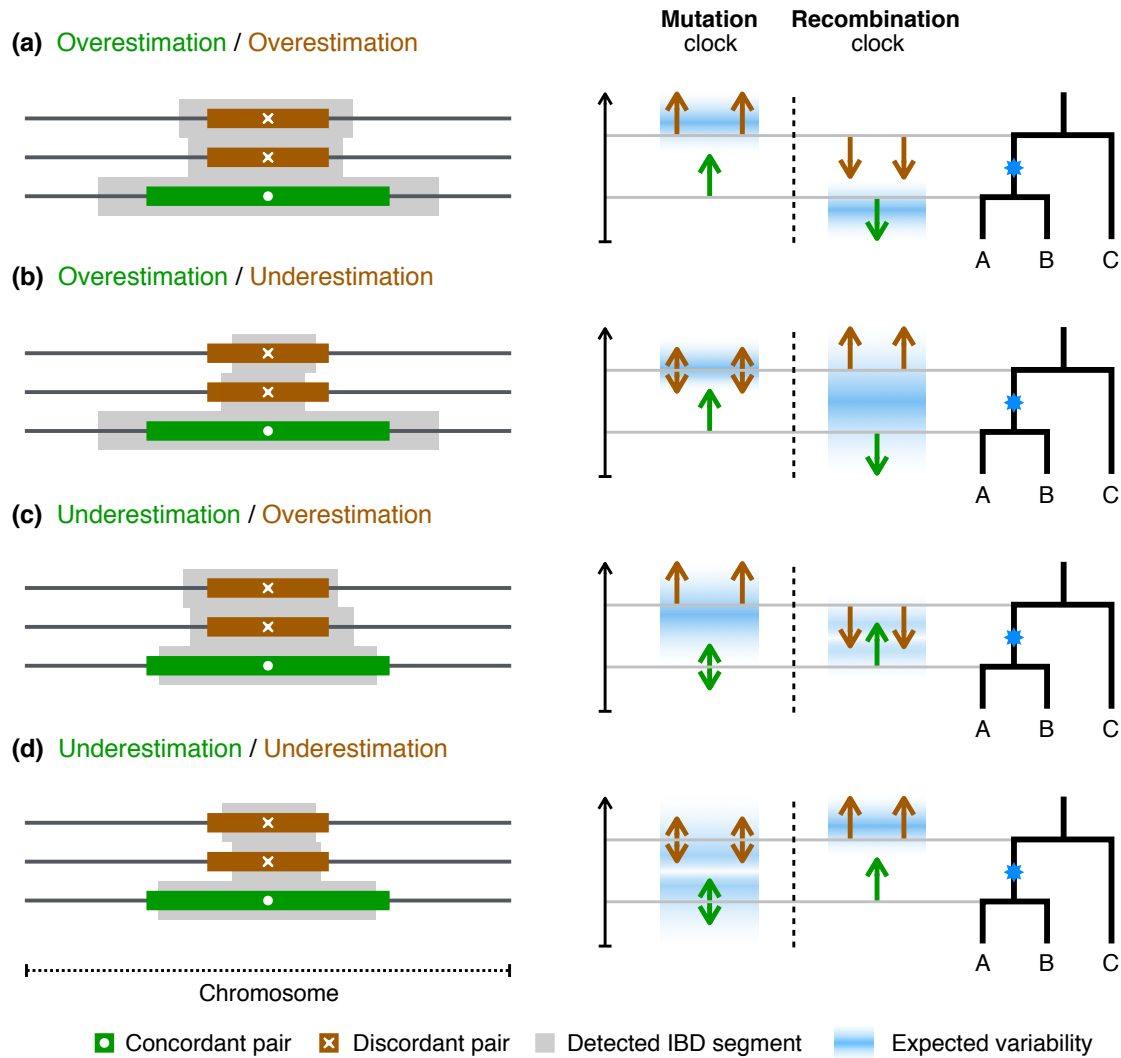


Figure 5.5: Expected estimation bias due to deficient IBD inference. A minimal example is illustrated for a sample of three chromosomes where $A, B \in X_c$ and $C \in X_d$. The focal mutation event is indicated in the genealogy of the sample (star). Each pair shares some haplotype region identical by descent, where the actual extent of the underlying IBD segment is shown for the concordant pair $\{A, B\}$ and the discordant pairs $\{A, C\}$ and $\{B, C\}$; indicated by green and brown bars, respectively. The allele shared in concordant pairs is indicated (circle), as well as the absence of allele sharing in discordant pairs (cross). Inferred IBD segments are shown as grey bars at each true IBD segment, which may overestimate or underestimate the actual shared haplotype length. Panels (a) to (d) illustrate the possible cases of over and underestimation when observed in concordant and discordant pairs. The arrows shown in relation to the times of coalescent events in the genealogy indicate the direction to which the estimation under a given clock model is expected to tend, given the respective pattern of over and underestimation in concordant and discordant pairs. The expected variability of the estimated age posterior distribution is indicated (blue). Note that only the mutation clock, T_M , and the recombination clock, T_R , are shown because T_{MR} is a combination of both models.

and constant recombination rate $\rho = 1 \times 10^{-8}$ per site per generation, using `msprime` (Kelleher *et al.*, 2016). Note that by setting the mutation and recombination rates to constant and equal values, the physical and genetic lengths are identical when measured in Megabase (Mb) and centiMorgan (cM), respectively. The size of the simulated dataset was 2,000 haplotypes, which were randomly paired to form a sample of $N = 1,000$ diploid individuals. The length of the simulated region was 100 Mb (100 cM), resulting in 326,335 variant sites. This dataset is denoted by \mathcal{D}_A .

Second, the dataset simulated in Chapter 3 was included here to evaluate the age estimation method in presence of genotype error. Briefly, the simulation was performed under a demographic model that recapitulates the human expansion out of Africa; following Gutenkunst *et al.* (2009). A sample of 5,000 haplotypes was simulated with $N_e = 7,300$, a mutation rate of $\mu = 2.35 \times 10^{-8}$ per site per generation, and variable recombination rates taken from human chromosome 20; Build 37 of the International HapMap Project (HapMap) Phase II (International HapMap Consortium *et al.*, 2007; International HapMap 3 Consortium *et al.*, 2010), yielding 0.673 million segregating sites over a chromosomal length of 62.949 Mb (108.267 cM). The simulated haplotypes were randomly paired to form a sample of $N = 2,500$ diploid individuals. Haplotype data were converted into genotypes and subsequently phased using SHAPEIT 2 (Delaneau *et al.*, 2008, 2013). Here, this permitted the assessment of the impact of phasing error on the age estimation process.

Third, the dataset described above was retrofitted in Chapter 4 to include realistic proportions of empirically estimated error, which was equally distributed in the derived genotype and haplotype datasets. Here, data *before* and *after* the inclusion of error are distinguished by referring to dataset \mathcal{D}_B and dataset \mathcal{D}_B^* , respectively. Note that in the following the term *genotype error* is used, even in analyses that operate on haplotype data, as error proportions were estimated from misclassified genotypes (see Chapter 4).

In each dataset, simulation records were queried to determine the underlying IBD structure of each pair of individuals analysed in this work. Note that the simulated genealogy underlying \mathcal{D}_B was identical to \mathcal{D}_B^* , such that direct comparisons were possible

between results obtained before and after error. True IBD intervals were found in simulated genealogies by scanning the sequence until the MRCA of a given pair of haplotypes changed, on both sides of a given target position. Interval breakpoints were identified on basis of the observed variant sites in the sample, such that the resulting true IBD segment defined the smallest interval detectable from available data. Note that this allowed overestimation of the actual genetic length of the IBD segment, but thereby provided a realistic benchmark for comparisons with IBD detection methods; namely the FGT, DGT, and the HMM-based approach as implemented in the `rvage` algorithm.

5.3.2 Accuracy analysis

Coalescent simulators may not define the exact time point at which a mutation event occurred, because mutations are independent of the genealogical process (if simulated under neutrality) and can therefore be placed randomly along the branches of the simulated tree; *i.e.* mutation times are not specified in `msprime`, but the times of coalescent events are recorded. In simulations, the probability of placing a mutation on a particular branch is directly proportional to its length, which itself is delimited by the time of the coalescent event below (joining the lineages that derive from that branch) and the time of the coalescent event above (joining that branch with the tree back in time). Here, the times of coalescence below and above a particular mutation event are denoted by t_c and t_d , respectively, against which the accuracy of the estimated allele age is measured.

Although the true time of a mutation event was not known from the simulations performed, an indicative value for the age of an allele was derived from the logarithmic “midpoint” (or *log-average*) between coalescent events, which is denoted by t_m and calculated as the geometric mean of t_c and t_d ; see below.

$$t_m = \exp \left[\log [t_c] + \frac{1}{2} \left(\log [t_d] - \log [t_c] \right) \right] = \sqrt{t_c t_d} \quad (5.19)$$

Accuracy was measured using Spearman’s rank correlation coefficient, r_s , which is a robust measure for the strength of the monotonic relationship between two variables;

i.e. the inferred allele age (\hat{t}) and true time proxies (t_c , t_m , or t_d). Note that the squared Pearson correlation coefficient, r^2 , was used in previous chapters but is less suitable here, as both the inferred and true age are expected to vary on log-scale, and the Pearson coefficient measures the linear relationship between variables.. In addition, the root mean squared logarithmic error (RMSLE) was calculated as a descriptive score for the magnitude of error (here defined on \log_{10}).

To better illustrate the distribution of age estimates obtained in an analysis, the *relative age* was computed, \hat{t}_{rel} , for each allele by normalising the time scale conditional on the time interval between the coalescent events at t_c and t_d , such that age estimates were “mapped” on the same scale relative to the branch length spanned between t_c and t_d ; this was calculated as below.

$$\hat{t}_{rel} = \frac{\log\left[\frac{\hat{t}}{t_c}\right]}{\log\left[\frac{t_d}{t_c}\right]} \quad (5.20)$$

As a result, the times of coalescent events at t_c and t_d are mapped to 0 and 1, respectively. An age estimate is defined as being “correct” if $t_c \leq \hat{t} \leq t_d$, which is equal to the condition $0 \leq \hat{t}_{rel} \leq 1$, such that $\hat{t}_{rel} < 0$ indicates underestimation and $\hat{t}_{rel} > 1$ overestimation in relation to the true interval in which the mutation event could have occurred.

5.4 Results

In each dataset, 10,000 rare variants were randomly selected as target sites for estimation of allele age. These were selected at shared allele frequency $\leq 1\%$, *i.e.* $f_{[2,20]}$ variants, in \mathcal{D}_A . Identical sets of target sites were randomly selected in \mathcal{D}_B and \mathcal{D}_B^* , at shared allele frequency $\leq 0.5\%$ ($f_{[2,25]}$ variants). Note that these were sampled from the subset of variants unaffected by genotype error, to ensure that alleles correctly identified haplotype sharing.

5.4.1 Validation of the method under different thresholds

Because an exhaustive analysis of all possible discordant pairs becomes computationally intractable, it is convenient to reduce the number of pairwise analyses that are conducted per target allele. For example, although the sample size of dataset \mathcal{D}_A was modest ($N = 1,000$), the total number of possible pairwise analyses for the set of 10,000 selected rare variants would have been 145.725 million. For realistic applications of the method, it is therefore essential to limit the number of discordant pairs, n_d , such that Ω_d consists of a substantially smaller set of randomly formed pairs. In this section, I analyse the impact on the accuracy of estimated allele age under different nominal thresholds of n_d (listed below). Importantly, to focus on the impact resulting from different n_d thresholds, the analysis was conducted using true IBD segments as determined from simulation records. Thus, this section provides a general validation analysis of the age estimation method.

n_d	Pairwise analyses
10	0.462 million
50	0.862 million
100	1.362 million
500	5.362 million
1,000	10.366 million

Each clock model was considered separately and the same set of 10,000 target sites was analysed under each threshold. This resulted in a total of 276.133 million pairwise analyses in this section alone. None of the analyses returned conflicting results; recall that *conflicts* were defined as invalid estimates resulting from erroneous patterns of coalescent times as computed through the CCF for the set of pairs considered. Note that discordant pairs were formed randomly and therefore differed in each analysis. The results are illustrated in Figure 5.6 (next page), which shows the density of true and estimated age under each clock model; results are shown for $n_d = 10$, $n_d = 100$, and $n_d = 1,000$, to better distinguish differences visually. Note that true age is set at t_m , but t_c and t_d are indicated in Figure 5.6.

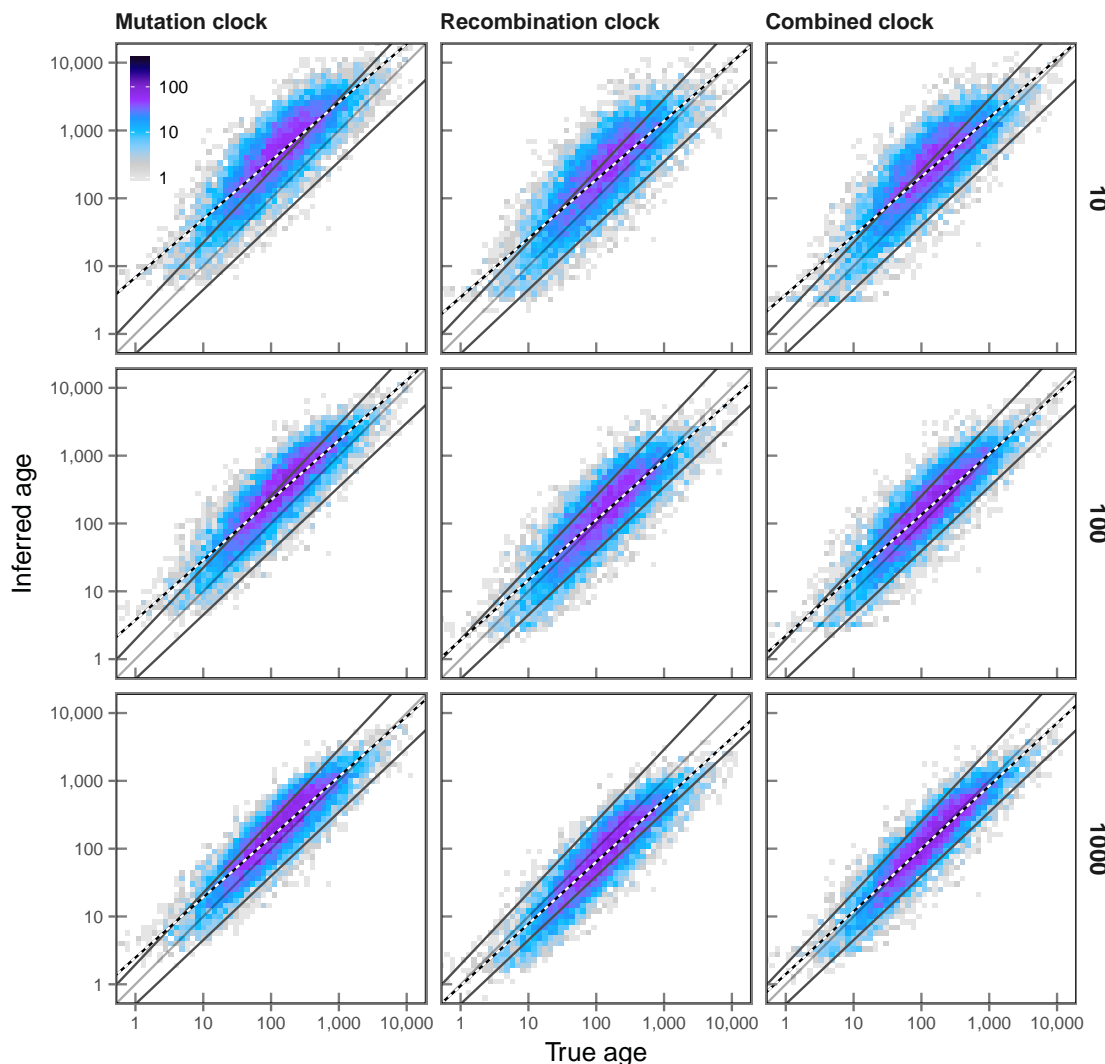


Figure 5.6: True and inferred age under varying numbers of discordant pairs. A set of 10,000 target sites was randomly drawn in $f_{[2,20]}$ (shared allele frequency $\leq 1\%$) in a simulated sample of 2,000 haplotypes. Different numbers of sampled discordant pairs were analysed on the same set of target variants, which is shown for $n_d = 10$, $n_d = 100$, and $n_d = 1,000$ (indicated at the right of each row). True IBD was used to estimate allele age. IBD breakpoints were determined from simulation records and defined as the first variant sites observed in the data following the two recombination events on each side of a given focal position. Age was estimated under each of the three clock models; *i.e.* mutation clock, T_M , recombination clock, T_R , and combined clock, T_{MR} (indicated at the top of each column). Each panel shows the density distribution of true and inferred age (numbers indicated by the colour-gradient). The true age of a focal allele was set at t_m , which is the geometric mean of t_c and t_d , *i.e.* the true time of the coalescent event from which the focal allele derived (t_c) and the true time of the coalescent event immediately preceding that event (t_d) in the history of the sample; these are indicated by their linear regression trend lines *below* and *above* the dividing line at t_m , respectively. The *black-white* line indicates the line of best fit resulting from linear regression of age estimates, using the posterior mode of the composite likelihood distribution as the inferred age value. Note that both true and inferred age are compared on log-scale, as the time to a coalescent event is expected to increase exponentially back in time.

Despite the substantial difference in the number of pairwise analyses, overall accuracy was high for each threshold and under each clock model. A higher n_d threshold was generally found to improve overall accuracy. At lower thresholds, each model showed a tendency to overestimate allele age, which most likely resulted from the smaller set of discordant pairs, as the individuals that are more closely related to the focal haplotypes may or may not be captured.

Interestingly, the recombination clock, \mathcal{T}_R , showed a tendency to underestimate allele age at higher thresholds, despite using true IBD segments. This observation may be the result of an overestimation of true IBD lengths, since IBD breakpoints were determined from the set of variant sites observed in the data, to provide a realistic benchmark for comparisons with IBD detection methods (see next section). Note that allele age is generally expected to be underestimated if genetic lengths in concordant or discordant pairs are overestimated, as a longer IBD segment is indicative for more recent haplotype sharing (*i.e.* recombination had less time the break down the length of a shared haplotype). The average distance between consecutive variant sites in \mathcal{D}_A was 3.064×10^{-4} cM (306.431 basepairs), showing that even small inaccuracies in IBD can affect the estimation of allele age (under the recombination clock).

The proportion of target alleles for which age was correctly estimated increased with higher n_d thresholds under each clock model. This was lowest in \mathcal{T}_M , where 36.610 %, 51.110 %, and 66.280 % were correctly inferred for n_d at 10, 100, and 1,000, respectively, and relatively high in \mathcal{T}_R , where 55.790 %, 70.600 %, and 70.510 % were correct, respectively. The highest proportion of correct alleles was 79.930 % in \mathcal{T}_{MR} and $n_d = 1,000$. The proportion of overestimated alleles ($\hat{t} > t_d$) decreased in all clock models at higher n_d thresholds, showing a modest decrease in \mathcal{T}_M (63.380 % to 32.660 % for n_d at 10 and 1,000, respectively), a substantial decrease in \mathcal{T}_R (43.450 % to 6.450 %, respectively), and a notable decrease in \mathcal{T}_{MR} (46.780 % to 15.640 %, respectively). Since \mathcal{T}_M showed a tendency to overestimate allele age, the proportion of underestimated alleles was low (1.060 % for $n_d = 1,000$), which was similarly low in \mathcal{T}_{MR} (4.430 %), and highest in \mathcal{T}_R (23.040 %).

Table 5.1: Estimation accuracy under varying numbers of discordant pairs. Different thresholds for the number of randomly formed discordant pairs, n_d , were analysed to evaluate the impact on the accuracy of allele age estimation. Note that all possible concordant pairs were included in each analysis; *i.e.* n_c was not reduced. True IBD segments were used to focus on the differences induced by varying n_d thresholds. Each analysis was conducted on the same set of 10,000 randomly selected rare variants at allele frequency $\leq 1\%$. Accuracy was measured using the rank correlation coefficient, r_S , and the magnitude of error, RMSLE, between the estimated age, \hat{t} and the times of coalescent events; *i.e.* the time until all haplotypes in X_c have coalesced, t_c , and the time of the immediately preceding coalescent event, t_d , which joined the lineages in X_c and X_d back in time, as well as the geometric mean of both, t_m .

Clock	n_d	Rank correlation (r_S)			RMSLE		
		t_c	t_m	t_d	t_c	t_m	t_d
\mathcal{T}_M	10	0.907	0.842	0.632	0.963	0.624	0.574
	50	0.918	0.872	0.674	0.823	0.487	0.528
	100	0.920	0.884	0.692	0.763	0.431	0.521
	500	0.920	0.907	0.731	0.626	0.308	0.533
	1,000	0.923	0.904	0.723	0.606	0.299	0.547
\mathcal{T}_R	10	0.881	0.816	0.612	0.714	0.443	0.609
	50	0.889	0.844	0.651	0.578	0.349	0.633
	100	0.892	0.857	0.671	0.519	0.319	0.653
	500	0.892	0.886	0.720	0.390	0.304	0.728
	1,000	0.889	0.895	0.739	0.345	0.329	0.772
\mathcal{T}_{MR}	10	0.891	0.829	0.624	0.745	0.455	0.589
	50	0.901	0.865	0.675	0.624	0.348	0.586
	100	0.905	0.881	0.699	0.574	0.309	0.593
	500	0.909	0.914	0.753	0.469	0.243	0.626
	1,000	0.911	0.914	0.751	0.464	0.243	0.629

A complete summary of results is given in Table 5.1 (this page). Throughout, rank correlation (r_S) was highest for $n_d = 1,000$; see Table 5.1. However, for all thresholds, correlations with t_c were higher than correlations with t_m , which in turn were higher than correlations with t_d . Such a pattern may be expected as the number of concordant pairs, n_c , was not reduced, such that the t_c was inferred with higher accuracy. Highest accuracy was seen for the mutation clock model, \mathcal{T}_M , where r_S for $n_d = 1,000$ was 0.923, 0.904, and 0.723 for t_c , t_m , and t_d , respectively. By comparison, the recombination clock, \mathcal{T}_R , yielded the lowest levels of overall accuracy at each threshold, but did not differ markedly from \mathcal{T}_M ; *e.g.* r_S for $n_d = 1,000$ was 0.889, 0.895, and 0.739 for t_c , t_m , and t_d , respectively. The combined clock, \mathcal{T}_{MR} , was found to be more accurate for t_m and t_d at higher thresholds. The magnitude of error, measured by RMSLE scores, was lowest for t_m , indicating that

the majority of alleles were correctly dated between t_c and t_d ; except in \mathcal{T}_M for $n_d = 10$, in which allele age was overestimated and therefore closer to t_d .

The difference between $n_d = 500$ and $n_d = 1,000$ was small overall (see Table 5.1), suggesting that further improvements in accuracy may not be attained by increasing the threshold.

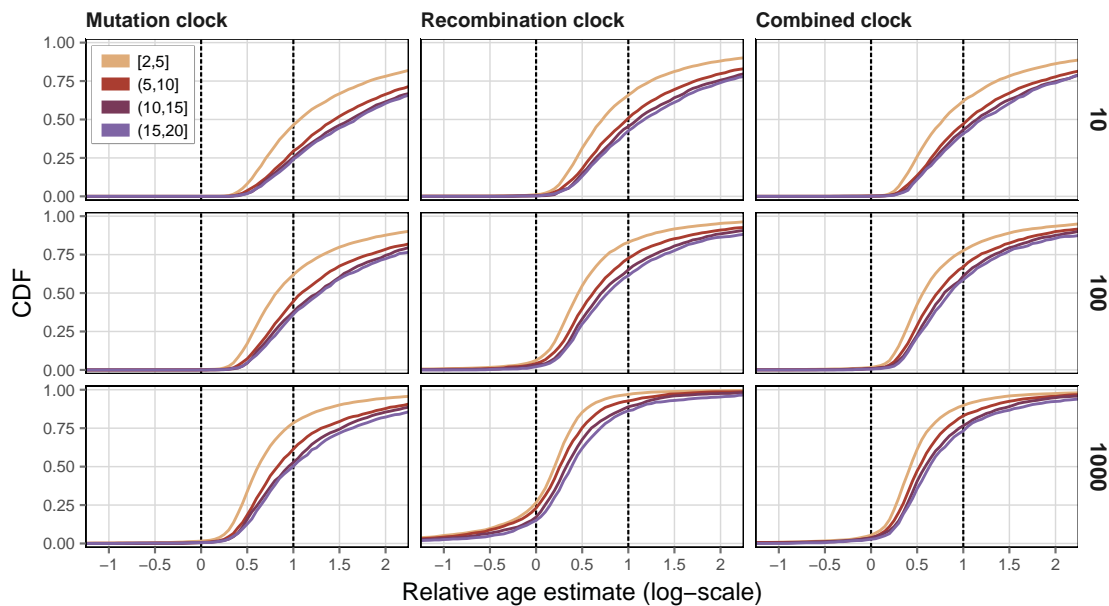


Figure 5.7: Relative age under varying numbers of discordant pairs. A randomly drawn set of 10,000 target sites at allele frequency $\leq 1\%$, i.e. $f_{[2,20]}$, was analysed under each of the three clock models (indicated at the top of each column) and with different numbers of sampled discordant pairs; $n_d = 10$, $n_d = 100$, and $n_d = 1,000$ (indicated at the right of each row). The analysis was conducted using the true IBD breakpoints as derived from simulation records, defined as the first variant sites observed in the data that immediately follow the two recombination events on each side distal to a given focal site. The relative age, \hat{t}_{rel} , was calculated as given in Equation (5.20), such that the true times of concordant and discordant coalescent events, t_c and t_d , sit at 0 and 1, respectively (dashed lines). Note that \hat{t}_{rel} is defined on log-scale. The CDF of relative age estimates is shown per f_k group, where target variants were pooled by their allele count in the data, in ranges of $f_{[2,5]}$, $f_{(5,10]}$, $f_{(10,15]}$, and $f_{(15,20]}$.

A comparison of the inferred age distributions at distinct f_k ranges is presented in Figure 5.7 (this page), again shown for $n_d = 10$, $n_d = 100$, and $n_d = 1,000$. Notably, the accuracy of target alleles at lower frequencies was overall higher compared to alleles observed at higher frequencies. This difference was consistent across n_d thresholds under the mutation clock model, \mathcal{T}_M . For example, at $n_d = 10$, the proportion of correctly dated

alleles was higher in the $f_{[2,5]}$ range (48.356 %) compared to alleles at $f_{(5,10]}$ (29.445 %). At $n_d = 1,000$, overall accuracy was increased but the difference for alleles at lower and higher frequencies remained; *i.e.* 77.819 % and 60.834 % at $f_{[2,5]}$ and $f_{(5,10)}$, respectively. Under the recombination clock model, T_R , these differences were reduced at higher n_d thresholds. At $n_d = 10$, 66.608 % and 50.344 % of alleles were correctly dated at $f_{[2,5]}$ and $f_{(5,10)}$, respectively, whereas at $n_d = 1,000$ these proportions were 72.258 % and 69.826 % at the same frequency ranges, respectively.

In summary, these results demonstrate that the method as well as the clock models proposed are able to estimate allele age from IBD information alone, without prior knowledge of the demographic history of the sample. However, because data were simulated under a simple demographic model (dataset \mathcal{D}_A), further evaluation is appropriate (*e.g.* using datasets \mathcal{D}_B and \mathcal{D}_B^* ; see further below). The analysis considered true IBD segments and therefore evaded the effects that would result from inexact IBD detection. Since true IBD was determined conditional on the observed variation in the data, the analysis reflected the practical feasibility of age estimation given available data.

The implemented sampling process seeks to find a compromise between computational tractability and the chance of randomly selecting haplotypes that are informative for the estimation. However, ideally, to minimise the computational burden while simultaneously improving estimation accuracy, it would be desirable to consider the nearest neighbours to the focal shared haplotypes in the local genealogy. If the nearest neighbours are found among the haplotypes in X_d and paired with the focal haplotypes in X_c they are likely to coalesce at t_d and are therefore most informative for the estimation of focal allele age. For instance, a simple approach would be to compute the Hamming distance between haplotypes in X_c and X_d within a short region around the position of a given target site, such that a subset of presumed nearest neighbours can be selected based on a distance ranking. In practice, however, there are three caveats to such an approach.

First, it would be computationally expensive to conduct an additional pairwise analysis for the (whole) sample at each target site, which may not outweigh the improvement gained through the reduction of n_d . Second, the identification of nearest neighbours

may be less accurate if only genotype data are available. Both the DGT and the HMM-based approach implemented in *rvage* are able to infer IBD in absence of haplotype information; thus, a method to identify nearest neighbours in genotype data would be required to achieve full compatibility with the algorithm. Regardless, third, a dilemma arises in presence of genotype error, as the identification of nearest neighbours is likely to give preference to haplotypes in which the focal allele has been missed. Such *false negatives* distort the estimation of allele age as the CCF computed for false discordant pairs would bias (or cancel out) the resulting composite likelihood distribution. In such cases, the estimated age is expected to be approximately equal to or smaller than t_c , such that \hat{t} is likely to be underestimated.

It is important to note that the problem of finding false negatives in the data (if genotype error is present) cannot be avoided if discordant pairs are formed by a random sampling process, but the chance of including false negatives is reduced if n_d is small in comparison to the (haploid) sample size. Hence, the n_d threshold defines a balance between accuracy and expected bias. Subsequent analyses were conducted using a threshold equal to the diploid sample size, N ; that is $n_d = 1,000$ in analyses using \mathcal{D}_A , and $n_d = 2,500$ using \mathcal{D}_B or \mathcal{D}_B^* . Since the results presented in this section were obtained on true IBD information, they serve as a benchmark against which different IBD detection methods are compared in the section below.

5.4.2 Comparison of IBD detection methods

The *tidy* algorithm for targeted IBD detection (see Chapters 3 and 4) was fully integrated in *rvage*, such that the FGT, DGT, and the HMM-based approach were available for the inference of IBD segments around focal variants. Note that genotype data are sufficient for IBD detection using the DGT and HMM, but haplotypes are required for estimation under the mutation clock model; *i.e.* to count pairwise differences, S , along haplotype sequences. Thus, analyses were conducted on the simulated haplotype dataset (\mathcal{D}_A), but haplotype phase was ignored during IBD detection in the DGT and HMM. The parameters required by the *rvage* algorithm were specified accordingly with simulation

parameters ($N_e = 10,000$; $\mu = 1 \times 10^{-8}$ per site per generation; $\rho = 1 \times 10^{-8}$ per site per generation). Here, because simulated data did not include genotype error, theoretical emission model was used in the HMM.

The results presented in this section were obtained on the previously selected 10,000 rare allele target sites, which were analysed using each of the three IBD detection methods and under each clock model, resulting in a total of 93.295 million pairwise analyses. The fraction of conflicting age estimates differed by clock model as well as IBD detection method; no conflicting estimates were returned when true IBD was used. Under the mutation clock, \mathcal{T}_M , analyses using the FGT returned 1.809 % conflicts. This fraction was higher using the DGT and HMM, with 2.601 % and 2.327 %, respectively. Conflicts were seen less under the recombination clock, \mathcal{T}_R , where none were returned using the FGT, but 0.010 % and 0.030 % using the DGT and HMM. The fraction under the combined clock, \mathcal{T}_{MR} , was smaller compared to \mathcal{T}_M , with 1.097 %, 2.266 %, and 1.819 % of conflicted sites using the FGT, DGT, and HMM, respectively. The remaining sites were intersected to compare clock models and IBD methods on the same set of target sites, retaining 9,434 variants.

The density distribution of true and inferred allele age is given in Figure 5.8 (next page). In all three methods, a tendency to overestimate allele age was seen, in particular under the mutation clock, \mathcal{T}_M . This overestimation was elevated when the DGT was used, and less prominent for the FGT or HMM. The latter methods showed similar age distributions in \mathcal{T}_M and under the combined clock model, \mathcal{T}_{MR} , in which alleles appeared to be less overestimated. Under the recombination clock, \mathcal{T}_R , alleles were underestimated in each method, but more severely in both the DGT and HMM.

Specifically, the method with the highest proportion of correctly estimated alleles was the FGT in all three clock models, where accuracy was highest under the recombination clock, \mathcal{T}_R , at 72.610 %, and lowest under the mutation clock, \mathcal{T}_M , with 34.460 %; under the combined clock, \mathcal{T}_{MR} , 55.395 % of alleles were correctly estimated when the FGT was used. The HMM achieved similar levels of accuracy, but the accuracy in \mathcal{T}_R was noticeably reduced (10.950 %) compared to \mathcal{T}_{MR} (51.876 %) and \mathcal{T}_M 32.415 %. Throughout, the lowest

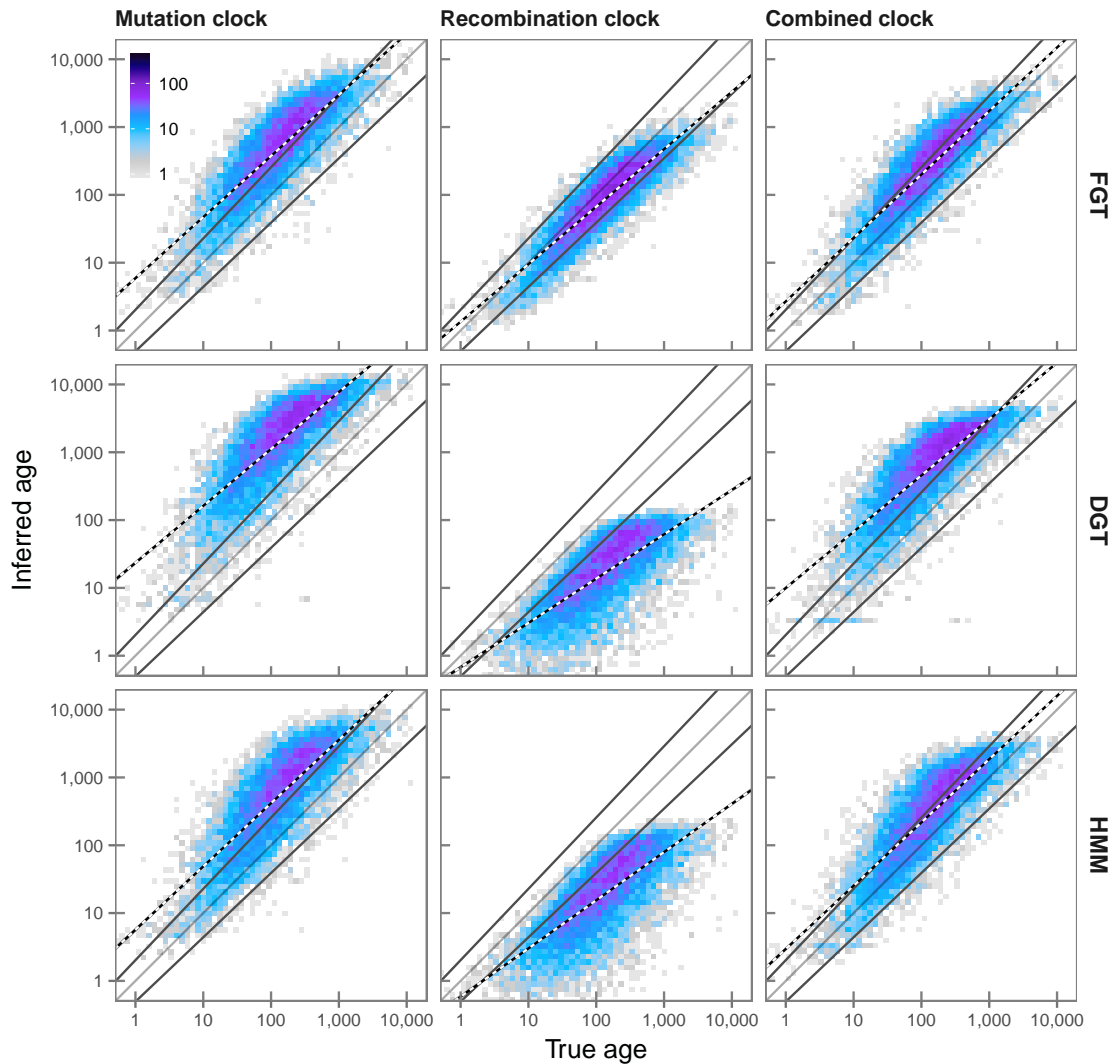


Figure 5.8: Distribution of true and inferred age using different IBD detection methods. The three IBD detection methods implemented in rvage were compared, *i.e.* FGT, DGT, and HMM (indicated at the *right* of each row), under each clock model (indicated at the *top* of each column). Analyses were compared on the same set of 9,434 target sites that were drawn from available $f_{[2,20]}$ variants in the simulated dataset of 2,000 haplotypes (allele frequency $\leq 1\%$). Each panel shows the density of true age (t_m) and inferred age (numbers indicated by the colour-gradient). Lines *below* and *above* the dividing line are regression trend lines of the corresponding true coalescent times around each mutation event, t_c and t_d , respectively. The regression trend line of inferred age (\hat{t}) is indicated by the *black-white* line, using the posterior mode of the composite likelihood estimation as the inferred age value.

proportions of correctly inferred alleles were found for the DGT, which also showed the lowest accuracy in \mathcal{T}_R (8.226 %) and comparatively low levels of accuracy in \mathcal{T}_M and \mathcal{T}_{MR} (14.554 % and 29.659 %, respectively). Overestimation of allele age was highest in \mathcal{T}_M , where 65.084 %, 85.277 %, and 66.960 % of alleles were underestimated by the FGT, DGT, and HMM, respectively. Conversely, the proportion of underestimated alleles was lowest in \mathcal{T}_M , at $\leq 1\%$ in each method, and similarly low in \mathcal{T}_{MR} with $\leq 2\%$ in each method. In contrast, alleles were markedly underestimated in \mathcal{T}_R ; the FGT resulted in 20.140 % of underestimated alleles, whereas 91.753 % and 88.934 % of alleles were underestimated when the DGT and the HMM were used for IBD inference, respectively.

Table 5.2: Estimation accuracy per IBD detection method. The accuracy was measured in analyses based on IBD detected by different methods; namely the FGT, DGT, and the HMM-based approach. See Table 5.1 (page 200) for comparison to results obtained using true IBD segments (for $n_d = 1,000$).

Clock	Method	Rank correlation (r_S)			RMSLE		
		t_c	t_m	t_d	t_c	t_m	t_d
\mathcal{T}_M	FGT	0.841	0.839	0.686	1.011	0.653	0.554
	DGT	0.830	0.813	0.650	1.460	1.086	0.832
	HMM	0.806	0.806	0.662	1.078	0.725	0.607
\mathcal{T}_R	FGT	0.899	0.887	0.718	0.339	0.330	0.775
	DGT	0.820	0.749	0.554	0.577	0.941	1.396
	HMM	0.821	0.751	0.556	0.533	0.892	1.348
\mathcal{T}_{MR}	FGT	0.863	0.873	0.723	0.755	0.422	0.524
	DGT	0.840	0.829	0.669	1.083	0.727	0.600
	HMM	0.826	0.834	0.692	0.806	0.485	0.554

The accuracy measured for each analysis is summarised in Table 5.2 (this page). The FGT under the recombination clock model, \mathcal{T}_R , showed a higher correlation and slightly reduced error with regard to t_d . There, rank correlation was $r_S = 0.899$ for the FGT and $r_S = 0.889$ for true IBD; likewise the magnitude of error (RMSLE) was 0.339 and 0.345 for FGT and true IBD, respectively. However, note that a higher accuracy at t_c does not necessarily reflect an improvement in the estimation of actual allele age. For example, the accuracy with regard to t_m or t_d was lower for the FGT compared to true IBD. In comparison to the other detection methods, the FGT outperformed both the DGT and

HMM with regard to each time measure. The HMM showed slightly higher levels of accuracy than the DGT in \mathcal{T}_R , where r_S was higher and RMSLE lower in terms of each time measure for the HMM. Similarly, in both \mathcal{T}_M and \mathcal{T}_{MR} , RMSLE scores were lower for the HMM compared to the DGT, whereas r_S measures were similar.

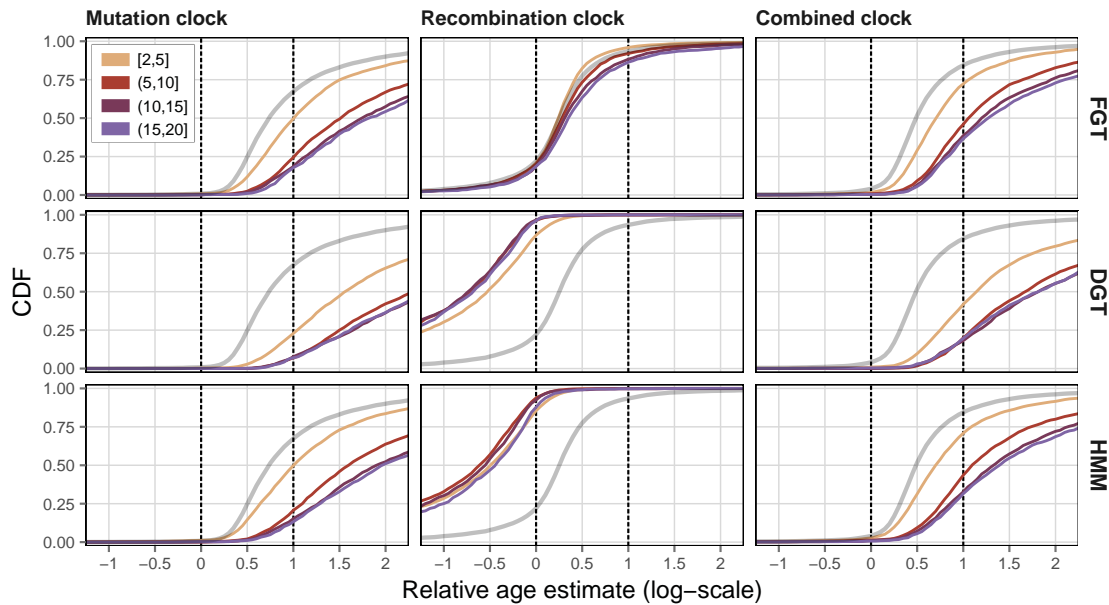


Figure 5.9: Relative age using different IBD detection methods. The three IBD detection methods implemented in rvage were compared, *i.e.* FGT, DGT, and HMM (indicated at the *right* of each row), under each clock model (indicated at the *top* of each column). The relative age, \hat{t}_{rel} , was calculated as given in Equation (5.20), such that t_c and t_d sit at 0 and 1, respectively (*dashed* lines). The CDF of relative age estimates is shown for different frequency ranges; namely $f_{[2,5]}$, $f_{(5,10]}$, $f_{(10,15]}$, and $f_{(15,20]}$.

Relative age estimates are shown for distinct f_k ranges in Figure 5.9 (this page), where the relative age of true IBD is indicated for comparison per clock model (calculated on the full f_k range). Analyses under the mutation clock and the combined clock models, \mathcal{T}_M and \mathcal{T}_{MR} , showed a substantial difference between alleles at lower and higher frequencies; *e.g.* overall accuracy of $f_{[2,5]}$ variants was increased compared to f_k variants at higher frequencies in each method. This difference was reduced under the recombination clock model, \mathcal{T}_R , but the DGT showed an accuracy decrease for $f_{[2,5]}$ variants.

The distribution of IBD lengths inferred using the FGT, DGT, and the HMM-based approach are shown in Figure 5.10 (next page). Segments inferred using the HMM were

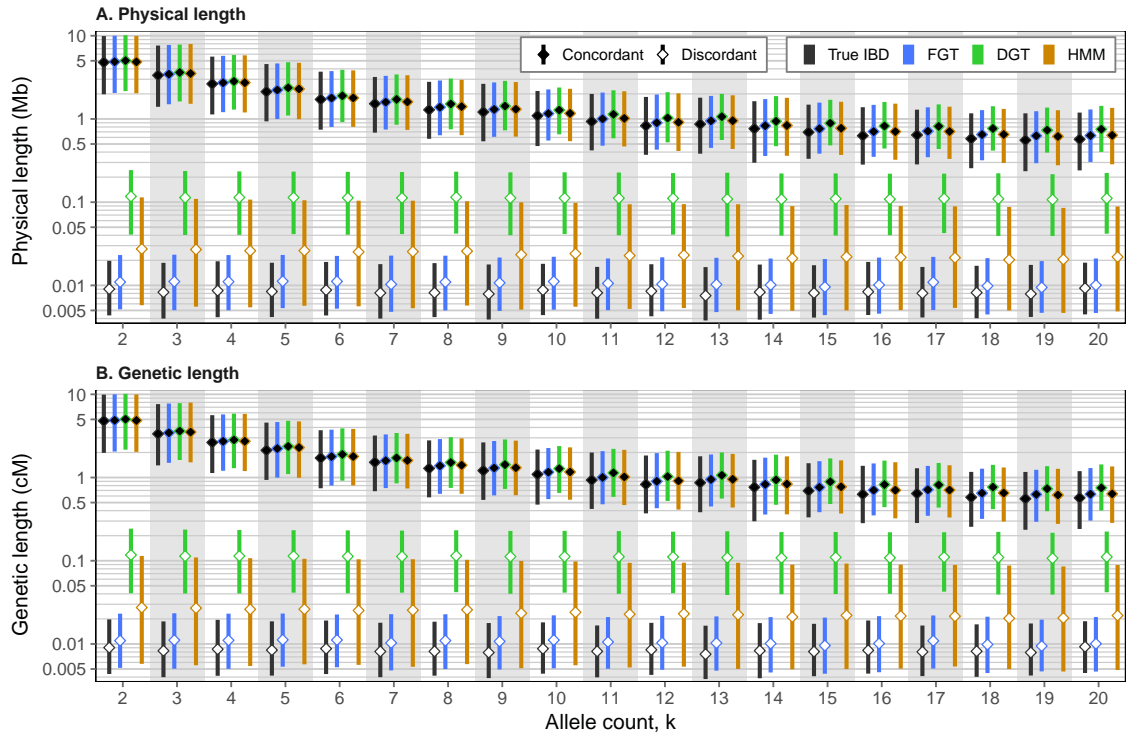


Figure 5.10: Length distribution of inferred IBD segments. Bottom and top of each bar indicate 1st and 3rd quartiles, respectively, between which the median (2nd quartile) is marked (*diamonds*). IBD detected for concordant and discordant pairs is distinguished; *solid* and *hollow* diamonds, respectively.

close to those detected using the FGT in concordant pairs. However, for discordant pairs, only the FGT produced IBD segments that were close to the length distribution of true IBD segments. The DGT showed the highest degree of overestimation for both concordant and discordant pairs.

In summary, these results suggest that the accuracy of estimated allele age is crucially dependent on correct inference of the underlying IBD structure. The overestimation of IBD lengths, which is generally expected for each method, affected each clock model differently. While \mathcal{T}_M overall resulted in an overestimation of allele age when IBD is overestimated, this pattern was reversed in \mathcal{T}_R . Although both models are combined in \mathcal{T}_{MR} , the impact of mutational differences, seen at the overestimated regions of detected IBD segments, was substantial and could not be mitigated by considering recombinational length. Further, I confirmed that the FGT was the best performing method for the targeted detection of IBD segments, in that the estimation of allele age was similar to

the expectations defined by true IBD information. However, the estimation was more accurate for target sites at lower allele frequencies. The DGT was least accurate in terms of estimated allele age in this comparison.

Recall that the probabilistic model of the HMM was developed to overcome the effects of genotype error encountered in real data (see Chapter 4). Thus, the results in this section reflect theoretical limitations of age estimation given IBD detected in flawless data, but may change drastically in presence of genotype error. This was explored in the section below.

5.4.3 Impact of genotype error on allele age estimation

The allele age estimation method was evaluated under each clock model and each method for IBD detection, on data before and after the inclusion of genotype error; *i.e.* using datasets \mathcal{D}_B and \mathcal{D}_B^* , respectively. Each analysis was performed on the same set of 10,000 target sites selected at $f_{[2,25]}$ in a sample of $N = 2,500$ diploid individuals, using a threshold of $n_d = 2,500$, which amounted to 25.281 million pairwise analyses per comparison. The FGT was applied to both the simulated (*true*) haplotypes as well as phased haplotype data. The HMM used theoretical emission model in analyses on \mathcal{D}_B and the empirical error model in analyses on \mathcal{D}_B^* . To enable direct comparisons, true IBD segments were determined from simulation records and separately analysed on the same number of concordant and discordant pairs in data before and after error. In total, for the results presented in this section, 758.437 million pairwise analyses were conducted.

Table 5.3: Conflicted estimates in analyses before and after error.

Method	Conflicts before error (%)			Conflicts after error (%)		
	\mathcal{T}_M	\mathcal{T}_R	\mathcal{T}_{MR}	\mathcal{T}_M	\mathcal{T}_R	\mathcal{T}_{MR}
FGT*	6.396	0.000	3.695	5.131	0.141	2.189
FGT**	6.587	0.422	4.388	4.940	0.341	3.123
DGT	10.945	0.161	8.384	5.211	1.767	3.956
HMM	5.884	0.392	4.418	13.335	0.823	9.268
True IBD	0.000	0.000	0.000	9.583	0.000	1.030

* FGT applied to true haplotypes

** FGT applied to phased haplotypes

As in the previous section, some of the analyses returned conflicting estimates; see Table 5.3. Again, no conflicts were seen when true IBD information was used. However, this changed after the inclusion of genotype error; the fraction of conflicting estimates was high in \mathcal{T}_M , zero in \mathcal{T}_R , and small in \mathcal{T}_{MR} . Before error, the largest fraction of conflicts was seen for the DGT in \mathcal{T}_M . Data from analyses before and after error were intersected across results obtained under each clock model and for each IBD method, which retained a set of 5,015 identical target sites. A complete summary of the accuracy per analysis is given below in Table 5.4 (page 220).

Estimation based on the true IBD structure of the sample is compared before and after error in Figure 5.11a (next page). The most striking discovery is the extent of overestimation after error under the mutation clock model, \mathcal{T}_M , which was similarly high in the combined clock, \mathcal{T}_{MR} . Alleles were overestimated because the presence of misclassified alleles substantially increased the number of observed mutational differences, S , along the sequence. For example, accuracy decreased in \mathcal{T}_M from $r_S = 0.870$ to $r_S = 0.518$ with regard to t_c , before and after error respectively, similarly in \mathcal{T}_{MR} , where r_S at t_c decreased from 0.884 to 0.593, respectively. The proportion of correctly estimated alleles ($t_c < \hat{t} < t_d$) in \mathcal{T}_M was 75.394 % before and 24.068 % after error, which was similar in \mathcal{T}_{MR} , where 80.518 % of alleles were correct before but only 39.402 % after error. The proportion of overestimated alleles was 18.046 % in \mathcal{T}_M and 9.212 % in \mathcal{T}_{MR} before error, but 74.397 % and 57.926 %, respectively, after error. Note that this did not vary noticeably by focal allele frequency; for example, the proportion of overestimated alleles in \mathcal{T}_M was 75.659 % at lower frequencies ($f_{[2,5]}$) and 79.375 % at higher frequencies ($f_{[20,25]}$), which was also the case in \mathcal{T}_{MR} , where 61.831 % and 1.250 % of alleles were overestimated at $f_{[2,5]}$ and $f_{[20,25]}$, respectively.

In contrast, the estimation under the recombination clock model, \mathcal{T}_R , was not affected by genotype error, due to using true IBD information to derive recombinational segment lengths. Note that analyses were performed on the same sets of concordant and discordant pairs, which is why the results in \mathcal{T}_R are identical before and after error. As in the previous analysis, alleles showed a tendency to be underestimated in \mathcal{T}_R . The average

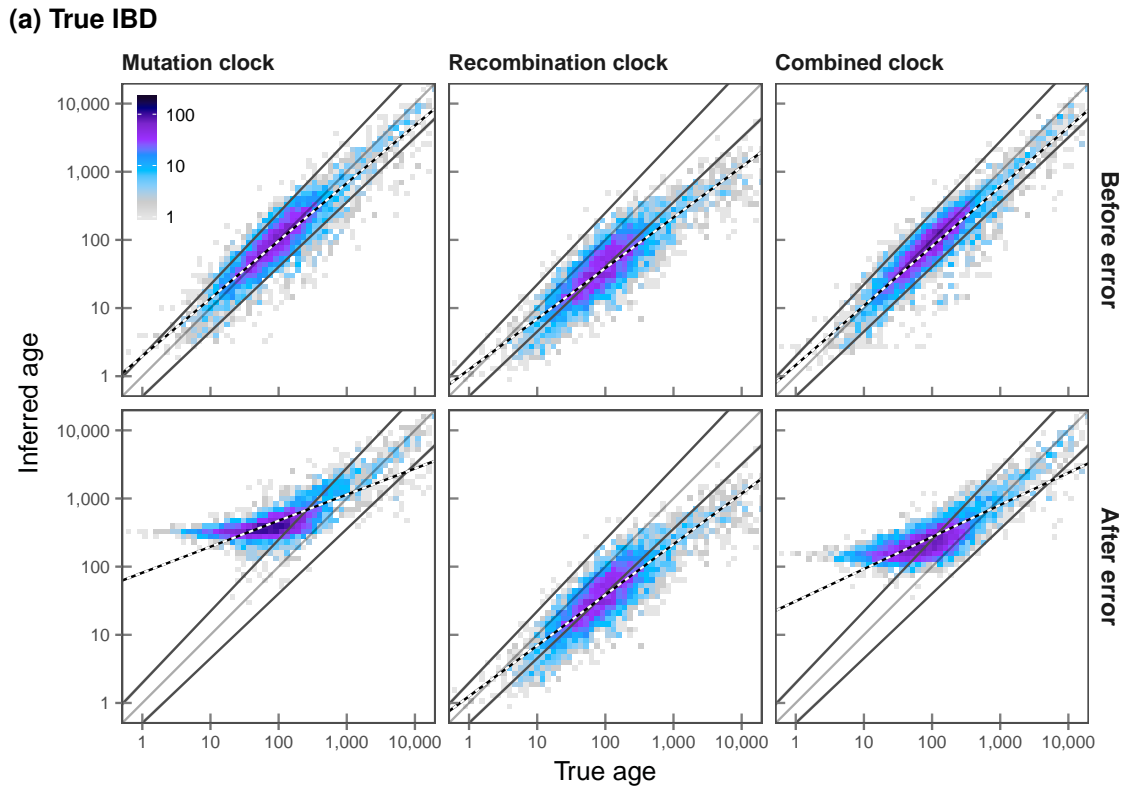


Figure 5.11: Density distribution of allele age before and after the inclusion of genotype error in simulated data. Allele age estimation was conducted on data in which empirical distributions of genotype error were simulated. The effects on the estimation process *before* and *after* error are compared (*top* and *bottom*, respectively). The dividing line is fixed at the true age (t_m), around which the lines *below* and *above* correspond to the regression trend lines of the times of coalescent events delimiting the branch on which focal mutations sit; *i.e.* t_c and t_d , respectively. The *black-white* line indicates the regression trend of the inferred age (\hat{t}). This panel (a) compares the distributions of true and inferred ages, which were estimated on basis of the true IBD structure of the sample as determined from simulation records. The other panels show estimation results based on the different IBD detection methods; FGT on both true and phased haplotypes (b, c; page 213), DGT (d; page 214), and the HMM-based approach (e; page 215). Each analysis was conducted on the same set of retained 5,015 target variants at allele frequency $\leq 0.5\%$ in simulated data of $N = 2,500$ diploid individuals.

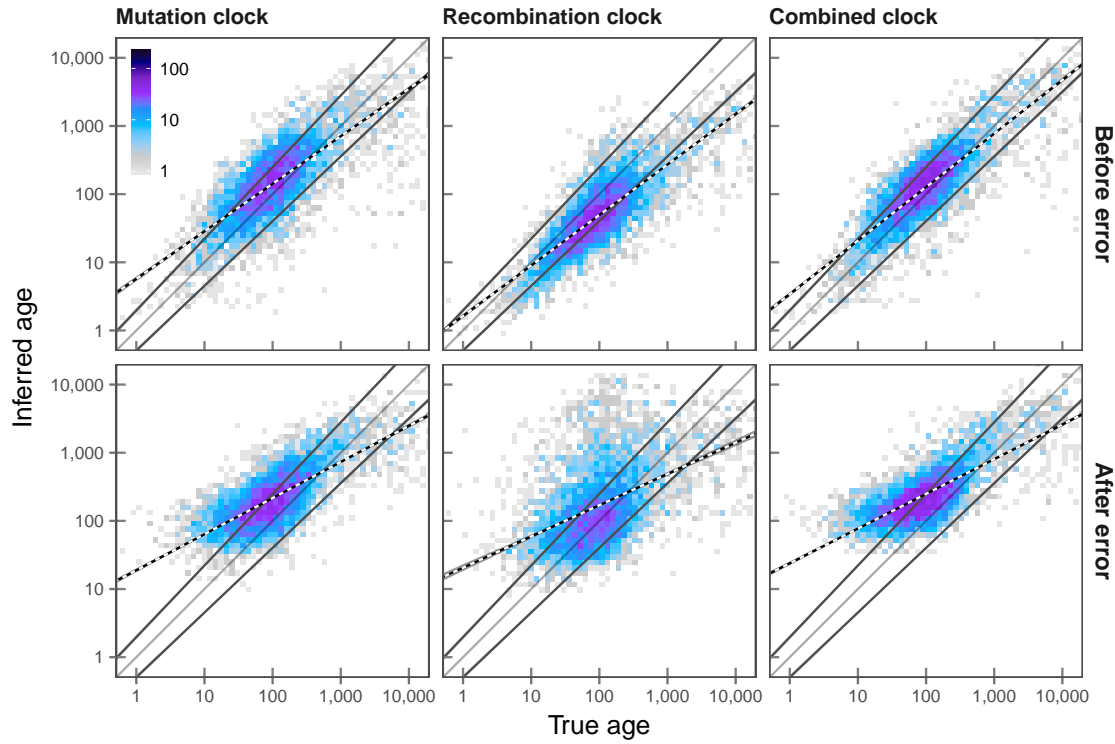
distance between consecutive SNPs was 1.609×10^{-4} cM (93.557 basepairs) in \mathcal{D}_B and \mathcal{D}_B^* ; *i.e.* the density of variant sites is higher compared to \mathcal{D}_A , such that a potential bias resulting from overestimation of true IBD lengths is expected to be reduced. Overall, 42.891 % of alleles were correctly inferred, but this was higher for at $f_{[2,5]}$ and lower at $f_{[20,25]}$; 48.681 % and 39.375 %, respectively. The proportion of underestimated alleles was 55.553 %, where 50.528 % and 52.500 % were underestimated at $f_{[2,5]}$ and $f_{[20,25]}$, respectively. The correlation between inferred and true age was generally high (r_S : 0.818,

0.843, and 0.666 at t_c , t_m , and t_d , respectively) but nonetheless slightly lower compared to corresponding results from dataset \mathcal{D}_A (0.889, 0.895, and 0.739, respectively); although, note that these results are not directly comparable as the underlying demographies were different and only half the number of target sites was analysed here.

When IBD was inferred, the accuracy of the estimation analysis was differently affected dependent on the IBD detection method used. Results based on the FGT are shown in Figure 5.11b and 5.11c (next page), which compare age estimates obtained on the same set of target sites based on IBD detected in true and phased haplotypes, respectively, both before and after error. Without genotype error, 53.021 %, 50.847 %, and 60.040 % of alleles were correctly inferred from true haplotype data in \mathcal{T}_M , \mathcal{T}_R , and \mathcal{T}_{MR} , respectively. When phased data were used, this changed only slightly; 50.828 %, 51.366 %, and 59.182 % of correct alleles in \mathcal{T}_M , \mathcal{T}_R , and \mathcal{T}_{MR} , respectively. Note that the proportion of correctly inferred alleles increased in \mathcal{T}_R due to phasing error. This is because the underestimation that was generally seen under the recombination clock model may have been mitigated by further reduction of IBD segment lengths resulting from flip or switch errors in phased data. The small difference between true and phased data was further reflected in the accuracy of each analysis, where r_S changed from 0.680 to 0.660 in \mathcal{T}_M , 0.780 to 0.764 in \mathcal{T}_R , and 0.742 to 0.731 in \mathcal{T}_{MR} , with regards to t_d .

When analyses were performed on data with genotype error, the overall proportion of correct alleles was reduced, but again the differences seen from true and phased data were small. On true haplotypes, the proportion of correct alleles was 44.267 %, 45.025 %, and 42.034 % in \mathcal{T}_M , \mathcal{T}_R , and \mathcal{T}_{MR} , respectively, whereas 43.549 %, 46.002 %, and 41.635 % of alleles were correct using phased haplotypes in \mathcal{T}_M , \mathcal{T}_R , and \mathcal{T}_{MR} , respectively. Likewise, accuracy was overall reduced but r_S and RMSLE scores did not suggest notable differences between estimation results from true and phased haplotypes; see Table 5.4 (page 220). Notably, the analysis on true IBD suggested that genotype error induces an overall overestimation of allele age in \mathcal{T}_M and \mathcal{T}_{MR} . However, this effect was mitigated by underestimating IBD lengths in the FGT, such that the number of pairwise differences,

(b) FGT, true haplotypes



(c) FGT, phased haplotypes

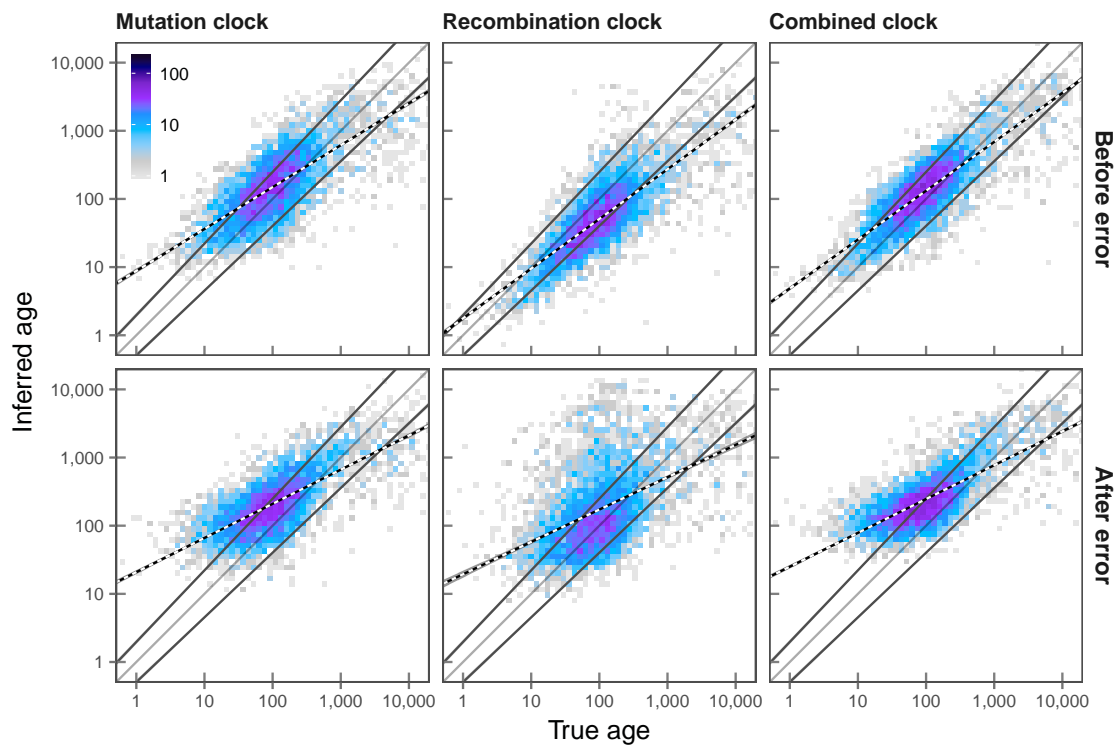


Figure 5.11: Continued.

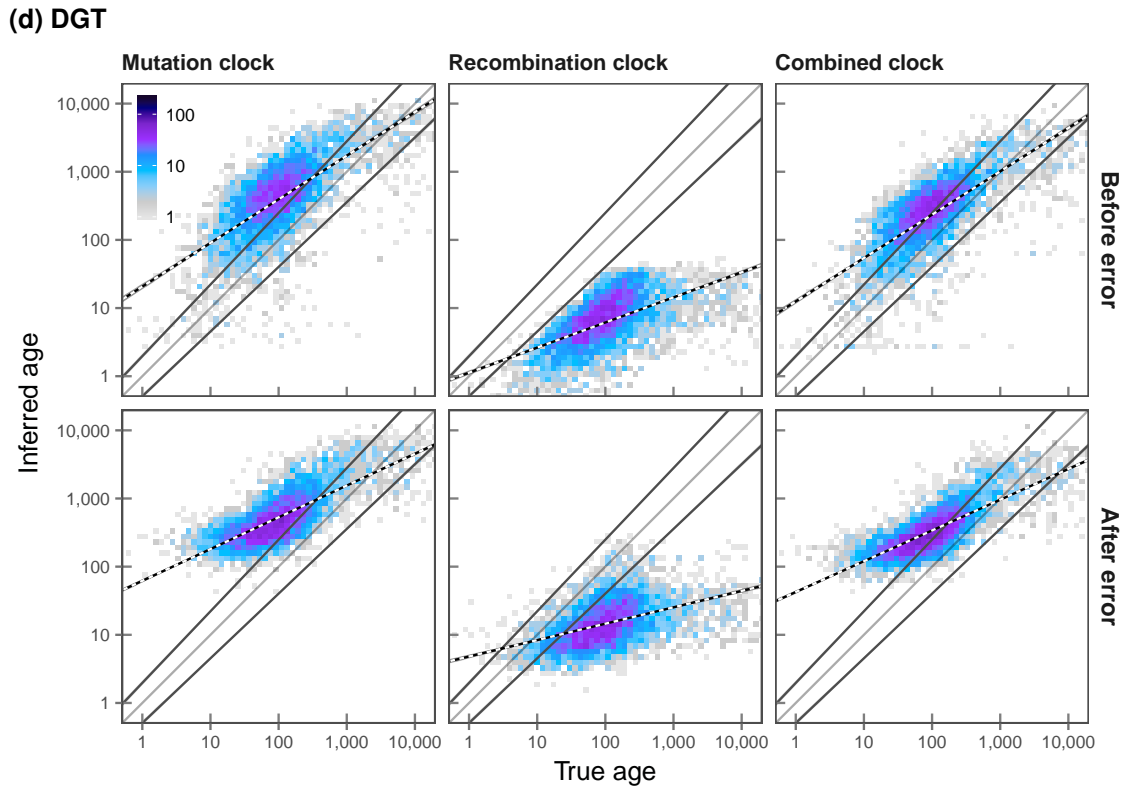
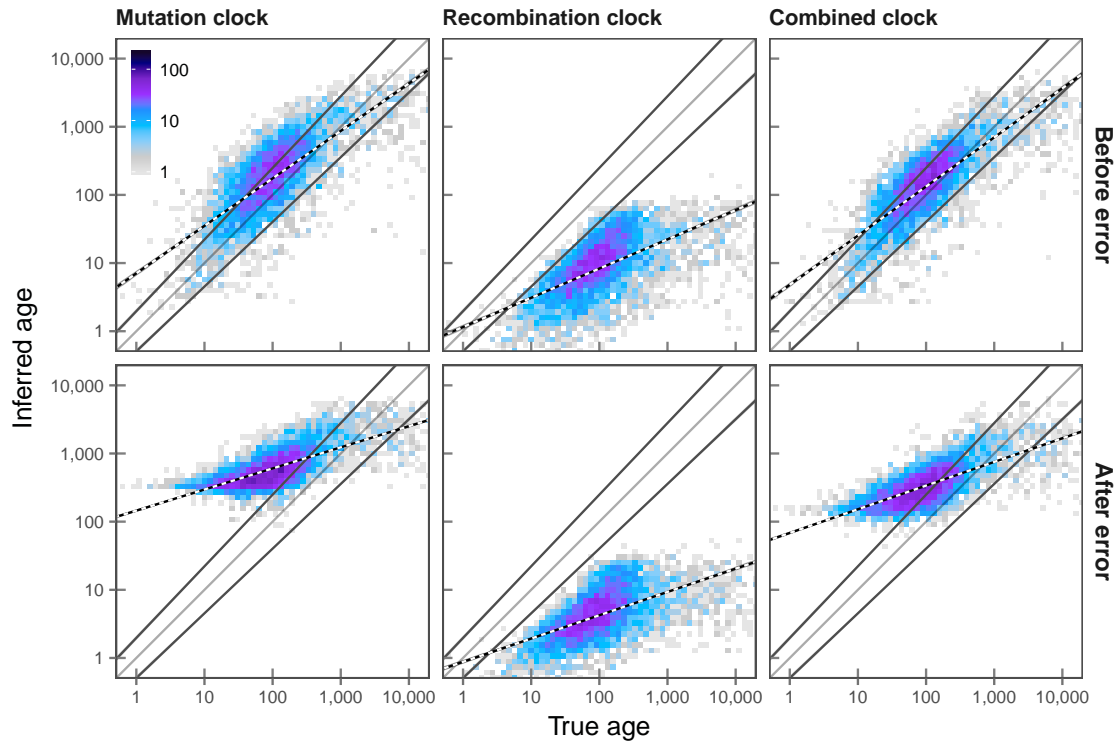


Figure 5.11: Continued.

S , may not be elevated as genotype errors that would increase the value of S may also lead to the premature detection of interval breakpoints.

Estimation results based on the DGT for IBD detection are shown in Figure 5.11d (this page). Before error, the proportions of correctly inferred allele age were the lowest in the present comparison in each clock model. Under both the mutation and combined clocks, \mathcal{T}_M and \mathcal{T}_{MR} , DGT-based age estimation resulted in 26.341 % and 36.949 % of correct alleles, respectively, whereas only 2.413 % were correct in \mathcal{T}_R . While the majority of alleles in \mathcal{T}_M and \mathcal{T}_{MR} were overestimated, 70.050 % and 57.846 % respectively, 97.587 % were underestimated in \mathcal{T}_R (none were overestimated). The tendency to overestimate allele age was increased after error; the proportions of alleles overestimated were 77.308 % and 67.856 % in \mathcal{T}_M and \mathcal{T}_{MR} , respectively. As this was also the case in \mathcal{T}_R , the proportion of correctly inferred alleles increased to 15.693 %, but this was an artefact resulting from an overall underestimation of IBD lengths. However, the loss in accuracy was reflected in the correlation between true and inferred allele age; r_S at t_c , t_m , and t_d was 0.746,

(e) HMM

**Figure 5.11:** Continued.

0.628, and 0.406 before error, and 0.588, 0.504, and 0.328 after error. Note that rank correlations at t_m and t_d were higher in \mathcal{T}_M and \mathcal{T}_{MR} , both before and after error. However, the same measures taken after error actually suggested that the accuracy increased in \mathcal{T}_M and \mathcal{T}_{MR} ; see Table 5.4 (page 220). Regardless, rank correlation measured at t_c was decreased after error under each clock model.

The accuracy of age estimation based on IBD inference using the HMM-based approach was overall highly accurate before error; more accurate in comparison to the FGT in \mathcal{T}_M , similar in accuracy to the DGT in \mathcal{T}_R , and similar to the FGT in \mathcal{T}_{MR} . The density distribution for results obtained using the HMM is given in Figure 5.11e (this page). Before error, the proportion of correct alleles was 47.537 % in \mathcal{T}_M , 3.629 % in \mathcal{T}_R , and 57.827 % in \mathcal{T}_{MR} . The majority of alleles was underestimated in \mathcal{T}_R (96.351 %). This was increased after error, *i.e.* 98.305 % in \mathcal{T}_R , as the proportion of correct alleles was overall reduced; 16.650 % and 27.657 % in \mathcal{T}_M and \mathcal{T}_{MR} , respectively. For example, RMSLE scores were lowest for the HMM under each clock model after error; see Table 5.4 (page 220).

The accuracy before and after error, measured as r_S at t_c , decreased from 0.702 to 0.535 in \mathcal{T}_M , and from 0.733 to 0.569 in \mathcal{T}_{MR} . However, importantly, the HMM-based estimation showed the highest levels of accuracy in \mathcal{T}_R compared to the other methods, *i.e.* r_S at t_c was 0.751 before and 0.737 after error. Although allele age was vastly underestimated, deviations appeared to be consistent.

The distribution of inferred IBD segment lengths for each approach are given in Figure 5.12 (next page). Notably, IBD segments detected using the FGT and DGT were overall underestimated after error; only the HMM maintained similarly accurate lengths before and after error, for both concordant and discordant pairs.

Generation of error correction models

Although the estimation showed strong tendencies to either over- or underestimate allele age, dependent on the clock model and IBD method used, some settings maintained relatively high levels of accuracy after error; in particular the HMM-based inference in \mathcal{T}_R . This suggested that deviations from the true age may follow a consistent pattern. As it is hoped that the age estimation method presented in this chapter is able to produce credible results when used on real data, I evaluated the reliability of each estimation approach by constructing error correction models specific to each setting.

The deviation of the estimated age, \hat{t} , from the actual true age of an allele, denoted by t^* , is simply the absolute value of their difference; calculated as $\delta = |\hat{t} - t^*|$. Given the expectation that the time to coalescence is exponentially distributed, the logarithmic difference is calculated as

$$\xi = \frac{t^* e^{-\delta}}{\hat{t}} \quad (5.21)$$

where $\xi = 0$ if true and estimated age are equal, $0 < \xi < 1$ if the age is overestimated, and $\xi > 1$ if age is underestimated. As the actual age of an allele was not known from coalescent simulations, here, the midpoint of the branch on which the mutation event occurred, t_m , was defined as the reference point against which the estimated age was

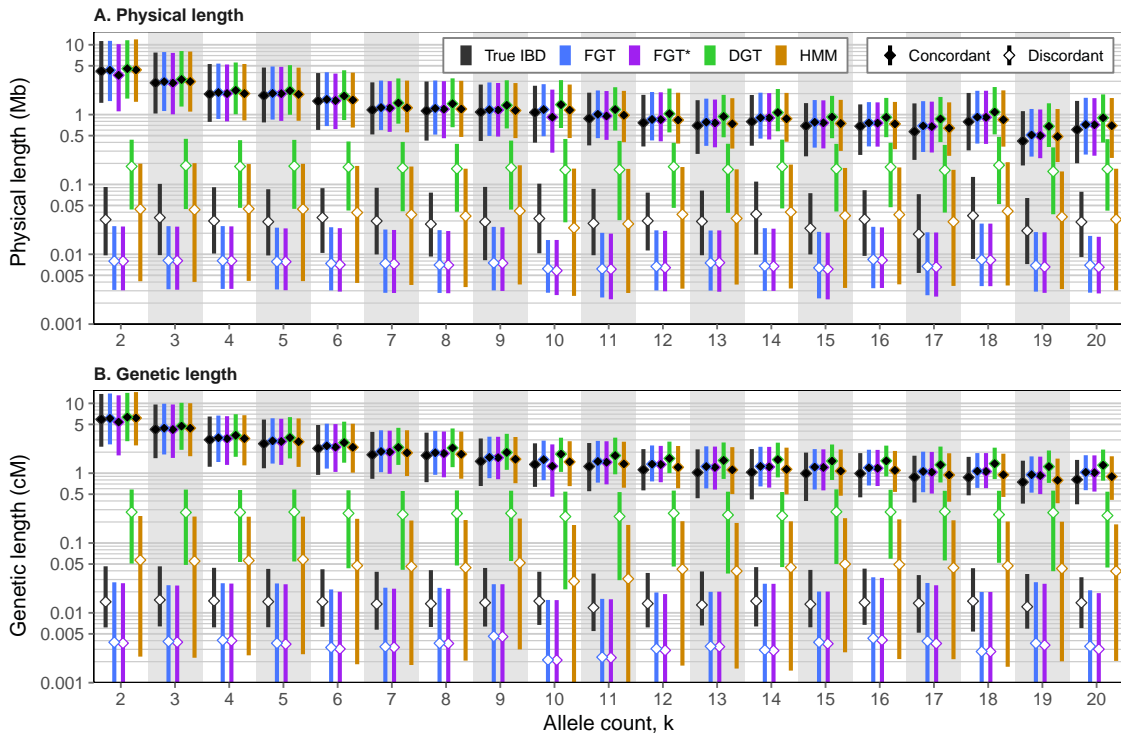
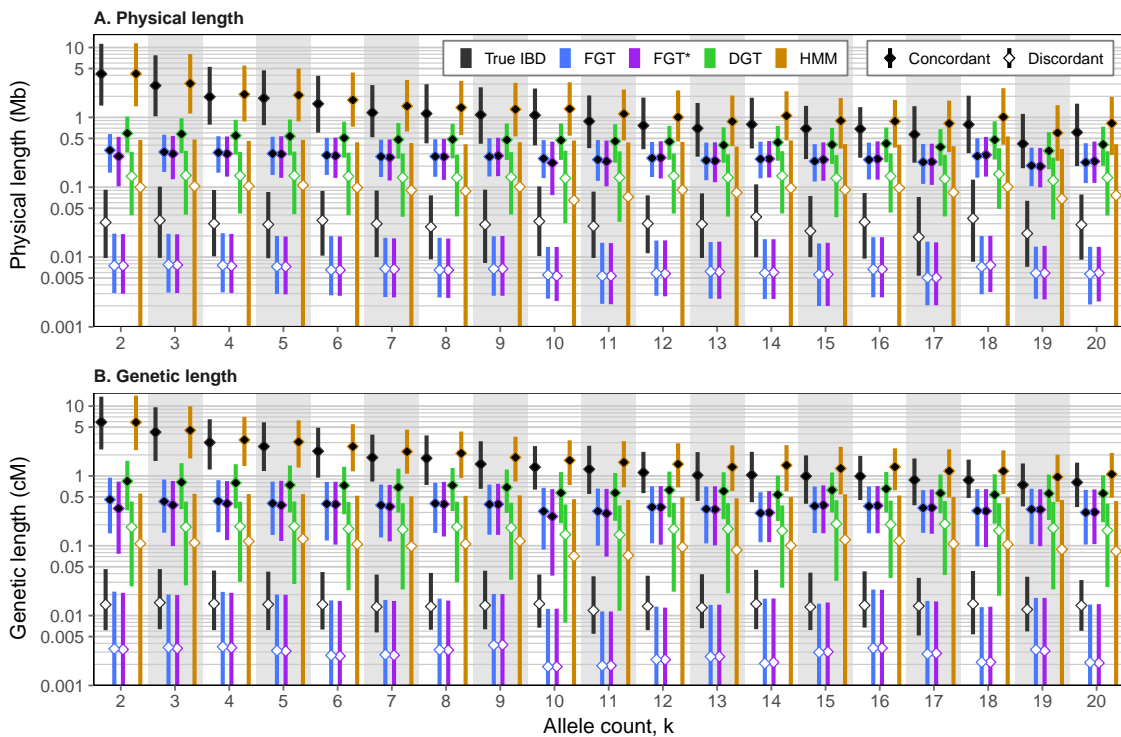
(a) Before error**(b) After error**

Figure 5.12: Length distribution of inferred IBD segments before and after error. Bottom and top of each bar indicate 1st and 3rd quartiles, respectively, between which the median (2nd quartile) is marked (*diamonds*). IBD detected for concordant and discordant pairs is distinguished; *solid* and *hollow* diamonds, respectively.

compared. In reverse, a constant ξ value was used as a correction factor applied to a given set of analysed alleles, considering the results obtained per clock model and IBD method, in order to minimise the mean of the difference distribution. The value of this correction factor was estimated by iteration through an array, denoted by Ξ , which is defined as a series of l factor values, denoted by $\xi_i \in \Xi$, where $i \in [1, 2, \dots, l]$. The minimum factor value was found through the following operation;

$$i = \arg \min_{\xi_i \in \Xi} \left(\left| \frac{1}{n} \sum_{j=1}^n \log [t_{mj}] - \log [\hat{t}_j \xi_i] \right| \right) \quad (5.22)$$

which is applied to a given set of n true and corresponding estimated times, t_{mj} and \hat{t}_j , respectively, where $j \in 1, 2, \dots, n$. I applied Equation (5.22) in a recursive algorithm in which I selected ξ_{i-1} and ξ_{i+1} after each step to redefine the limits of Ξ and to recalculate l new factor values for the next step. This greatly improved the speed and resolution of the computation.

The algorithm outlined above was applied on the results obtained per set of f_k variants estimated in each clock model and IBD method, as well as true IBD, before and after error. Computed correction factors are shown in Figure 5.13, which highlights that deviations followed a general trend in each analysis. For example, before error, allele age estimated using true IBD showed the lowest amount of deviation in T_M and T_{MR} , but where alleles at lower frequencies showed a tendency to be overestimated on average and underestimated at higher frequencies. However, in T_R , true IBD showed larger deviations compared to the FGT (on both true and phased haplotype data), but this may result from the assumption that t_m approximates the actual age of an allele. After error, notably, factor deviations showed spurious patterns for most approaches, except for the HMM-based estimation of allele age, which indicated a consistent trend. Note that the factor distributions of true IBD in T_R were identical before and after error, as genotype error did not affect the estimation under the recombination clock when IBD is known.

Generated error correction factors were applied to the estimated age results, after error, at corresponding f_k variants under each clock model and in each IBD method, which

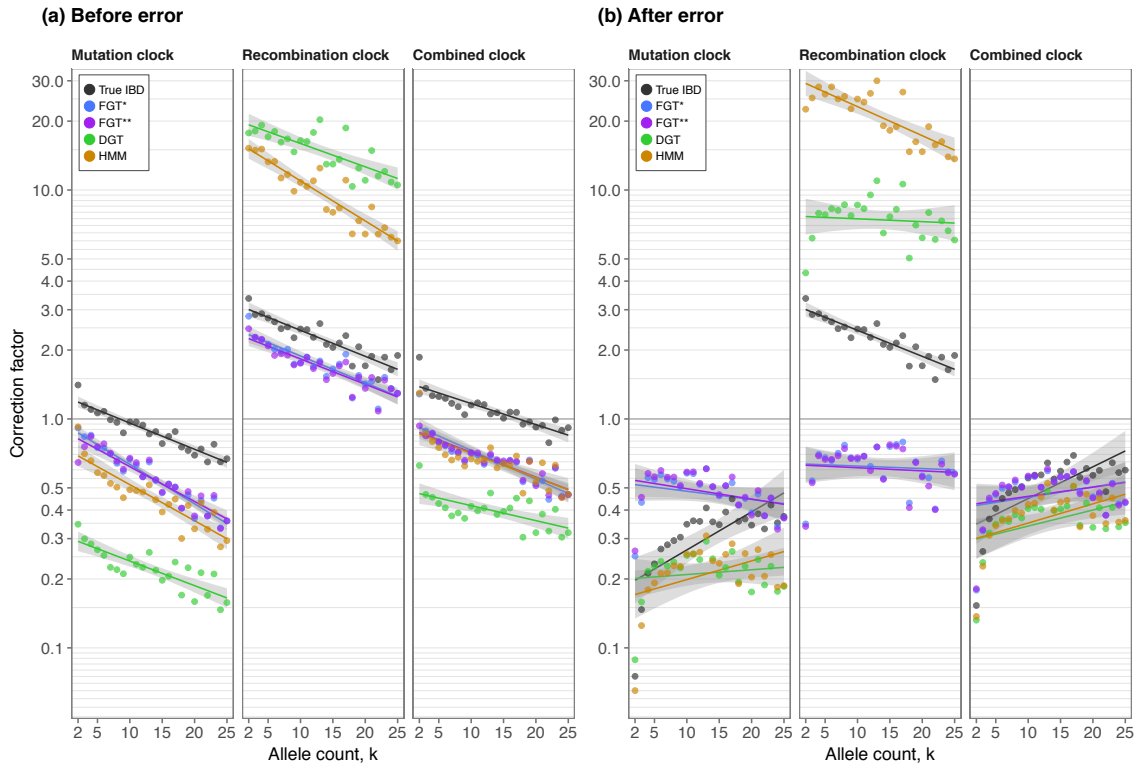


Figure 5.13: Estimated correction factors before and after error. Correction factors were estimated per set of f_k variants for which allele age was estimated in each analysis under a given clock model and IBD detection method. Values below and above 1 indicate that true age was overestimated and underestimated on average, respectively. The line shown per analysis indicates the trend of the corrected deviation (\pm SE), which was calculated through simple nonlinear regression by allele frequency. Note that IBD detection using the FGT was performed on true haplotype data (*) as well as phased haplotypes (**).

minimised deviations in relation to t_m . As a consequence, accuracy was overall improved in each approach; see Table 5.4 (next page). Notably, however, the rank correlation measured for the HMM in T_R was least affected; before applying correction factors, r_S was 0.737, 0.621, and 0.398 at t_c , t_m , and t_d , respectively, which was marginally improved after correction, yielding 0.738, 0.624, and 0.402, respectively. Nonetheless, the HMM indicated the highest levels of accuracy at these measures in comparison to the other IBD methods. Hence, this result corroborates the reliability of the HMM in T_R .

The HMM was developed to account for genotype error in the inference of IBD segments. It may therefore be expected that the HMM outperformed the FGT and DGT in this comparison. However, this had little influence on the estimation in T_M and T_{MR} . This is because the HMM was implemented such that the interval of the IBD segment

Table 5.4: Effect of genotype error on age estimation accuracy. Allele age was estimated based on IBD inferred using the FGT, DGT, and HMM on the same set rare allele target sites at shared allele frequency $\leq 0.5\%$ in simulated data of 5,000 haplotypes. The number of discordant pairs was limited to $n_d = 2,500$ in each analysis. Note that the HMM used the theoretical emission model in the analysis before error (dataset \mathcal{D}_B), and the empirical emission model after error (\mathcal{D}_B^*). True IBD refers to the first breakpoints that are detectable in the data to both sides of a given target position, which were determined from simulation records. The estimates obtained on data with genotype error were additionally corrected using the correction factors calculated per set of f_k variants estimated under each clock model and in each IBD method (including true IBD).

Clock	Method	Before error			After error			After error, corrected		
		t_c	t_m	t_d	t_c	t_m	t_d	t_c	t_m	t_d
Rank correlation coefficient (r_S)										
\mathcal{T}_M	FGT*	0.680	0.736	0.597	0.556	0.696	0.615	0.613	0.721	0.607
	FGT**	0.660	0.711	0.576	0.543	0.673	0.591	0.597	0.696	0.582
	DGT	0.618	0.685	0.563	0.577	0.724	0.649	0.669	0.753	0.620
	HMM	0.702	0.738	0.599	0.535	0.686	0.621	0.676	0.715	0.563
	<i>True IBD</i>	0.870	0.871	0.673	0.518	0.694	0.646	0.712	0.752	0.590
\mathcal{T}_R	FGT*	0.780	0.782	0.601	0.405	0.481	0.407	0.462	0.515	0.414
	FGT**	0.764	0.780	0.603	0.406	0.485	0.414	0.461	0.519	0.420
	DGT	0.746	0.628	0.406	0.588	0.504	0.328	0.630	0.530	0.336
	HMM	0.751	0.632	0.411	0.737	0.621	0.398	0.738	0.624	0.402
	<i>True IBD</i>	0.818	0.843	0.666	0.818	0.843	0.666	0.801	0.849	0.684
\mathcal{T}_{MR}	FGT*	0.742	0.792	0.644	0.528	0.689	0.629	0.640	0.741	0.617
	FGT**	0.731	0.787	0.643	0.520	0.679	0.619	0.631	0.732	0.609
	DGT	0.666	0.727	0.597	0.596	0.757	0.689	0.694	0.781	0.645
	HMM	0.733	0.781	0.641	0.569	0.693	0.606	0.679	0.718	0.568
	<i>True IBD</i>	0.884	0.885	0.696	0.593	0.735	0.655	0.740	0.778	0.613
Root mean squared logarithmic error (RMSLE)										
\mathcal{T}_M	FGT*	0.696	0.436	0.639	0.864	0.516	0.524	0.615	0.394	0.662
	FGT**	0.715	0.444	0.623	0.859	0.524	0.547	0.625	0.416	0.678
	DGT	1.083	0.743	0.657	1.190	0.809	0.606	0.593	0.382	0.668
	HMM	0.754	0.478	0.633	1.250	0.882	0.681	0.598	0.425	0.713
	<i>True IBD</i>	0.454	0.255	0.666	1.146	0.770	0.587	0.562	0.362	0.671
\mathcal{T}_R	FGT*	0.380	0.471	0.909	0.881	0.638	0.728	0.738	0.594	0.815
	FGT**	0.413	0.480	0.903	0.890	0.641	0.722	0.742	0.594	0.811
	DGT	0.905	1.252	1.690	0.703	0.991	1.413	0.631	0.533	0.822
	HMM	0.796	1.141	1.585	1.031	1.380	1.814	0.590	0.488	0.798
	<i>True IBD</i>	0.337	0.504	0.960	0.337	0.504	0.960	0.508	0.284	0.645
\mathcal{T}_{MR}	FGT*	0.624	0.364	0.626	0.915	0.548	0.496	0.601	0.373	0.649
	FGT**	0.641	0.367	0.608	0.916	0.551	0.503	0.609	0.384	0.654
	DGT	0.869	0.557	0.611	1.019	0.645	0.523	0.587	0.372	0.661
	HMM	0.644	0.398	0.647	1.021	0.672	0.585	0.595	0.421	0.712
	<i>True IBD</i>	0.381	0.260	0.716	0.919	0.555	0.506	0.542	0.330	0.656

* FGT applied to true haplotypes

** FGT applied to phased haplotypes

is reported, but without further guiding the estimation process. For example, but it would be possible to calculate the posterior probabilities of the hidden states (defined as *ibd* and *non*; see Chapter 4) to weight observed mutational differences at each site along the sequence to determine the value of S . This was not considered in the current implementation of the rvage algorithm, but could be extended in future versions.

5.5 Age of alleles with predicted effects in 1000 Genomes data

The method presented in this chapter was applied the final release dataset of the 1000 Genomes Project (1000G) Phase III (1000 Genomes Project Consortium *et al.*, 2012, 2015), where I estimated allele age on a selected set of target sites using the HMM-based approach under the recombination clock model, \mathcal{T}_R . To regard inferred allele age in relation to the functional consequences of specific variants, I prioritised SNPs that have been annotated by the Ensembl Variant Effect Predictor (VEP) (McLaren *et al.*, 2016).^{*} In particular, VEP classifies variants into four *impact* categories which broadly distinguishes the severity of the consequences predicted; namely *high*, *moderate*, and *low* impact, as well as *modifiers*.

5.5.1 Quality control

Because genotype error was expected to be present in the data, alleles observed at selected target sites may not correctly identify haplotype sharing by descent in all individuals. Alleles can either be missed (*false negatives*) or incorrectly observed (*false positives*), such that allocation into the set of sharers, X_c , and the set of non-sharers, X_d , is biased. This is likely to disrupt the estimation of the composite likelihood, *i.e.* by including CCFs at wrong ends of Equation (5.14), to the extent that the resulting posterior probabilities may become spurious or cancel out (referred to as *disconformity*). In general, the identification of missed or falsely observed alleles is not straightforward, in particular towards lower allele frequencies. While it would be possible to reduce the risk of including false negatives

* Ensemble Variant Effect Predictor (VEP): <http://www.ensembl.org/info/docs/tools/vep/index.html>
[Date accessed: 2017-02-15]

in Ω_d by lowering the n_d threshold, the inclusion of false positives would not be affected, but could be reduced by applying a threshold to n_c . However, this would not be possible for f_2 variants, unless they are categorically excluded.

As an alternate solution, here, I attempted to exclude target sites in a *post hoc* analysis using the following quality control measure. The median of the posterior probability of the CCF in each pair was taken to calculate the geometric mean (or *log-average*) across pairs contained in Ω_c and Ω_d , respectively, computed as

$$\tilde{y}_x = \left(\prod_{i,j \in \Omega_x} [\Lambda_{ij}]_2 \right)^{-n_x} \quad (5.23)$$

where $x \in \{c, d\}$, referring to either set Ω_c or Ω_d , and $[\Lambda_{ij}]_2$ is the median (2nd quartile) of the CCF computed for individuals i and j taken from that set. The intuition is that \tilde{y}_c and \tilde{y}_d are indicators of the central tendency of the time of coalescent events found through concordant and discordant pairs, such that $\tilde{y}_c < \tilde{y}_d$ is expected if the estimation was not or less affected by false negatives or positives. By also considering $\tilde{y}_m = \sqrt{\tilde{y}_c \tilde{y}_d}$ as a robust measure of allele age, here, target sites were removed if the condition $\tilde{y}_c < \tilde{y}_m < \tilde{y}_d$ was violated.

5.5.2 Error correction based on allele frequency

The error correction model constructed in Section 5.4.3 (page 216) was used to correct estimated age values dependent on the allele frequency observed at a given target site. In particular, a simple nonlinear regression model was used to fit empirically computed factor values, such that correction factors could be predicted by the allele frequency observed in 1000 Genomes Project (1000G) data. The following exponential model was used.

$$\hat{\xi}_k = b e^{ka} \quad (5.24)$$

The fitted model parameters were $a = -0.029$ and $b = 30.975$ for the HMM in $\mathcal{T}_{\mathcal{R}}$.

5.5.3 Results

Target sites were randomly selected from the set of SNPs in available VEP results, across chromosomes 1–22, at shared allele frequencies below 1 % observed across the whole sample of $N = 2504$ diploid individuals; *i.e.* f_k variants with $k \in [2, 50]$. In total, approximately 150,000 target sites were analysed, using the following model parameters; $N_e = 10,000$, constant mutation rate of $\mu = 1.200 \times 10^{-8}$ per site per generation (following Scally and Durbin, 2012), recombination rates according to genetic maps per chromosome provided by HapMap Phase II, Build 37 (International HapMap Consortium *et al.*, 2007), and $n_d = 2,504$. The HMM used the empirical emission model that was generated from genotype error identified in 1000G data (chromosome 20); see Chapter 4.

The total number of pairwise analyses conducted was 460,051 million. A fraction of 2.613 % was conflicting and 2.899 % were indicated in quality control; together, 3.497 % of target sites were removed. Notably, the proportion of variants removed in both filtering steps was highest at lower allele frequencies; for example, 10.761 % of f_2 variants and only 0.852 % of f_5 variants were removed.

The number of retained estimates was 141,069, which included 1,255 variants of *high* impact (splice acceptor and splice donor variants, and stop gained and stop lost variants), 44,131 variants with *moderate* impact (missense variants only), 9,990 variants with *low* impact (synonymous variants only), and 85,694 *modifier* variants (non-coding variants, *e.g.* intron and intergenic variants, and regulatory region variants).

The distribution of allele age before and after correction is shown in Figure 5.14 (next page). Before correction, median ages per category were inferred at 5.661, 6.329, 7.567, and 11.828 generations in *high*, *moderate*, *low*, and *modifier*, respectively, which were corrected to 158.163, 174.435, 203.952, and 289.557 generations, respectively. The correlation between estimated age and allele frequency was measured using r_S , which was 0.829, 0.834, 0.851, and 0.867 in *high*, *moderate*, *low*, and *modifier*, respectively. Although differences were small, this suggested that the estimated allele age was less correlated with allele frequency if the severity of the presumed consequences was high.

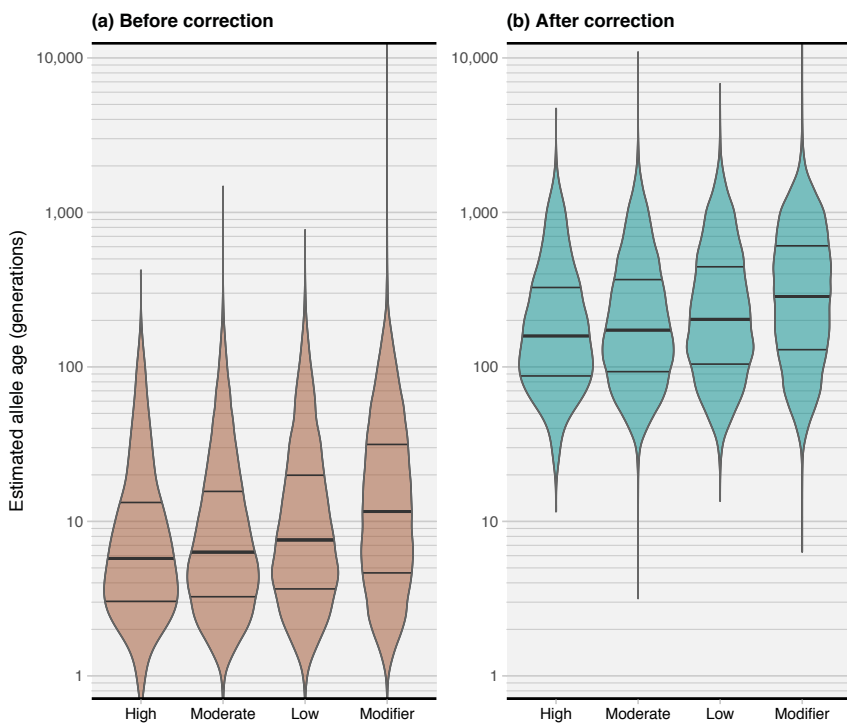


Figure 5.14: Allele age estimated on functionally annotated data in 1000 Genomes. The distribution of inferred allele age is shown in Violin plots by predicted impact category for the whole sample of the 1000G dataset, before and after correction; 1st, 2nd, and 3rd quartiles are indicated.

The 1000G dataset is composed of several continental population samples (or *super-populations*) in which allele frequencies may differ. I applied the correction as per frequency observed in each population; variants were excluded if monomorphic per population. Although target sites were selected at $\leq 1\%$ allele frequency in the whole sample, some alleles were found at relatively high frequencies in certain populations, but which did not exceed 5% allele frequency. The distribution of allele age per population is shown in Figure 5.15a. Variants of *high* impact were overall estimated to be younger, e.g. median age was 276.716 generations in AFR and 113.895 generations in EAS. Non-coding variants, *modifiers*, were older throughout, e.g. 528.812 generations in AFR, but were not notably older in EAS, where median age was 135.348 generations. Alleles in the AMR sample were overall more widely distributed and indicated an older median age per impact category. Rank correlation with allele frequency, r_S , was high in AFR (0.731), but not substantial in EAS (0.439), EUR (0.409), and SAS (0.347). In AMR, age and

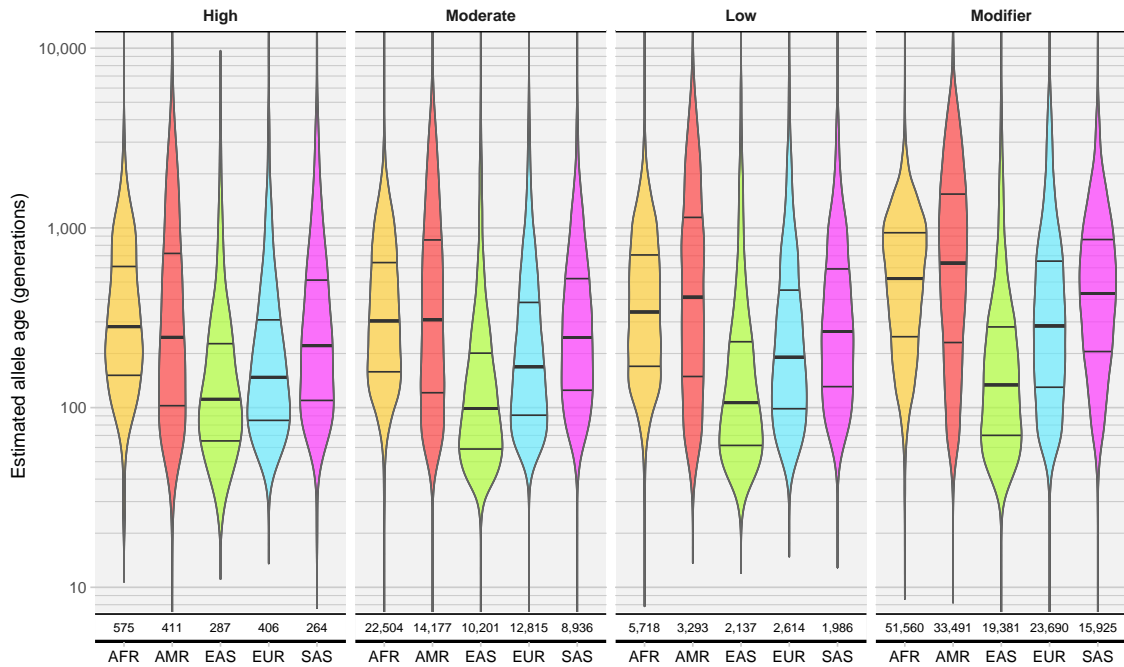
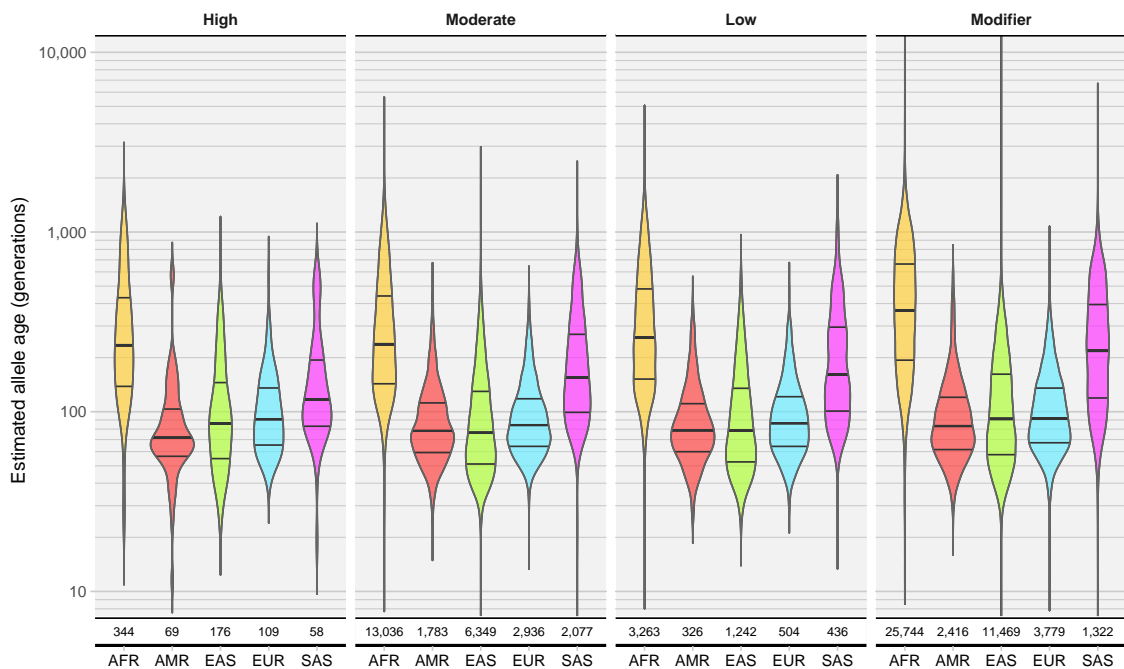
(a) All alleles analysed**(b) Population-specific alleles**

Figure 5.15: Allele age after correction on population-specific frequency in 1000 Genomes. The distribution of inferred allele age is shown in Violin plots by predicted impact category for each population in the 1000G dataset; 1st, 2nd, and 3rd quartiles are indicated. In Panel (a), all variants retained after quality control were included in the comparison, which included $n = 141,069$ target sites. Note that this also included alleles shared among populations. In Panel (b), only the subset of population-specific variants was included ($n = 77,438$). The number of alleles retained in each impact category and population are shown below each graph. The colours used follow the 1000G colour-scheme.

frequency appeared to be weakly related (0.092), which may be the result of population admixture, which characterises this population sample.

Table 5.5: Allele age per population in the 1000 Genomes sample. Inferred allele age was corrected in reference to population allele frequencies in the five population groups in 1000G data, shown per VEP impact category. In total, 141,070 variants were analysed (**a**), of which 77,439 were population-specific (**b**).

Impact	Median estimated age (generations)					Correlation with frequency (r_s)				
	AFR	AMR	EAS	EUR	SAS	AFR	AMR	EAS	EUR	SAS
(a) All alleles analysed										
<i>High</i>	276.7	238.3	113.9	145.8	219.0	0.697	0.164	0.445	0.581	0.441
<i>Moderate</i>	305.2	311.5	99.0	169.1	247.7	0.707	0.143	0.432	0.469	0.386
<i>Low</i>	341.4	414.0	105.0	191.9	266.3	0.738	0.116	0.388	0.445	0.410
<i>Modifier</i>	528.8	645.6	135.3	287.3	435.3	0.729	0.058	0.435	0.349	0.340
(b) Population-specific alleles										
<i>High</i>	227.2	67.7	86.9	87.8	116.7	0.886	0.673	0.861	0.738	0.865
<i>Moderate</i>	239.8	77.4	76.8	84.6	154.9	0.892	0.647	0.878	0.746	0.907
<i>Low</i>	256.4	78.0	78.0	87.2	154.9	0.905	0.616	0.881	0.751	0.907
<i>Modifier</i>	369.7	82.7	91.8	91.9	221.6	0.920	0.707	0.897	0.808	0.935

Variants that appeared in more than one population were removed to focus on population-specific, presumably more recent alleles; see Figure 5.15b. This reduced the number of alleles to 77,438. Notably, alleles retained in AMR were youngest in all impact categories, whereas the alleles specific to the AFR sample were seen to be the oldest; *e.g.* median age was 227.240 generations in *high* and 369.733 generations in the *modifier* category. Rank correlation between between allele frequency and inferred age showed a more consistent relationship in each population; AFR (0.917), EAS (0.890), EUR (0.780), SAS (0.921). Notably, the variants specific to AMR now showed a moderately high correlation between age and frequency (0.677). These results are summarised in Table 5.5 (this page).

5.6 Discussion

I demonstrated the validity of the age estimation framework using simulated data where I showed that age can be estimated with very high accuracy. However, certain problems may

arise when working with real data. The impact of phasing error is small in comparison to genotypic (or allelic) misclassification, which is likely to bias the estimation process.

Generally, imperfect data may affect the estimation of allele age in two ways. First, the method was shown to be highly susceptible to inaccurate IBD inference, where each clock model behaves differently to the over or underestimation of IBD length. In this regard, the HMM-based approach for IBD inference was shown to maintain consistency even if genotype error is present. However, second, even if IBD is detected with high accuracy, the alleles observed at a focal variant in the sample may wrongly identify haplotype sharing by descent. To account for the possibility that some concordant pairs may actually be discordant pairs, for example, a separate filtering method would be needed to exclude pairs before or after the computation of the CCF, to reduce the chance that the calculation of the composite likelihood is biased. However, because such a method would effectively predict missed alleles in the data, a solution to this problem may not be straightforward. Yet it would be possible, for example, to exclude pairs on basis of patterns of allele sharing or consistency of the inferred IBD structure. Alternatively, instead of excluding pairs, the target site itself would need to be excluded from the analysis if bias is likely. A simple solution was presented in the previous section, where sites are excluded if the lower and upper bounds indicate a reverse order, but further evaluation is required to determine the effectiveness of this filtering criterion.

Lastly, note that both the DGT and the HMM-based approach operate on genotype data to detect IBD, but because the mutation clock model, \mathcal{T}_M , requires haplotypes, it would be desirable to estimate pairwise differences, S , in genotype data, so as to make these methods fully compatible with \mathcal{T}_M and \mathcal{T}_{MR} . A possible solution is presented in Chapter 3, where haplotype phase was determined from genotype pairs in detected IBD segments, based on the genealogical constraints that arise under haplotype sharing by descent. Yet, further work is needed to determine the feasibility of such an approach.

Write a wise saying and your name will live forever.

— Anonymous

6

Discussion

Contents

6.1 Implications for genome-wide association studies	228
6.2 The importance of haplotype sharing by descent	230
6.3 The potential of estimating the age of alleles	232

In this thesis, I have demonstrated the value of analysing rare variants to further our understanding of recent human demographic history, in an attempt to contribute to complex disease research. The unique features of low-frequency and rare variants necessitate the refinement of existing methodologies, yet can yield important results. While the major findings of this approach have been presented and discussed in detail in the preceding chapters, I use the sections below to briefly summarise the intuition behind the methods developed and their applications. I further highlight some specific problems identified, together with potential solutions.

6.1 Implications for genome-wide association studies

Genotyping methods used in GWA studies are typically designed to probe genetic markers expected to maximise the genetic variation observed between individuals, thereby limiting their capacity to capture and interrogate low-frequency and rare variants. Consequently, imputation from a reference panel is used to predict variants at lower frequencies; however, despite constant growth in available reference datasets, each panel alone represents only a snapshot of the existing genetic variation in the human genome, and in particular,

alleles observed at lower frequencies are more likely to be specific to the cohort or population investigated.

I addressed this “fragmentation” of data in Chapter 2, where I presented *meta-imputation* as a viable solution through combining information across multiple reference datasets. Notably, the solution I proposed differs from the one achieved by the Haplotype Reference Consortium (HRC). While the HRC combined raw sequencing data from multiple independent studies to form a single, canonical reference for imputation (McCarthy *et al.*, 2016), the idea behind meta-imputation is to leverage the information contained within different studies indirectly by combining genotype data after performing separate imputations from different reference panels into a given study sample. The meta-imputation approach thereby provides greater flexibility, as it allows the inclusion of novel datasets.

I have shown that meta-imputation of multiple reference datasets can improve the accuracy of the resulting data, and the power to detect associations in GWAS simulations. These improvements were limited to intermediate or high penetrance variants, and to simulated low-frequency risk alleles; negligible effects were seen for common risk variants or at very low frequencies. As expected, the largest improvements were achieved when data from different ethnic backgrounds were combined.

Despite the demonstrated success of meta-imputation in the contexts described here, there have been other parallel advances in the field. In particular, the recent introduction of the HRC imputation service has been and will continue to be a game changer, although currently only samples of European ancestry are included in the panel. However, meta-imputation may be more appropriate in certain applications, such as by the inclusion of a reference dataset obtained on specific populations, for which no other sources of information may exist.

A caveat to the meta-imputation strategy is its reliance on imputation; it does not perform imputation by itself, and is only as reliable as the imputation methods used. Looking ahead, future genome-wide association (GWA) studies may not in fact require imputation; due to ongoing advances in high-throughput sequencing technologies, it is

likely that we soon reach the point when the generation of whole-genome sequencing data becomes affordable even on a large scale.

6.2 The importance of haplotype sharing by descent

Rare variants are particularly useful in identifying recent relatedness in samples of reportedly unrelated individuals. Given the site of a particular allele, it is straightforward to identify individuals sharing that allele in sample data. For rare alleles, it is likely that the chromosomes carrying that allele are the nearest genealogical neighbours in the sample at that position in the sequence. The low frequency suggests that the allele was inherited from a common ancestor only a few generations ago, such that recombination has had less time to break down the length of the co-inherited haplotype region.

Based in this insight, in Chapter 3, I developed a method for the discovery of shared identity by descent (IBD) haplotypes, referred to as the tidy algorithm, which utilises rare variants as “bookmarks” to highlight the positions at which the individuals sharing a focal allele are also likely to share a relatively long haplotype that is identical by descent. Notably, the method presented is non-probabilistic and relies on the observation of certain allelic or genotypic configurations to infer recombination in pairs of diploid individuals. IBD segments can be detected using either haplotype or genotype data.

In addition, I explored the viability of using IBD information obtained from genotype data to distinguish haplotypes, *i.e.* to locally phase genotypes based on the inferred allelic sequence of the underlying shared haplotype. I showed that such an IBD-based phasing approach became error-prone towards the terminal ends of detected segments, due to overestimation of haplotype length. Nonetheless, this approach worked perfectly when the IBD information was correct. Future implementations of such an approach may therefore consider rare variants as anchor points around which the shared haplotype could be inferred to locally correct for flip or switch errors occurring in the phasing process. Nonetheless, genotype error may have negative effects on such an implementation; for example, because a focal rare allele may have been falsely typed or called (false positive), which I found was more likely towards the lower end of the allele frequency spectrum.

On that note, the accuracy of data produced by current genotyping or sequencing technologies is sufficiently high at common variants, which may not pose a problem, for example, for analytical methods used in GWA studies. Regardless, genotype error rates are typically seen to increase towards the lower end of the frequency spectrum. In practice, many studies therefore treat rare variants with caution or even exclude sites below a certain frequency threshold. The presence of genotype error substantially affected the IBD detection method described in Chapter 3 in two ways. First, it is likely that a number of rare variants were irretrievably missed while other alleles were falsely observed, thereby leading to incorrect identification of haplotype sharing at a focal position. This problem was compounded by genotype errors at sites surrounding the target allele, which may have led to the discovery of false breakpoints or the disregard of actual breakpoints in the IBD detection process. It was therefore not surprising to see spurious results in the application of this method to real data.

Hence, the main goal of Chapter 4 was to establish an empirical model of frequency-dependent error rates based on observed genotype misclassification in real data, which I established from several datasets obtained on different genotyping and sequencing platforms. I presented a Hidden Markov Model (HMM) which incorporated an empirically constructed error model. I implemented as this approach an extension of the tidy algorithm for targeted IBD detection and showed that the HMM-based approach is able to achieve similar levels of accuracy compared to the non-probabilistic approach in the absence of genotype error, and that accuracy is maintained if genotype error is present. Notably, the HMM-based approach is genotype-based, such that phasing of genotype data is not required.

One limitation to this approach was that the error model did not consider the accumulation of mutations. This is perhaps reflected in the observed higher accuracy for “younger” segments; *i.e.* those co-inherited recently. An extension of the method would be to use a fully probabilistic model to compute emission probabilities in the HMM, as for the transition probabilities, which were calculated conditionally on the expected age of the focal allele. More work has to be invested into the exploration of this possibility.

6.3 The potential of estimating the age of alleles

While the frequency of an allele is itself an estimator for the age of that allele (Kimura and Ota, 1973; Griffiths and Tavaré, 1998), detailed knowledge about the genealogy of the sample and the demographic history of the population would be required to unravel the complex relations between the demographic processes which resulted in the observed genetic variation. Notably, the age estimation method presented in Chapter 5 does not require such prior knowledge, but instead derives information from the underlying IBD structure inferred through the targeted IBD detection method presented in Chapters 3 and 4. Subsequently, by knowing the age of an allele, much can be learned about the changes that occurred over time in a population.

I presented three approaches (clock models) to estimate the time of a coalescent event that separates a pair of individuals; these are based on pairwise differences that accumulated through mutation events on each lineage, the genetic distance between recombination breakpoints, or both. These measures are used to estimate the time to the most recent common ancestor (T_{MRCA}) of specific haplotype pairs, so as to determine the sequence of coalescent events. The age of a given target allele is estimated based on patterns of haplotype sharing and the inferred coalescent times, using a composite likelihood approach. I demonstrated the feasibility of this method by comparing the estimated age of an allele to its true age (known from simulation records), both before and after the inclusion of genotype error.

Whilst the methods described achieved reasonable accuracy under ideal conditions, they are dependent on the accuracy of inferred IBD segments, in both concordant and discordant pairs. For example, considerable differences were seen between the different clocks in the presence of genotype error, such that only the HMM-based approach for IBD inference was robust enough to produce reliable results. Notably, IBD for discordant pairs is less straightforward to detect (using the methodology developed in Chapters 3 and 4), as the two individuals considered do not share a recently co-inherited allele at a given target position. Therefore, more work is necessary to optimise IBD detection in this context,

while still operating in a targeted manner. For example, some improvements to the HMM-based approach could be thought of, in particular with regard to the aforementioned idea to replace the empirical emission model with a fully probabilistic one.

The key test for an acronym is to ask whether it helps or hurts communication.

— Elon Musk

Abbreviations

1000G	1000 Genomes Project
ARG	Ancestral recombination graph
CCF	Cumulative coalescent function
CDF	Cumulative distribution function
cM	CentiMorgan
DGT	Discordant genotype test
DNA	Deoxyribonucleic acid
EBI	European Bioinformatics Institute
FGT	Four-gamete test
FNR	False negative rate
FPR	False positive rate
GoT2D	Genetics of Type 2 Diabetes Project
GWA	Genome-wide association
HapMap	International HapMap Project
HGP	Human Genome Project
HMM	Hidden Markov Model
HRC	Haplotype Reference Consortium
HWE	Hardy-Weinberg equilibrium
IBD	Identity by descent
IBS	Identity by state
IPG	Illumina Platinum Genomes Project
LD	Linkage disequilibrium
LOD	Logarithm of odds
LR	Likelihood ratio
LRP	Long range phasing
MAF	Minor allele frequency
Mb	Megabase
MRCA	Most recent common ancestor
NGS	Next-generation sequencing
NHGRI	National Human Genome Research Institute
OR	Odds ratio
PCR	Polymerase chain reaction
PDF	Probability density function
QC	Quality control
RFLP	Restriction fragment length polymorphism
RMSLE	Root mean squared logarithmic error
RNA	Ribonucleic acid

SE	Standard error
SNP	Single-nucleotide polymorphism
T_{MRCA}	Time to the most recent common ancestor
VCF	Variant Call Format
VEP	Variant Effect Predictor
WGS	Whole-genome sequencing

My definition of a scientist is that you can complete the following sentence: 'he or she has shown that ...'

— E. O. Wilson

Bibliography

- 1000 Genomes Project Consortium, Abecasis, G. R., Auton, A., Brooks, L. D., DePristo, M. A., Durbin, R. M., Handsaker, R. E., Kang, H. M., Marth, G. T., and McVean, G. A. (2012). An integrated map of genetic variation from 1,092 human genomes. *Nature*, **491**(7422), 56–65.
- 1000 Genomes Project Consortium, Auton, A., Brooks, L. D., Durbin, R. M., Garrison, E. P., Kang, H. M., Korbel, J. O., Marchini, J. L., McCarthy, S., McVean, G. A., and Abecasis, G. R. (2015). A global reference for human genetic variation. *Nature*, **526**(7571), 68–74.
- Abecasis, G. R., Cherny, S. S., and Cardon, L. R. (2001). The impact of genotyping error on family-based analysis of quantitative traits. *European Journal of Human Genetics*, **9**(2), 130–134.
- Albrechtsen, A., Korneliussen, T. S., Moltke, I., Hansen, T. v. O., Nielsen, F. C., and Nielsen, R. (2009). Relatedness Mapping and Tracts of Relatedness for Genome-Wide Data in the Presence of Linkage Disequilibrium. *Genetic Epidemiology*, **33**(3), 266–274.
- Altshuler, D., Daly, M. J., and Lander, E. S. (2008). Genetic Mapping in Human Disease. *Science*, **322**(5903), 881–888.
- Altshuler, D. L., Bentley, D. R., Chakravarti, A., Collins, F. S., Donnelly, P., Gabriel, S. B., Knoppers, B. M., Lander, E. S., Lehrach, H., Mardis, E. R., Nickerson, D. A., Peltonen, L., Wang, J., Wilson, R. K., Gibbs, R. A., Deiros, D., Metzker, M., Wheeler, D., Li, J., Jian, M., Li, G., Li, R., Liang, H., Tian, G., Wang, B., Wang, W., Yang, H., Zhang, X., Zheng, H., Ambrogio, L., Bloom, T., Sougnez, C. L., Gormley, N., Humphray, S., Kingsbury, Z., Koko-Gonzales, P., Stone, J., McKernan, K. J., Costa, G. L., Ichikawa, J. K., Lee, C. C., Borodina, T. A., Dahl, A., Davydov, A. N., Marquardt, P., Mertes, F., Nietfeld, W., ROSENSTIEL, P., Schreiber, S., Soldatov, A. V., Timmermann, B., Tolzmann, M., Egholm, M., Affourtit, J., Ashworth, D., Attiya, S., Bachorski, M., Buglione, E., Burke, A., Caprio, A., Celone, C., Clark, S., Connors, D., Gu, L., Guccione, L., Kao, K., Kebbel, A., Knowlton, J., Labrecque, M., McDade, L., Mealmaker, C., Minderman, M., Nawrocki, A., Niazi, F., Pareja, K., Ramenani, R., Riches, D., Song, W., Turcotte, C., Wang, S., Fulton, L., Weinstock, G., Burton, J., Carter, D. M., Churcher, C., Coffey, A., Cox, A., Quail, M., Skelly, T., Stalker, J., Swerdlow, H. P., Turner, D., De Witte, A., Giles, S., Sabo, A., Yu, J., Fang, X., Guo, X., Li, Y., Luo, R., Tai, S., Wu, H., Zheng, H., Zheng, X., Zhou, Y., Wang, J., Huang, W., Indap, A., Kural, D., Lee, W.-P., Stromberg, M. P., Ward, A. N., Lee, C., Mills, R. E., Shi, X., Daly, M. J., DePristo, M. A., Ball, A. D., Browning, B. L., Cibulskis, K., Garimella, K. V., Grossman, S. R., Hanna, M., Jaffe, D. B., Kernytsky, A. M., Li, H., Maguire, J. R., McCarroll, S. A., McKenna, A., Nemesh, J. C., Philippakis, A. A., Poplin, R. E., Price, A., Rivas, M. A., Sabeti, P. C., Schaffner, S. F., Shefler, E., Shlyakhter, I. A., Cooper, D. N., Ball, E. V., Mort, M., Phillips, A. D., Stenson, P. D., Sebat, J., Makarov, V., Ye, K., Yoon, S. C., Clark, A. G., Boyko, A., Degenhardt, J., Gutenkunst, R. N., Kaganovich, M., Keinan, A., Lacroute, P., Ma, X., Reynolds, A., Clarke, L., Cunningham, F., Herrero, J., Keenen, S., Kulesha, E., Leinonen, R., McLaren, W. M., Radhakrishnan, R., Smith, R. E., Zalunin, V., Zheng-Bradley, X., Korbel, J. O., Stütz, A. M., Bauer, M., Keira Cheetham, R., Cox, T., Eberle, M., James, T., Kahn, S., Murray, L., Ye, K., De La Vega, F. M., Fu, Y., Hyland, F. C. L., Manning, J. M., McLaughlin, S. F., Peckham, H. E., Sakarya, O., Sun, Y. A., Tsung, E. F., Batzer, M. A., Konkel, M. K., Walker, J. A., Sudbrak, R., Albrecht, M. W., Amstislavskiy, V. S., Herwig, R., Parkhomchuk, D. V., Agarwala, R., Khouri, H. M., Morgulis, A. O., Paschall, J. E., Phan, L. D., Rotmistrovsky, K. E., Sanders, R. D., Shumway, M. F., Xiao, C., Lunter, G., Marchini, J. L., Moutsianas, L., Myers, S., Tumian, A., Desany, B., Knight, J., Winer, R., Craig, D. W., Beckstrom-Sternberg, S. M., Christoforides, A., Kurdoglu, A. A., Pearson, J. V., Sinari, S. A., Tembe, W. D., Haussler, D., Hinrichs, A. S., Katzman, S. J., Kern, A., Kuhn, R. M., Przeworski, M., Hernandez, R. D., Howie, B., Kelley, J. L., Cord Melton, S., Abecasis, G. R., Li, Y., Anderson, P., Blackwell, T., Chen,

- W., Cookson, W. O., Ding, J., Min Kang, H., Lathrop, M., Liang, L., and Moffatt, M. F. a. (2010). A map of human genome variation from population-scale sequencing. *Nature*, **467**(7319), 1061–1073.
- Bodmer, W. and Bonilla, C. (2008). Common and rare variants in multifactorial susceptibility to common diseases. *Nature Genetics*, **40**(6), 695–701.
- Boehnke, M. and Cox, N. J. (1997). Accurate Inference of Relationships in Sib-Pair Linkage Studies. *The American Journal of Human Genetics*, **61**(2), 423–429.
- Boomsma, D. I., Wijmenga, C., Slagboom, E. P., Swertz, M. A., Karssen, L. C., Abdellaoui, A., Ye, K., Guryev, V., Vermaat, M., van Dijk, F., Francioli, L. C., Hottenga, J. J., Laros, J. F. J., Li, Q., Li, Y., Cao, H., Chen, R., Du, Y., Li, N., Cao, S., van Setten, J., Menelaou, A., Pulit, S. L., Hehir-Kwa, J. Y., Beekman, M., Elbers, C. C., Byelas, H., de Craen, A. J. M., Deelen, P., Dijkstra, M., den Dunnen, J. T., de Knijff, P., Houwing-Duistermaat, J., Koval, V., Estrada, K., Hofman, A., Kanterakis, A., van Enckevort, D., Mai, H., Kattenberg, M., van Leeuwen, E. M., Neerincx, P. B. T., Oostra, B., Rivadeneira, F., Suchiman, E. H. D., Uitterlinden, A. G., Willemse, G., Wolffenbuttel, B. H., Wang, J., de Bakker, P. I. W., van Ommen, G.-J., and van Duijn, C. M. (2013). The Genome of the Netherlands: design, and project goals. *European Journal of Human Genetics*, **22**(2), 221–227.
- Borodulin, K., Virtainen, E., Peltonen, M., Jousilahti, P., Juolevi, A., Laatikainen, T., Mannisto, S., Salomaa, V., Sundvall, J., and Puska, P. (2015). Forty-year trends in cardiovascular risk factors in Finland. *European Journal of Public Health*, **25**(3), 539–546.
- Botstein, D. and Risch, N. (2003). Discovering genotypes underlying human phenotypes: past successes for mendelian disease, future approaches for complex disease. *Nature Genetics*, **33**(3s), 228–237.
- Botstein, D., White, R. L., Skolnick, M., and Davis, R. W. (1980). Construction of a genetic linkage map in man using restriction fragment length polymorphisms. *American journal of human genetics*, **32**(3), 314–331.
- Browning, B. L. and Browning, S. R. (2011a). A fast, powerful method for detecting identity by descent. *American journal of human genetics*, **88**(2), 173–182.
- Browning, B. L. and Browning, S. R. (2013). Improving the accuracy and efficiency of identity-by-descent detection in population data. *Genetics*, **194**(2), 459–471.
- Browning, B. L. and Browning, S. R. (2016). Genotype Imputation with Millions of Reference Samples. *American journal of human genetics*, **98**(1), 116–126.
- Browning, S. R. (2008). Estimation of pairwise identity by descent from dense genetic marker data in a population sample of haplotypes. *Genetics*, **178**(4), 2123–2132.
- Browning, S. R. and Browning, B. L. (2010). High-Resolution Detection of Identity by Descent in Unrelated Individuals. *The American Journal of Human Genetics*, **86**(4), 526–539.
- Browning, S. R. and Browning, B. L. (2011b). Haplotype phasing: existing methods and new developments. *12*(10), 703–714.
- Browning, S. R. and Browning, B. L. (2012). Identity by Descent Between Distant Relatives: Detection and Applications. *Annual Review of Genetics*, **46**(1), 617–633.
- Buetow, K. H. (1991). Influence of aberrant observations on high-resolution linkage analysis outcomes. *The American Journal of Human Genetics*, **49**(5), 985–994.
- Burdett, T., Hall, P., Hasting, E., Hindorff, L., Junkins, H., Klemm, A., MacArthur, J., Manolio, T., Morales, J., Parkinson, H., et al. (2016). The nhgri-ebi catalog of published genome-wide association studies. Available at: www.ebi.ac.uk/gwas. Accessed 2017-01-20, version 1.0.

- Bustamante, C. D., Burchard, E. G., and De La Vega, F. M. (2011). Genomics for the world. *Nature*, **475**(7355), 163–165.
- Cai, L., Fisher, A. L., Huang, H., and Xie, Z. (2016). CRISPR-mediated genome editing and human diseases. *Genes & Diseases*, **3**(4), 244–251.
- Chen, J., Zhang, J.-G., Li, J., Pei, Y.-F., and Deng, H.-W. (2013). On Combining Reference Data to Improve Imputation Accuracy. *PloS one*, **8**(1).
- Choi, Y., Wijsman, E. M., and Weir, B. S. (2009). Case-control association testing in the presence of unknown relationships. *Genetic Epidemiology*, **33**(8), 668–678.
- Cirulli, E. T. and Goldstein, D. B. (2010). Uncovering the roles of rare variants in common disease through whole-genome sequencing. *Nature Publishing Group*, **11**(6), 415–425.
- Colombo, R. (2007). Dating mutations. *eLS*.
- Correns, K. F. J. (1899). Untersuchungen über die Xenien bei *Zea mays*. *Berichte der Deutschen Botanischen Gesellschaft*, **17**, 410–418.
- Cotterman, C. W. (1940). *A calculus for statistico-genetics*. Ph.D. thesis, The Ohio State University.
- Coventry, A., Bull-Otterson, L. M., Liu, X., Clark, A. G., Maxwell, T. J., Crosby, J., Hixson, J. E., Rea, T. J., Muzny, D. M., Lewis, L. R., Wheeler, D. A., Sabo, A., Lusk, C., Weiss, K. G., Akbar, H., Cree, A., Hawes, A. C., Newsham, I., Varghese, R. T., Villasana, D., Gross, S., Joshi, V., Santibanez, J., Morgan, M., Chang, K., Hale IV, W., Templeton, A. R., Boerwinkle, E., Gibbs, R., and Sing, C. F. (2010). Deep resequencing reveals excess rare recent variants consistent with explosive population growth. *Nature communications*, **1**(8), 131–6.
- Cox, D. G. and Kraft, P. (2006). Quantification of the Power of Hardy-Weinberg Equilibrium Testing to Detect Genotyping Error. *Human heredity*, **61**(1), 10–14.
- Crow, J. F. (1954). Breeding structure of populations. ii. effective population number. *Statistics and mathematics in biology*, **543**, 556.
- Daly, M. J., Rioux, J. D., Schaffner, S. F., Hudson, T. J., and Lander, E. S. (2001). High-resolution haplotype structure in the human genome. *Nature Genetics*, **29**(2), 229–232.
- de Bakker, P. I. W., Yelensky, R., Pe'er, I., Gabriel, S. B., Daly, M. J., and Altshuler, D. (2005). Efficiency and power in genetic association studies. *Nature Genetics*, **37**(11), 1217–1223.
- De Vries, H. M. (1900). Sur la loi de disjonction des hybrides. *Comptes rendus de l'Académie des Sciences*, **130**, 845–847.
- Deelen, P., Kanterakis, A., van Dijk, F., Medina-Gomez, C., Kreiner-Møller, E., Rivadeneira, F., Gutierrez-Achury, J., van Enckevort, D., Dijkstra, M., Byelas, H., Genome of Netherlands Consortium, de Bakker, P. I. W., and Swertz, M. A. (2014). Improved imputation quality of low-frequency and rare variants in European samples using the 'Genome of The Netherlands'. *European Journal of Human Genetics*, **22**(11), 1321–1326.
- Delaneau, O., Coulonges, C., and Zagury, J.-F. (2008). Shape-IT: new rapid and accurate algorithm for haplotype inference. *9*(1), 540.
- Delaneau, O., Marchini, J., and Zagury, J.-F. (2011). A linear complexity phasing method for thousands of genomes. *Nature methods*, **9**(2), 179–181.

- Delaneau, O., Zagury, J.-F., and Marchini, J. (2013). Improved whole-chromosome phasing for disease and population genetic studies. *Nature methods*, **10**(1), 5–6.
- Devlin, B., Roeder, K., and Wasserman, L. (2001). Genomic control, a new approach to genetic-based association studies. *Theoretical population biology*, **60**(3), 155–166.
- Donnelly, K. P. (1983). The probability that related individuals share some section of genome identical by descent. *Theoretical population biology*, **23**(1), 34–63.
- Douglas, J. A., Boehnke, M., and Lange, K. (2000). A Multipoint Method for Detecting Genotyping Errors and Mutations in Sibling-Pair Linkage Data. *The American Journal of Human Genetics*, **66**(4), 1287–1297.
- Douglas, J. A., Skol, A. D., and Boehnke, M. (2002). Probability of Detection of Genotyping Errors and Mutations as Inheritance Inconsistencies in Nuclear-Family Data. *The American Journal of Human Genetics*, **70**(2), 487–495.
- Eberle, M. A., Fritzilas, E., Krusche, P., Kallberg, M., Moore, B. L., Bekritsky, M. A., Iqbal, Z., Chuang, H.-Y., Humphray, S. J., Halpern, A. L., Kruglyak, S., Margulies, E. H., McVean, G., and Bentley, D. R. (2016). A reference data set of 5.4 million phased human variants validated by genetic inheritance from sequencing a three-generation 17-member pedigree. *Genome Research*, **27**(1), 1–9.
- Ewens, W. J. (2012). *Mathematical Population Genetics 1: Theoretical Introduction*, volume 27. Springer Science & Business Media.
- Fisher, R. A. (1930). *The genetical theory of natural selection*. Oxford University Press, Oxford.
- Fisher, R. A. (1949). The theory of inbreeding. *The theory of inbreeding*.
- Fisher, R. A. (1954). A fuller theory of “junctions” in inbreeding. *Heredity*, **8**(2), 187–197.
- Forney, G. D. (1973). The viterbi algorithm. In *Proceedings of the IEEE*, pages 268–278.
- Frazer, K. A., Murray, S. S., Schork, N. J., and Topol, E. J. (2009). Human genetic variation and its contribution to complex traits. *Nature Reviews Genetics*, **10**(4), 241–251.
- Freedman, M. L., Reich, D., Penney, K. L., McDonald, G. J., Mignault, A. A., Patterson, N., Gabriel, S. B., Topol, E. J., Smoller, J. W., Pato, C. N., Pato, M. T., Petryshen, T. L., Kolonel, L. N., Lander, E. S., Sklar, P., Henderson, B., Hirschhorn, J. N., and Altshuler, D. (2004). Assessing the impact of population stratification on genetic association studies. *Nature Genetics*, **36**(4), 388–393.
- Fu, W., O'Connor, T. D., Jun, G., Kang, H. M., Abecasis, G., Leal, S. M., Gabriel, S., Altshuler, D., Shendure, J., Nickerson, D. A., Bamshad, M. J., Project, N. E. S., and Akey, J. M. (2012). Analysis of 6,515 exomes reveals the recent origin of most human protein-coding variants. *Nature*, **493**(7431), 216–220.
- Fu, Y.-X. and Li, W.-H. (1999). Coalescing into the 21st Century: An Overview and Prospects of Coalescent Theory. *Theoretical population biology*, **56**(1), 1–10.
- Fuchsberger, C., Flannick, J., Teslovich, T. M., Mahajan, A., Agarwala, V., Gaulton, K. J., Ma, C., Fontanillas, P., Moutsianas, L., McCarthy, D. J., Rivas, M. A., Perry, J. R. B., Sim, X., Blackwell, T. W., Robertson, N. R., Rayner, N. W., Cingolani, P., Locke, A. E., Tajes, J. F., Highland, H. M., Dupuis, J., Chines, P. S., Lindgren, C. M., Hartl, C., Jackson, A. U., Chen, H., Huyghe, J. R., van de Bunt, M., Pearson, R. D., Kumar, A., Müller-Nurasyid, M., Grarup, N., Stringham, H. M., Gamazon, E. R., Lee, J., Chen, Y., Scott, R. A., Below, J. E., Chen, P., Huang, J., Go, M. J., Stitzel, M. L., Pasko, D., Parker, S. C. J., Varga, T. V., Green, T., Beer, N. L., Day-Williams, A. G., Ferreira, T., Fingerlin, T., Horikoshi, M., Hu, C., Huh, I., Ikram, M. K., Kim, B.-J., Kim, Y., Kim, Y. J., Kwon, M.-S., Lee, J., Lee, S., Lin, K.-H., Maxwell, T. J., Nagai, Y., Wang, X., Welch, R. P., Yoon, J., Zhang, W., Barzilai, N., Voight, B. F., Han, B.-G., Jenkinson, C. P., Kuulasmaa, T.,

- Kuusisto, J., Manning, A., Ng, M. C. Y., Palmer, N. D., Balkau, B., áková, A. S., Abboud, H. E., Boeing, H., Giedraitis, V., Prabhakaran, D., Gottesman, O., Scott, J., Carey, J., Kwan, P., Grant, G., Smith, J. D., Neale, B. M., Purcell, S., Butterworth, A. S., Howson, J. M. M., Lee, H. M., Lu, Y., Kwak, S.-H., Zhao, W., Danesh, J., Lam, V. K. L., Park, K. S., Saleheen, D., So, W. Y., Tam, C. H. T., Afzal, U., Aguilar, D., Arya, R., Aung, T., Chan, E., Navarro, C., Cheng, C.-Y., Palli, D., Correa, A., Curran, J. E., Rybin, D., Farook, V. S., Fowler, S. P., Freedman, B. I., Griswold, M., Hale, D. E., Hicks, P. J., Khor, C.-C., Kumar, S., Lehne, B., Thuillier, D., Lim, W. Y., Liu, J., van der Schouw, Y. T., Loh, M., Musani, S. K., Puppala, S., Scott, W. R., Yengo, L., Tan, S.-T., Taylor, H. A., Thameem, F., Wilson, G., Wong, T. Y., Njølstad, P. R., Levy, J. C., Mangino, M., Bonnycastle, L. L., Schwarzmayr, T., Fadista, J., Surdulescu, G. L., Herder, C., Groves, C. J., Wieland, T., Bork-Jensen, J., Brandslund, I., Christensen, C., Koistinen, H. A., Doney, A. S. F., Kinnunen, L., Esko, T., Farmer, A. J., Hakaste, L., Hodgkiss, D., Kravic, J., Lyssenko, V., Hollensted, M., Jørgensen, M. E., Jørgensen, T., Ladenvall, C., Justesen, J. M., Käräjämäki, A., Kriebel, J., Rathmann, W., Lannfelt, L., Lauritzen, T., Narisu, N., Linneberg, A., Melander, O., Milani, L., Neville, M., Orho-Melander, M., Qi, L., Qi, Q., Roden, M., Rolandsson, O., Swift, A., Rosengren, A. H., Stirrups, K., Wood, A. R., Mihailov, E., Blancher, C., Carneiro, M. O., Maguire, J., Poplin, R., Shakir, K., Fennell, T., DePristo, M., de Angelis, M. H., Deloukas, P., Gjesing, A. P., Jun, G., Nilsson, P., Murphy, J., Onofrio, R., Thorand, B., Hansen, T., Meisinger, C., Hu, F. B., Isomaa, B., Karpe, F., Liang, L., Peters, A., Huth, C., O'Rahilly, S. P., Palmer, C. N. A., Pedersen, O., Rauramaa, R., Tuomilehto, J., Salomaa, V., Watanabe, R. M., Syvänen, A.-C., Bergman, R. N., Bharadwaj, D., Bottinger, E. P., Cho, Y. S., Chandak, G. R., Chan, J. C. N., Chia, K. S., Daly, M. J., Ebrahim, S. B., Langenberg, C., Elliott, P., Jablonski, K. A., Lehman, D. M., Jia, W., and Ma, R. (2016). The genetic architecture of type 2 diabetes. *Nature*, **536**(7614), 41–47.
- Genome of the Netherlands Consortium (2014). Whole-genome sequence variation, population structure and demographic history of the Dutch population. *Nature Genetics*, **46**(8), 818–825.
- Gordon, D., Heath, S. C., Liu, X., and Ott, J. (2001). A Transmission/Disequilibrium Test That Allows for Genotyping Errors in the Analysis of Single-Nucleotide Polymorphism Data. *The American Journal of Human Genetics*, **69**(2), 371–380.
- Gordon, D., Finch, S. J., Nothnagel, M., and Ott, J. u. r. (2002). Power and Sample Size Calculations for Case-Control Genetic Association Tests when Errors Are Present: Application to Single Nucleotide Polymorphisms. *Human heredity*, **54**(1), 22–33.
- Gore, A., Li, Z., Fung, H.-L., Young, J. E., Agarwal, S., Antosiewicz-Bourget, J., Canto, I., Giorgetti, A., Israel, M. A., Kiskinis, E., Lee, J.-H., Loh, Y.-H., Manos, P. D., Montserrat, N., Panopoulos, A. D., Ruiz, S., Wilbert, M. L., Yu, J., Kirkness, E. F., Izpisua Belmonte, J. C., Rossi, D. J., Thomson, J. A., Eggan, K., Daley, G. Q., Goldstein, L. S. B., and Zhang, K. (2011). Somatic coding mutations in human induced pluripotent stem cells. *Nature*, **471**(7336), 63–67.
- Griffiths, R. C. (1991). The Two-Locus Ancestral Graph. In *Selected Proceedings of the Sheffield Symposium on Applied Probability*, pages 100–117. Institute of Mathematical Statistics, Hayward, CA.
- Griffiths, R. C. and Marjoram, P. (1996). Ancestral inference from samples of DNA sequences with recombination. *Journal of Computational Biology*, **3**(4), 479–502.
- Griffiths, R. C. and Marjoram, P. (1997a). An ancestral recombination graph. *Institute for Mathematics and its Applications*, **87**, 257.
- Griffiths, R. C. and Marjoram, P. (1997b). Progress in population genetics and human evolution.
- Griffiths, R. C. and Tavaré, S. (1998). The age of a mutation in a general coalescent tree. *Communications in Statistics. Stochastic Models*, **14**(1-2), 273–295.
- Gusev, A., Lowe, J. K., Stoffel, M., Daly, M. J., Altshuler, D., Breslow, J. L., Friedman, J. M., and Pe'er, I. (2009). Whole population, genome-wide mapping of hidden relatedness. *Genome Research*, **19**(2), 318–326.

- Gutenkunst, R. N., Hernandez, R. D., Williamson, S. H., and Bustamante, C. D. (2009). Inferring the Joint Demographic History of Multiple Populations from Multidimensional SNP Frequency Data. *PLoS Genetics*, **5**(10), e1000695–11.
- Haldane, J. (1919). The combination of linkage values and the calculation of distances between the loci of linked factors. *J Genet*, **8**(29), 299–309.
- Hardy, G. H. (1908). Mendelian Proportions in a Mixed Population. *Science*, **28**(706), 49–50.
- Harris, K. and Nielsen, R. (2013). Inferring Demographic History from a Spectrum of Shared Haplotype Lengths. *PLoS Genetics*, **9**(6).
- Hayes, B. J., Visscher, P. M., McPartlan, H. C., and Goddard, M. E. (2003). Novel multilocus measure of linkage disequilibrium to estimate past effective population size. *Genome Research*, **13**(4), 635–643.
- Hein, J., Schierup, M., and Wiuf, C. (2004). *Gene genealogies, variation and evolution: a primer in coalescent theory*. Oxford University Press, Oxford.
- Henn, B. M., Gutenkunst, R. N., Indap, A. R., Marth, G. T., Clark, A. G., Yu, F., Gibbs, R. A., 1000 Genomes Project, Durbin, R. M., Flicek, P., Gabriel, S. B., Lander, E. S., Wheeler, D., Cibulskis, K., Fennell, T. J., Jaffe, D. B., Shefler, E., Egholm, M., Fulton, R., Bainbridge, M., Challis, D., Sabo, A., Wang, J., Lee, C., Korn, J. M., Sudbrak, R., Auton, A., Iqbal, Z., Desany, B., Dooling, D., Hurles, M. E., MacArthur, D. G., Abyzov, A., Zhang, Z., Garrison, E. P., Banks, E., Handsaker, R. E., Hartl, C., De La Vega, F. M., Alkan, C., Snyder, M., Muzny, D., Reid, J., Quinlan, A. R., Stewart, C., Wu, J., Gravel, S., Sherry, S. T., McVean, G. A., Abecasis, G. R., Koboldt, D. C., Palotie, A., Bustamante, C. D., Schafer, A. J., and Brooks, L. D. (2011). Demographic history and rare allele sharing among human populations. *Proceedings of the National Academy of Sciences*, **108**(29), 11983–11988.
- Howie, B., Marchini, J., and Stephens, M. (2011a). Genotype imputation with thousands of genomes. *G3 (Bethesda, Md.)*, **1**(6), 457–470.
- Howie, B., Marchini, J., and Stephens, M. (2011b). Genotype Imputation with Thousands of Genomes. *G3 (Bethesda, Md.)*, **1**(6), 457–470.
- Howie, B. N., Donnelly, P., and Marchini, J. (2009). A Flexible and Accurate Genotype Imputation Method for the Next Generation of Genome-Wide Association Studies. *PLoS Genetics*, **5**(6), e1000529.
- Hudson, R. (1990). Gene genealogies and the coalescent process. *Oxford surveys in evolutionary biology*, **7**(1), 44.
- Hudson, R. and Kaplan, N. L. (1985). Statistical Properties of the Number of Recombination Events in the History of a Sample of Dna-Sequences. *Genetics*, **111**(1), 147–164.
- Hudson, R. R. (1983). Properties of a neutral allele model with intragenic recombination. *Theoretical population biology*, **23**(2), 183–201.
- Hudson, R. R. (2001). Two-locus sampling distributions and their application. *Genetics*, **159**(4), 1805–1817.
- Hudson, R. R. (2002). Generating samples under a Wright-Fisher neutral model of genetic variation. *Bioinformatics*, **18**(2), 337–338.
- International HapMap 3 Consortium, Schaffner, S. F., Peltonen, L., Dermitzakis, E., Bonnen, P. E., Altshuler, D. M., de Bakker, P. I. W., Deloukas, P., Gabriel, S. B., Gwilliam, R., Hunt, S., Inouye, M., Jia, X., Palotie, A., Parkin, M., Whittaker, P., Yu, F., Chang, K., Hawes, A., Lewis, L. R., Ren, Y., Wheeler, D., Gibbs, R. A., Muzny, D. M., Barnes, C., Darvishi, K., Hurles, M., Korn, J. M., Kristiansson, K., Lee, C., McCarrol, S. A., Nemesh, J., Keinan, A., Montgomery, S. B., Pollack, S., Soranzo, N., Gonzaga-Jauregui, C., Anttila, V.,

- Brodeur, W., Daly, M. J., Leslie, S., McVean, G., Moutsianas, L., Nguyen, H., Zhang, Q., Ghori, M. J. R., McGinnis, R., McLaren, W., Price, A. L., Takeuchi, F., Grossman, S. R., Shlyakhter, I., Hostetter, E. B., Sabeti, P. C., Adebamowo, C. A., Foster, M. W., Gordon, D. R., Licinio, J., Manca, M. C., Marshall, P. A., Matsuda, I., Ngare, D., Wang, V. O., Reddy, D., Rotimi, C. N., Royal, C. D., Sharp, R. R., Zeng, C., Brooks, L. D., and McEwen, J. E. (2010). Integrating common and rare genetic variation in diverse human populations. *Nature*, **467**(7311), 52–58.
- International HapMap Consortium (2003). The International HapMap Project. *Nature*, **426**(6968), 789–796.
- International HapMap Consortium, Frazer, K. A., Ballinger, D. G., Cox, D. R., Hinds, D. A., Stuve, L. L., Gibbs, R. A., Belmont, J. W., Boudreau, A., Hardenbol, P., Leal, S. M., Pasternak, S., Wheeler, D. A., Willis, T. D., Yu, F., Yang, H., Zeng, C., Gao, Y., Hu, H., Hu, W., Li, C., Lin, W., Liu, S., Pan, H., Tang, X., Wang, J., Wang, W., Yu, J., Zhang, B., Zhang, Q., Zhao, H., Zhao, H., Zhou, J., Gabriel, S. B., Barry, R., Blumenstiel, B., Camargo, A., Defelice, M., Faggart, M., Goyette, M., Gupta, S., Moore, J., Nguyen, H., Parkin, M., Roy, J., Stahl, E., Winchester, E., Ziaugra, L., Shen, Y., Yao, Z., Huang, W., Chu, X., He, Y., Jin, L., Liu, Y., Shen, Y., Sun, W., Wang, H., Wang, Y., Wang, Y., Xiong, X., Xu, L., Waye, M. M. Y., Tsui, S. K. W., Xue, H., Wong, J. T.-F., Galver, L. M., Fan, J.-B., Gunderson, K., Murray, S. S., Oiphant, A. R., Chee, M. S., Montpetit, A., Chagnon, F., Ferretti, V., Leboeuf, M., Olivier, J.-F., Phillips, M. S., Roumy, S., Sallée, C., Verner, A., Hudson, T. J., Kwok, P.-Y., Cai, D., Koboldt, D. C., Miller, R. D., Pawlikowska, L., Taillon-Miller, P., Xiao, M., Tsui, L.-C., Mak, W., Song, Y. Q., Tam, P. K. H., Nakamura, Y., Kawaguchi, T., Kitamoto, T., Morizono, T., Nagashima, A., Ohnishi, Y., Sekine, A., Tanaka, T., Tsunoda, T., Deloukas, P., Bird, C. P., Delgado, M., Dermitzakis, E. T., Gwilliam, R., Hunt, S., Morrison, J., Powell, D., Stranger, B. E., Whittaker, P., Bentley, D. R., de Bakker, P. I. W., Barrett, J., Chretien, Y. R., Maller, J., McCarroll, S., Patterson, N., Pe'er, I., Price, A., Purcell, S., Sabeti, P., Saxena, R., Schaffner, S. F., Sham, P. C., Varilly, P., Altshuler, D., Stein, L. D., Krishnan, L., Smith, A. V., Tello-Ruiz, M. K., Thorisson, G. A., Chakravarti, A., Chen, P. E., Cutler, D. J., Kashuk, C. S., Lin, S., Abecasis, G. R., Guan, W., Li, Y., Munro, H. M., Qin, Z. S., Thomas, D. J., McVean, G., Auton, A., Bottolo, L., Cardin, N., Eyheramendy, S., Freeman, C., Marchini, J., Myers, S., Spencer, C., Stephens, M., Donnelly, P., Cardon, L. R., Clarke, G., Evans, D. M., Morris, A. P., Weir, B. S., Mullikin, J. C., Sherry, S. T., Feolo, M., Skol, A., Zhang, H., Matsuda, I., Fukushima, Y., Macer, D. R., Suda, E., Rotimi, C. N., Adebamowo, C. A., Ajayi, I., Aniagwu, T., Marshall, P. A., Nkwodimma, C., Royal, C. D. M., Leppert, M. F., Dixon, M., Peiffer, A., Qiu, R., Kent, A., Kato, K., Niikawa, N., Adewole, I. F., Knoppers, B. M., Foster, M. W., Clayton, E. W., Watkin, J., Muzny, D., Nazareth, L., Sodergren, E., Weinstock, G. M., Yakub, I., Onofrio, R. C., Richter, D. J., Birren, B. W., Daly, M. J., Wilson, R. K., Fulton, L. L., Rogers, J., Burton, J., Carter, N. P., Clee, C. M., Griffiths, M., Jones, M. C., McLay, K., Plumb, R. W., Ross, M. T., Sims, S. K., Willey, D. L., Chen, Z., Han, H., Kang, L., Godbout, M., Wallenburg, J. C., L'Archevêque, P., Bellemare, G., Saeki, K., Wang, H., An, D., Fu, H., Li, Q., Wang, Z., Wang, R., Holden, A. L., Brooks, L. D., McEwen, J. E., Guyer, M. S., Wang, V. O., Peterson, J. L., Shi, M., Spiegel, J., Sung, L. M., Zacharia, L. F., Collins, F. S., Kennedy, K., Jamieson, R., and Stewart, J. (2007). A second generation human haplotype map of over 3.1 million SNPs. *Nature*, **449**(7164), 851–861.
- International Human Genome Sequencing Consortium (2001). Initial sequencing and analysis of the human genome. *Nature*, **409**(6822), 860–921.
- International Human Genome Sequencing Consortium (2004). Finishing the euchromatic sequence of the human genome. *Nature*, **431**(7011), 931–945.
- Kaiser, J. (2008). A plan to capture human diversity in 1000 genomes (Science (395)). *Science*, **319**(5868), 1336.
- Kang, S. J., Gordon, D., and Finch, S. J. (2004). What SNP genotyping errors are most costly for genetic association studies? *Genetic Epidemiology*, **26**(2), 132–141.
- Keinan, A. and Clark, A. G. (2012). Recent explosive human population growth has resulted in an excess of rare genetic variants. *Science*, **336**(6082), 740–743.

- Kelleher, J., Etheridge, A. M., and McVean, G. (2016). Efficient Coalescent Simulation and Genealogical Analysis for Large Sample Sizes. *PLoS computational biology*, **12**(5), e1004842–22.
- Kimura, M. (1969). The number of heterozygous nucleotide sites maintained in a finite population due to steady flux of mutations. *Genetics*, **61**(4), 893–903.
- Kimura, M. and Ota, T. (1973). The age of a neutral mutant persisting in a finite population. *Genetics*, **75**(1), 199–212.
- Kingman, J. F. C. (1982a). Exchangeability and the evolution of large populations. *Exchangeability in Probability and Statistics*, pages 97—112.
- Kingman, J. F. C. (1982b). On the genealogy of large populations. *Journal of Applied Probability*, **19**(A), 27–43.
- Kingman, J. F. C. (1982c). The coalescent. *Stochastic processes and their applications*, **13**(3), 235–248.
- Klein, R. J., Zeiss, C., Chew, E. Y., Tsai, J.-Y., Sackler, R. S., Haynes, C., Henning, A. K., SanGiovanni, J. P., Mane, S. M., Mayne, S. T., Bracken, M. B., Ferris, F. L., Ott, J., Barnstable, C., and Hoh, J. (2005). Complement Factor H Polymorphism in Age-Related Macular Degeneration. *Science*, **308**(5720), 385–389.
- Kong, A., Masson, G., Frigge, M. L., Gylfason, A., Zusmanovich, P., Thorleifsson, G., Olason, P. I., Ingason, A., Steinberg, S., Rafnar, T., Sulem, P., Mouy, M., Jonsson, F., Thorsteinsdottir, U., Gudbjartsson, D. F., Stefansson, H., and Stefansson, K. (2008). Detection of sharing by descent, long-range phasing and haplotype imputation. *Nature Genetics*, **40**(9), 1068–1075.
- Kruglyak, L. (1999). Prospects for whole-genome linkage disequilibrium mapping of common disease genes. *Nature Genetics*, **22**(2), 139–144.
- Kryukov, G. V., Pennacchio, L. A., and Sunyaev, S. R. (2007). Most rare missense alleles are deleterious in humans: implications for complex disease and association studies. *The American Journal of Human Genetics*, **80**(4), 727–739.
- Lawson, D. J., Hellenthal, G., Myers, S., and Falush, D. (2012). Inference of population structure using dense haplotype data. *PLoS Genetics*, **8**(1), e1002453.
- Leutenegger, A.-L., Prum, B., Génin, E., Verny, C., Lemainque, A., Clerget-Darpoux, F., and Thompson, E. A. (2003). Estimation of the Inbreeding Coefficient through Use of Genomic Data. *American journal of human genetics*, **73**(3), 516–523.
- Li, N. and Stephens, M. (2003). Modeling linkage disequilibrium and identifying recombination hotspots using single-nucleotide polymorphism data. *Genetics*, **165**(4), 2213–2233.
- Li, W. H. (1975). The first arrival time and mean age of a deleterious mutant gene in a finite population. *The American Journal of Human Genetics*, **27**(3), 274–286.
- Li, Y., Willer, C., Sanna, S., and Abecasis, G. (2009). Genotype imputation. *Annual review of genomics and human genetics*, **10**, 387–406.
- Li, Y., Willer, C. J., Ding, J., Scheet, P., and Abecasis, G. R. (2010). MaCH: using sequence and genotype data to estimate haplotypes and unobserved genotypes. *Genetic Epidemiology*, **34**(8), 816–834.
- Lim, E. T., Würtz, P., Havulinna, A. S., Palta, P., Tukiainen, T., Rehnström, K., Esko, T., Mägi, R., Inouye, M., Lappalainen, T., Chan, Y., Salem, R. M., Lek, M., Flannick, J., Sim, X., Manning, A., Ladenvall, C., Bumpstead, S., Hämäläinen, E., Aalto, K., Maksimow, M., Salmi, M., Blankenberg, S., Ardissino, D., Shah, S., Horne, B., McPherson, R., Hovingh, G. K., Reilly, M. P., Watkins, H., Goel, A., Farrall, M., Girelli, D., Reiner, A. P., Stitzel, N. O., Kathiresan, S., Gabriel, S., Barrett, J. C., Lehtimäki, T., Laakso, M., Groop, L.,

- Kaprio, J., Perola, M., McCarthy, M. I., Boehnke, M., Altshuler, D. M., Lindgren, C. M., Hirschhorn, J. N., Metspalu, A., Freimer, N. B., Zeller, T., Jalkanen, S., Koskinen, S., Raitakari, O., Durbin, R., MacArthur, D. G., Salomaa, V., Ripatti, S., Daly, M. J., Palotie, A., and for the Sequencing Initiative Suomi (SISu) Project (2014). Distribution and Medical Impact of Loss-of-Function Variants in the Finnish Founder Population. *PLoS Genetics*, **10**(7), e1004494–12.
- Liu, L., Li, Y., Li, S., Hu, N., He, Y., Pong, R., Lin, D., Lu, L., and Law, M. (2012). Comparison of Next-Generation Sequencing Systems. *Journal of biomedicine & biotechnology*, **2012**(7), 1–11.
- Loh, P.-R., Palamara, P. F., and Price, A. L. (2016a). Fast and accurate long-range phasing in a uk biobank cohort. *Nature genetics*.
- Loh, P.-R., Danecek, P., Palamara, P. F., Fuchsberger, C., Reshef, Y. A., Finucane, H. K., Schoenherr, S., Forer, L., McCarthy, S., Abecasis, G. R., Durbin, R., and Price, A. L. (2016b). Reference-based phasing using the Haplotype Reference Consortium panel. Technical report.
- Malécot, G. (1948). Mathematics of heredity. *Les mathématiques de l'hérédité*.
- Manolio, T. A., Collins, F. S., Cox, N. J., Goldstein, D. B., Hindorff, L. A., Hunter, D. J., McCarthy, M. I., Ramos, E. M., Cardon, L. R., Chakravarti, A., Cho, J. H., Guttmacher, A. E., Kong, A., Kruglyak, L., Mardis, E., Rotimi, C. N., Slatkin, M., Valle, D., Whittemore, A. S., Boehnke, M., Clark, A. G., Eichler, E. E., Gibson, G., Haines, J. L., Mackay, T. F. C., McCarroll, S. A., and Visscher, P. M. (2009). Finding the missing heritability of complex diseases. *Nature*, **461**(7265), 747–753.
- Marchini, J. and Howie, B. (2010). Genotype imputation for genome-wide association studies. *11*(7), 499–511.
- Marchini, J., Howie, B., Myers, S., McVean, G., and Donnelly, P. (2007). A new multipoint method for genome-wide association studies by imputation of genotypes. *Nature Genetics*, **39**(7), 906–913.
- Mardis, E. R. (2006). Anticipating the 1,000 dollar genome. *Genome biology*, **7**(7), 112.
- Mardis, E. R. (2017). DNA sequencing technologies: 2006–2016. *Nature Protocols*, **12**(2), 213–218.
- Marth, G. T., Yu, F., Indap, A. R., Garimella, K., Gravel, S., Leong, W. F., Tyler-Smith, C., Bainbridge, M., Blackwell, T., Zheng-Bradley, X., Chen, Y., Challis, D., Clarke, L., Ball, E. V., Cibulskis, K., Cooper, D. N., Fulton, B., Hartl, C., Koboldt, D., Muzny, D., Smith, R., Sougnez, C., Stewart, C., Ward, A., Yu, J., Xue, Y., Altshuler, D., Bustamante, C. D., Clark, A. G., Daly, M., DePristo, M., Flicek, P., Gabriel, S., Mardis, E., Palotie, A., Gibbs, R., and 1000 Genomes Project (2011). The functional spectrum of low-frequency coding variation. *Genome biology*, **12**(9), R84.
- Maruyama, T. (1974). The age of an allele in a finite population. *Genetical research*, **23**(2), 137–143.
- Mathieson, I. and McVean, G. (2012). Differential confounding of rare and common variants in spatially structured populations. *Nature Genetics*, **44**(3), 243–U29.
- Mathieson, I. and McVean, G. (2014). Demography and the Age of Rare Variants. *PLoS Genetics*, **10**(8), e1004528.
- Maynard Smith, J. (1989). *Evolutionary genetics*. Oxford University Press.
- McCarroll, S. A., Kuruvilla, F. G., Korn, J. M., Cawley, S., Nemesh, J., Wysoker, A., Shapero, M. H., de Bakker, P. I. W., Maller, J. B., Kirby, A., Elliott, A. L., Parkin, M., Hubbell, E., Webster, T., Mei, R., Veitch, J., Collins, P. J., Handsaker, R., Lincoln, S., Nizzari, M., Blume, J., Jones, K. W., Rava, R., Daly, M. J., Gabriel, S. B., and Altshuler, D. (2008). Integrated detection and population-genetic analysis of SNPs and copy number variation. *Nature Genetics*, **40**(10), 1166–1174.

- McCarthy, M. I., Abecasis, G. R., Cardon, L. R., Goldstein, D. B., Little, J., Ioannidis, J. P. A., and Hirschhorn, J. N. (2008). Genome-wide association studies for complex traits: consensus, uncertainty and challenges. *Nature Publishing Group*, **9**(5), 356–369.
- McCarthy, S., Das, S., Kretzschmar, W., Delaneau, O., Wood, A. R., Teumer, A., Kang, H. M., Fuchsberger, C., Danecek, P., Sharp, K., Luo, Y., Sidore, C., Kwong, A., Timpson, N., Koskenen, S., Vrieze, S., Scott, L. J., Zhang, H., Mahajan, A., Veldink, J., Peters, U., Pato, C., van Duijn, C. M., Gillies, C. E., Gandin, I., Mezzavilla, M., Gilly, A., Cocca, M., Traglia, M., Angius, A., Barrett, J. C., Boomsma, D., Branham, K., Breen, G., Brummett, C. M., Busonero, F., Campbell, H., Chan, A., Chen, S., Chew, E., Collins, F. S., Corbin, L. J., Smith, G. D., Dedoussis, G., Dorr, M., Farmaki, A.-E., Ferrucci, L., Forer, L., Fraser, R. M., Gabriel, S., Levy, S., Groop, L., Harrison, T., Hattersley, A., Holmen, O. L., Hveem, K., Kretzler, M., Lee, J. C., McGue, M., Meitinger, T., Melzer, D., Min, J. L., Mohlke, K. L., Vincent, J. B., Nauck, M., Nickerson, D., Palotie, A., Pato, M., Pirastu, N., McInnis, M., Richards, J. B., Sala, C., Salomaa, V., Schlessinger, D., Schoenherr, S., Slagboom, P. E., Small, K., Spector, T., Stambolian, D., Tuke, M., Tuomilehto, J., Van den Berg, L. H., Van Rheenen, W., Volker, U., Wijmenga, C., Toniolo, D., Zeggini, E., Gasparini, P., Sampson, M. G., Wilson, J. F., Frayling, T., de Bakker, P. I. W., Swertz, M. A., McCarroll, S., Kooperberg, C., Dekker, A., Altshuler, D., Willer, C., Iacono, W., Ripatti, S., Soranzo, N., Walter, K., Swaroop, A., Cucca, F., Anderson, C. A., Myers, R. M., Boehnke, M., McCarthy, M. I., Durbin, R., Abecasis, G., and Marchini, J. (2016). A reference panel of 64,976 haplotypes for genotype imputation. *Nature Genetics*, **48**(10), 1279–1283.
- McClellan, J. and King, M.-C. (2010). Genetic Heterogeneity in Human Disease. *Cell*, **141**(2), 210–217.
- McLaren, W., Gil, L., Hunt, S. E., Riat, H. S., Ritchie, G. R. S., Thormann, A., Flücke, P., and Cunningham, F. (2016). The Ensembl Variant Effect Predictor. *Genome biology*, pages 1–14.
- McQuillan, R., Leutenegger, A.-L., Abdel-Rahman, R., Franklin, C. S., Pericic, M., Barac-Lauc, L., Smolej-Narancic, N., Janicijevic, B., Polasek, O., Tenesa, A., MacLeod, A. K., Farrington, S. M., Rudan, P., Hayward, C., Vitart, V., Rudan, I., Wild, S. H., Dunlop, M. G., Wright, A. F., Campbell, H., and Wilson, J. F. (2008). Runs of Homozygosity in European Populations. *The American Journal of Human Genetics*, **83**(3), 359–372.
- McVean, G., Awadalla, P., and Fearnhead, P. (2002). A coalescent-based method for detecting and estimating recombination from gene sequences. *Genetics*.
- McVean, G. A. T., Myers, S. R., Hunt, S., Deloukas, P., Bentley, D. R., and Donnelly, P. (2004). The fine-scale structure of recombination rate variation in the human genome. *Science*, **304**(5670), 581–584.
- Mendel, G. (1866). Versuche über Pflanzenhybriden. *Verhandlungen des naturforschenden Vereines in Brünn*, **4**, 3–47.
- Metzker, M. L. (2009). Sequencing technologies — the next generation. *Nature Publishing Group*, **11**(1), 31–46.
- Milligan, B. G. (2003). Maximum-Likelihood Estimation of Relatedness. *Genetics*, **163**(3), 1153–1167.
- Moore, G. E. (1965). Cramming more components onto integrated circuits. *Electronics*, **38**(8).
- Morgan, T. H. (1911). Random segregation versus coupling in Mendelian inheritance. *Science*, **34**(873), 384–384.
- Morral, N., Bertranpetti, J., Estivill, X., and Nunes, V. (1994). The origin of the major cystic fibrosis mutation (DF508) in European populations. *Nature*.
- Morris, A. and Cardon, L. (2007). Whole genome association. *Handbook of Statistical Genetics, Third Edition*, pages 1238–1263.
- Moskvina, V. and Schmidt, K. M. (2006). Susceptibility of Biallelic Haplotype and Genotype Frequencies to Genotyping Error. *Biometrics*, **62**(4), 1116–1123.

- Moskvina, V., Craddock, N., Holmans, P., Owen, M., and O'Donovan, M. (2005). Minor genotyping error can result in substantial elevation in type i error rate in haplotype based case control analysis. In *American Journal of Medical Genetics Part B-Neuropsychiatric Genetics*, volume 138, pages 19–19.
- Moutsianas, L., Agarwala, V., Fuchsberger, C., Flannick, J., Rivas, M. A., Gaulton, K. J., Albers, P. K., GoT2D Consortium, McVean, G., Boehnke, M., Altshuler, D., and McCarthy, M. I. (2015). The Power of Gene-Based Rare Variant Methods to Detect Disease-Associated Variation and Test Hypotheses About Complex Disease. *PLoS Genetics*, **11**(4), e1005165–24.
- Myers, S., Bottolo, L., Freeman, C., McVean, G., and Donnelly, P. (2005). A fine-scale map of recombination rates and hotspots across the human genome. *Science*.
- Naidoo, N., Pawitan, Y., Soong, R., Cooper, D. N., and Ku, C.-S. (2011). Human genetics and genomics a decade after the release of the draft sequence of the human genome. *Human Genomics*, **5**(6), 577–622.
- Neuhauser, C. (2001). Mathematical models in population genetics. *Handbook of statistical genetics*.
- Nordborg, M. (2001). Coalescent theory. *Handbook of statistical genetics*.
- O'Connell, J., Gurdasani, D., Delaneau, O., Pirastu, N., Uliivi, S., Cocca, M., Traglia, M., Huang, J., Huffman, J. E., Rudan, I., McQuillan, R., Fraser, R. M., Campbell, H., Polasek, O., Asiki, G., Ekoru, K., Hayward, C., Wright, A. F., Vitart, V., Navarro, P., Zagury, J.-F., Wilson, J. F., Toniolo, D., Gasparini, P., Soranzo, N., Sandhu, M. S., and Marchini, J. (2014). A General Approach for Haplotype Phasing across the Full Spectrum of Relatedness. *PLoS Genetics*, **10**(4), e1004234–21.
- Ott, J. (1999). *Analysis of human genetic linkage*. JHU Press.
- Pajunen, P., Rissanen, H., Häkkinen, T., Jula, A., Reunanen, A., and Salomaa, V. (2010). The metabolic syndrome as a predictor of incident diabetes and cardiovascular events in the Health 2000 Study. *Diabetes and Metabolism*, **36**(5), 395–401.
- Palamara, P. F. and Pe'er, I. (2013). Inference of historical migration rates via haplotype sharing. *Bioinformatics*, **29**(13), i180–i188.
- Palamara, P. F., Lencz, T., Darvasi, A., and Pe'er, I. (2012). Length Distributions of Identity by Descent Reveal Fine-Scale Demographic History. *The American Journal of Human Genetics*, **91**(5), 809–822.
- Palin, K., Campbell, H., Wright, A. F., Wilson, J. F., and Durbin, R. (2011). Identity-by-descent-based phasing and imputation in founder populations using graphical models. *Genetic Epidemiology*, **35**(8), 853–860.
- Pasaniuc, B., Zaitlen, N., Shi, H., Bhatia, G., Gusev, A., Pickrell, J., Hirschhorn, J., Strachan, D. P., Patterson, N., and Price, A. L. (2014). Fast and accurate imputation of summary statistics enhances evidence of functional enrichment. *Bioinformatics (Oxford, England)*, **30**(20), 2906–2914.
- Pe'er, I., de Bakker, P. I. W., Maller, J., Yelensky, R., Altshuler, D., and Daly, M. J. (2006). Evaluating and improving power in whole-genome association studies using fixed marker sets. *Nature Genetics*, **38**(6), 663–667.
- Pennisi, E. (2007). Human Genetic Variation. *Science*, **318**(5858), 1842–1843.
- Powell, J. E., Visscher, P. M., and Goddard, M. E. (2010). Reconciling the analysis of IBD and IBS in complex trait studies. *Nature Publishing Group*, **11**(11), 800–805.
- Price, A. L., Patterson, N. J., Plenge, R. M., Weinblatt, M. E., Shadick, N. A., and Reich, D. (2006). Principal components analysis corrects for stratification in genome-wide association studies. *Nature Genetics*, **38**(8), 904–909.

- Pritchard, J. K. (2001). Are rare variants responsible for susceptibility to complex diseases? *The American Journal of Human Genetics*, **69**(1), 124–137.
- Purcell, S., Neale, B., Todd-Brown, K., Thomas, L., Ferreira, M. A. R., Bender, D., Maller, J., Sklar, P., de Bakker, P. I. W., Daly, M. J., and Sham, P. C. (2007). PLINK: a tool set for whole-genome association and population-based linkage analyses. *The American Journal of Human Genetics*, **81**(3), 559–575.
- Rabiner, L. R. (1989). A tutorial on hidden Markov models and selected applications in speech recognition. In *Proceedings of the IEEE*, pages 257–286. Alcatel-Lucent Bell Labs, Murray, United States.
- Rasmussen, M. D., Hubisz, M. J., Gronau, I., and Siepel, A. (2014). Genome-Wide Inference of Ancestral Recombination Graphs. *PLoS Genetics*, **10**(5), e1004342–27.
- Reich, D. E., Cargill, M., Bolk, S., Ireland, J., Sabeti, P. C., Richter, D. J., Lavery, T., Kouyoumjian, R., Farhadian, S. F., Ward, R., and Lander, E. S. (2001). Linkage disequilibrium in the human genome. *Nature*, **411**(6834), 199–204.
- Risch, N. and Merikangas, K. (1996). The future of genetic studies of complex human diseases. *Science*, **273**(5281), 1516–1517.
- Risch, N., de Leon, D., Ozelius, L., Kramer, P., Almasy, L., Singer, B., Fahn, S., Breakefield, X., and Bressman, S. (1995). Genetic analysis of idiopathic torsion dystonia in Ashkenazi Jews and their recent descent from a small founder population. *Nature Genetics*, **9**(2), 152–159.
- Risch, N. J. (2000). Searching for genetic determinants in the new millennium. *Nature*, **405**(6788), 847–856.
- Roach, J. C., Glusman, G., Smit, A. F. A., Huff, C. D., Hubley, R., Shannon, P. T., Rowen, L., Pant, K. P., Goodman, N., Bamshad, M., Shendure, J., Drmanac, R., Jorde, L. B., Hood, L., and Galas, D. J. (2010). Analysis of Genetic Inheritance in a Family Quartet by Whole-Genome Sequencing. *Science*, **328**(5978), 636–639.
- Roshyara, N. R. and Scholz, M. (2015). Impact of genetic similarity on imputation accuracy. *BMC Genetics*, **16**(1), 1–16.
- Rousset, F. (2002). Inbreeding and relatedness coefficients: What do they measure? *Heredity*, **88**(5), 371–380.
- Sanger, F. and Coulson, A. R. (1975). A rapid method for determining sequences in DNA by primed synthesis with DNA polymerase. *Journal of molecular biology*, **94**(3), 441–448.
- Sanger, F., Nicklen, S., and Coulson, A. R. (1977). DNA sequencing with chain-terminating inhibitors. *Proceedings of the National Academy of Sciences of the United States of America*, **74**(12), 5463–5467.
- Scally, A. and Durbin, R. (2012). Revising the human mutation rate: implications for understanding human evolution. *Nature Reviews Genetics*, **13**(10), 745–753.
- Schork, N. J., Murray, S. S., Frazer, K. A., and Topol, E. J. (2009). Common vs. rare allele hypotheses for complex diseases. *Current opinion in genetics & development*, **19**(3), 212–219.
- Schroff, M. H. (2016). *Genealogical properties of rare variation and their implications for demographic inference*. Ph.D. thesis, University of Oxford.
- Serre, J. L., Simon-Bouy, B., Mornet, E., Jaume-Roig, B., Balassopoulou, A., Schwartz, M., Taillandier, A., Boue, J., and Boue, A. (1990). Studies of RFLP closely linked to the cystic fibrosis locus throughout Europe lead to new considerations in populations genetics. *Human genetics*, **84**(5), 449–454.

- Shields, D. C., Collins, A., Buetow, K. H., and Morton, N. E. (1991). Error filtration, interference, and the human linkage map. *Proceedings of the National Academy of Sciences of the United States of America*, **88**(15), 6501–6505.
- Simons, Y. B., Turchin, M. C., Pritchard, J. K., and Sella, G. (2014). The deleterious mutation load is insensitive to recent population history. *Nature Publishing Group*, **46**(3), 220–224.
- Slack, J. (2014). *Genes: A Very Short Introduction*. Oxford University Press, Oxford.
- Slatkin, M. (2000). Allele age and a test for selection on rare alleles. *Philosophical Transactions of the Royal Society B: Biological Sciences*, **355**(1403), 1663–1668.
- Slatkin, M. (2008a). Inbreeding coefficients and coalescence times. *doi.org*, pages 1–9.
- Slatkin, M. (2008b). Linkage disequilibrium – understanding the evolutionary past and mapping the medical future. *Nature Reviews Genetics*, **9**(6), 477–485.
- Slatkin, M. and Bertorelle, G. (2001). The use of intraallelic variability for testing neutrality and estimating population growth rate. *Genetics*, **158**(2), 865–874.
- Slatkin, M. and Rannala, B. (2000). Estimating allele age. *Annual review of genomics and human genetics*, **1**(1), 225–249.
- Sobel, E., Papp, J. C., and Lange, K. (2002). Detection and integration of genotyping errors in statistical genetics. *The American Journal of Human Genetics*, **70**(2), 496–508.
- Stam, P. (1980). The distribution of the fraction of the genome identical by descent in finite random mating populations. *Genetical research*, **35**(02), 131.
- Stephens, M., Smith, N. J., and Donnelly, P. (2001). A new statistical method for haplotype reconstruction from population data. *The American Journal of Human Genetics*, **68**(4), 978–989.
- Stone, M. (1961). The Opinion Pool. *The Annals of Mathematical Statistics*, **32**(4), 1339–1342.
- Sturtevant, A. H. (1913). The linear arrangement of six sex-linked factors in drosophila, as shown by their mode of association. *Journal of Experimental Zoology Part A: Ecological Genetics and Physiology*, **14**(1), 43–59.
- Su, Z., Marchini, J., and Donnelly, P. (2011). HAPGEN2: simulation of multiple disease SNPs. *Bioinformatics*, **27**(16), 2304–2305.
- Tajima, F. (1983). Evolutionary relationship of DNA sequences in finite populations. *Genetics*, **105**(2), 437–460.
- Tajima, F. (1993). Measurement of dna polymorphism. *Mechanisms of molecular evolution*, pages 37–59.
- Takahata, N. (1993). Allelic genealogy and human evolution. *Molecular Biology and Evolution*, **10**(1), 2–22.
- Tavaré, S. (2004). Part I: Ancestral inference in population genetics. In *Lectures on probability theory and statistics*, pages 1–188. Springer.
- Tavaré, S., Balding, D. J., Griffiths, R. C., and Donnelly, P. (1997). Inferring coalescence times from DNA sequence data. *Genetics*, **145**(2), 505–518.
- Tennessen, J. A., Bigham, A. W., O'Connor, T. D., Fu, W., Kenny, E. E., Gravel, S., McGee, S., Do, R., Liu, X., Jun, G., Kang, H. M., Jordan, D., Leal, S. M., Gabriel, S., Rieder, M. J., Abecasis, G., Altshuler, D., Nickerson, D. A., Boerwinkle, E., Sunyaev, S., Bustamante, C. D., Bamshad, M. J., Akey, J. M., GO, B., GO, S., and Project, N. E. S. (2012). Evolution and Functional Impact of Rare Coding Variation from Deep Sequencing of Human Exomes. *Science*, **337**(6090), 64–69.

- Thompson, E. A. (1974). Gene Identities and Multiple Relationships. *Biometrics*, **30**(4), 667.
- Thompson, E. A. (1975). The estimation of pairwise relationships. *Annals of human genetics*, **39**(2), 173–188.
- Thompson, E. A. (1976). Estimation of age and rate of increase of rare variants. *The American Journal of Human Genetics*, **28**(5), 442–452.
- Thompson, E. A. (2008). The IBD process along four chromosomes. *Theoretical population biology*, **73**(3), 369–373.
- Thompson, E. A. (2013). Identity by descent: variation in meiosis, across genomes, and in populations. *Genetics*, **194**(2), 301–326.
- Tschermark, E. (1900). Über künstliche Kreuzung bei *Pisum sativum*. *Berichte der Deutschen Botanischen Gesellschaft*, **18**, 232–239.
- UK10K Consortium, Walter, K., Crooks, L., Memari, Y., Perry, J. R. B., Xu, C., Futema, M., Lawson, D., Iotchkova, V., Schiffels, S., Hendricks, A. E., Li, R., Floyd, J., Wain, L. V., Humphries, S. E., Barrett, J. C., Plagnol, V., Richards, J. B., Greenwood, C. M. T., Timpson, N. J., Soranzo, N., Danecek, P., Barroso, I., McCarthy, S., Tachmazidou, I., Durbin, R., Hurles, M. E., Kennedy, K., Palotie, A., Zeggini, E., Cucca, M., Huang, J., and Min, J. L. (2015). The UK10K project identifies rare variants in health and disease. *Nature*, **526**(7571), 82–90.
- Vartiainen, E., Laatikainen, T., Peltonen, M., Juolevi, A., Mannisto, S., Sundvall, J., Jousilahti, P., Salomaa, V., Valsta, L., and Puska, P. (2010). Thirty-five-year trends in cardiovascular risk factors in Finland. *International Journal of Epidemiology*, **39**(2), 504–518.
- Venter, J. C., Adams, M. D., Myers, E. W., Li, P. W., Mural, R. J., Sutton, G. G., Smith, H. O., Yandell, M., Evans, C. A., Holt, R. A., Gocayne, J. D., Amanatides, P., Ballew, R. M., Huson, D. H., Wortman, J. R., Zhang, Q., Kodira, C. D., Zheng, X. H., Chen, L., Skupski, M., Subramanian, G., Thomas, P. D., Zhang, J., Miklos, G. L. G., Nelson, C., Broder, S., Clark, A. G., Nadeau, J., McKusick, V. A., Zinder, N., Levine, A. J., Roberts, R. J., Simon, M., Slayman, C., Hunkapiller, M., Bolanos, R., Delcher, A., Dew, I., Fasulo, D., Flanigan, M., Florea, L., Halpern, A., Hannenhalli, S., Kravitz, S., Levy, S., Mobarry, C., Reinert, K., Remington, K., Abu-Threideh, J., Beasley, E., Biddick, K., Bonazzi, V., Brandon, R., Cargill, M., Chandramouliswaran, I., Charlab, R., Chaturvedi, K., Deng, Z., Di Francesco, V., Dunn, P., Eilbeck, K., Evangelista, C., Gabrielian, A. E., Gan, W., Ge, W., Gong, F., Gu, Z., Guan, P., Heiman, T. J., Higgins, M. E., Ji, R.-R., Ke, Z., Ketchum, K. A., Lai, Z., Lei, Y., Li, Z., Li, J., Liang, Y., Lin, X., Lu, F., Merkulov, G. V., Milshina, N., Moore, H. M., Naik, A. K., Narayan, V. A., Neelam, B., Nusskern, D., Rusch, D. B., Salzberg, S., Shao, W., Shue, B., Sun, J., Wang, Z. Y., Wang, A., Wang, X., Wang, J., Wei, M.-H., Wides, R., Xiao, C., Yan, C., Yao, A., Ye, J., Zhan, M., Zhang, W., Zhang, H., Zhao, Q., Zheng, L., Zhong, F., Zhong, W., Zhu, S. C., Zhao, S., Gilbert, D., Baumhueter, S., Spier, G., Carter, C., Cravchik, A., Woodage, T., Ali, F., An, H., Awe, A., Baldwin, D., Baden, H., Barnstead, M., Barrow, I., Beeson, K., Busam, D., Carver, A., Angela Center, Cheng, M. L., Curry, L., Danaher, S., Davenport, L., Desilets, R., Dietz, S., Dodson, K., Doucet, L., Ferriera, S., Garg, N., Gluecksmann, A., Hart, B., Haynes, J., Haynes, C., Heiner, C., Hladun, S., Hostin, D., Houck, J., Howland, T., Ibegwam, C., Johnson, J., Kalush, F., Kline, L., Koduru, S., Love, A., Mann, F., May, D., McCawley, S., McIntosh, T., McMullen, I., Moy, M., Moy, L., Murphy, B., Nelson, K., Pfannkoch, C., Pratts, E., Puri, V., Qureshi, H., Reardon, M., Rodriguez, R., Rogers, Y.-H., Romblad, D., Ruhfel, B., Scott, R., Sitter, C., Smallwood, M., Stewart, E., Strong, R., Suh, E., Thomas, R., Tint, N. N., Tse, S., Vech, C., Wang, G., Wetter, J., Williams, S., Williams, M., Windsor, S., Winn-Deen, E., Wolfe, K., Zaveri, J., Zaveri, K., Abril, J. F., Guigo, R., Campbell, M. J., Sjolander, K. V., Karlak, B., Kejariwal, A., Mi, H., Lazareva, B., Hatton, T., Narechania, A., Diemer, K., Muruganujan, A., Guo, N., Sato, S., Bafna, V., Istrail, S., Lippert, R., Schwartz, R., Walenz, B., Yooseph, S., Allen, D., Basu, A., Baxendale, J., Blick, L., Caminha, M., Carnes-Stine, J., Caulk, P., Chiang, Y.-H., Coyne, M., Dahlke, C., Mays, A. D., Dombroski, M., Donnelly, M., Ely, D., Esparham, S., Fosler, C., Gire,

- H., Glanowski, S., Glasser, K., Glodek, A., Gorokhov, M., Graham, K., Gropman, B., Harris, M., Heil, J., Henderson, S., Hoover, J., Jennings, D., Jordan, C., Jordan, J., Kasha, J., Kagan, L., Kraft, C., Levitsky, A., Lewis, M., Liu, X., Lopez, J., Ma, D., and Majoros... (2001). The Sequence of the Human Genome. *Science*, **291**(5507), 1304–1351.
- Viterbi, A. J. (1967). Error Bounds for Convolutional Codes and an Asymptotically Optimum Decoding Algorithm. *IEEE Transactions on Information Theory*, **13**(2), 260–269.
- Voight, B. F. and Pritchard, J. K. (2005). Confounding from Cryptic Relatedness in Case-Control Association Studies. *PLoS Genetics*, **1**(3), e32–10.
- Wakeley, J. (2008). *Coalescent Theory: An Introduction*. W. H. Freeman.
- Wakeley, J. and Wilton, P. (2016). Coalescent and models of identity by descent. In R. M. Kliman, editor, *Encyclopedia of Evolutionary Biology*, pages 287 – 292. Academic Press, Oxford.
- Watson, J. D. and Crick, F. H. (1953). Molecular structure of nucleic acids; a structure for deoxyribose nucleic acid. *Nature*, **171**(4356), 737–738.
- Watterson, G. (1996). Motoo Kimura's Use of Diffusion Theory in Population Genetics. *Theoretical population biology*, **49**(2), 154–188.
- Watterson, G. A. (1975). On the number of segregating sites in genetical models without recombination. *Theoretical population biology*, **7**(2), 256–276.
- Watterson, G. A. (1976). Reversibility and the age of an allele. i. moran's infinitely many neutral alleles model. *Theoretical Population Biology*, **10**(3), 239–253.
- Weinberg, W. (1908). Über den Nachweis der Vererbung beim Menschen. *Jahreshefte des Vereins für vaterländische Naturkunde in Württemberg.*, **64**, 368–382.
- Weissenbach, J. (1993). A second generation linkage map of the human genome based on highly informative microsatellite loci. *Gene*, **135**(1-2), 275–278.
- Wheeler, D. A., Srinivasan, M., Egholm, M., Shen, Y., Chen, L., McGuire, A., He, W., Chen, Y.-J., Makijani, V., Roth, G. T., Gomes, X., Tartaro, K., Niazi, F., Turcotte, C. L., Irzyk, G. P., Lupski, J. R., Chinault, C., Song, X.-z., Liu, Y., Yuan, Y., Nazareth, L., Qin, X., Muzny, D. M., Margulies, M., Weinstock, G. M., Gibbs, R. A., and Rothberg, J. M. (2008). The complete genome of an individual by massively parallel DNA sequencing. *Nature*, **452**(7189), 872–876.
- Winkler, H. (1920). *Verbreitung und Ursache der Parthenogenesis im Pflanzen- und Tierreich*. Verlag G. Fischer, Jena.
- Wiuf, C. and Hein, J. (1997). On the number of ancestors to a DNA sequence. *Genetics*, **147**(3), 1459–1468.
- Wright, S. (1921). Systems of Mating. I. the Biometric Relations between Parent and Offspring. *Genetics*, **6**(2), 111–123.
- Wright, S. (1922). Coefficients of Inbreeding and Relationship. *The American Naturalist*, **56**(645), 330–338.
- Wright, S. (1931). Evolution in Mendelian Populations. *Genetics*, **16**(2), 97–159.
- Yu, N., Zhao, Z., Fu, Y. X., Sambuughin, N., Ramsay, M., Jenkins, T., Leskinen, E., Patthy, L., Jorde, L. B., Kuromori, T., and Li, W. H. (2001). Global patterns of human DNA sequence variation in a 10-kb region on chromosome 1. *Molecular Biology and Evolution*, **18**(2), 214–222.